INVESTIGATIONS ON REACTIVELY DRIVEN ETCHING MECHANISMS IN PLASMA JET-BASED PRECISION SURFACE MACHINING OF BOROSILICATE CROWN OPTICAL GLASS

Von der Fakultät Maschinenwesen

der

Technischen Universität Dresden

zur

Erlangung des akademischen Grades

Doktor-Ingenieur (Dr.-Ing.)

angenommene Dissertation

von

M.Sc. Faezeh Kazemi
geboren am 3. Juni 1985 in Estahban

Tag der Einreichung: 8. März 2021
Tag der Verteidigung: 28. Juli 2021

Gutachter: Prof. Dr. rer. nat. Thomas Arnold
Prof. Dr.-Ing. Andrés F. Lasagni

Vorsitzende der Promotionskommission:
Prof. Dr. rer. nat. habil. Cornelia Breitkopf

Diese Arbeit wurde im Zeitraum Mai 2017 bis März 2021 am Leibniz-Institut für Oberflächenmodifizierung e.V., Leipzig angefertigt.
This work was prepared from May 2017 until March 2021 at the Leibniz Institute of Surface Emgineering (IOM), Leipzig.
Betreuer: Prof. Dr. rer. nat. T. Arnold

To my beloved parents …

گر مرا هیچ نباشد نه به دنیا نه به عقبی، چون تو دارم همه دارم دگرم هیچ نباید.

-- سعدی

Wenn ich nichts habe, weder in dieser Welt noch im Jenseits,
weil ich dich habe, habe ich alles, und das ist genug.

If I have nothing, neither in the world nor hereafter,

because I have you, I have everything, and that is enough.

-- Saadi

Bibliographische Beschreibung

Kazemi, Faezeh

Investigations on reactively driven etching mechanisms in plasma jet-based precision surface machining of borosilicate crown optical glass

Technische Universität Dresden, Dissertation.

142 Seiten, 239 Quellen, 83 Abbildungen, 17 Tabellen, 46 Gleichungen.

KURZFASSUNG

Der steigende Bedarf an hochpräzisen optischen Elementen, die komplexe Oberflächendesigns aufweisen, wie z. B. Freiformlinsen, erfordert eine stetige Verbesserung der optischen Fertigungstechnologien. Aufgrund der variierenden lokalen Steigungen werden bei deterministischen Oberflächenbearbeitungsprozessen in der Regel lokal wirkende, sogenannte Subapertur-Werkzeuge eingesetzt, die darauf abzielen, den Restfehler in Bezug auf die vorgegebene Oberflächenform zu minimieren. Ein gemeinsames Merkmal deterministischer Bearbeitungstechnologien ist die Tatsache, dass die Werkzeugfunktion eine charakteristische lokale Verteilung des Materialabtrags aufweist. Abhängig von der jeweiligen Bearbeitungstechnologie kann die Werkzeugfunktion ein nichtlineares komplexes Verhalten aufweisen, das in den Algorithmen zur Verweilzeitberechnung entsprechend berücksichtigt werden muss. Die reaktive Plasmastrahl-Bearbeitung (PJM) ist ein Werkzeug zum Ätzen von Subaperturen, das zunehmend bei der Herstellung von optischen Freiform-Elementen aus Silizium, Quarzglas oder Siliziumkarbid sowie bei einigen anderen Arten von optischen Gläsern eingesetzt wird. Beim lokalisierten chemischen Trockenätzen hängt die Abtragsrate zum einen von der Konzentrationsverteilung der reaktiven Spezies und zum anderen von der Temperaturverteilung der Oberfläche ab.

Die vorliegende Dissertation zielt darauf ab, fortschrittliche Strategien zu entwickeln, um die Anwendung von PJM auf optische Gläser über das reine optische Glas auf Quarzbasis hinaus zu erweitern. Borosilikat-Kronglas (bekannt z.B. als N-BK7®) wird aufgrund seiner komplexen chemischen Zusammensetzung und seiner breiten Anwendung in verschiedenen optischen Systemen als das zu untersuchende Material gewählt. In diesem Fall sind die Plasmaoberflächenwechselwirkungen wesentlich komplexer und beeinflussen die raum-zeitliche Entwicklung der Werkzeugfunktion erheblich, die in einigen Fällen stark von einer gaußnahen Funktion abweicht. Solche Werkzeugfunktionsformen werden durch inhomogene Anlagerung der nichtflüchtigen Ätznebenprodukte verursacht. Es wird ein semiempirisches quantitatives Modell entwickelt, um die nichtlinearen Eigenschaften der Werkzeugfunktion zu beschreiben. Das entwickelte Vorhersagemodell zeigt, dass solche Werkzeugfunktionen aufgrund der Welligkeitsbildung und der hohen Oberflächenrauhigkeit nicht für stabile Bearbeitungsprozesse geeignet sind. Die Untersuchungen in dieser Arbeit zeigen jedoch auch, dass das Ätzen bei erhöhten Substratoberflächentemperaturen die Bildung einer gleichmäßiger strukturierten Restschicht fördert, was zu einer Werkzeugfunktion führt, die eine nahezu Gaußsche Funktionsform aufweist. Allerdings hängt auch dann die lokale Ätzrate von dem lokalen Dicken der gebildeten Restschicht während eines dynamischen Bearbeitungsprozesses ab, und somit weicht die resultierende Werkzeugfunktion von der stabilen Rotationsform ab. Folglich können Standardmethoden zur Verweilzeitberechnung, die auf Werkzeugfunktionen mit konstanter Funktionsform beruhen, hier nicht angewendet werden. Daher wird das Verhalten der

Abtragsratenfunktion in Abhängigkeit von der Restschichtdicke untersucht. Mit diesen Informationen wird ein numerisches Modell zur Berechnung des Materialabtrags entwickelt, das die raum-zeitliche Variation der Ätzrate berücksichtigt. Basierend auf diesem Modell wird ein rekursiver Algorithmus zur Bestimmung der lokalen Verweilzeiten eingeführt, um eine vordefinierte Entfernungs-Tiefenkarte zu erhalten.

Darüber hinaus wird unter Verwendung des Deal-Grove-Konzepts ein umfassendes chemisch/physikalisches Modell entwickelt, um den Einfluss der Restschicht und der Oberflächentemperatur auf die Entwicklung der N-BK7-Ätztiefe über die Plasmaverweilzeit vorherzusagen. Das vorgeschlagene Modell kann den plasmabasierten deterministischen Freiformflächenbearbeitungsprozess von optischen Gläsern potenziell verbessern.

Schließlich wird als alternative Lösung ein Verfahren bestehend aus PJM und laserunterstützter (LE) Reinigung für die Bearbeitung von N-BK7 bei Raumtemperatur ohne Vorwärmung der Oberfläche vorgeschlagen. Insbesondere ein hybrides Plasma-Laser-Verfahren erscheint aufgrund der geringen Rauheit, der konstanten Ätzrate und der Möglichkeiten zur zusätzlichen Gestaltung der Werkzeugfunktion vielversprechend für den Einsatz in der Ultrapräzisionsbearbeitung und strukturierung von optischem Glas.

ABSTRACT

The increasing demand for high-precision optical elements that exhibit complex surface designs such as freeform lenses call for steady improvements of optical manufacturing technologies. Because of the varying local slopes, locally acting so called sub-aperture tools are usually used in deterministic surface machining processes aiming at minimizing residual error with regard to the specified surface shape. A common feature of deterministic processing technologies is the fact that the tool function exhibits a characteristic local distribution of material removal. Depending on the respective machining technology, the tool function can exhibit a nonlinear complex behavior that must be considered appropriately in the dwell time calculation algorithms. Reactive plasma jet machining (PJM) is an etching sub-aperture tool increasingly applied in the production of freeform optical elements made of silicon, fused silica, or silicon carbide, as well as to some other types of optical glasses. Caused by localized chemical dry etching process, the removal rate depends on the one hand on the concentration distribution of reactive species and on the other hand on the surface temperature distribution.

The present dissertation aims to develop advanced strategies for extending the application of PJM to optical glasses beyond the pure silica-based optical glass. Borosilicate crown glass (known e.g. as N-BK7®) is chosen as the material under investigation due to its complex chemical composition and its wide application in various optical systems. In this case, the plasma-surface interactions are much more complex and affect the spatiotemporal development of the tool function significantly, which in some cases differs strongly from a near-Gaussian function. Such tool function shapes are caused by inhomogeneous build-up of the nonvolatile etching byproducts. A semi-empirical quantitative model is developed to describe the non-linear characteristics of the tool function. The developed prediction model reveals that such tool functions are not suitable for stable machining processes due to the formation of waviness and high level of surface roughness. However, investigations in thesis also demonstrate that etching at increased substrate surface temperatures promotes the formation of a more uniformly structured residual layer leading to a footprint tool function exhibiting a near-Gaussian functional form. However, even then the local etching rate depends on the local thickness of the formed residual layer during a dynamic machining process, and hence the resulting tool function deviates from the stable rotationally form. Consequently, standard methods used for dwell time calculation, that are based on tool functions exhibiting a constant functional form, cannot be applied here. Therefore, the removal rate function behavior is investigated depending on residual layer thickness. With this information, a numerical model for the calculation of material removal is developed that takes the spatiotemporal variation of the etching rate into account. Based on this model, a recursive algorithm is introduced for the determination of local dwell times achieving a predefined removal depth map.

Moreover, by inspiring the Deal-Grove concept, a comprehensive chemical/physical model is developed to predict the effect of the residual layer and surface temperature on the evolution of N-BK7

etch depth over plasma dwell time. The proposed model can potentially improve plasma-based deterministic freeform surface machining process of optical glasses.

Finally, as an alternative solution, a procedure consisting of PJM and laser enhanced (LE) cleaning is proposed for the machining of N-BK7 at room temperature without preheating the surface. Especially, a hybrid plasma-laser technique seems promising for the application in ultra-high precision machining and structuring of optical glass due to the low roughness, constant etching rate, and the possibilities for additional shaping of the tool function.

ACKNOWLEDGMENTS

The work presented in this thesis was carried out at the Leibniz Institute of Surface Engineering (IOM). Financial support provided by German Federal Ministry of Education and Research (BMBF) within the framework of the InnoProfile-Transfer initiative 03IPT706X “Ultra-precision manufacturing using atomic particle beams” is gratefully acknowledged.

First and foremost, my heartfelt thanks to my *Doktorvater* Prof. Dr. rer. nat. Thomas Arnold for not only giving me the opportunity to work on this fascinating topic, but also for supporting me with patience. Despite his busy agenda, he always found the time to train me through enlightening discussions how to perform different experiments, analyze the data, do simulations, and present the results in the best way. Your profound depth of knowledge and masterly supervision style have made my path much brighter throughout my work and have always been a valuable source of inspiration to me. For all these reasons, I owe a debt of gratitude to you for every single one of my career successes from now to future.

I would like sincerely thank Prof. Dr. André Anders for leading the IOM and his work in maintaining the pleasant working conditions. Many thanks go to Dr. Georg Böhm for providing constructive discussions and support. I would like to extend my thanks to Dr. Klaus Zimmer and Dr. Martin Ehrhardt for pleasant collaboration and constructive discussions.

My thanks go to my colleagues, Mr. Hendrik Pätzelt, Dr. Antje Lehmann, Ms. Heike Müller, Mr. Fred Pietag and Mr. Florian Hölzel as well as the whole IOM community for creating a comfortable working atmosphere. I sincerely thank Mr. Dietmar Hirsch, Mr. Toni Liebeskind and Dr. Jens Bauer for supplying the measurement systems.

My deep gratitude goes to my family and friends, all around the world, for their support and love throughout my whole life. Most of all, I thank my parents who taught me the real value of life: to be first an altruistic person and then successful one. *Maman & Baba,* I know the separation from me was the bitterest possible thing for you, but you endured it cordially just to support my desire; if I become a mother, you are my true role models. Thank you, my wonderful brothers Ali and Hamid, for always being such caring persons and of course for all the fun we have. From bottom of my heart, I would like to thank my loving husband, Pasha. First and foremost, you are my best friend.

Finally, I would like to thank Germany with all my heart. The beautiful and green country that welcomed me eight years ago as an international student and provided generously the platform for growth and progress to the point where it has become my first home.

INDEX OF CONTENTS

1 Introduction 1

1.1 Motivation 1

1.2 Thesis outline 2

2 General Concepts 4

2.1 History of optical manufacturing 4

2.2 Basic principles of theoretical optics 5

2.2.1 Wavefront propagation and optical path difference (OPD) 6

2.2.2 Optical aberration and imaging error 7

2.3 Types and form-complexities of optical elements 8

2.4 General specifications of optics 12

2.5 Applications of modern optics 16

2.5.1 (E)UV-lithography 16

2.5.2 Mirror telescope 17

2.5.3 Imaging optics 18

2.5.4 Illumination optics 18

2.5.5 Laser beam shaping 19

2.5.6 Synchrotron beam line optics/FEL optics 20

3 The-State-of-the-Art in Manufacturing Precision Optical Elements 21

3.1 Classification of processing technologies 21

3.2 Replicative (forming) manufacturing 22

3.2.1 High-precision plastic molding 22

3.2.2 High-precision glass molding 23

3.2.3 Hybrid press technology 23

3.3 Subtractive manufacturing and possible processing chains 24

3.3.1 Surface figuring 25

3.3.2 Polishing 26

3.3.3 Local figure correction 27

3.3.4 Advances in abrasive methods for precision aspheres manufacturing 32

3.4 Laser-based methods 33

3.5 Ion beam technology 35

3.6 Classification and generation of plasmas 36

3.6.1 Plasma-based pure chemical etching: mechanisms and kinetics 37

3.6.2 Plasma technology for high efficiency machining of optical elements 38

3.6.3 Plasma jet machining (PJM) 39

3.7 Aspects of optical testing techniques 41

4 Experimental Methods 44
4.1 Experimental setup 44
4.1.1 Plasma jet facility 44
4.1.2 Laser workstation 46
4.2 Optical glass samples: N-BK7 and fused silica 47
4.2.1 Surface temperature measurement 48
4.3 Methods of plasma jet machining 48
4.4 Sample preparation 50
4.5 Measurement techniques for surface analysis 51
4.5.1 Topography analysis 51
4.5.2 Surface structure assessment 52
4.5.3 Surface chemistry analysis 52
5 Results and Discussion 54
5.1 Evaluation of pre-processing cleaning step 54
5.2 Investigation of fluorine-based plasma jet interactions with optical glass 55
5.2.1 Influence of O_2 addition on CF_4 decomposition in plasma jet 55
5.2.2 Effect of temperature on surface interactions with plasma 58
5.2.3 Variation of etching rate with mean input power 59
5.2.4 Influence of distance between substrate surface and plasma discharge 61
5.3 Freeform figuring of optical glass by PJM 62
5.4 Surface characterization of plasma-treated N-BK7 64
5.4.1 Analysis of the residual layer formed on the surface 65
5.4.2 Lateral distribution of residual layer 67
5.4.3 Etch depth profile as a function of plasma dwell-time 69
5.4.4 Roughness measurement 70
5.5 Development of a model for numerical convolution 71
5.5.1 Estimation of spatiotemporal behavior of etching rate *R(r,t)* 71
5.5.2 Non-linear characteristics of plasma tool function 72
5.5.3 Modeling of dynamic machining process 73
5.6 Improvement of the plasma jet machining process at elevated surface temperature 76
5.6.1 Variation of material removal by surface temperature 77
5.6.2 Analysis of residual layer at different surface temperatures 79
5.6.3 Area etching at elevated surface temperature 86
5.7 Modelling approaches to deterministic freeform surface machining 88
5.7.1 Determining depth-dependent removal function *R(r, D(r,t))* at elevated temperature.. 88
5.7.2 Simulative approach to calculate material removal 93
5.7.3 Recursive algorithm for calculation of dwell-time matrix 96

5.8 Deal-Grove inspired model for simulating plasma etching 99
5.8.1 Concept of Deal-Grove model 100
5.8.2 Modelling plasma jet etching 100
5.9 Laser-enhanced plasma jet machining (LE-PJM) 110
5.9.1 Cleaning techniques for surface residues on plasma etching tracks 110
5.9.2 Proposed sequential approach for steady state etching 113
6 Conclusions 120
7 Outlook 124
8 References 125

LIST OF ABBREVIATIONS

Arc-enhanced plasma machining technology	AEPM
Atmospheric pressure plasma processing	APPP
Atomic force microscopy	AFM
Computer controlled bonnet polishing	CCBP
Deal-Grove	DG
Digital micromirror devices	DMD
Energy dispersive X-ray	EDX
Energy-dispersive X-ray spectroscopy	EDS
Field of view	FOV
Finite element method	FEM
Fluid jet polishing	FJP
Focused ion beam	FIB
Free-electron laser	FEL
Free-space optical	FSO
Full width at half maximum	FWHM
Fused silica	FS
High-intensity discharge	HID
Inductively coupled plasma	ICP
Infrared	IR
Ion beam figuring	IBF
Ion beam smoothing	IBS
Laser-enhanced	LE
Laser-enhanced plasma jet machining	LE-PJM
Laser etching at surface adsorbed layers	LESAL
Laser-induced backside wet etching	LIBWE
Laser-induced backside dry etching	LIBDE
Light emitting diode	LED
Liquid crystal display	LCD
Local thermodynamic equilibrium	LTE
Magnetorheological fluid	MRF

Non-local thermodynamic equilibrium	NLTE
Numerical aperture	NA
Optical path difference	OPD
Peak value	PV
Plasma chemical vaporization machining	PCVM
Plasma jet machining	PJM
Poly-ellipsoid	PE
Power spectral density	PSD
Radio frequency	RF
Reactive atom plasma technology	RAPT
Root mean square	RMS
Secondary-ion mass spectrometry	SIMS
Scanning electron microscope	SEM
Subsurface damage	SSD
Ultra-violet	UV
Vacuum ultraviolet	VUV
Visual	VIS
Volumetric removal rate	VRR
White light interference	WLI
White light interference microscopy	WLIM
X-Ray diffraction	XRD
X-Ray photoelectron spectroscopy	XPS

LIST OF SYMBOLS

Latin Symbols

A	Surface area
$A_{\mathrm{In}}(r)$	Amplitude of incident plane wave
$A_{\mathrm{Out}}(r)$	Amplitude of optical output wave
B	Quadratic rate constant
B/A	Linear rate constant
c	Curvature of the conic
C_{p}	Preston coefficient
C	Concentration of reactant molecules forming a unit volume of residual layer
C_1	Equilibrium concentration of the fluorine in the surrounding gas
C_2	Concentration of the fluorine at the outer surface
C_3	Concentration of residual layer near the residues-substrate interface
$C(v)$	Compensation function
d	Thickness
D_{max}	Maximum depth
D_2	Effective diffusion coefficient
$D(x,y)$	Target removal depth
$\widehat{D}(x,y)$	Resulted removal depth
$\mathrm{d}C_2/\mathrm{d}x$	Concentration gradient in the residual layer
E_a	Activation energy
E_R	Residual topography error
f	Frequency
F	Focal length of lens
f_p	Pulse repetition frequency
$f(\rho)$	Sagitta error
h_1	Gas-phase transport coefficient
I	Total number of time steps for the given maximum etching time
J_1	Flux of fluorine in gas
J_2	Flux of fluorine in residual layer

J_3	Flux of fluorine in reaction with substrate material
$j(r)$	Radial current density distribution
k	Surface rate constant
k_B	Boltzmann constant in eV
L	Residual layer thickness
Q	Load
MRR	Material removal rate
n	Line iteration index
N	Number of iterations in dynamic etching
N_d	Number of defects
n_{ref}	Refractive index of lens
$\mathrm{OP}(r)$	Optical path
p	Time-step index
PV	Peak value
P_E	Effective power
P_M	Mean input power
P_p	Pulse peak power
P_R	Reflected mean power
C	Concentration of reactant molecules forming a unit volume of the residual layer
r	Radial distance
R_q	Root mean square roughness
R_z	Maximum profile height (peak to valley) value
$R(x,y)$	Tool function
S_a	Roughness
t	Dwell time
T_g	Transformation/transition temperature
T_h	Initial temperature
T_i	Temperature of ions
t_{max}	Maximum etching time
T_{max}	Peak value of surface temperature distribution
t_{on}	Laser pulse duration
t_p	Pulse width

T_r	Temperature of molecules with rotational degree of freedom
T_s	Local surface temperature
T_e	Electron temperature
T_v	Temperature of vibrational excitation of molecules
T_0	Temperature of heavy neutrals
$W_{\mathrm{In}}(r)$	Incident plane wave
$W_{\mathrm{Out}}(r)$	Optical output wave
x	Lateral distance
$z(r)$	Impedance
$z_1(r)$	Input substrate-air surface
$z_2(r)$	Output substrate-air surface

Greek Symbols

$\alpha_1(r)$	Pre-exponential constant
$\alpha_2(r)$ [m.s^{-1}]	Pre-exponential constant
Δl	Layer thickness
Δf	Frequency change
Δy	Line feed
Δd	Working distance
ε	Emissivity
$\Phi_{\mathrm{Out}}(r)$	Phase of optical output wave
κ	Conic constant
λ	Wavelength
ρ	Cylindrical coordinate
σ	Tilt angle in arc minutes
Γ	Magnification
Φ	Laser fluence
v	Scan velocity
σ	Standard deviation
τ	Time related parameter in Deal-Grove model

1 Introduction

1.1 Motivation

Advanced optical systems have substantial impact on everyday life by finding a variety of applications in (E)UV lithography, laser beam shaping, free-electron laser (FEL), illumination system, imaging system (i.e., mobile camera), space telescope and so on. Such optical systems rely on high-precision and ultra-precision optical elements with complex surface designs including aspherical and freeform lenses for fabrication of which steady improvements of leading-edge optical manufacturing technologies are demanded.

A lot of effort has been spent recently for the development of novel optical manufacturing technologies that are as accurate, robust, and affordable as conventional ones for spherical shapes. However, there is still a large room for improvement as for instance fabricating freeform lenses with high surface quality is much more costly than the corresponding spherical ones. Because of the lacking rotational symmetry and varying local slopes, intrinsic difficulties exist for production of asymmetrical optical elements. Significant improvement is achieved by introducing different types of locally acting, so-called sub-aperture tools employed in deterministic surface machining processes for highly efficient and affordable surface figuring and local figure correction of optical elements. Amongst them, plasma jet machining (PJM) technique has been recently successfully applied in the production of freeform optical elements made of silicon, fused silica, or silicon carbide, as well as to some other types of optical glasses. Here, the underlying principle of material removal is a localized chemical dry etching process performed by a fluorine-containing jet-like plasma discharge that interacts with the substrate material whereby the material is converted to gaseous state. The chemical mechanism of material removal is, however, limiting the applicability of PJM, since only materials that can be fully converted to volatile products are easily accessible to plasma jet-based processing. On the other hand, application-specific optical glass properties are achieved by utilizing complex material compositions including silica as the main constituent as well as different admixtures like e.g. metal oxides. Plasma jet machining of such materials in deterministic processing scheme has shown to be problematic since a non-volatile surface layer may form during etching depending on the respective glass composition, which affects the local etching rate, and thus the plasma tool function (i.e., the characteristic lateral material removal rate function). Consequently, such behavior leads to a complex time-dependent etching process. Since deterministic surface machining processes depend on a well-describable etch rate distribution that is sufficiently stable in time, precise surface machining of optical glasses is currently not possible without deeper knowledge of the mechanisms at work and their model description.

To extend the applicability of PJM to optical glasses beyond the pure silica-based materials, borosilicate crown glass (known e.g., as N-BK7® made by Schott) is chosen as the material under investigation due to its complex chemical composition and its wide application in various optical systems.

The main objectives of this work are

(i) to understand the general principles of plasma jet surface interactions that lead to a modified surface with respect to layer formation and material removal,

(ii) to identify processing conditions that are potentially suitable for application in a deterministic processing scheme,

(iii) to develop simulation approaches that account for the spatiotemporal variations in the removal function,

(iv) to show the applicability of such approaches in a deterministic process to produce a freeform surface of a desired prescribed shape.

Based on these research objectives, this dissertation is organized into sections that describe the novel workflow for manufacturing freeform surfaces out of N-BK7 using fluorine-based PJM.

1.2 Thesis outline

This thesis is organized into seven core chapters, each of those directing specific inquiries and issues. The key contents of each chapter are presented as follow.

Chapter 2 is the introductory chapter for the concepts which are used in the thesis. It starts with the history of optical manufacturing. Then, the necessary theoretical background of optics is explained by studying the propagation of an optical wavefront through a single lens. The upper limit for the performance of optical elements is discussed. Moreover, a classification of optical elements based on their main functionalities and form complexities is presented. The general specifications of optics are defined according to DIN ISO 10110. Finally, several application-cases using freeform and aspherical elements are provided.

In **Chapter 3**, an overview on a variety of processing technologies available in manufacturing of precision optical elements is provided. The major differences between these manufacturing technologies, and their dependence on materials, the production volume and the required tolerance values are outlined. Moreover, the mechanism, limitations, advantages, and the highest achievable accuracy of each manufacturing technique are pointed out.

Chapter 4 presents the experimental part of the investigation. The used setups including plasma jet facility and laser workstation are described in detail. Moreover, the choice of the materials used for

experiments is introduced, and the measurement techniques adopted for analyzing the results are explained.

Chapter 5 provides the comprehensive results and discussion carried out in this thesis. The first four sections describe optimization and applicability of PJM for deterministic surface processing of optics particularly regarding to challenges in freeform figuring of N-BK7. The experimental results are analyzed and modeled by simulation algorithms. Based on these findings, the development of a semi-empirical quantitative model is described to explain the non-linear characteristics of the tool function on N-BK7. Afterwards, effectiveness of temperature treatment on surface machining is investigated, and simulation approaches are introduced based on the obtained results for deterministic freeform surface machining. Furthermore, in this chapter, the Deal-Grove (DG) concept is inspired to derive a physical /chemical model that includes all aspects in the complexity of interactions at the N-BK7–plasma interface on an atomic level. Finally, the sequentially combined laser-enhanced plasma jet machining (LE-PJM) is introduced as an alternative solution for application of ultra-high precision machining of N-BK7.

Chapter 6 provides conclusions and summary for the approaches presented in this thesis and review the accomplishments of the investigation. At the end, in **Chapter 7**, the prospect of future development and potential challenges are discussed.

2 General Concepts

2.1 History of optical manufacturing

The history of optical manufacturing goes back to around 3000 B.C. when the art of glass melting was developed in Egypt and Mesopotamia[1]. Nevertheless, the deliberate use of glass for optical applications came much later. Optics commenced with the development of lenses made from polished crystal, often quartz, dated from as early as 2000 B.C.[2]. These practical advances were kept on by the evolution of theories of light and vision as well as the development of geometrical optics[3]. The invention of spectacles in the 13th century from the hemispherical plano-convex lenses was an important step in the development of all subsequent optical instruments, such as telescopes and microscopes[4]. Optical theory proceeded in the mid-17th century, and a variety of optical phenomena including diffraction, reflection and refraction were described[5-7]. In the 18th century, soda glass was produced for the first time. The resulting soda glass could significantly expand the possibilities of optical glass production leading to invention of novel optical devices. Prominent milestones in the development of optical devices were the inventions of the microscope and telescope. Relying on those achievements, in the 19th century, an efficient lens telescope was designed and developed by Fraunhofer[8]. Meanwhile, the optical glass quality was enhanced with regard to streaks and bubbles, the manufacturing process of optics became industrialized by developing machines for processing larger-diameter glasses, and measurement procedures were developed for testing the surface quality[9-11].

A further milestone in the development of the optical industry was reached at the end of the 19th century. At that time, the collaboration between Zeiss, Abbe and Schott became the basis of the optical industry and the further development of optical devices in precision optical engineering[12]. In addition to a large number of newly developed optical glasses, the invention of the heat-resistant borosilicate glass in 1887 by the Jena glass chemist was one of the noticeable achievements[4].

Modern optics, that became popular in the 20th century, associate mainly with the electromagnetic or quantum properties of light but do encompass optical engineering[13-15]. The major subfield of modern optics, optical engineering, specifically deals with illumination engineering, photonics, and optoelectronics with practical applications like lens design, fabrication and testing of optical components, and image processing[16]. To date, special areas of optical research focus on the simulation, construction, material selection, coatings, assembly, measurement technology, and prototype development of advanced optical technologies[17]. The (E)UV lithography, laser beam shaping, free-electron laser (FEL), illumination system, imaging system (i.e., mobile camera) and space telescope are some examples of advanced optical technologies eventuated from modern optics[18-21]. Such technologies require optical elements with freeform shape and ultra-precision surface quality to achieve further optimization of beam paths, improvement of imaging performance and miniaturization of systems[22]. Over the last ten years, leading-edge optical manufacturing technologies, which are the key know-how

for generating modern optics, have been steadily improving. The invention of the copy grinding machine, the application of CNC machining for polishing and grinding, and the advances in local figure correction methods without a polishing pad have been the three manifest milestones that revolutionized the fabrication of modern optics like freeform surfaces. The first shape-copy machine was designed by Descartes in 1638 where a grinding stone was applied as a master[23]. Later in 1920, Descartes concept was inspired and a copy grinding machine was built at Zeiss for fabricating aspheres[24]. In this machine, the aspherical lens rotates while it has a line contact with the grinding wheel that is moved in an adjusted polar coordinate system. This copy grinding technique was used for primary zonal grinding, but the surface form precision was restricted due to a lacking constancy of the machine during the scanning of the master. Later, the zonal grinding process with CNC machines considerably improved the manufacturing of aspherical and freeform surfaces. Subsequently, between 1968 and 1976, early approaches to computer-assisted zonal polishing and grinding of aspheres were introduced. Afterwards, the invention of a series of advanced sub-aperture machining technologies used for local figure correction methods made a significant leap towards the cost-optimized production of such sophisticated optical surfaces[25-26]. Research in this area is still ongoing, and many activities are targeted to develop optical freeform manufacturing methods as precise and cost-effective as those for spherical lenses. In **Figure 2.1**, the progress of optical manufacturing over history is summarized.

Figure 2.1 *Historical progress in optical manufacturing.*

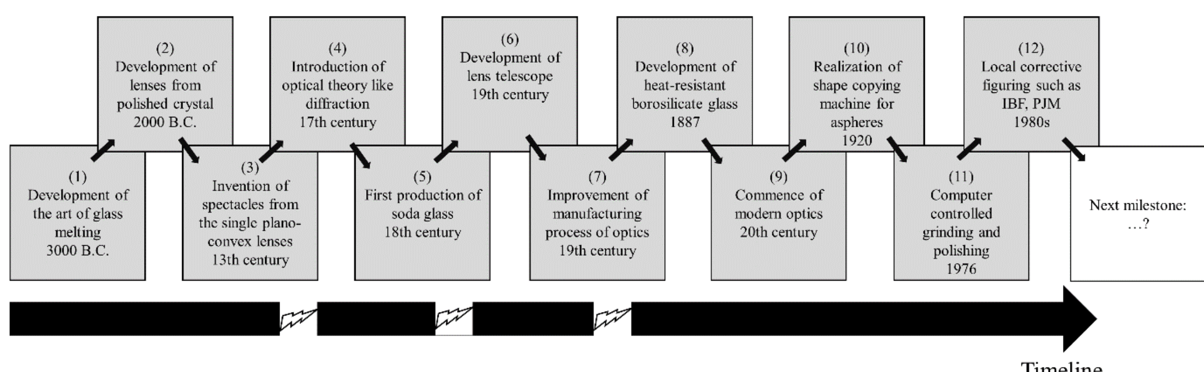

2.2 Basic principles of theoretical optics

In this section, to assert the physical concepts of image generation, as the simplest case, the propagation of a monochromatic plane wave in a single lens is investigated. The contribution of the optical material parameters and the geometry parameters of the lens surfaces in the wavefront error is explained to achieve ideal optical path difference (OPD). Moreover, the upper limit for performance of optical elements imposed by either the diffraction effects or manufacturing and design process is discussed.

2.2.1 Wavefront propagation and optical path difference (OPD)

A simple lens is a piece of transmissive element of thickness *d* with two appropriately designed substrate-air surfaces. As light passes through a lens, it is affected by the lens' profile or substrate. A single lens transfers an incident plane wave $W_{In}(r)$ of amplitude $A_{In}(r)$ and zero phase into an optical output wave $W_{Out}(r)$ of amplitude $A_{Out}(r)$ and phase $\Phi_{Out}(r)$ where r is the radial distance in the coordinate normal to the wave propagation direction z. The phase change $\Phi_{Out}(r)$ determines the optical quality of image while the amplitude change can reduce the wave intensity.

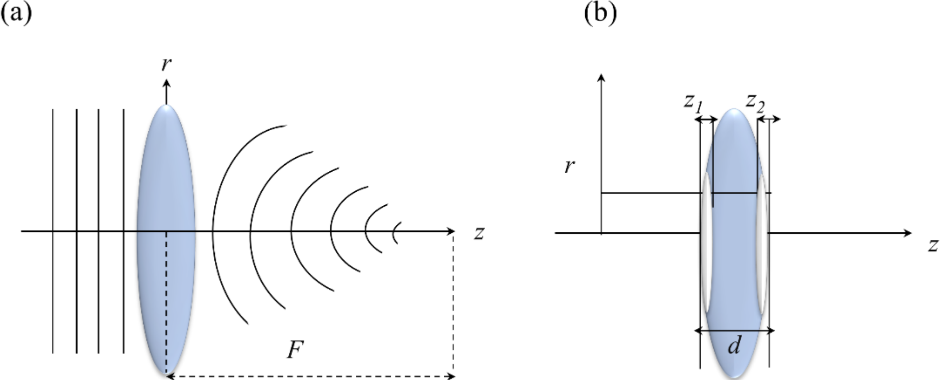

Figure 2.2 *(a) Transformation of an incident plane wave into spherical wave by a single lens where F denotes the focal length of lens, (b) illustration of three different phase contributions including input substrate-air surface* z_1*, the substrate medium of thickness d and output substrate-air surface* z_2*.*

The phase change $\Phi_{Out}(r)$ for a light propagating in air is defined as follows

$$\Phi_{\mathrm{Out}}(r) = \frac{2\pi}{\lambda}\, z(r). \tag{2.1}$$

However, inside lens with the refractive index n_{ref} and the wavelength is $\hat{\lambda} = \lambda/n_{ref}$, the phase change is given by

$$\Phi_{\mathrm{Out}}(r) = \frac{2\pi}{\lambda}\, n_{\mathrm{ref}}(r)\, z(r) = \frac{2\pi}{\lambda} * \mathrm{OP}(r), \tag{2.2}$$

where OP$(r) = n_{\mathrm{ref}}(r)*z(r)$ denotes the optical path. The optical path difference OPD(r) known also as the "wavefront error" is the difference in output phase changes between the position r and the optical center $r = 0$,

$$\mathrm{OPD}(r) = \mathrm{OP}(r) - \mathrm{OP}(0) = \frac{\lambda}{2\pi}\, \Phi_{\mathrm{Out}}(r). \tag{2.3}$$

Figure 2.2(a) shows the transformation of an incident plane wave to a spherical wave converging at the focal length F of lens. The undesirable spot broadening of spherical outgoing wave can be attributed to wavefront error. Effects of wavefront error OPD(r) on optical performance is a rather complex issue. Any deviation in the wavefront-form from spherical one degrades quality of point images, and hence

reduces the quality of the whole image[27-28]. As shown in **Figure 2.2(b)**, the physical property of a lens can be divided into three parts including the input substrate-air surface $z_1(r)$, the substrate medium of thickness d, and the output substrate-air surface $z_2(r)$. By assuming $z_1(0)=z_2(0)=0$ and $n_{\text{ref}}(r)=n_{\text{ref}}(0)$, the wavefront error OPD(r), is obtained as

$$\text{OPD}(r) = -[\,n_{\text{ref}}(r) - 1]\,[z_1(r) + z_2(r)]. \tag{2.4}$$

The fabrication process and material parameters determine the wavefront error OPD(r). To achieve ideal OPD, the choice of material, the appropriate surface shape, and the lens thickness d should be considered by an optical designer. Then, the acceptable amount of wavefront error for any specific application can be determined to find the tolerance of material and surface parameters, quantitatively. According to Rayleigh criterion[29], the performance of an optical system is not significantly impaired as long as the maximum wavefront error (OPD) does not exceed 1/4 λ, or if the wavefront is contained between two concentric spheres separated up to 1/4 λ. Nevertheless, Rayleigh criterion is not completely precise, as different forms of nominally equal wavefront error OPD have noticeably different effects on optical quality. For instance, 1/4 wave OPD of coma aberration lowers image contrast less than half as much as identical wavefront error of spherical aberration[30-33].

2.2.2 Optical aberration and imaging error

Effects of wavefront error on image quality is a rather complex issue. Any deviation in the wavefront-form away from ideal state leads to optical aberration. In the development process, optical systems are designed in such a way to optimize imaging performance and minimize optical aberration. For this purpose, the tolerable amount of wavefront error for any specific application should be determined. Nevertheless, every optical element has an absolute upper performance limit imposed on the one hand by the law of physics and on the other hand by a design- and/ or manufacturing process. For instance, a real spherical lens does not focus light precisely to a single point, even if it is perfectly built. These deviations from the ideal lens performance are called optical aberrations. In practice, there are four main reasons that cause optical aberrations including (i) aberrations caused by diffraction, (ii) design-related imaging errors, (iii) material defects, and (iv) manufacturing and assembly errors. The aberrations caused by diffraction are, however, naturally present and cannot be influenced by the manufacturer in the process. Even a perfect lens, that is not limited by design, will be “diffraction limited”[34-37].

Imaging errors are divided into two classes including “monochromatic” and “chromatic” aberrations[38]. Monochromatic aberrations (i.e., sharpness errors) are caused by the geometry of the lens or mirror and arise when light is either reflected or refracted[39]. The defocus, spherical aberration, coma, astigmatism, field curvature, and image distortion are the most common monochromatic aberrations. These imaging errors can appear even if monochromatic light is used. Optical elements are provided with spherical surfaces, if possible, as they are the easiest to manufacture. If one uses such a system to image an

infinitely distant point with a converging lens, then the rays do not combine in one image point. The off-axis rays refract stronger than the rays near the axis leading to “spherical aberration”[40]. In practice, several spherical lenses are therefore combined to form multi-lens systems, or alternatively aspherical and freeform lens surfaces are used. In this case, additional aberration errors can also occur during assembly due to alignment errors. Position errors affect the geometry of the resulting image in terms of scale fidelity and plane position[41]. Chromatic aberrations (also known as color fringing or dispersion) are imposed by dispersion that is the variation of optics refractive index with wavelength. Because of dispersion, different wavelengths of light cannot be focused at one single point such that the size and position of the images are different. This imaging error is a common problem if monochromatic light is not used. Lateral and axial aberrations are two types of chromatic aberration. Lateral aberration appears when dissimilar wavelengths are focused at different spots in the focal plane, as the magnification of the lens also differs with wavelength. Accordingly, the images of various colors show different sizes[42]. On the other hand, axial aberration happens when different wavelengths of light are focused on different distances from the lens. In this circumstance, the images of different colors are in different positions though they have the same size[43].

2.3 Types and form-complexities of optical elements

Optical elements are part of everyday life that are often designed using specific substrates and procedures to optimize optical performance in designated ultra-violet (UV), visual (VIS), or infrared (IR) wavelength ranges. They are used to alter the state of light through a variety of means including refracting, reflecting and diffracting. Optical elements contribute to a limitless number of optical systems such as telescopes, interferometry and image processing devices. Each individual optical element integrated in an optical system is required to have a special property and design. Though not all optical elements can be classified exclusively in one unique class, the classification of them is usually based on their property, which determines their main functionality[44-46]. Common differentiation criteria are summarized in **Table 2.1**.

Table 2.1 *Classification of the optical elements.*

Optical property	Exemplary elements
Reflective	Gratings
Refractive	Lenses, prisms
Diffractive	Spiegel, reflective gratings
Transmitting	Optical fibers
Partially transparent	Beam splitter
Absorbent	Receiver

Most fabrication methods deal with the production of optical elements with different form-complexities.

Figure 2.3 illustrates form-evolution of reflective or refractive optical elements from sphere to freeform concerning more complexity. They can have rotationally symmetric (i.e., flat and spherical), axially symmetric (i.e., aspherical) or completely asymmetric (i.e., freeform) surfaces[47-49].

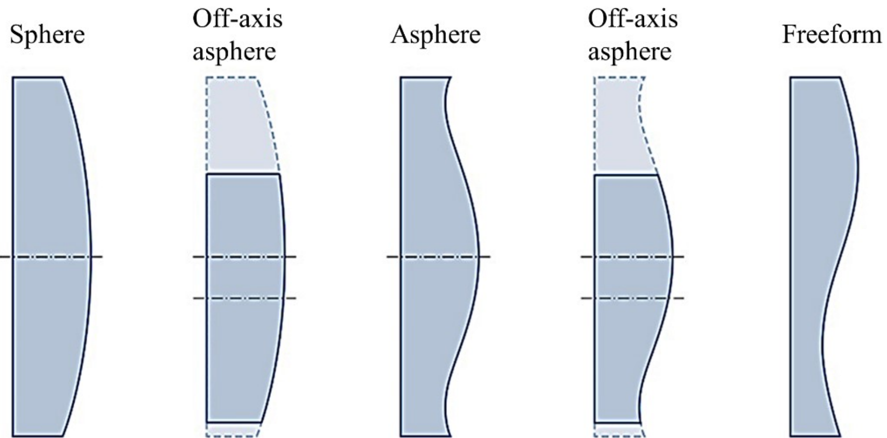

Figure 2.3 *Form-evolution of reflective or refractive optical elements from sphere to freeform (with increase in complexity from left to right).*

Reflective or refractive optical elements are normally provided with "spherical" surfaces, if possible, as they are the easiest and cheapest to manufacture. Spherical surfaces are characterized by a radius of curvature with constant value that uniquely describes their shape. A single spherical surface does not have an optical axis but only a single point of symmetry at the center of curvature which can be manufactured easily using large-format tools. These tools move randomly across the surface which avoids the generation of "zonal" artifacts in the surface structure leading to very high form accuracies. An optical element with flat surface can be also considered as a sphere that has an infinitely long radius of curvature. However, as discussed in **Section 2.2.2**, a spherical lens usually has a disadvantage of very poor imaging quality. Therefore, in practice, several lenses should be combined to form multi-lens systems, or alternatively aspherical or freeform surfaces should be used[50-54]. The easiest way of generating freeform optics is the decentered use of a rotationally symmetrical lens, which is thereby adjusted to the "off-axis sphere". The related slice is cut out (**Figure 2.3)**, also to miniaturize a system. However, a disadvantage of such a lens is the increase of aberrations with oblique light, which eventually result in a rapid decrease in image quality[55].

Another promising solution to increase optical quality is use of "aspherical" surface in system. A single aspherical surface can often replace several spherical surfaces in a design. Aspherical surfaces lack the symmetry of spheres, and their local curvature changes across the surface. "Off-axis aspherics", on the other hand, have no rotational symmetry and are possibly more difficult to fabricate. Many aspherical surfaces can be assessed as conic sections and polynomial aspherics, though some of them are

manufactured as off-axis pieces from the complete shape. The surface function of second order with axial symmetry according to the standard DIN ISO 10110, Part 12 is described as

$$f(\rho) = \frac{c\rho^2}{1+\sqrt{1-(1+\kappa)c^2\rho^2}} + \sum_{m=0}^{M} a_m \, \rho^{2m+4}, \quad (2.5)$$

where *f(ρ)* denotes the sagitta error, ρ cylindrical coordinate, κ the conic constant and c stands for the curvature of the conic. Because of the rotational and axial symmetry, the sagitta error *f(ρ)* has only one independent variable ρ. Depending on the shape, the conic constant takes different values, e.g., κ =0 for spheres, κ = -1 for parabolas, κ < -1 for hyperbolas, -1< κ <0 for oblate, and κ > 0 for prolate ellipses.

The sagitta value *f(ρ)* in **Equation 2.5** is equivalent to deviation of the optical surface from a plane. Due to the lacking rotational symmetry and varying local slopes, aspherical surfaces are much more difficult to produce than the spheres such that conventional large-format tools do not converge to the desired shape. Small acting tools are needed for both grinding and polishing which are more susceptible to the deteriorations and can increase risk of artifacts. Hence, more accurate machines and complex correction approaches are required. Due to the necessity of performing several correction loops, artificial ripples in the structures of aspherical surfaces cannot be prevented thoroughly, and they should be tolerated. Additionally, highly precise measuring techniques with accuracies below 1 nm are necessary. These difficulties in manufacturing process greatly limit applications of aspherical surfaces, that is unfortunate as a single aspherical surface can often substitute several spherical surfaces in a design[56-60].

"Freeform" optics is another type of refractive and reflective surfaces that has no symmetry and deviate considerably from spherical and aspherical geometries. Compared to only one degree of freedom for spherical surfaces, a freeform surface has up to six degrees of freedom due to its continually changing curvature. Because of their special geometry and large number of degrees of freedom, they implement a completely novel concept for optical systems and can be designed precisely for specific correction purpose. In comparison to spheres and aspheres, advances in field of view (FOV), and numerical aperture (NA) as well as the reduction in size are achieved in optical systems by using freeform surfaces (**Figure 2.4**). The use of freeform optics can reduce the number of elements in an optical system, allowing smaller, lighter and more efficient systems. Depending on their specific surface shape, freeform optics deliver functionalities that cannot be obtained with conventional optics. Particularly, in optical systems requiring a folding of the beam path (e.g., monoliths), freeform optical surfaces are practically beneficial, and they can replace existing large components such as mirror systems. However, a high quality of the freeform optics is an absolute prerequisite to provide the excellent optical efficiency. On the other hand, the optical design and manufacturing process of freeform surfaces are much more complex compared to conventional symmetrical lenses requiring a high degree of precision and manufacturing know-how.

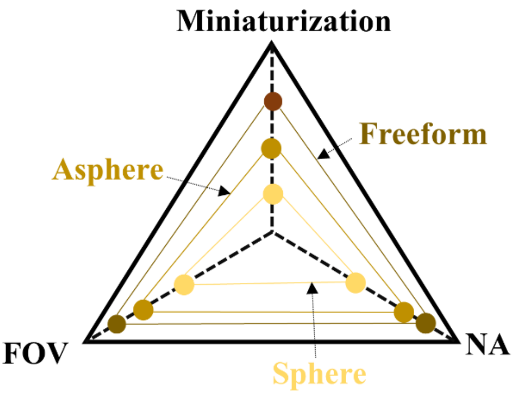

Figure 2.4 *Comparison between sphere, asphere and freeform in terms of field of view (FOV), numerical aperture (NA) and miniaturization.*

Although their manufacturing is somehow similar to that of highly complex aspheres, the surface shape and local changes in deviation influence the complexity of the geometry, the manufacturing process and the measurement. Normally, the manufacturing process starts with the definition of the specified surface. In addition to a clear description of the optics, mathematical form, point cloud or 3D model are needed in this process[61-68].

The combination of diffractive functions with standard optical elements in one "hybrid optical element" offers advantages to optimize complex optical systems. The efficiency of a hybrid optical element is determined by the interaction of light from refractive and diffractive surfaces and equals to the summation of efficiencies of these individual surfaces. Either mechanical abrasive methods (i.e., diamond turning) or replicative approaches (i.e., injection molding) can be used for fabricating hybrid elements. Mechanical abrasive methods, as discussed in **Chapter 3**, are suitable for single-element production with very high surface quality. Nevertheless, manufacturing a single optical element with the mechanical abrasive process is time-consuming, laborious to deploy for mass production and their application for lenses having diameter less than 10 mm is challenging. Hybrid elements can replace a multi-element optical system design to miniaturize the size. Moreover, hybrid elements can bring some other advantages for optical systems. Chromatic aberration, that as discussed in **Section 2.2.2** occurs in conventional lenses, can be removed by single hybrids. Another advantage of hybrid optics is that they are less susceptible to thermal variations due to their special design. However, several drawbacks are related to hybrid optics. Fabrication of hybrid optical elements similarly to freeform optics is more costly than conventional optics due to the recurring added cost for diamond turning, or a tooling cost for injection molding. Moreover, diffraction efficiency of hybrid optical elements varies at different wavelengths when they are used with a broadband light source. Additionally, the hybrid optical designs are not appropriate for applications at short wavelengths, and possibly can result in extreme reduction of the lens' performance as the short wavelengths are frequently lower than the linear tolerances of the

hybrid optical design. Currently, hybrid optics are used in a variety of applications. For instance, they are suitable for imaging, broadband illumination, and laser applications[69-77].

A typical micro-optics lens has generally diameter as small as 10 µm. It is a single element with one plane surface and one spherical convex surface to refract the light. More complex micro-optics may use aspherical or freeform surfaces. A different type of micro lens uses several layers of optical material to realize their expected design performance. Micro-Fresnel lenses are a class of micro lens which are thin and lightweight. They have a set of concentric curved surfaces that focus light by refraction. Another class of micro lenses, known as binary-optic micro lenses, focus light by diffraction. They can provide an approximation of the ideal shape by their several grooves with stepped edges or multi-levels. Micro-lens arrays are designed by placing multiple lenses on a supporting substrate in a one-dimensional or two-dimensional array. A variety of methods can be used to fabricate micro lenses. In most cases, molding or embossing from a master lens array is used to copy several micro-lenses. Whereas micro lens arrays are usually used to improve the light collection efficiency, single micro lenses are suitable for coupling light to optical fibers. Novel imaging properties can be achieved by combinations of micro-lens arrays. Unlike conventional lenses, they have capability of forming an image at unit magnification and without invertibility. Micro-lens arrays have been developed to realize compact imaging devices for applications such as photocopiers and mobile-phone cameras[78-81].

2.4 General specifications of optics

The requirements specified by the designers for the optical elements or systems are generally defined according to DIN ISO 10110 and have tolerance specifications that should be met in the production process. Aspherical and freeform surfaces are becoming increasingly important. DIN ISO 10110, Part 12 describes the basic mathematical forms as well as the technical forms of representation. For an example, **Figure 2.5** shows a drawing of aspherical focusing lens with its coordinate axes, used in laser processing with the specifications referring to the left and right surface as well as the material data. The design equation with its constant and coefficient and the abbreviated data are specified according to DIN ISO 10110[82].

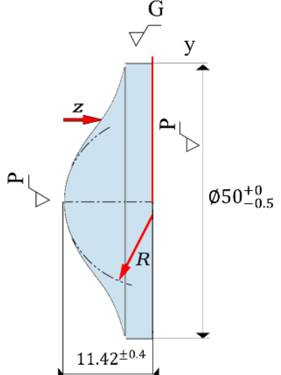

Formula of the aspheric surface

$$Z = \frac{cy^2}{1+\sqrt{1-(1+k)c^2y^2}} + A_4y^4 + A_6y^6 + A_8y^8 + A_{10}y^{10} + A_{12}y^{12}$$

Constants and coefficients

C = 1/ -71,42
K= 0
A_4= 0, 566322E-06
A_6= 0,174788E-9
A_8= -0,218582E-12
A_{10}= 0,195829E-15
A_{12}= -0,70000E-19

Slope tolerance

Reference length: 0,5±0,05
Max: 50″
Min: 7 ″

Left surface	Material data	Right surface
R 40,5308 CX	Schott BK7	R ∞
Øe 50,0	n (1064 nm) 1.506635± 0.01	Øe 50.0
λ Anti-reflection layer (Specification No.67413)	ν 64.17 ± 8%	λ Anti-reflection layer (Specification No. 67413)
3/ 10(2)	0/ 10	3/ 10(2)
4/ 10′	1/ 5 × 0.4	4/ 10′
5/ 5 × 0.4	2/ 1; 1	5/ 5 × 0.4

Figure 2.5 *Example of the aspherical focusing lens used in the field of laser optics with specifications according to DIN ISO 10110 for the focusing lens*[82].

Material specifications defines the choice of the glass types as well as the permissible deviations of the material properties[83-85]. Often, the identification number, the refractive index and Abbe's number are indicated according to DIN ISO 7944 as well.

Corresponding shape specifications of the optical elements are defined regionally. The specification of the radius *r* of curvature is given in millimeters or inches and, if necessary, with the required tolerance. The direction of curvature is divided into three classes: (i) convex surface CX, (ii) concave surface CC, and (iii) plane surface ∞. Furthermore, thicknesses, diameters and lengths are given as nominal dimensions along with the required tolerance. Tolerance of surface shape (i.e., fit error) specifies the maximum permissible deviation of manufactured actual form from the desired one. Rotationally and non-rotationally symmetric deviations should be controlled by indicating the permissible irregularity specified by this standard. Furthermore, local shape deviations with strong slopes can appear, that should be limited by an additional tolerance for the maximum permissible angular deviation of the local normal from the referenced one. This deviation is named centering error. DIN ISO 10110 defines the rules to specify these form tolerances in the drawings of optical elements. The unites of tolerance and specified information on testing of optical elements, particularly by interferometric methods, are also given by DIN ISO 10110. Main description of shape specifications as well as the tolerance values for the exemplary case (i.e., aspherical focusing lens shown in **Figure 2.5**) are provided according to DIN ISO 10110 in **Table 2.2**.

Table 2.2 *Main description of shape specifications according to DIN ISO 10110.*

Index	Required properties	Specification	Aspherical focusing lens (Figure 2.5)
3	Tolerance of surface shape (fit error)	3/A (B/C) (where A, B, C are arrow height error, irregularities and rotationally symmetrical irregularities in interference fringes)	3/10 (2) (tolerance of arrow height error can be max. 10 interference fringes while irregularity must not exceed 2)
4	Centering error	4/σ (where σ is tilt angle in arc minutes)	4/10 (maximum permissible tilt angle of 10)

The surface specifications determine the defects, the surface quality and the required treatment and coating of surface. All surface parameters are to be applied according to DIN EN ISO 4287. The key figure of surface specification and the required values for the exemplary case (i.e., aspherical focusing lens shown in **Figure 2.5**) is listed according to DIN ISO 10110 in **Table 2.3.**

Table 2.3 *Main description of surface specifications according to DIN ISO 10110.*

Index	Required properties	Specification	Aspherical focusing lens (Figure 2.5)
5	Surface defects	5/ N_d × A (N_d is number of surface defects; A is magnitude of surface defects in numbers of steps)	5/5 × 0.4 (max. 5 permissible errors with the number of stages 0.4)

Surface quality is referred to as a global statistical characteristic related to the profile of the optical surface. The root mean square (RMS) roughness R_q is the most representative surface parameter that indicates the standard deviation of the profile coordinates. The RMS roughness values R_q can be determined over the entire surface or only for a specific region. The maximum profile height (peak to valley) value R_z indicates the maximum surface deviation by which local defects such as scratches and protrusions are described.

Another way to describe the surface is the use of the power spectral density (PSD)[37]. PSD contains the spectrum of spatial frequencies and its representation can be either one- or two-dimensional. The PSD function allows the complete description of the surface quality characteristics and proves to be particularly suitable for polished surfaces or for applications with extreme requirements. The two-dimensional isotropic PSD is defined as follows

$$\text{PSD} = \frac{P}{2\pi f(\Delta f)} \tag{2.6}$$

where P denotes the power under a part of the area (in nm^2), Δf the frequency change (in nm^{-1}), and f is the frequency that corresponds to a certain area size (in nm^{-1}). More detailed description can be found in DIN ISO 10110, Part 8.

The shape of optical elements is mainly obtained by grinding or lapping in which the errors of the surface shape are below 500 nm. Thermal drift of the machine and the tool wear can lead to shape deviations from the defined mathematical description. Depending on the largeness of the deviations on

machined surfaces, optical surface topography is commonly classified into three main different spatial regions, namely long-wave shape deviation, waviness, and roughness (**Table 2.4**).

Long-wave shape deviation (also known as geometry error) refers to a general macroscopic scale specified by spatial wavelengths larger than 1 mm. This deviation causes imaging error (aberration). Random and quasi-periodical height variations (called roughness and waviness) can be generated either by machine vibrations or tool feed in the final steps of surface machining, generally consisting of polishing. Waviness and roughness are distributed over the entire surface and are jointly named surface texture and localized imperfections and result into blur image and contrast loss. Waviness has often regular structures characterized by spatial wavelengths in range of 20 µm to 1mm. Roughness is often isotropic distributed unevenness, described by the short-wavelength (or high spatial frequency) component of a measured surface. It can be caused by microscopic processes in tool-surface interaction. Nevertheless, most polished surfaces have a mixture of roughness, waviness, and geometry errors that cannot be distinguished effortlessly. The spatial wavelength regions can be detached from each other by spatial filtering.

Table 2.4 *Classification of surface topography error.*

Roughness (short spatial wavelength)	**Waviness (mid spatial wavelength)**	**Long-wave shape deviation (large spatial wavelength)**
$\lambda \leq 20$ µm	20 µm $\leq \lambda \leq$ 1 mm	$\lambda \geq$ 1 mm

The polishing grades are related to maximum permissible number of micro defects on the surface determined by scanning a given distance on the surface, for instance, by using a stylus with a suitably tiny tip radius. The degree of polishing is specified in four ranges and is assigned to defined limits. **Table 2.5** provides information about the number of micro defects N_d per 10 mm scanning length for the respective polishing grade.

Table 2.5 *Classification of degrees of polishing according to DIN ISO 10110.*

Degree of polishing	**Number N_d of micro defects per 10 mm scanning length**
P1	$80 < N_d < 400$
P2	$16 < N_d < 80$
P3	$3 < N_d < 16$
P4	$N_d < 3$

Main description of material specifications as well as the tolerance values for the exemplary case (i.e., aspherical focusing lens shown in **Figure 2.5**) is provided according to DIN ISO 10110 in **Table 2.6**.

Table 2.6 *Main description of the material specifications according to DIN ISO 10110.*

Index	Required properties	Specifications	Tolerance values fur aspherical focusing lens (Figure 2.5)
0	Stress birefringence	0/A (where A is max. permissible stress birefringence in nanometers per centimeter of optical path length)	0/10 (max. permissible stress birefringence 10 $nm.cm^{-1}$)
1	Permissible bubbles and other inclusions	$1/N_d \times$ A (number of defects × size of errors; number of steps)	1/5 × 0.4 (max. 5 permissible errors with number of steps 0.4)
2	Inhomogeneities and streaks	2/A; B (where A is inhomogeneity class; B is streak class)	2/1; 1 (according to class 1)

2.5 Applications of modern optics

Practical applications of modern optics with complex surface designs including aspherical and freeform lenses are found in a variety of technologies and everyday objects such as (E)UV lithography, laser beam shaping, free-electron laser, illumination system, imaging system (i.e., mobile camera), and space telescope. In this section, the characteristic features of each technology and the relevant optical elements are described, individually.

2.5.1 (E)UV-lithography

The increasing trend towards greater integration density of microelectronic circuits permanently demands smaller feature-sizes. The microlithography printing system with a high resolution (i.e.,100 nm or below) is necessary to generate these small feature-sizes. The resolution of a lithographic printing system can be improved either by transition to a shorter wavelength or by increasing numerical aperture (NA) of lenses according to the Rayleigh criterion. Designing compact, high NA projection lenses for lithography is a challenging task. Very high-resolution lenses across the entire field of view should be realized at large NAs of microscope objectives while preserving almost ideal wavefront correction. This can be implemented by optical design modification, and the use of aspherical or freeform lenses. Nevertheless, enlarging NA of lenses is theoretically restricted, and hence improving the resolution of lithographic methods based on NA has a limited point[18].

Another alternative solution for extending the resolution limit of lithographic methods is to use a shorter wavelength (e.g., EUV). However, the absorption of EUV radiation is extremely high in bulk material, and hence the use of refractive lens is problematic. To overcome this difficulty, refractive optics is replaced with multilayer mirrors with about 70% maximum reflectivity. Still because of the 30% absorption of these optical elements, it should be tried to use the minimum number of them in the design. This minimizes the degree of freedom for the design process and imposes an upper limit for the etendue of the lens. Therefore, the extra degree of freedom should be rewarded by using freeform mirrors[86-87].

Currently, fabrication of freeform deformation of a few millimeters and mirrors with large diameter and higher surface quality are some challenges to realize leading-edge optical systems used in (E)UV-lithography. Hence, optical manufacturing technologies, which are the key know-how for generating freeform mirror surfaces with sub nanometer precision, should constantly improve[88].

2.5.2 Mirror telescope

Free-space optical (FSO) communication applies light propagation in free space to wirelessly transmit data. In future, optical fiber and FSOs will be used increasingly for high-speed data exchange over long distance. Theoretically, the beam divergence is proportional to the ratio of the transmitted wavelength λ over the transmitter aperture diameter. As optical beams have considerably shorter wavelength than radio frequency (RF), much higher intensity can be projected to the receiver for the same power at the transmitter. Nevertheless, the slender beam of optics is an issue to wirelessly transmit data as the receiver must capture the narrow beam. Hence, the optical connection should operate with sub-arcsecond accuracy. To exchange data between two stations optically, a transceiver at both ends of communication systems is necessary. The telescope is the main part of optical transceiver which is typically an all-mirror system. The all-mirror telescopes with compact size are deigned and used currently not only for space communication but also mostly for astronomical observations. The all-mirror telescope should offer three fundamental properties: (i) the emitted forward wavefront must be diffraction limited to focus sufficient light at the opposite station, (ii) the diameter of entrance pupil must be suitably large to capture sufficient backward light, (iii) the mirrors should be made of particular materials with low mass, great thermal expansion, and they must have long term stability against space environmental loads[89].

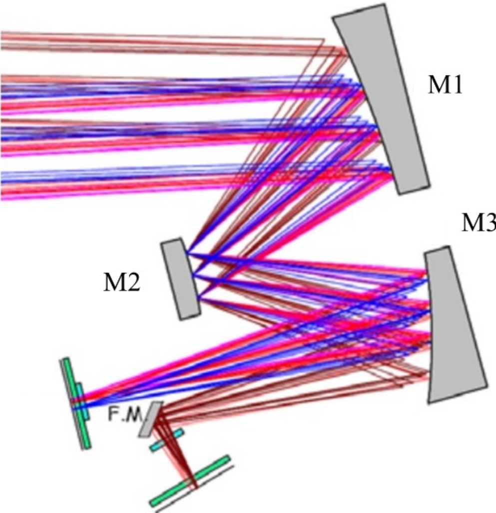

Figure 2.6 *Afocal all-mirror free space system in application for optical intersatellite communication telescope*[47].

An exemplary afocal all-mirror system in application for optical intersatellite communication telescope is shown in **Figure 2.6**. It consists of three off-axis aspherical mirrors (two parabolic mirrors M1 and M4 and a hyperbolic mirror M2) that are attached around the x-axis. To minimize the manufacturing complexity, the aspherical shape of all mirror is only conical. Since these mirrors are slightly tilted around the x-axis, a plane folding mirror M3 with a freeform correction is exploited as a corrector element. This design allows to avoid beam obscuration and reduce the intensity loss of the beam emitted to the other terminal. A precision surface machining technique is required to fabricate an aspheric shape mirrors with an accuracy of 1 µm. Accordingly, afocal all-mirror systems deliver a communication beam divergence of 2-3 arceseconds over very long distance (up to 60000 km)[22].

Zerodur is a type of glass-ceramic material with a great thermal expansion and high rigidity against high-energy radiation loads. Due to these properties, Zerodur is a favorite choice for all-mirror telescope. However, there is a risk of different failures like sub-surface damage during machining of Zerodur that is the disadvantage of it.

2.5.3 Imaging optics

Imaging optics like camera lenses are used in a variety of applications requiring different lenses from small to large size, low- to high- aperture, and wide-angle to telephoto. For large-format cameras, symmetric lenses can be used, where distortion and color aberrations can be handled, conveniently. However, because of the ongoing miniaturization and improving quality of imaging devices, the use of asymmetric optics with the small size is increasing. The aspherical and freeform lenses are often used in cameras which allow the manufacturers to fulfill the increasingly strict requirements of imaging optics. Compared to only one degree of freedom for spherical surfaces, aspherical and freeform lenses have up to six degrees of freedom due to their constantly changing local curvature. Based on this feature, aspherical and freeform surfaces can be designed precisely for a particular error correction purpose. Initially, aspherical lens was employed in cameras to correct monochromatic errors such as spherical aberration, imaging distortion, coma and astigmatism. Currently, camera lenses for mobile phones consist of several aspherical lenses.

2.5.4 Illumination optics

These days, typical illumination systems such as digital projectors and rear-projection televisions as well as automotive headlights should be mass-produced while maintaining strong customer requirements including low cost, high efficiency and space restrictions. To meet such requirements, the use of modern optics in these products is unavoidable.

Conventionally, parabolic mirrors have been used in car headlights to collect light while structured cover glasses distributed the light onto the road. Application of high-intensity discharge (HID) lamps

raised demands to precisely collect and distribute the light according to relevant safety standards. The recent advances are super poly-ellipsoid (PE) projection systems with transparent cover glasses. In these systems, a multi-ellipsoidal, aspherical, or freeform reflector is used to efficiently capture the light from HID lamp arc. Cost- and space-saving requirements while preserving performance have led the designer to use one single aspherical and freeform lens as projection lens instead of multi-lens system. Therefore, asymmetries in light distribution and all other requirements listed in the safety standard were defined for one single lens surface. Accuracy requirement of aspherical and freeform lens used in car headlights can tolerate global surface deviation within 30 μm from referenced shapes while local deviation should be less than few micrometers[90].

Compact digital projectors have today wide range of applications from business purposes to entertainment. To project image on a screen, digital image data was modulated onto the light beam by the liquid crystal display (LCD) or digital micromirror device (DMD) in these projectors. However, the transmissivity of the displays was not satisfactory. Moreover, the filaments of halogen lamps and arc discharge lamps were bulky and did not match with the expected aperture of screen. Therefore, a more compact light source with considerably smaller arc gaps and higher brightness efficiency was developed. In the layout of digital projectors, light from the discharge lamp is collected by an ellipsoidal mirror with a coating to inhibit UV and IR from entering the system[91].

More recently, for achieving a more efficient system, light emitting diode (LED) is introduced. Latest advances in LED allows the production of power-efficient, ultra-compact pocket projectors. Today, such projectors are widely applied in consumer rear-projection televisions.

2.5.5 Laser beam shaping

Beam shaping is a process in which both the irradiance and phase of an optical beam radiation is redistributing. Beam shaping is used in a variety of applications such as laser/material processing, optical image processing, lithography, printing, and laser art patterns. There is no single beam shaping approach that can be suitable for all cases. In some applications, mask imaging or direct focusing is not simply sufficient, and more complicated spatial beam shaping is required. The “beam aperturing” is a simple but quite applicable beam shaping method. In this configuration, the input beam is expanded into beamlets by a lenslet array, and then superimposed by the primary lens in the output plane. The output pattern results from summation of all diffraction patterns selected by the lenslet apertures. Refractive or diffractive optical elements are used for the conversion of a Gaussian input beam to a super Gaussian irradiance output profile at the desired plane. Advantages of using these optical elements are the greater process speed and higher overall feature quality. Refractive beam shaping optics provides high transmission but is restricted to input beam geometries. On the other hand, diffractive beam shaping optics can provide comprehensive and flexible output beam shapes although they are more susceptible to particular input laser beam parameters[92-93].

2.5.6 Synchrotron beam line optics/FEL optics

A free-electron laser (FEL) is a synchrotron light source generated by accelerating a beam of electrons to nearly the speed of light. FEL resembles laser in different aspects except that it uses relativistic electrons as a gain medium instead of exploiting stimulated emission from atomic or molecular excitations. The generated beam passes through a periodic structure of magnets with swapping poles (called undulator) across the beam path creating a side-to-side magnetic field. This array of magnets is called an undulate. Acceleration of the electrons across the beam path causes the release of photons (synchrotron radiation), that are monochromatic but still incoherent as the electromagnetic waves of randomly distributed electrons have stochastic constructive and destructive interference in time. The output radiation power depends linearly on the number of electrons. An appropriate optical mirror should be used at each end of the undulator to generate an optical cavity resulting in the radiation to form standing waves. For this purpose, there are recently increasing demands for single layer mirrors with large diameter and high surface quality in sub-nanometer scale. Accordingly, surface finishing technology is currently capable of generating large mirrors (of size up to 1 m) with surface roughness below few nanometers[94].

3 The-State-of-the-Art in Manufacturing Precision Optical Elements

3.1 Classification of processing technologies

Currently, there are many different processing technologies available in manufacturing of precision optical elements. Depending on their mechanism, these technologies can be mainly classified to “replicative” and “subtractive” manufacturing methods. The appropriate techniques are selected typically based on the production volume, the types of materials, the degree of complexity, and the required tolerance values[95-99]. **Figure 3.1** provides an overview on different types of processing technologies used for manufacturing of precision optical elements.

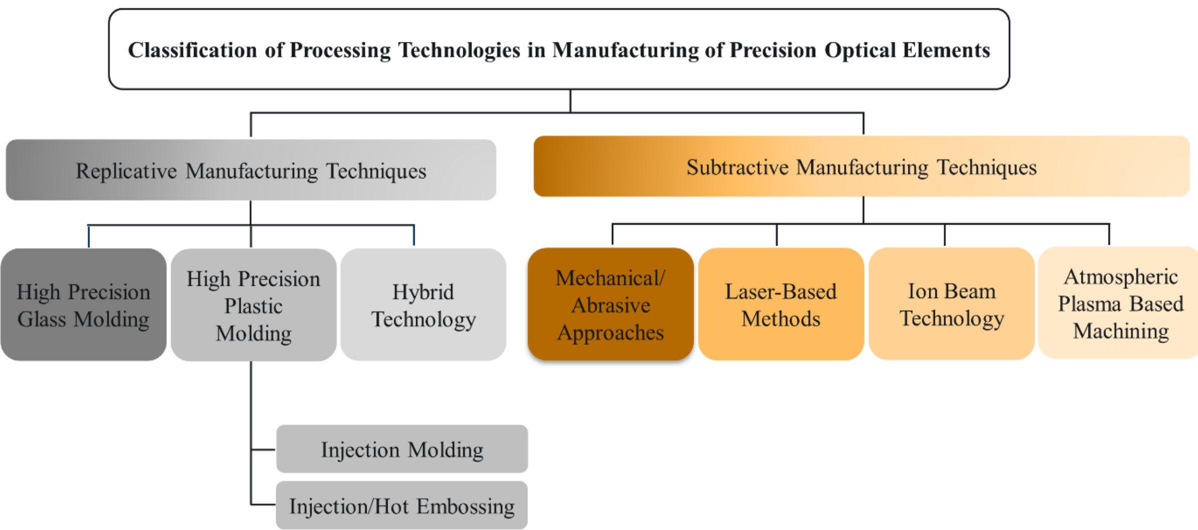

Figure 3.1 *Overview of different types of processing technologies used for manufacturing of precision optical elements.*

Subtractive manufacturing technique has, as its greatest advantage, a very high flexibility regarding to geometry and material. No advanced molding machine or special coating technology is required, and almost any brittle material can be machined. As a cold surface-finishing process, it can be applied to a wide variety of glasses with low and high transformation temperature T_g. Additionally, in the final step of subtractive manufacturing chain, the locally acting so called sub-aperture tools can be applied for local figure correction to reach the highest form accuracy of the optical surfaces. On the other hand, replicative manufacturing methods have been developed to facilitate an economic mass production of precise spherical, aspherical, and freeform optical surfaces. Depending on the type of material and its application, different approaches of this category can be applied. For instance, precision glass molding is of great interest for production of imaging and lighting components from special “glasses” the so-called “low-T_g glasses”. This is while high quality aspherical and freeform optics made of “plastic” are mass produced by the process of high precision injection molding. Characteristic features of each process step are discussed in the following[100-104].

3.2 Replicative (forming) manufacturing

Molds for fabricating asymmetric optical elements out of either glass or plastic were introduced along with other advances in generating aspherical optics in 1970. The manufacturing of molds mainly determines the possibility as well as the efficiency of the actual precision glass and plastic molding. The different processing technologies such as grinding, milling and subsequent polishing are used to manufacture molds. Many small aspheric and freeform lenses like camera lenses are produced by the direct molding of glass or plastic into an aspheric or freeform mold. The molds are generated from special materials that can tolerate the prerequisite high temperatures. The molds are designed to have the opposite shape of the finished lenses. Hybrid technology is an alternative, cold replicative manufacturing approach suited for generating optics with high accuracy where a thin polymer layer is molded on a polished glass surface. **Table 3.1** provides a brief overview on the features of different replicative processing technologies in optical surface fabrication. Characteristic features of each process step are discussed in the following[26].

Table 3.1 *Overview on features of different replicative processing technologies in optical surface fabrication.*

Process	Material	Advantages	Disadvantages	Optics size (mm)	Shape deviation (nm) PV	Surface roughness (nm) RMS
Precision glass molding	- Low T_g glasses	- Potential for mass production - Complicated shapes possible	- Size limitation - Limited accuracy - Long cycle time - Undefined machining operation	0.5-35	1 – 5	2
Injection or hot embossing	- Polymer	- Low birefringence - Reduced weight - Potential for complex mounting features integrated with optics	- Limited Thickness - Low cycle time accuracy	0.5-200	1 – 10	5
Injection molding	- Polymer	- Potential for mass production - Complicated shapes possible	- Low birefringence - Microstructure	0.5-200	1 – 10	5
Hybrid technology	- Combination of polymer and glass	- Cost effective with larger quantities	- Sensitive to humidity and scratching	0.5-50	1 – 10	5

3.2.1 High-precision plastic molding

Plastic optics can replace molded glass lenses in different applications. Low weight and the capability of developing complicated mounting features combined with optical systems are some benefits of plastic optics. Conventionally, for fabricating plastic optics, three different types of processes are used, namely (i) injection molding, (ii) injection embossing, and (iii) hot embossing. In the case of injection

molding, the pressure is applied to fill mold with liquid plastic. For injection embossing, liquid plastic drops are injected into an extended shape and then pressed onto the master shape. When a plastic disc is warmed up and subsequently pressed onto the master form, the process is called hot embossing. However, conventional injection molding is not applicable for manufacturing of high-precision freeform surfaces, and more advanced process is required. Hence, advanced technologies and molding machines have been developed to fabricate high-precision plastic lenses and mirrors. Currently, by controlling the process parameters such as temperature and pressure carefully step-by-step, and based on the advanced molding machines and technologies, precise aspherical, and freeform plastic lenses and mirrors can be mass fabricated by the high-precision plastic molding. No requirement for surface finishing, cost-effective mass production, and its suitability for manufacturing complex surfaces are the main features of high-precision plastic molding that make it appealing for market demands. However, the disadvantage of this process is that the molding machines and the tooling are quite expensive if it is not aimed for mass production[105-107].

3.2.2 High-precision glass molding

High-precision glass molding technology is of great interest for mass production of precision optics from special glasses, the so-called low-T_g glasses, by hot forming and without any cold post-processing. In this process, the glass is warmed up to temperatures larger than T_g (i.e., between 350 °C and 650 °C) until the glass is soft enough to be shaped. Then, it is molded into the final shape by being pressed into a master shape. In contrast to other hot forming processes used for glasses, the viscosity here is quite larger. Though large viscosity increases cycle time, it can be beneficial to eliminate destructive effects like shrinkage. Fabrication of high precision molds is the most challenging step in the process chain that demands extensive know-how in tooling and molding process, and hence it may be expensive. Nevertheless, this process is suited for mass production of imaging and lighting components as well as small lenses with aspherical and freeform shapes especially in those cases where standard subtractive methods like grinding and polishing are not affordable. The quality of optical elements is comparably like those obtained by grinding and polishing. Currently, high-precision glass molding is used commonly to fabricate small spherical, aspherical and freeform lenses (with diameters less than 10 mm) providing diffraction-limited performance and excellent surface finishing. Still precision glass molding is used to build large condenser lenses used for projectors that tolerate reduced quality[108-109].

3.2.3 Hybrid press technology

The hybrid press method is “cold” replicative manufacturing process ideal for fabricating precision optical elements consisting of glass and polymer layer with a complex, and even freeform shape. As the quantities increase, this method becomes more cost-effective. In this process, an aspherical or freeform mold is used to press extremely transparent optical polymer with thickness of 1-30 µm on a

preliminary model of polished glass. Optical, physical, and thermal properties of fabricated surfaces are comparably like that of preliminary polished glass. Currently, the hybrid press method is used to efficiently fabricate aspherical and freeform lenses with diameters up to 50 mm providing excellent surface finishing. However, the hybrid optical elements may show higher susceptibility to humidity and scratching that is the main drawback of this method[26].

3.3 Subtractive manufacturing and possible processing chains

Figure 3.2 is a brief effort to distinguish between four different commonly used subtractive process techniques including mechanical-abrasive approaches, laser-based method, ion beam technology and plasma-based methods. The typical process chain for precision manufacturing of optical surfaces follows three steps consisting of surface figuring, polishing and local figure correction. With these three processing steps, the bulk material is converted to spherical, and even freeform shapes. Rather than applying an individual subtractive process technique, an appropriate combination of different techniques also can be used to improve the surface quality or to make the process cost-effective. For one of these examples, the freeform lens can be shaped by zonal grinding, subsequent polishing with ion beam smoothing, and lastly fine focused plasma jet for local figure correction[110-111].

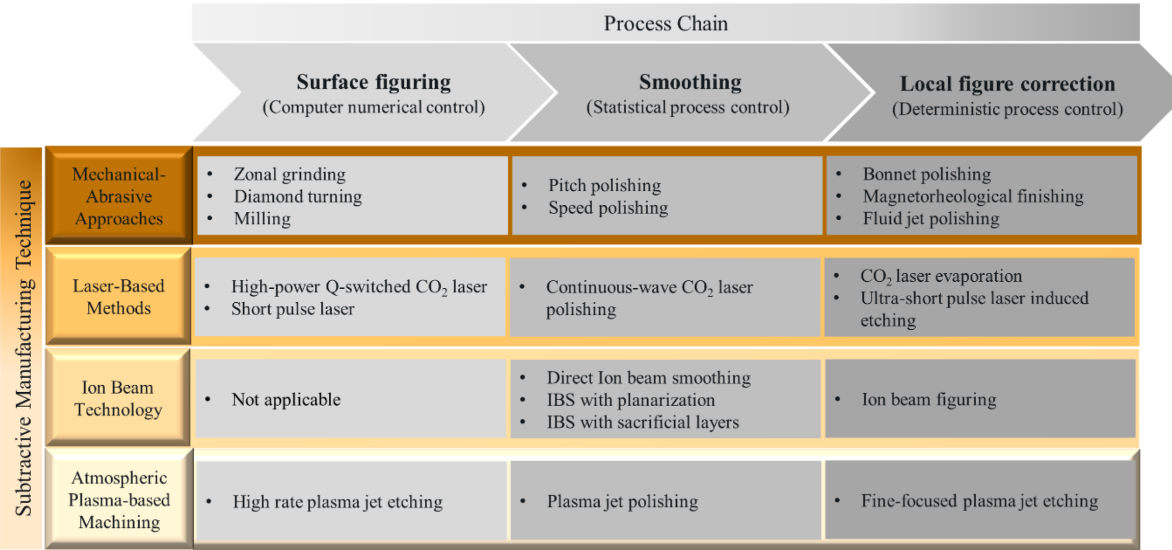

Figure 3.2 *Overview on different subtractive process techniques and their processing chain used for optical surface fabrication.*

3.3.1 Surface figuring

Surface figuring is the first step in the process chain of subtractive techniques for manufacturing of optics (**Figure 3.2)**. This step has the role of generating precise shape but still microscopic rough surface that is not suitable for optical applications. Subsurface damage and roughness, formed in this step, require to be removed by subsequent polishing step. A variety of different techniques, that are available for surface figuring, are compared in **Table 3.2**. Characteristic features of these techniques are discussed in the following section. The appropriate technique is selected typically based on the production volume and the properties as well as types of material. However, mechanical-abrasive approaches like zonal grinding are mostly chosen for the fast surface figuring of prototypes of any brittle material due to their high flexibility and short step-time. **Figure 3.3** presents the structure of the material removal process on the bulk glass by using a single point acting tool (i.e., zonal grinding)[112-114].

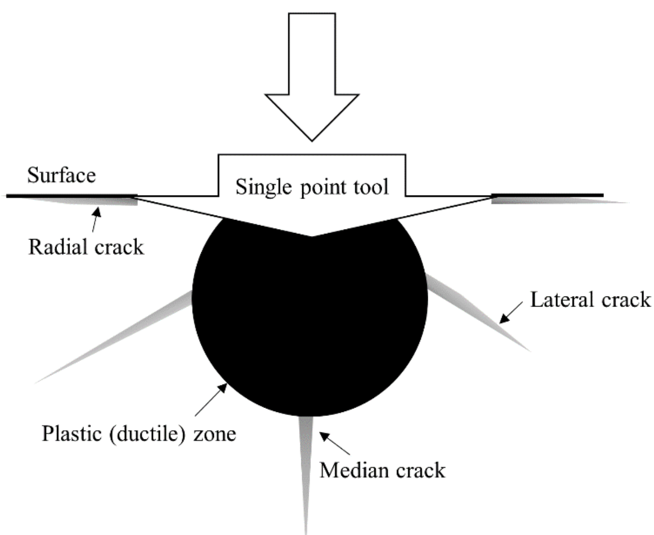

Figure 3.3 *Material removal process on the bulk glass by a single point acting tool.*

Depending on the loads and mechanism of engaged acting tool, material removal as well as variety of different cracks are formed beneath the tool. The zonal loads with accurately controlled machines lead to a plastically deformed zone known as ductile removal mode. However, applying global loads by manually controlled machines may yield radial and lateral cracks. The radial cracks are the reason of the subsurface damage and their largeness determines the depth of subsurface damage. On the other hand, lateral cracks are responsible for the brittle mode of surface when they reach to the surface. Stable acting tools with high-precision CNC machines (i.e., deterministic process) are necessary to perform merely in the regime of the ductile removal mode[115-116].

***Table 3.2** Overview on different existing methods for shape generating on optics used in the first step of process chain of subtractive techniques.*

Surface figuring technique	Material	Advantages	Disadvantages	Shape deviation (nm) PV	Surface roughness (nm) RMS
Zonal grinding	- Almost all brittle materials	- Fast generation process	- Subsurface damage	2000	50-1000
Diamond turning	- Almost all brittle materials	- No subsurface damage - Sufficient roughness for IR	- Surface roughness	300	5-20
High-power Q-switched CO_2 laser/ Pulse VUV laser	- Fused silica - N-BK7 - S-TIH6	- No subsurface damage - Contactless	- Surface roughness due to glass ablation	2000	50
High-rate plasma jet etching	- Silicon - Fused silica - ULE - SiC	- No subsurface damage - Contactless - Low physical load	- Limited choice of material - Surface roughness due to chemical process	2000	50

3.3.2 Polishing

In the second step of subtractive manufacturing process chain, polishing is performed to meet the requirement for the optical quality. The role of the polishing process is to eliminate microscopic roughness, subsurface damage, and mid-frequency surface error after the surface figuring step while the form accuracy is preserved. The amount of material that needs to be removed in this step depends on the depth of subsurface damage. If the material removal in the former step (i.e., surface figuring step) is carried out in ductile removal mode by deterministic process (i.e., CNC machines), the subsurface damage becomes nearly zero. In this case, the amount of material that should be removed is very small, and only the smoothing of the surface is enough. However, the optical elements are frequently shaped by manually controlled machines causing a large subsurface damage such that rigorous and zonal polishing is required[117-122].

The material removal rate *MRR* [m/s] achieved by polishing can be estimated with the Preston equation as

$$MRR = C_P \frac{Q}{A} . v \tag{3.1}$$

where C_p denotes the Preston coefficient, A [m²] the surface area where the removal takes place, v [m/s] the relative velocity of the work piece to the tool, and Q is the load [N]. For zonal polishing, sub-aperture tools within a tolerance of few micrometers are used which are flexible enough to adapt

themselves to the local curvature of different optical surface shapes such as asphere or freeform[123]. A variety of different techniques that are available for polishing are compared in **Table 3.3**.

Table 3.3 *Overview on different existing methods for polishing on optics used in the second step of process chain of subtractive techniques.*

Smoothing technique	Material	Advantages	Disadvantages	Surface roughness (nm) RMS
Speed/pitch polishing	- Almost all brittle materials	-Very low surface roughness - Fast polishing process	- Not effective for correction of local surface deviations	0.2-0.5
Continuous-wave CO_2 laser polishing/ Ultrashort pulse VUV laser	- Fused silica - N-BK7 - S-TIH6	- No subsurface damage - Contactless	- Surface roughness due to glass ablation	1
Direct ion beam smoothing	- SiC - Si - SiO_2 - GaN - ZnO	- Effective for surface roughness with very high spatial frequencies 0.001 nm^{-1}	- Less effective for low frequency roughness - Surface erosion	0.1-0.4
Ion beam smoothing with planarization	- Optical surfaces -Semiconductor	- Suitable for high-spatial frequency roughness	- Spray-coating by photoresist layer is required	0.8
Plasma jet polishing	- Fused silica - ULE	- No subsurface damage - Low physical load	- Limited choice of material - Surface roughness	Less than 1

3.3.3 Local figure correction

After the polishing process, the roughness of the surface with freeform shape has an optical quality, but still the surface accuracies cannot reach below 1 μm. Therefore, a third step known as "local figure correction" within the process chain is prerequisite to meet the final surface specification[124]. The goal of this step is to minimize residual surface deviations from specified shape. This can be fulfilled by target removal depth $D(x,y)$ in the localized areas of the optical element based on measurement performed in advance. Due to the lacking rotational symmetry and varying local slopes, a locally acting so called sub-aperture tools are usually employed in deterministic surface machining processes. In recent years, a series of sub-aperture tools have been developed that revolutionized the fabrication of aspherical and freeform optical surfaces[125-128]. **Table 3.4** provides a brief overview on the features of different techniques that are available currently for local figure correction. The sub-aperture tools are usually characterized by the certain tool function $R(x,y)$ that determines the material removal rate. The shape of the tool function $R(x,y)$ has significant effect on the convergence of process.

Table 3.4 *Overview on different existing methods for local figure correction used in the third step of process chain of subtractive techniques.*

Local corrective figuring	Material	Advantage	Disadvantage	Shape deviation (nm) PV	Surface roughness (nm) RMS
Sub-aperture bonnet polishing	- Almost all brittle materials	- Fast polishing process	-Tool wear - Edge roll-off	30	0.5
Magnetorheological finishing	- Almost all brittle materials	- No edge roll-off - No tool wear - Low damage	- Central artifact for tool path - Required fluid	10	0.3
Fluid jet	- Almost all brittle materials	- No edge roll-off	- Stability of footprint	30	0.5
CO_2 laser evaporation (laser beam figuring)	- Fused silica - N-BK7 - S-TIH6	- No subsurface damage - Contactless	- Surface waviness	5	Less than1
Ion beam figuring		- No edge roll-off - No tool wear - Low damaged	- Low removal rate - Requires vacuum	5	0.2
Fine-focused plasma jet etching	- Silicon - Fused silica - ULE - SiC	- No tool wear - Low SSD	- Limited choice of material	5	Less than 1

On the one hand, it must be narrow banded to remove the appropriate amount of material precisely; on the other hand, it must be smooth enough to create smooth surface. It is found out that Gaussian-like tool is one of the most desirable shapes. It is smooth and removes most of material within a small central area. Additionally, due to its normal shape, it reduces the required positioning correctness of the acting tool, that allows more stochastic moves tending to smooth the machined surface out[130].

The sub-aperture tool with a determined tool function *R(x,y)* moves over the surface to be corrected in either “feedrate” or “dwell-mode” to realize a target removal depth *D(x,y)*. Within the dwell-mode, the tool moves alternatingly at tool path points for a given time. Here, the tool is continually accelerated from zero to maximum speed of the machine imposing undesirable stress and vibrations. Furthermore, extreme runtime is an issue particularly for machining process requiring highly repetitive sweeping movement[131].

Within feedrate mode, the tool moves between the dwell points with a constantly varying feed. This mode is most widely used as it does not suffer from the drawbacks of dwell mode. The determination of the feed rates is accomplished by “dwell time” calculation algorithms that are either based on

"numerical deconvolution" method[132-134] or "linear matrix model"[135-136]. Then, the determined feedrate commands are sent to CNC controller to machine the surface based on the target removal depth[137]. **Figure 3.4** provides a typical workflow of the standard deterministic surface machining based on the dwell-time method using sub-aperture tool[129].

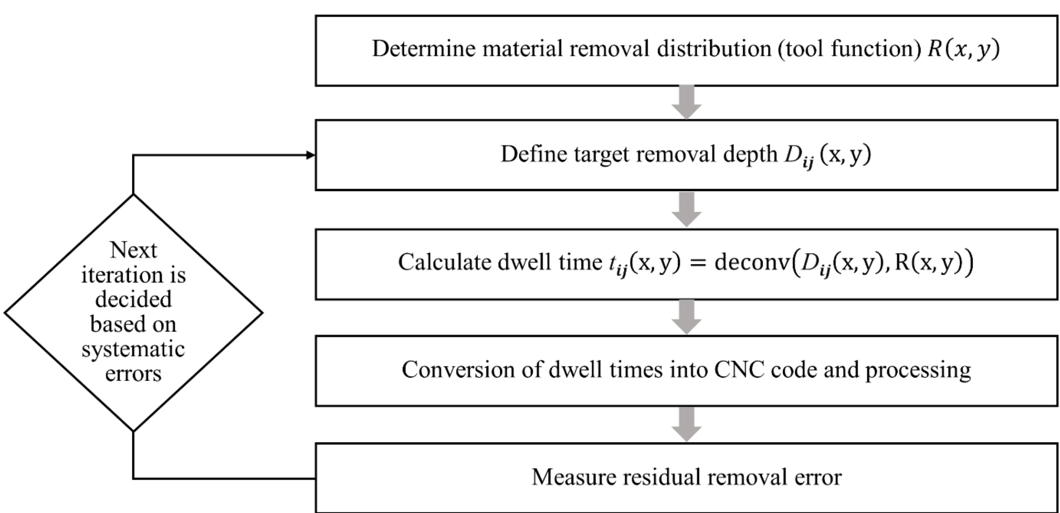

Figure 3.4 *Typical workflow of the standard deterministic surface machining process based on the dwell-time method using sub-aperture tool*[129].

The resulted removal $\widehat{D}(x,y)$ can be derived by the convolution of the tool function *R(x,y)* with the dwell time *t* .

$$\widehat{D}(x,y) = \iint R(x-\acute{x}, y-\acute{y})\, t(\acute{x},\acute{y})\, d\acute{x} d\acute{y} = R \otimes t \tag{3.2}$$

Figure 3.5 shows the target and resulted removal depth obtained in both simulation and experimental measurement for deterministic surface machining process using fine-focused plasma jet as a sub-aperture tool[138]. The evaluation of results indicates the existence of a residual removal error $E_R = D - R \otimes t$.

The residual removal error E_R is normally in the range of medium-frequency structures that cannot be removed easily although the RMS-value of E_R decreases as the tool becomes smaller. Hence, the tool should be adapted to the error structure. **Table 3.5** shows effect of the size of Gaussian tool function on the RMS-value of the residual removal error E_R and the corresponding processing time during deterministic machining on fused silica [138]. The results indicate the reduction of residual error as the size of tool function decreases. However, the RMS-value of residual removal error does not approach to zero as the tool size cannot be arbitrary small. The process time increases rapidly with decreasing the tool size. For instance, in the case that the sub-aperture tool has a Gaussian tool function, the processing time t_{total} cab be estimated as follows

$$t_{total} = \frac{\text{volume to be removed}}{\text{volume removal rate}} \propto \frac{1}{FWHM^2} \tag{3.3}$$

where FWHM indicates the full width at half maximum. Furthermore, depending on the respective machining technology and sub-aperture tool, the tool function *R(x,y)* may exhibit a nonlinear temporal behavior that must be taken into account appropriately in the dwell time calculation algorithms. To tackle this problem, regularization methods were proposed in applying a typical damping factor based on the tool function to adjust the convergence rate and dynamic fluctuation of dwell time[139-140]. However, these indirect feedrate scheduling methods have some problems in integrating the variable behavior of tools (for instance imposed by the machine dynamic stressing) directly into the dwell time optimization algorithm.

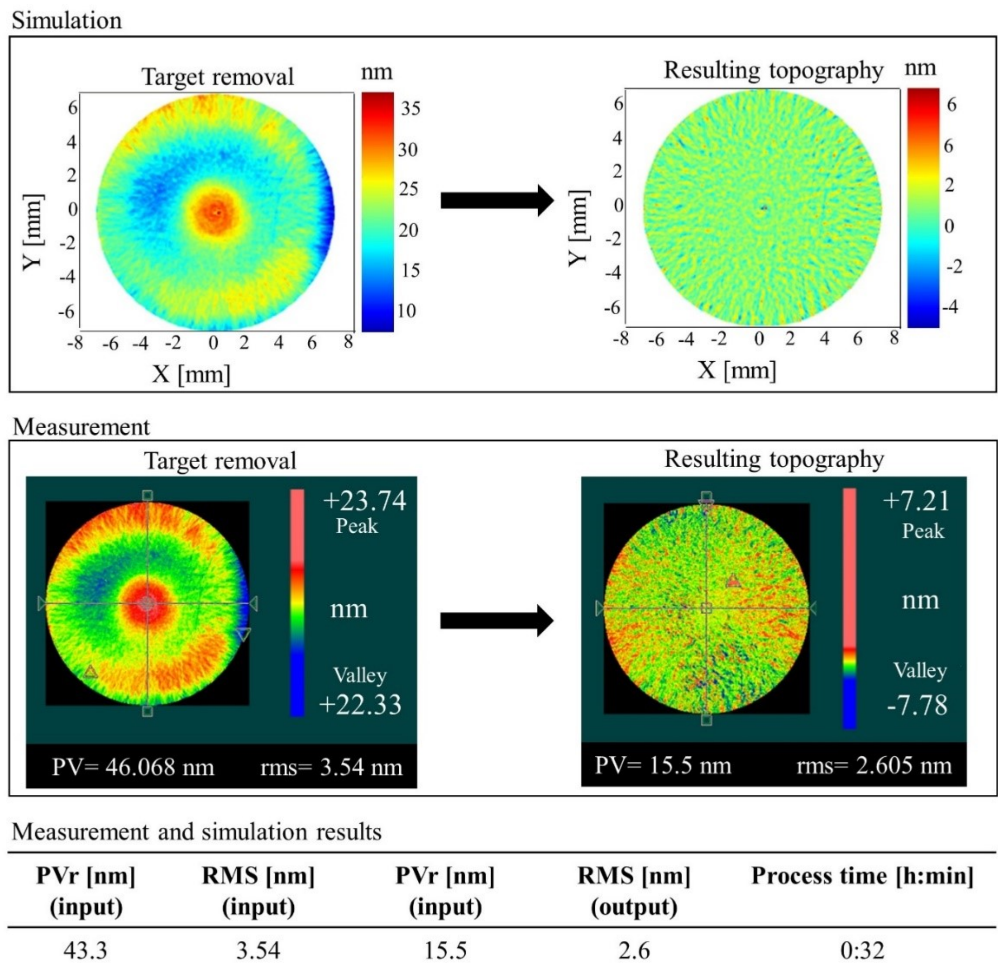

PVr [nm] (input)	RMS [nm] (input)	PVr [nm] (input)	RMS [nm] (output)	Process time [h:min]
43.3	3.54	15.5	2.6	0:32

Figure 3.5 *Target and resulted removal depth obtained in both simulation and experimental measurement for deterministic surface machining process using fine-focused plasma jet as a sub-aperture tool.*

Table 3.5 *Effect of the size of Gaussian tool function on the RMS-value of the residual removal error E_R and the corresponding processing time during deterministic machining on fused silica*[138].

Gaussian tool functions	FWHM [mm]	Theoretical residual error	RMS [nm]	process time [min]
	20		1.2	25
	10		0.7	50
	5		0.6	100

Hence, a more direct and novel scheduling method was required to enhance the scope of variable deterministic processes. The linefeed scheduling (varying linefeed along the tool function), the tool scheduling (adjusting path spacing across the surface) and scheduling volumetric removal rate (VRR) across the surface through process parameters are some recent novel scheduling approaches to optimize deterministic material removal in time-dependent processes. For instance, adaptive polishing paths in form correction were introduced to reduce ripple error and optimize the dwell-time distribution[141-142]. Furthermore, it was proposed to actively adjust the pressure in tool function to obtain uniform material removal distribution for curved surface polishing[143]. In another study, the removal uniformity of polished low-rigidity parts was improved by adjusting the processing distance of the tool, dynamically[144]. During the surface figuring using pure chemical PJM, the tool function is highly affected with the workpiece surface temperature induced by jet heat flux. Thus, a comprehensive method of determining the corresponding model parameters was developed based on temperature measurements to adapt the tool function at any given time[145]. However, there is still a lack of a unified scheduling model for deterministic processing applicable to a variety of different sub-aperture tools and optical elements. For instance, when the material removal of optics containing metal compositions is realized by a chemical dry etching process (i.e., PJM), the resulting non-volatile etch by-products can influence the tool function in non-linear way leading to a time-dependent process[146]. To tackle this problem, in **Chapter 5** of this thesis, an iterative algorithm is proposed for dwell time calculation to rescale the reactive tool function on N-BK7 depending on feed rate.

3.3.4 Advances in abrasive methods for precision aspheres manufacturing

The benefits of aspheres and freeform in optical designs such as better performance and a lower number of elements have been recognized for several years. However, the difficulties in fabricating them was always an obstacle. Due to the deviation of aspherical surfaces from spherical optics, grinding with full-size shaping tools does not work properly, and peripheral grinding with quasi-point engagement is required. Nevertheless, the principle of the spherical CNC machining with fixed abrasives can be still exploited to realize a reproducible fabrication with standard cup tools. Precisely controllable positioning of the tool and a transition from a line contact (during spherical grinding) to point contact allowed a deterministic and reproducible production of aspherical surfaces. In contrast to the spherical surfaces, the contour of the asphere surface is followed as a path. In this way, various radii of curvature can be generated by variation of the tool angle and without any form tools[122].

After aspherical shaping by zonal grinding, the surface needs subsequent polishing step. In this step, high stock removal is required to eliminate subsurface damage, perfectly. However, the full aperture polishing tools cannot be applied here due to the local curvature variation of freeform surfaces. In such cases, a controlled zonal polishing method with adaptive sub aperture tools is desirable. The sub-aperture tools can be adjusted to the surface, for instance, by an elastic pad or by air pressure behind the polishing pad. Individual methods for zonal polishing of optical elements are used by designers where each of them has its own manual and empirical solution. The commence of computer technology allowed to automate the zonal polishing process. The first commercially available CNC machines for zonal polishing of aspheres with shorter diameter ranges (< 100 mm) entered the market in the mid-1990s. To date, sub-aperture polishing with CNC machines has been applied for almost all kinds of optics with specifications of $\lambda/2$ or even less, and diameters ranging from a few millimeters up to 8 meters[47].

Following up the zonal polishing process, the use of computer-controlled bonnet polishing (CCBP) for a correction of the surface deformation allowed to improve the optical performance of treated element and reduce the number of iterations. These methods have the advantage of being applied for different substrate materials with various shapes (from planar to freeform surfaces) and diameters. However, CCBP methods still suffer from tool wear during process that results in deviation of the tool function[125].

Alternatively, the advanced local figure correction methods without a polishing pad such as magnetorheological fluid (MRF) and fluid jet polishing (FJP) made it possible to remarkably decrease the deviation of the tool function. The strength lies in its flexibility, principally achieved by exploiting no special tool[127].

MRF is best suited for the fast fabrication of preliminary models of aspherical and freeform surfaces in the low- and even mid-size series. As it requires no particular tools, it represents a minimal preparation time and high flexibility. A wheel with a magnetorheological liquid is used instead of sub-aperture pad.

The effect of tool wear (i.e., the main problem in CCBP process) is removed by using a fluid which can be adjusted via its viscosity by applying external magnetic field. The stable tool function is achieved by stabilization of the fluid viscosity and constant modification of the contact zone between tool and workpiece. In this way, it is possible to preform deterministic ultra-precision surface finishing in the scale of nanometers of nearly any surface, in particular, aspheres and freeform. The measured surface deformation of a polished asphere is deterministically corrected by dwell time-based approach.

FPJ is a sub-aperture finishing technique that uses an abrasive slurry jet for polishing optical surfaces. A pressure ranging from 3 to 20 bar is applied through a nozzle to guide a premixed slurry to the surface of the workpiece. The characteristics of the tool function are determined by the process parameters (e.g., the form of the nozzle and the direction of the slurry beam w.r.t. the local surface normal) but not with the given tool geometry. As no tool wear appears during the manufacturing process, the tool removal function remains constant. Thus, FPJ is appropriate for deterministic shape corrections of nearly any surface with different shapes and materials, especially for the brittle materials such as glass[147].

3.4 Laser-based methods

Laser ablation of optical glasses is a challenging task as the laser photon absorption is usually low while a good machining performance requires sufficient absorption. By pulsed vacuum ultraviolet (VUV) lasers (157 nm), a sufficient absorption for machining of optical glass like fused silica can be achieved even for nanosecond lasers[148-149]. Due to the nonlinearity of absorption processes, ultra-short laser pulses are applied to allow laser ablation at reduced fluences and hence to enable machining of these materials[150-151]. However, the ablation rate is rather high (~100 nm/pulse), and the surface quality is regularly limited due to the impact of melting or laser-induced (periodic) surface structures. Hence, a different approach has been developed for laser ablation of optical glasses that makes use of an absorbing material attached to the surface to be etched. The absorbing material enhances the absorption of the laser photons and induces processes that finally result in a precise etching of the surface with low roughness and small etching rates. The properties of absorbing materials correlate with the etching rates; for liquid hydrocarbons (LIBWE – laser-induced backside wet etching), [152] hydrocarbon gasses (LESAL – laser etching at surface adsorbed layers)[153], and metal films (LIBDE – laser-induced backside dry etching) [154] etching rates of approx. 10 nm/pulse, less than 1 nm/pulse and less than 20 nm/pulse have been respectively determined. The mechanism of LIBWE is rather complex but, in the case that halogenated organic solvents are used, can involve processes of chemical etching with activated halogen components. [155] However, the requirement of laser photon absorption at the interface of the sample material and the absorber limits the applicability of this approach. Therefore, several laser-enhanced chemical etching technologies have been introduced that utilize the laser beam to stimulate inherent chemical reactions of gaseous etchants with surfaces. These techniques are

demonstrated mainly for pure optical materials such as silicon or GaAs, which make use of highly reactive gases like chlorine and require usually absorbing sample materials[156]. The combination of laser and plasma processing simultaneously or sequentially has been already investigated. The simultaneous application of a pulsed VUV laser beam with a plasma jet in a co-axial configuration has been used for optical glass surfaces. However, the expected modification of the glass surface by the plasma source is not appropriate for a substantial alteration of the laser glass interaction process. The surface characteristics of the laser-irradiated glass mostly correspond to the laser ablation process since the laser energy density in the laser spot is 700-times larger than that of the plasma jet[157-159]. In the case of the sequential approach, in which firstly a laser irradiation with ultra-short laser pulses is applied and afterwards it is followed by a microwave plasma etching process, the differences in the surface morphology are observed. It seems, that the surface morphology of the combinatorial process is a mixture of those achieved by each of the techniques separately[160].

Ablation of fused silica as well as some other glass materials can be reached also by using CO_2 lasers. It was shown that an initial roughness with RMS value of 0.33 nm can be improved to 0.27 nm by applying the defocused continuous-wave CO_2 laser radiation and a meandering scanning scheme. Moreover, the pulsed CO_2 laser based polishing method was introduced for industrial applications to fabricate micro-optics. Because of the fast movement of the defocused continuous-wave CO_2 laser beam, a homogenous temperature distribution in the quasi line on the surface was achieved that reduced the surface roughness by a remelting process to some extent[161-167].

However, the achieved roughness with different types of laser polishing was not enough for illuminating and imaging optics due to a roughness $S_a > 1$ nm that is still not suited for spatial wavelengths of $\lambda > 100$ µm. On the other hand, the fabrication of high-quality freeform optics by laser-based process requires further process steps including surface figuring and local figure correction[168-171]. More recently, a CO_2 laser process was introduced by Fraunhofer Institute that changed the picture. Sophisticated and freeform shapes can be fabricated from bulk glass through a three-step laser-based process including the ablation, surface polishing, and local figure correction. By applying two acousto-optic modulators, the laser radiation is generated within two modes: (i) Q-switched pulse mode for ablation, and (ii) modulated pulse mode for local figure correction. In the first step, Q-switched pulse is applied for surface figuring with the average power of 200 W, the pulse duration $\geq$ 250 ns and the maximum repetition rate of 150 kHz. The selective ablation of bulk glass with the relatively high VRR value of 2.35 mm^3/s is accomplished allowing fabrication of any freeform shapes though it is microscopically rough. This remaining large roughness after the ablation process can be reduced in the second step by using continuous-wave CO_2 laser radiation. In this step, the surface roughness decreases below 1 nm via a remelting process. Eventually, in the third step called laser beam figuring, modulated pulses with the average power of 50 W are applied that have lower material removal rates suited for local figuring correction and elimination of residual waviness. By adjusting the pulse duration of each laser pulse,

material can be ablated locally with lower depths down to 3 nm. It was demonstrated that the surface quality of the fabricated optics by this laser-based process is sufficient for illuminating optics[172].

3.5 Ion beam technology

Ion beam technology is a contactless surface machining technique that uses an ion gun instead of sub-aperture tool in CCBP process to manufacture precision optical elements. An ion source from a plasma of rare gas (e.g., argon) is used to create ions in vacuum chamber where they are accelerated by a negative voltage. The ions hit the surface with kinetic energy of several keV and absorb inside the workpiece. Each incoming ion is able to extract one to two atoms of the workpiece. The sputter rate of the ion beam can be calculated exactly based on the elastic and inelastic scattering rule. One of the reasons that makes the process stable and predictable is the absence of chemical interaction. Extensive investigations have been performed to exploit ion beam for generating a variety of microscopic surface topographies on optical components[173, 187]. These studies have revealed that a nano-pattern or in some cases a smoothing effect can occur depending on ion beam sputtering conditions and relative materials properties. More recently, some efforts concerning applications of ion beam techniques for ultra-precision optical freeform design have been conducted. The latest outcome is technically exploited as ion beam figuring (IBF) and ion beam smoothing (IBS) which are employed respectively in surface figuring and local figure correction of optical surfaces with accuracies in a nanometer range as required for optical applications[187]. IBF is a highly deterministic method for the final figuring of curved substrates such as aspherical lenses or freeform mirrors. A scanning ion beam is used in IBF that can be adjusted to the surface form, which is not reachable with any conventional polishing technologies. Several IBF technologies have been introduced aimed for deterministic figuring of either plane or freeform surfaces with different lateral dimensions of optical surfaces. These technologies operate based on a deterministic dwell time approach in which the dwell time distributions are qualified for the proposed profile depth. In this respect, the central point of beam is derived on a curving path with variable rate along the surface to figure the freeform target shape. The aim is to figure final surface shape with RMS value of surface roughness below 1 nm.

IBS is used for smoothing of optics to generate ultra-smooth surfaces with RMS values less than 0.2 nm. Compared to IBF, the IBS process is less deterministic as it is based on atomic (or molecular) material removal mechanism, and hence it is characterized for much shorter spatial length scales. Different types of IBS have been used as unconventional tools for the preparation of ultra-smooth surfaces with RMS values $\leq$0.2 nm. They are used for the treatment of nanometer-precision optical surfaces, where smoothing properties dominate over ion beam roughening during the surface morphology evolution. Recently, developed IBS processes can be categorized into beam direct smoothing, smoothing with planarization[173-175].

3.6 Classification and generation of plasmas

Plasma is an ionized gas described as the fourth aggregate state of matter. Plasma is an electrically neutral medium of unbound positive and negative particles which occurs naturally but also can be artificially created by exposing a neutral gas to a strong energy until an eclectically conductive ionized gaseous matter is achieved[235]. This energy can be thermal or carried by either electric current or electromagnetic radiations. Most of industrial plasmas are generated by introducing high-voltage DC electric power fields in which the energy in plasma is first transmitted to electrons due to their greatest movability[236-237]. Then, the electrons can transfer the energy to heavy particles by either elastic or inelastic collisions. Plasma temperature is determined by average energies of plasma components, electrons and their related degrees of freedom including translational, rotational, vibrational, and electronic excitation. Electrons temperature T_e in plasma is initially greater than heavy particles T_0 since electrons are much lighter, and during ionization process, merely slight quantities of electrons energy is consumed through the collision with heavy particles. However, if time and energy are adequate, the consecutive collisions of electrons with heavy particles can equilibrate plasma temperatures locally. Otherwise, plasma temperature cannot reach to the equilibrium locally and present different ranges of temperatures. Based on plasma temperature, plasma is classified to thermal (or local thermodynamic equilibrium (LTE)) and non-thermal (or non-local thermodynamic equilibrium (NLTE))[176]. In LTE plasma, ionization and chemical process is controlled by temperature although the electrical fields can also affect indirectly through Joule heating. LTE plasmas are very powerful with temperatures of around 10,000 K and are used in wide variety of applications from academia to industry. LTE plasmas are particularly suitable for material processing approaches such as melting, cutting, welding, or coating. On the other hand, in NLTE plasma, only velocity of electrons follows Maxwell-Boltzmann distribution. In this case, the electron temperature T_e is remarkably higher than that of heavy particles T_0 (i.e., $T_e >> T_0$)[176]. In NLTE plasmas that are weakly ionized, electron temperature T_e is the largest in the system and may even reach to 1 eV (about 10,000 K) followed by the temperature of vibrational excitation of molecules T_v. The temperatures of gas (i.e., heavy neutrals) T_0, ions T_i as well as molecules T_r with rotational degree of freedom are roughly close to each other and make the lowest temperature in system and even they can reach to room temperature. Therefore, the relation of different plasma temperatures in NLTE plasmas can be realized as $T_e > T_v > T_r \simeq T_i \simeq T_0$[176]. Due to low temperature, NLTE plasmas can be used in a wide variety of applications in different areas of engineering particularly for plasma chemistry. Despite their lower power compared to LTE plasmas, NLTE plasma can be more selective. Although LTE and NLTE plasma have very different types of ionized gases, both have some common features which can be used for ionization and chemical process. Based on the general rule in chemical kinetics, the total energy for ionization is estimated about 10 eV. However, the energy required for initiating chemical process is Arrhenius activation energy which is about 10% of the total required energy (1 eV). This amount of activation energy can be provided by both LTE and NLTE plasmas as

they have the highest temperature (electron temperature T_e) on the order of magnitude of 1 eV, which is about 10% of the total energy required for ionization (i.e., 10 eV). This energy can be used as activation of the ionization and chemical process[238].

Furthermore, plasmas are classified according to gas pressure and degree of ionization. Plasma generated under pressure of 10^{-4} to 10^{-2} kPa is known as low-pressure plasma. Low pressure plasmas are usually NLTE. During the low-pressure plasma process, the surface can be modified through the ion bombardment using energetic species, the chemical interaction of the ionized gases with the substrate surface, and the UV radiation. Hence, low-pressure plasma is used widely for the act of treating, etching, and coating of surfaces of different materials by bringing physical and chemical features which are different from the ones initially found on the surface of a material. In Atmospheric pressure plasma the gas is ionized under atmospheric pressure by a high voltage such that a plasma discharge is emitted with compressed air from the nozzle to be ignited. During the atmospheric-pressure plasma, surface can be etched or modified by reactive particles contained in plasma source. In addition, loose, adherent particles can be detached from solid surface by gas flow in the accelerated plasma jet. Surface modification accomplished by plasma jets can have comparable results with that obtained by low-pressure plasma[239]. The plasma source can have different lengths and treat a substrate surface with different widths depending on the power and gas flow. In this work, reactive atmospheric-pressure NLTE plasma source is used for optical surface figuring through chemical etching.

3.6.1 Plasma-based pure chemical etching: mechanisms and kinetics

Surface etching is a type of treatment by which a desired pattern is created on the substrate surface by removal of material chemically. Since the chemical and disposal costs for deploying wet etching are high, modern processes make use of plasma etching rather than wet etching. Plasma-based pure chemical etching functions under atmospheric pressure without any contribution of energetic ions. The non-thermal plasma sources generate high concentration of active particles, which are able to react with surface chemically to form volatile products. The volatile products exhaust away immediately by the continuous gas flow, and then the surface is etched. As plasma generated particles attack the surface from all angles, isotropic process is made. The plasma etching rate is determined by several parameters such as plasma composition, supplied power, substrate and other working conditions. Gas mixture used for plasma source affects etching features like rate and selectivity. The role of different gas mixtures in a non-thermal plasma contributing to etching can be categorized into the following clusters:

I. Saturated compounds: different chemically inactive gases such as NF_3, CF_4, COF_4, SF6, CCl_4 can be used to dissociate in plasma for generating chemically active particles like etchants and unsaturated compounds.

II. Unsaturated compounds: radicals such as CF_3 and CCl_3, and molecules like C_2F_4, C_2F_6 and C_3F_8 react with surface which mostly ends up with forming residual layers. However, it is possible that in some cases volatile etch products are generated to remove material from surface.

III. Etchants: atoms such as F and Cl and molecules like F_2 and Cl_2 are the most reactive components of plasma discharge which interact with substrate surface immediately to remove material.

IV. Oxidants: O and O_2 are mixed to plasma feeding gas in order to react with unsaturated compounds transforming them into etchants.

V. Reductants: H, H_2 gases are mixed to plasma feeding gas in order to react with etchants to neutralize them generating inert volatile components.

VI. Inert gases: additives like N_2, Ar and He are supplied to plasma feeding gas for adjusting surface temperature of substrate, shielding of discharge and controlling electrical features of plasma.

The flux ratio of “etchants” to “unsaturated compounds” plays an important role in etching process. A low flux ratio can form residual layers and suppress etching while isotropic etching is achieved for a large flux ratio. The flux ratios can be boosted by feeding plasma with the gases that are able to produce only etchants but not unsaturated compounds like F_2. Alternatively, oxygen can be added to the gas mixture to increase the flux ratio by transforming unsaturated compounds to etchants[176-177].

3.6.2 Plasma technology for high efficiency machining of optical elements

In the past 25 years, plasma-based machining was investigated for highly efficient surface figuring and local figure correction of optical elements under atmospheric pressure. Mostly, a barrier-like method is exploited for producing plasma sources which are either spatially limited to the space between the electrodes or embedded in a kind of chamber. The plasma source can be supplied with noble gases (i.e., argon and helium) mixed with potentially reactive gas containing fluorine (i.e., NF_3, CF_4, SF_6). The interaction of plasma generated active fluorine with Si atoms in glass results in “volatile products” and material removal. The ability of achieving enhanced gas phase chemistry without need for elevated gas temperatures makes reactive plasma discharge a valuable source to remove material of optical surfaces in multiple directions with the uniform rate (i.e., isotropic etching). The surface is scanned by reactive plasma source in place of a sub-aperture tool causing a geometric self-determination to largely reduce the existing constrains in the manufacturing precision optical surfaces with an individualized design. The atomistic material removal mechanism without applying any significant mechanical forces on the surface is the main advantage that plasma-based machining has over mechanical-abrasive correction methods. No subsurface damage (SSD) is introduced to the surface providing a long-term stable etching tool predetermined for the freeform optical fabrication. In contrast to IBF, this process does not require ultrahigh vacuum conditions. The removal rate of plasma etching is a factor 10 to 20 higher compared to IBF. A reactive plasma torch with the large lateral dimension of several millimeters can be used for surface figuring as substitutional approach for conventional methods like the mechanical grinding. Also,

the fine focused plasma jet can be used for local figure correction as a replacement for IBS or magnetorheological finishing (MRF).

However, due to the pure chemical nature of plasma-based machining, the choice of material that can be etched is limited. Moreover, the surface roughness can be sometimes insufficient for optical application. In this circumstance, the process chain should comprise additional mechanical polishing steps, for example, shape-preserving bonnet polishing to meet the obligatory specification for surface roughness. The plasma chemical vaporization machining (PCVM), reactive atom plasma technology (RAPT), atmospheric pressure plasma processing (APPP), arc-enhanced plasma machining technology (AEPM) and PJM are some of the main plasma-based machining techniques currently applied in the production of optical elements.

PCVM is RF-driven Capacitive coupled discharge (13.56 MHz) used commonly for surface figuring and machining of fused silica with the VRR efficiency equivalent to that of the precision grinding. The findings show that the device allows high-precision fabrication from nanometers to micrometers. The shaped surface is sufficiently smooth for optical use[179].

RAPT is an inductively coupled plasma (ICP) developed for surface machining of ULE optical elements providing high VRR (up to 0.55 mm^3/s) and low surface roughness. VRR and the surface temperature both depend on plasma parameters such as the RF power and the travel speed of plasma source[180].

APPP is a coaxial electrode type plasma source using capacitive coupled discharge that is an efficient tool for precise figuring process of fused silica. The APPP can operate by either jet or contact discharge mode where the VRR efficiency of contact discharge mode is much higher than that of jet processing mode[181].

AEPM is an arc-enhanced plasma machining technology introduced for high efficiency and near-zero damage machining of silicon carbide (SiC). Due to the high chemical stability of SiC, most of plasma etching methods seem incapable of obtaining a high VRR for SiC. It was shown that VRR can be considerably enhanced while the electric spark develops between the plasma discharge and the SiC surface. The VRR of 0.35 mm^3/min is obtained, that is about 10 times as high as the other plasma-based machining methods. Due to the negligible thermal effect, the surface figuring can be achieved using the conventional dwell time method. Furthermore, the shape error of a flat SiC surface is corrected by using AEPM[182].

3.6.3 Plasma jet machining (PJM)

The development of PJM has been started in IOM approximately 20 years ago[183]. PJM is an atmospheric pressure non-thermal reactive plasma jet used as an etching tool providing possibility of varying the corresponding radical beam from small to large lateral dimensions. PJM is mostly supplied by a

combination of fluorine containing gas and oxygen as the precursor gas dissociating in the plasma jet to form reactive gas. The energy of source is provided either by a microwave or RF power for triggering plasma at the tip of the inner nozzle where the high electric field power ionizes gases to create jet-like plasma discharges[184-185].

PJM is currently successfully applied in the production of freeform optical elements made of silicon, fused silica, or silicon carbide, as well as to some other types of optical glasses. Here, the underlying principle of material removal is a localized chemical dry etching process performed by a fluorine-containing jet-like plasma discharge that interacts with the substrate material whereby the substrate surface is converted to gaseous state. In the case of fused silica etching, the reactive species form mainly SiF_4 and O_2 as reaction products. Caused by the chemical material removal mechanisms, the removal rate depends on the one hand on the concentration distribution of reactive species (i.e., fluorine) and on the other hand on the surface temperature distribution[186-188].

Deterministic dwell-time approach for freeform surface machining has been used so far for easy-to-etch materials (e.g., fused silica). Depending on the corresponding assignment, plasma jet with certain tool widths (i.e., FWHM) is used leading to desired etch-profile depth and VRR.

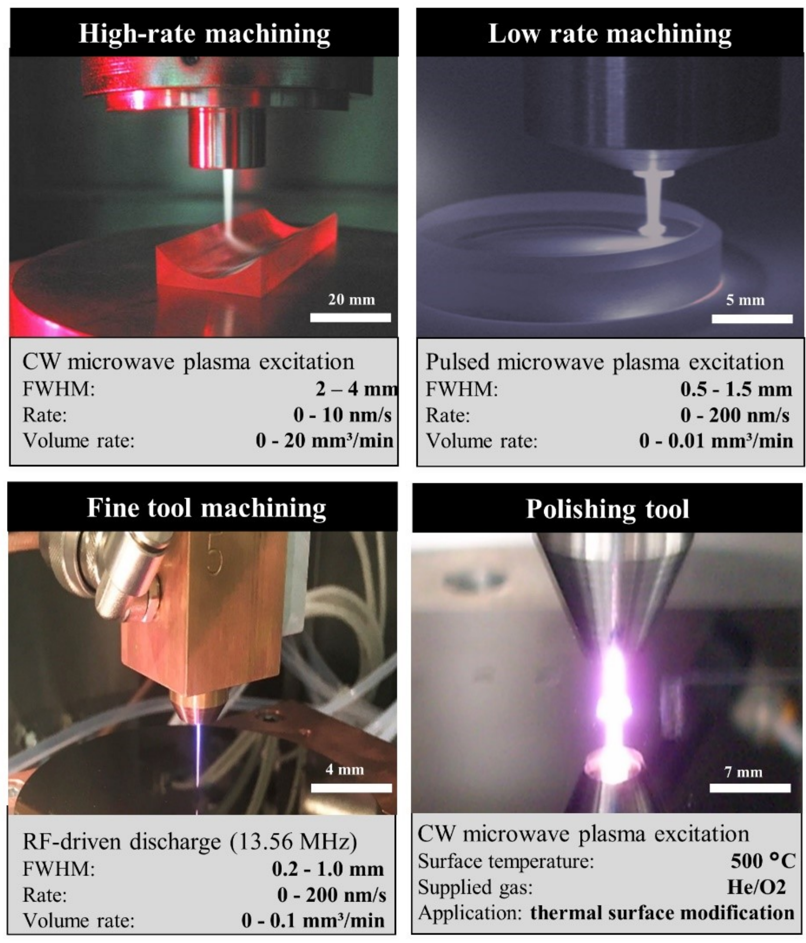

Figure 3.6 *Different types of PJM designed for precision surface machining of optical elements.*

For surface form generation, a high-rate plasma jet etching with the microwave power of 200-400 W and tool width (Gaussian FWHM) about 2-4 mm is developed. By applying plasma jet to surface in downstream mode, the maximum VRR 20 mm^3/min can be obtained. Surface temperature of this plasma jet is in the range of 200 °C to 600 °C which imposes high non-linearity to etching rate (**Figure 3.6(a)**). Such behavior can be considered in iterative dwell time calculation algorithms by appropriate rescaling of the tool function depending on the feed rate[145].

A low-rate plasma jet etching is made by a pulsed microwave excitation with the mean input power 6-30 W and the tool width about 0.4-1 mm used for low depth surface figuring as well as residual error correction. This plasma is applied currently for surface figuring of N-BK7 and fused silica with maximum VRR 0.03 mm^3/min and 0.01 mm^3/min, respectively (**Figure 3.6(b)**).

For local figure correction, fine focused plasma jet etching with a low etching rate is required to work in direct mode. For this purpose, capacitively coupled plasma jet driven by a RF-power supply (13.56 MHz) with maximum mean input power 60 W is developed. These compact systems can reduce the lateral dimension of the plasma jet to the submillimeter range aiming to correction of residual error. Currently, capacitively coupled plasma jet with tool width down to 0.2 mm is available. These plasmas are used for correction of mid-spatial frequency structures of fused silica, Si and ULE. Maximum VRR 0.1 mm^3/min is obtained in the case of fused silica (**Figure 3.6(c)).**

Plasma jet polishing of optical glasses is used for preparation of surface machining such as cleaning surfaces and formation of diffusion layers. Instead of mechanical polishing procedures which are time-consuming and have limited flexibility, thermal surface modification by plasma jet polishing can be used alternatively for removal of damages. The plasma jet is supplied by a combination of carrier gases like helium and oxygen as the reactive precursor gas mixture (**Figure 3.6(d)**).

The application-required specific glass properties are achieved by a unique complex material composition, which is challenging for PJM. For instance, PJM of N-BK7 (as a metal oxide containing glass) by fluorine-based plasma jet has some limitations in process due to formation of non-volatile etching by-products. Therefore, the focus of this thesis is to investigate the interaction of PJM on N-BK7 surface aiming to extend deterministic plasma-based machining particularly for freeform surface figuring of optical glasses beyond the pure silica-based material.

3.7 Aspects of optical testing techniques

Surface topography is one of the most significant features of optics indicating shape, texture as well as roughness of the surface. Both applications and properties of optics depend on their surface topography. Efficient analysis of surface topography becomes achievable only when testing devices with adequate

magnification-capability are available. In this way, structures of different surfaces can be analyzed effectively to determine the dissimilarities between areal surface and general characterization of surface shape with high accuracy. Different types of techniques are used currently to measure surface shape and roughness with sub-nanometer accuracy. **Table 3.6** summarizes the main features of four different commonly used optical testing techniques including contact and pseudo-contact measurement, interferometry, wavefront sensor and scattering measurements[191-200].

Table 3.6 *Overview on different commonly used optical testing techniques.*

Optical testing technique	Accuracy (nm)	Disadvantage	Diameter (mm)
Contact and pseudo-contact measurement	3.2 - 0.8	- Require calibration process - Measurement of aspheres is not possible	1-200
Interferometry	λ/20 - λ/4 (1 nm for high precision)	- Need for use of null lens for Measurement of aspheres and freeforms	2 -250
Wavefront sensor	λ/20 - λ/4 (1 nm for high precision)	- Ambiguity	2-100
Scattering measurement	1 - 0.1	- Radius of local curvature bigger 10 spot size	4-400

Mechanical profilometer is a contact metrology consisting of a sensor (i.e., ruby ball or diamond tip) that is moved in touch with a sample perpendicularly, and then displaced horizontally through the sample for a certain distance and contact force. The goal is to examine the shape as well as the roughness of optical surfaces within different states of the production process. No a priori information about the shape is required. This approach can be classified as 2D- and 3D-scanning systems. The accuracy requirements are comparable to the visual inspection methods in interferometry (i.e., λ/10 with λ= 633 nm). Mechanical profilometer can be used to measure aspherical and freeform surface deformations. Pseudo-contact approaches refer to atomic force microscopy (AFM) and scanning tunneling microscopy. Sensor types can be classified to optical, pneumatic, and atomic force sensors. AFM is commonly used for surface roughness measurement with very high-resolution ranging from fractions of a nanometer to about thousand times greater than the optical diffraction limit. The surface roughness is quantified by employing tapping mode with an atomic force sensor, and accurate scanning is achieved by piezoelectric elements.

Interferometry refers to a technique in which electromagnetic waves are superimposed resulting in interference. This phenomenon of interference is used to extract information. Scale of interferometry is the wavelength of light. Polished optical surfaces with different shapes either spherical or freeform surfaces can be measured by this approach with high precision. Interferometry can be used to measure surface deformation, micro roughness, as well as material homogeneity and birefringence for both reflective and refractive elements. Additionally, interferometry can be applicable for lens thickness measurement. Typically, 10^4-10^6 points can be delivered in one interferometry measurement providing

a 2D map of optical path differences and surface deviations from a reference based on defined setups and calibration data. For measurement of aspheriacal and freeform surfaces, no reference is usually available, and hence a null corrector (null optics) is required. Aspheriacal and freeform surfaces with up to a few 100 μm deviation from the best-fitting sphere can be estimated with the precision of 1 nm or even less. However, the typical interferometry setups are calibrated for small deviations from the null setup such that extra errors appear, and interferogram indicates more than a few fringes. Extremely aspherical and freeform surfaces generate fringe patterns which are too many to be analyzed. Accordingly, the local slope and high surface deviation limit the applications of the technique[201-206].

4 Experimental Methods

4.1 Experimental setup

4.1.1 Plasma jet facility

Machining of optical surfaces throughout this thesis was performed in a chamber which is equipped with a plasma jet source, a 3-axis motion system, a substrate heater, and an infrared thermography camera (Optris PI 160) (**Figure 4.1**). The substrates are placed on the heater that can be moved in *x* and *y* direction, respectively. The plasma jet is mounted on the *z*-axis of the motion system (**Figure 4.1**). Mass flow controllers (Bronkhorst EL-FLOW) are used to adjust the gas feed rates of the plasma jet. The inner nozzle of plasma jet is fed by an inert carrier gas as well as a reactive gas. As an inert shielding gas, N_2 is provided through the outer nozzle of plasma jet to stabilize the plasma jet discharge. The gas feeding nozzles of plasma jet are made of metal, and hence they act as inner and outer electrical conductors of a coaxial line to conduct microwave excitation energy. A custom-made solid-state generator provides microwave power at 2.45 GHz, and a pulse generator is employed to produce the pulsed microwave signal. Microwave power is coupled into the plasma jet source in the form of rectangular pulses. The effective power P_E which is defined as the difference of mean input power P_M and the reflected mean power P_R was measured by a directional power sensor (Rohde & Schwarz NRT Z44) located between the microwave generator and the plasma source. The reflected power P_R can be increased or decreased based on the choice of inert carrier gas and tuning of the coaxial system. For the experiments, helium plasma with low electron density provides low reflected power P_R, and hence the obtained effective power P_E is practically high, i.e., 85%. The maximum electric field intensity arises around the tip of the inner nozzle where the plasma is ignited. For all experiments, a repetition frequency of 2.1 kHz was adjusted, while the peak power P_p and the pulse width t_p were respectively set to 200 W and 38 µs, resulting into a mean power of approximately 16 W. The working distance between the nozzle and sample during the etching process was set to 5 mm[207].

For the experiments carried out in this thesis, an atmospheric pressure non-thermal fluorine-based plasma jet was developed to be used as a deterministic etching tool. This plasma jet is made of a stainless-steel pipe with the exterior diameter of 2 mm and inner diameter of 0.2 mm inserted into the middle of brass nozzle with the inner diameter 12 mm (**Figure 4.2**). The inserted stainless-steel pipe is fed by 400 sccm helium (He) as an inert carrier gas. Additionally, 1 sccm carbon tetrafluoride (CF_4) is fed into the pipe as the reactive precursor gas mixture to form reactive particles in the plasma jet. Furthermore, 400 sccm nitrogen (N_2) is supplied as inert shielding gas through the exterior brass nozzle to stabilize the gas flow in the plasma jet discharge. The gas feeding pipes act as inner and outer electrical conductors of a coaxial system to conduct the microwave energy towards the inner tube outlet.

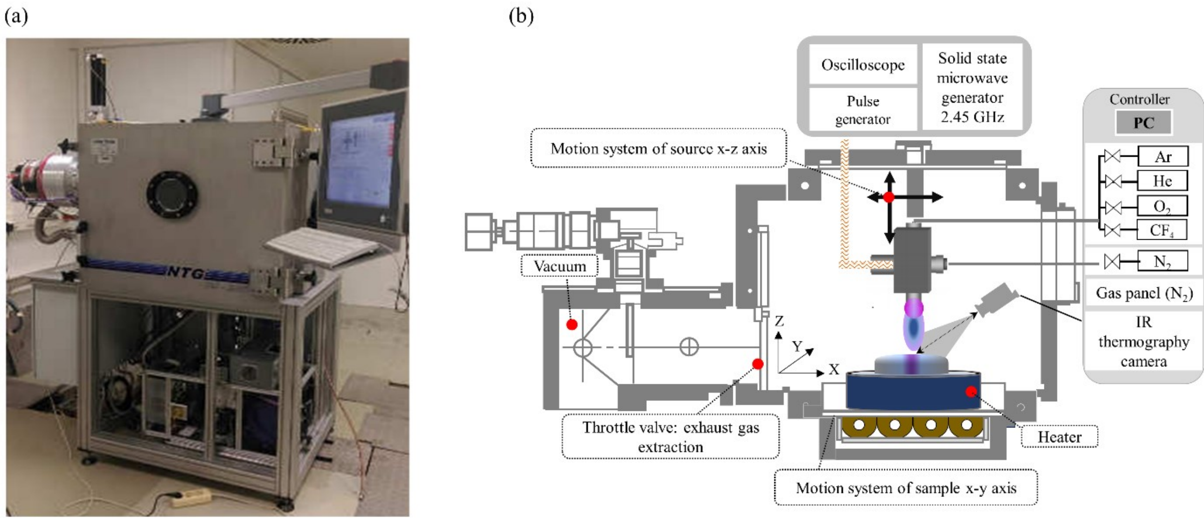

Figure 4.1 *(a) Plasma jet facility used for performing machining of optical surfaces, and (b) graphical scheme of test facility.*

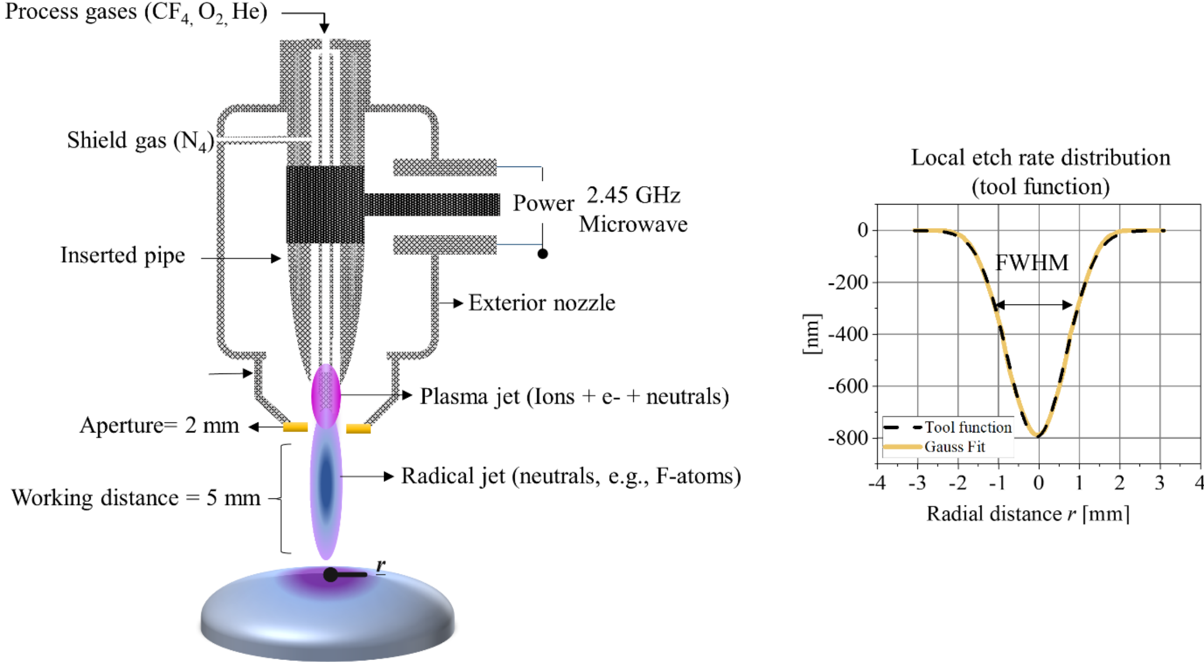

Figure 4.2 *Atmospheric pressure fluorine-based plasma jet used as a deterministic etching tool.*

The energy is provided by a pulsed 2.45 GHz microwave for triggering plasma at the tip of the inner nozzle where the high electric field power ionizes gases to create jet-like plasma discharges. The microwave power is initially transferred to free electrons which have the greatest mobility, and then the electrons are accelerated causing both elastic and inelastic collisions with the molecules of gas mixture. The inelastic collisions generate etchants (i.e., F atoms and molecules) as well as unsaturated products (i.e., CF_3 radicals and C_2F_4 molecules) which depart from the tip of the inner nozzle with high velocity.

Etching performance depends on the flux ratio of etchants to unsaturated products at the substrate surface. When this ratio is high, a pure chemical etching becomes dominant, resulting in isotropic etching[176]. On the contrary, a low flux ratio causes the formation of fluorocarbon film on the surface, which can stop etching. The etchants-to-unsaturated products flux ratio can be raised by adding adequate oxidants to the supplied gas mixture, which are able to convert unsaturated products into etchants (e.g., CF_3+O → COF_2+F). Hence, a certain amount of oxygen is added depending on the etched material and the amount of fluorine containing gas CF_4. For instance, in this present work, 1 sccm oxygen for fused silica, and 2 sccm for N-BK7 is admixed to CF_4 in all experiments[207].

4.1.2 Laser workstation

Throughout this work, laser cleaning of optical surfaces, performed after plasma etching, was carried out in a laser workstation equipped with a laser source, a dielectric attenuator, an x-y-z positioning stage, a camera position system, a beam shaping and homogenizing optics (**Figure 4.3**). A krypton fluoride (KrF) excimer laser (LPX220i from Lambda Physik) was used as laser source for generating the shock waves. The wavelength λ of the laser radiation emitted by this type of laser source is determined by the gas mixture which acts as active laser medium. For this work, a gas mixture of 6.0 % Krypton (Kr) and 0.2 % Fluorine (F) was used for the generation of the noble gas-halogen excimer which forms the active laser medium. The main part of the gas mixture was 93.8 % neon (Ne) acting as buffer gas. The emitted wavelength λ = 248 nm is obtained by consuming this composition of the gas mixture. Owing to the use of excimers as active laser medium, excimer lasers can only be operated in pulsed mode. The excitation is done by a gas discharge in the gas mixture which is generated by a high voltage pulse (discharge voltage). The adjustable voltages are between 16 - 24 keV. The pulse repetition frequency is limited to maximum f = 100 Hz, and the emitted laser pulse duration t_{on} is set to ~ 25 ns. The pulse energy of at the laser output is determined by the discharge voltage. Due to the laser operation, the KrF gas mixture is subjected to an ageing process by secondary effects, which influences the output pulse energy. In order to keep the pulse energy constant, the pulse energy of each laser pulse can be monitored, and the discharge voltage can be readjusted via a control loop. The laser radiation is guided to the respective experiments in a controlled manner by inserting into a laser workstation. In the laser workstation, two different beam paths are built as shown in **Figure 4.3**. The pulse energy is controlled by means of a beam attenuator in both beam paths. After the passage of the laser beam through the attenuator, the laser beam can be guided into either beam path "I" or "II". In beam path "I", the laser beam is focused on the sample surface by a lens with the focal length F = 75 mm. The maximum possible laser pulse energy in the beam path "I" is ~ 4 µJ which corresponds to a fluence of ~ 40 J/cm³. The laser spot sizes on the sample surface are ~ 250 µm x 400 µm. In the beam path "II", the lateral beam profile of the laser pulses is processed by a homogenizer system. After shaping and homogenization, the laser beam has a flat top beam profile (5% energy deviation). The shaped beam was used for illumination of a motorized aperture that was projected onto the sample surface through a

Schwarzschild objective (magnification Γ = 1:15). Typical spot sizes on the sample surface are ~ 100 µm x 100 µm by using beam path "II". To avoid damage to the Schwarzschild objective by the laser pulses, the pulse energy had to be reduced to such an extent that a maximum laser fluence of F = 4 J/cm² is achieved on the sample surface.

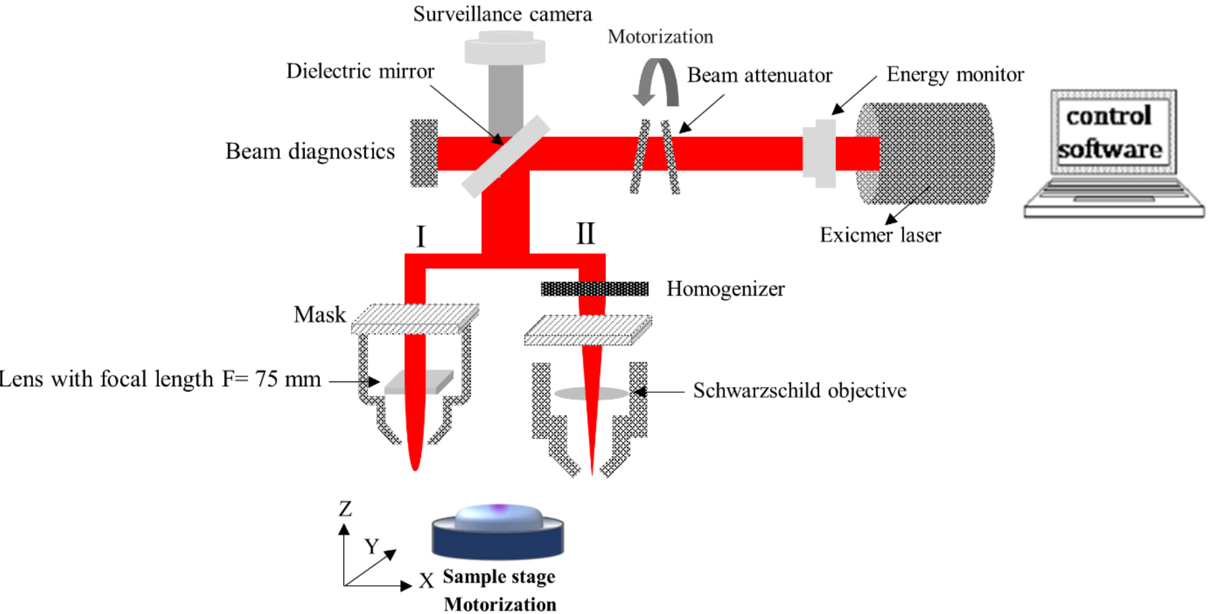

Figure 4.3 *Schematic of laser workstation used for laser cleaning of optical surfaces.*

In both beam paths "I" and "II", the sample was transported below the focus or imaging plane of the respective beam path by a computer-aided movement system. The laser pulse energy is measured with a laser energy sensor. In this work, after every plasma jet treatment, an array of ~ 100 µm × 100 areas were laser cleaned into beam path "II". The estimated total error in determining the laser fluence is ≤ |±5%| that is given by the laser pulse energy fluctuations and the precision of the pulse energy measurement. For the experiments, the laser fluence Φ was fixed to a value of ~ 2.8 J/cm² to prevent damaging of the substrate surface. This laser fluence Φ is below the ablation threshold of the chosen optical glass (N-BK7), and in consequence, no material ablation or optical visible material modification could be observed after applying more than 10000 laser pulses at a reference area of the N-BK7 optical glass[209,215].

4.2 Optical glass samples: N-BK7 and fused silica

The etching process was performed on optically polished N-BK7 wedged windows and fused silica windows (supplied by Schott Optics) with a thickness of 3 mm and diameter of 50 mm. The typical feature of N-BK7 in comparison to fused silica glass (99.93 % silica) is the presence of about 20% of boron trioxide and alkaline oxide in its chemical composition, which affects its properties. The nominal

composition of the initial N-BK7 surface is given in **Table 4.1** according to literature[216], which was also confirmed by the XPS analysis[208].

Table 4.1 *Nominal composition of the untreated N-BK7 surface*[208].

Element	O	Si	C	Na	B	K	Ca	Mg	N	Zn	Ba
Proportion (at-%)	57.9	25.4	4.7	3.9	3.5	3.2	0.5	0.4	0.3	0.2	0.1

4.2.1 Surface temperature measurement

Substrate surface temperature distributions were measured by an IR thermography camera (Optris PI 160) that is capable of acquiring temperatures in the range between 0 °C and 550 °C. The calibration of the emissivity ε for the surface temperature measurements on polished N-BK7 was performed based on the comparison of the surface temperature of a black sooth layer (with $\varepsilon = 0.98$) partly applied on the N-BK7 substrate and the temperature of the bare glass surface, while the substrate was externally heated to several temperature levels. The emissivity ε of polished N-BK7 was determined to be 0.7. The IR-camera was located at a fixed position focusing onto the substrate surface. Thus, the temporal temperature curves and local temperature distributions are referred to the plasma jet center point. The local surface temperature T_s during the surface machining increases by the plasma heat flow since the plasma jet acts as a significant heat source for the substrate surface. Depending on the plasma mean input power P_M, dwell time t, and thermal coupling of the substrate to the environment, a characteristic spatiotemporal temperature distribution develops during the etching process. It should be noted that the transition temperature T_g of N-BK7 is 550 °C[210]. Thus, during the machining process, the surface temperature T_s was controlled to ensure it is well below T_g.

4.3 Methods of plasma jet machining

For understanding the fundamentals of etching mechanism using a fluorine-based plasma jet, three different schemes on the optical surfaces were generated, namely the footprint, groove and area etching. The footprint etching formed by a static machining process where the plasma jet dwelled on one spot for a certain time. Groove and area patterns were created by a dynamic machining process using a driving plasma jet. For the footprint generation, the plasma jet was placed perpendicular to the substrate surface. Depending on the dwell time t, a footprint with a certain etching depth D is created. It was confirmed by the experiments that the footprint profile has a rotational symmetry as shown for instance by the white light interference (WLI) images obtained from the footprint pattern in static etching of N-

BK7 (e.g., **Figure 5.27** in **Section 5.6**). Then, the VRR is calculated in terms of the local etching depth *D(r)* and dwell time *t* as follows[208]

$$\mathrm{VRR} = \frac{1}{t}\int_{-\infty}^{+\infty} D(r)\, 2\pi r\, dr, \tag{4.1}$$

For achieving a groove etching, the plasma jet is horizontally moved by a three-axis motion system relative to the substrate surface while the working distance is fixed. A straight line on the surface is then treated iteratively with the constant scan velocity *v* resulting in a groove. In this case, the VRR is derived by[208]

$$\mathrm{VRR} = \frac{v}{N}\int_{-\infty}^{+\infty} D(x)\, dx \tag{4.2}$$

where *N* denotes the number of iterations, and *x* is the lateral distance. An area etching is performed by moving plasma jet over the surface in raster path mode. For the experiments, several area etchings with individual scan velocities *v* are generated in experiments by moving the plasma jet over the surface in a raster path mode with a constant line feed Δy of 0.1 mm. The working distance was fixed. An etched area with the desirable size is obtained by adjusting the number and length of lines which are used in the experiment. In this case, the VRR is computed as follows,

$$\mathrm{VRR} = v\, D\, \Delta y \tag{4.3}$$

For illustrative purpose, the schematics of footprint, groove and area etchings showing the axis definitions and motion directions are presented in **Figure 4.4**.

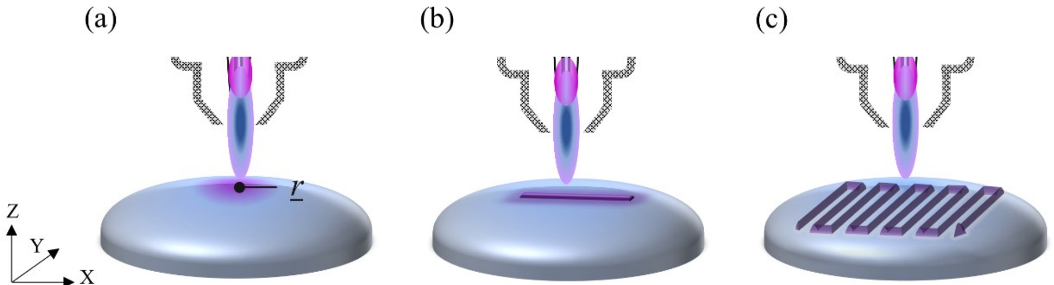

Figure 4.4 *Schematics of (a)static footprint, (b) groove, and (c) area etchings showing the axis definitions and directions*[208].

Moreover, in this work, the fluorine-based plasma jet is used as a deterministic etching tool aiming to optimize applications towards the fine residual removal error correction and freeform surface figuring of optics particularly made of N-BK7. To follow the deterministic surface machining scheme, plasma jet and sample stage are moved by the 3-axis motion system. The motion schemes are controlled by a dwell time matrix calculated by a numerical deconvolution algorithm between the defined freeform shape and the etch rate function. Based on the dwell time matrix, for points with large local depth, a

large local dwell time is assessed and vice versa. For clarification, the schematic of freeform surface generation by plasma jet is presented in **Figure 4.5**.

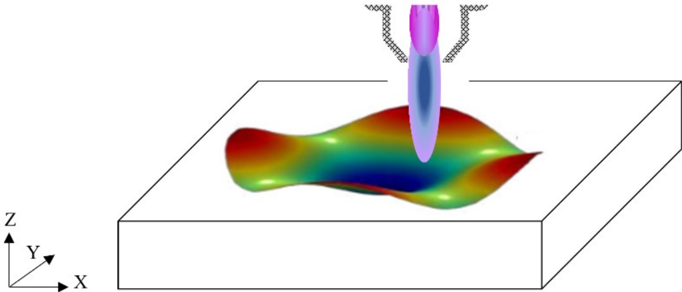

Figure 4.5 *Schematic of freeform surface machining by using reactive plasma jet as deterministic etching tool*[208].

4.4 Sample preparation

Prior to performing the surface treatment whether by plasma or laser, all specimens were cleaned following the RCA clean. The RCA clean is a standard procedure of sample cleaning required before surface treatment (i.e., etching and oxidation) of silicon-based materials in semiconductor manufacturing[211]. In this procedure, samples are prepared by rinsing them into four different solutions in order to remove organic contaminants, thin oxide layers and ionic impurities from the surface. The RCA clean consists of four steps which are described in the following[211]:

I. The specimens are prepared by soaking them in deionized water. In the case that the specimens are noticeably contaminated and have obvious residues, they may need a primary cleaning in a mixture of sulfuric acid (H_2SO_4), water, and hydrogen peroxide (H_2O_2). This solution is known as Piranha solution. It should be noticed that between each cleaning step, the specimens should be carefully washed with deionized water.
II. The second step is accomplished in an ultrasonic cleaning bath for 30 minutes at 50 °C by a solution of 1 part of ammonium hydroxide (NH_4OH), 2 parts of hydrogen peroxide (H_2O_2) and 40 parts of H_2O. This base-peroxide solution mixture eliminates organic contaminations. This mixture can even eliminate insoluble residues successfully since it modifies the surface and initiates the particle zeta potentials. The zeta potential can be a key indicator of repelling insoluble particles and residues from surface. Nevertheless, in this cleaning step, a low amount of metallic impurity (particularly iron) can be formed on the surface along with a thin silicon dioxide layer which will be washed away in the following steps.
III. The third step is accomplished with a solution of 1 part of hydrogen chloride (HCl), 2 parts of H_2O_2, and 8 parts of H_2O for 30 minutes at 50 °C. During this cleaning step, a thin passivizing

layer forms on the substrate surface, which shields the surface from later contamination. Moreover, a certain degree of metallic and ionic impurities which remained on the surface from the previous cleaning step are washed away in this step.

IV. The last step includes rinsing and drying. In case that the former steps in RCA clean are applied properly, a clean surface is obtained for the sample which is still entirely underwater. Hence, careful rinsing and drying steps are required to prevent the recontamination of the surface with organics and particulates floating on the water. Therefore, the specimens were cleaned with flowing water and subsequently dried in a vacuum drying container.

Besides the RCA clean that is used prior to etching, a cleaning step is additionally required for the etched optical glasses with complex composition like N-BK7 as these materials develop a residual layer during plasma etching. The residual by-products must be removed to ensure a precise depth profile measurement by an optical surface profiler on the etched surfaces. It was found in this work that most of these residual products are mainly soluble in water/ethanol solution[208]. Thus, after the etching process, the N-BK7 specimens are cleaned with the solution of 1 part of H_2O, 1 part of C_2H_5OH. This procedure ensures a precise depth profile measurement on the etched surfaces by optical surface profiler.

4.5 Measurement techniques for surface analysis

4.5.1 Topography analysis

Different types of techniques can be used based on either contactless optical method or contact and pseudo-contact methods to measure a surface topography quantifying surface profile and its roughness[212]. Scanning white light interference microscopy (WLIM) is a contactless optical tool for surface height measurement on 3-D structures with surface profiles ranging from nanometers to centimeters. Throughout this work, the cross-section profiles of etched structures on the optical surfaces were determined by using WLI microscope (NPFLEX-Bruker) where ten depth profiles were averaged for each structure. Micro roughness was measured by the WLI microscope using 50X objective.

The cross-section profiles of etched structures were examined additionally throughout this work by the mechanical profilometer (PGI freeform - Ametek®) as a contact method. The mechanical profilometer consists of a diamond stylus that is moved in contact with a sample perpendicularly and then displaced horizontally through the sample for a certain distance and contact force. Depending on the position of the diamond stylus, an analog signal is created that is converted into a digital signal[213]. A profilometer that is used in this investigation can measure small vertical topographies fluctuating in height from 1 nm to 10 mm. The diamond stylus has a radius ranging from 20 nm to 50 µm. The resolution is determined by the scan rate and the sampling rate of signals.

AFM is a scanning probe microscopy with very high-resolution ranging from fractions of a nanometer to about thousand times greater than the optical diffraction limit. In this work, surface roughness is additionally quantified by AFM employing tapping mode with a mechanical probe. Piezoelectric elements that facilitate tiny but accurate and precise movements on (electronic) command enable exact scanning. The measured data presented in this work was obtained with a dimension 3000 stage with a Nano Scope IIIa controller from Veeco Instruments. All the measurements were performed in air applying silicon tips with a nominal radius smaller than 10 nm and sidewall angles of 18°. For a quantitative analysis of the surface roughness, the scan sizes of (10 × 10) μm^2 were used with 512 × 512 points[214].

4.5.2 Surface structure assessment

Scanning electron microscope (SEM) is one type of electron microscope that generates pictures of a sample by scanning the surface with a focused beam of electrons. In this work, SEM technique is equipped with Energy-dispersive X-ray spectroscopy (EDS) which is an analytical technique employed for the elemental examination or chemical analysis of a workpiece. It is based on an interaction of some source of X-ray excitation and a substrate surface. Its characterization abilities are relied on the fundamental principle of spectroscopy that each chemical element has an individual atomic configuration permitting a unique arrangement of peaks on its electromagnetic emission spectrum. In this investigation, the surface composition mapping was performed by secondary-electron microscope energy dispersive X-ray (SEM-EDX) measurements in a Zeiss Gemini Ultra 55 machine with a Bruker XFlash 3001 detector.

Focused ion beam (FIB) can also be combined with SEM, letting the same feature to be examined. In this investigation, FIB was used to prepare vertical cross sections through the formed residual layer, which have been subsequently analyzed by SEM.

X-Ray Diffraction (XRD) is used as a non-destructive method to analyze the atomic and molecular structure of crystalline materials. The XRD analysis is used to recognize the crystalline phases existing in a material in which the crystalline structure produces a beam of incident X-rays to diffract into many individual directions. The XRD measurements were performed in this work to examine the crystallinity of the residual layer formed on the N-BK7 after plasma etching.

4.5.3 Surface chemistry analysis

X-ray photoelectron spectroscopy (XPS) as a surface-sensitive quantitative spectroscopic method is used for performing semi quantitative analysis of elemental compositions that are within a material. By exposing X-rays to the substrate surface and instantaneously computing the kinetic energy and number of electrons emitted from the surface, XPS spectra are derived. X-rays hit the solid surfaces to knock electrons out of the specimen surface, and then the energy of these electrons are collected and analyzed

to determine the chemical composition of the solid surfaces. XPS technique can be used to determine not only the elements within a specimen surface, but also number of other elements bounded to them. This means that by detection of a metal oxide on the surface, XPS can reveal if the metal is in a +1 or +2 state. However, the average depth of analysis for an XPS measurement is limited to the maximum depth of 10 nm. In this investigation, XPS (Instrument Axis Ultra DLD, KRATOS Manchester) was used to determine the chemical composition of the surface.

Secondary-ion mass spectrometry (SIMS) is used to investigate chemical composition of substrate surfaces and is considered as one of the most profound surface analysis techniques[224]. Through SIMS, the substrate surface is primarily sputtered with a focused primary ion beam, and subsequently an emitted secondary ion is gathered by using a mass spectrometer. Based on the assessment of mass/charge ratios of secondary ion, elemental or molecular composition of the material surface is determined up to the depth of 2 nm. In SIMS, as a highly precise surface analysis technique, the elemental detection margins can vary from parts-per-million (ppm) to parts-per-billion (ppb). Even though SIMS is regarded as a qualitative technique because of the large difference in ionization possibilities among diverse materials, the quantitative measurement is still possible by referencing it to standards. In this investigation, SIMS is used to determine the elements present in the outer layers of the surface and to probe the depth distributions of elements below the outermost surface up to 100 nm.

5 Results and Discussion

5.1 Evaluation of pre-processing cleaning step

As already described in **Section 4.4**, before surface processing of optical glasses, an accurate and standard surface-cleaning step is required. The RCA clean that is a standard set of wafer cleaning steps is used in this investigation. However, cleaning of optical glasses containing alkali metal ions like N-BK7 can cause undesirable modification of the surface as its metal ions can leach out. Hence, the cleaning steps should be carefully examined to ensure that the metal ions of the N-BK7 surface are not significantly drained to change the chemical surface-composition. To evaluate the effect of the cleaning methods on the elements present in the outer layers of N-BK7 surface, besides the RCA clean, two other types of cleaning methods including oxygen plasma and ethanol were used. Afterwards, the surfaces cleaned by these different methods were analyzed by XPS (**Figure 5.1**). The chemical composition of the untreated surface of N-BK7 is additionally measured as reference. By comparing the results**,** it can be observed that the effects of the cleaning methods on the arrangement, type, and ratio of atoms present in the outer layers of N-BK7 surface are not significant enough to impact the subsequent surface machining process.

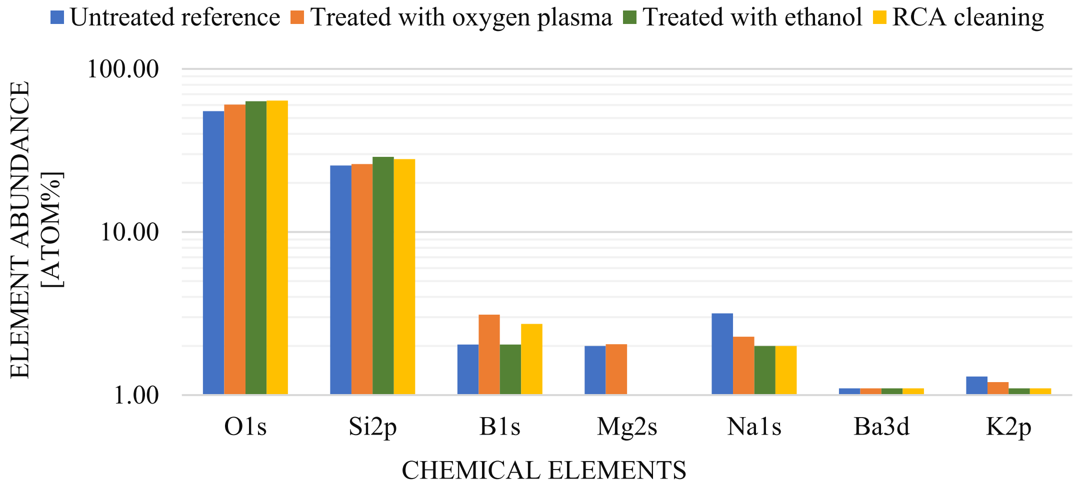

Figure 5.1 *Comparing the effects of cleaning methods on the elements present in the outer layers of N-BK7 surface by using XPS analysis.*

For more investigation, the surface chemical analysis by means of SIMS is used to determine the elements present in the outer layers of surface and to probe the depth distributions of elements below the outermost surface up to 100 nm before and after applying the RCA clean (**Figure 5.2(a)** and **Figure 5.2(b)**, respectively). The comparison of the results reveals that the RCA clean process cannot modify the surface chemical composition of N-BK7, and hence it cannot have any significant effect on the etching performance of N-BK7 surface.

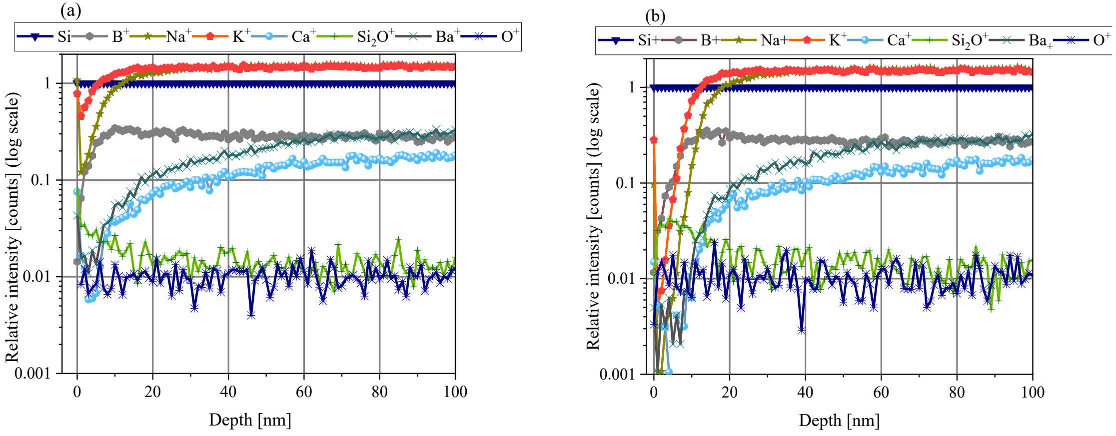

Figure 5.2 *SIMS analysis of the outer layers of N-BK7 surface in depth distributions of different elements below the outermost surface up to 100 nm, (a) before applying the RCA clean, (b) after applying the RCA clean.*

5.2 Investigation of fluorine-based plasma jet interactions with optical glass

In this section, the results for interactions of borosilicate crown optical glass with the fluorine-based plasma jet are presented, highlighting the difference among different amounts of O_2 addition into the CF_4/He gas mixture**,** surface temperature, mean input power and working distance. Furthermore, the results for fused silica as an easy-to-etch optical glass are also provided under the same conditions for comparison. The aim of the experiments is to explore the PJM performance of optical glasses under different processing conditions and gather experimental data for the development of a general model for the deterministic surface machining. For the following optimization experiments, the plasma jet moves on the surface iteratively in a straight line with the constant scan velocity $v = 2$ mm/s to create a groove etching. The number of line iterations N was set to 2 to have a small plasma dwell time t. In fact, for a small dwell time t, the resulting residual layer formed on the N-BK7 surface is too thin, and hence it cannot affect the performance of PJM[208].

5.2.1 Influence of O_2 addition on CF_4 decomposition in plasma jet

As discussed in **Section 4.1.1**, the plasma jet is supplied by 1 sccm CF_4 as the potentially reactive precursor gas to form chemically active fluorine in the plasma discharge. It is supposed that the addition of the low amount of O_2 into gas mixture can increase the etching rate. The O_2 flow rate was varied from 0 sccm to 4 sccm to find the optimal amount of O_2 addition, while the flow rates of CF_4 was fixed to 1 sccm. **Figure 5.3(a-b)** shows the dependence of the etch depth profile on the proportion of O_2 in the CF_4/He gas mixture for the groove etchings performed on the optical surfaces of both N-BK7 and fused silica. The corresponding VRR is presented in **Figure 5.3(c)**.

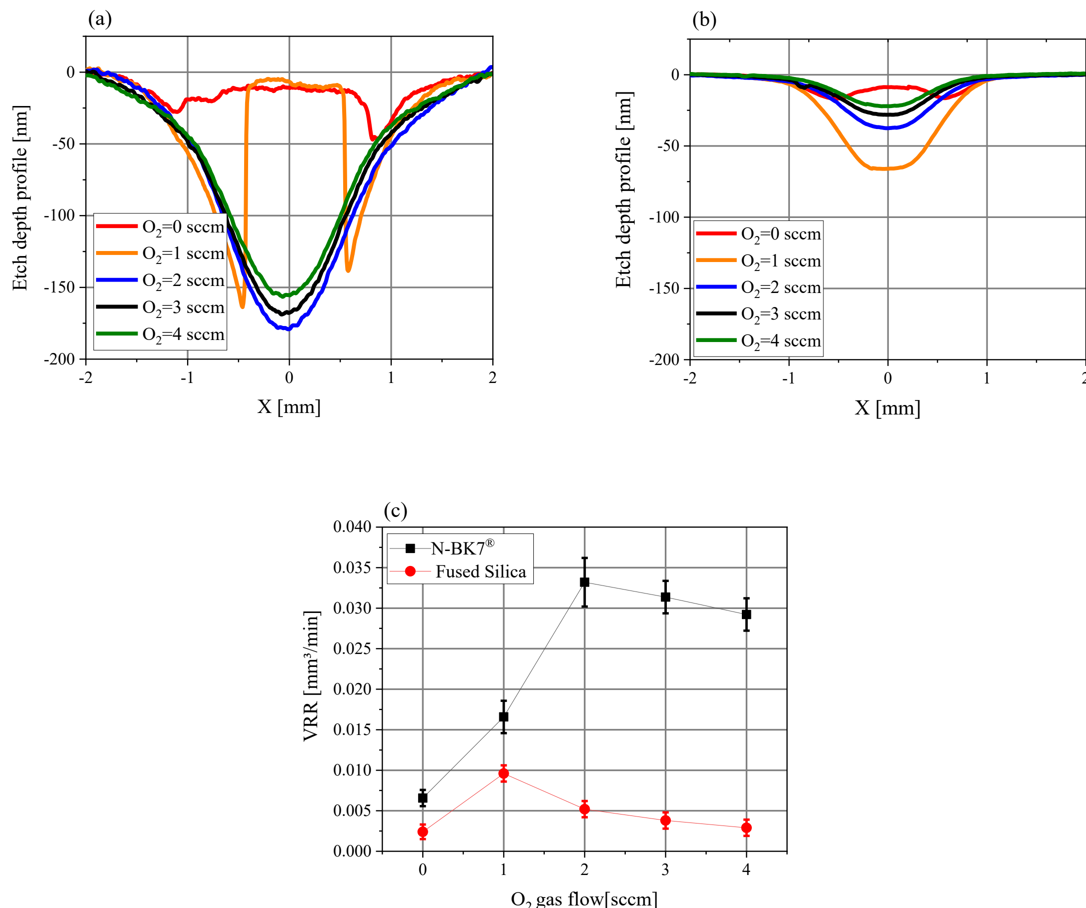

***Figure 5.3** Dependence of etch depth profile on the O_2 gas flow rate [sccm] for (a) N-BK7, (b) fused silica, and (c) the corresponding VRR values.*

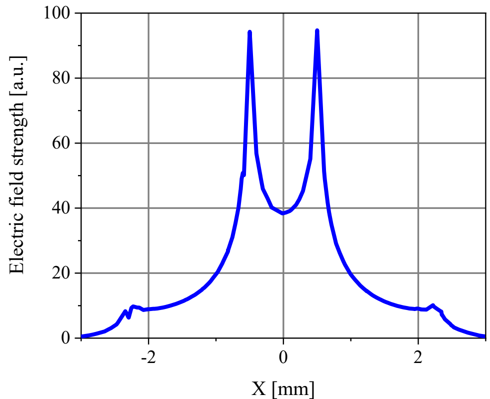

***Figure 5.4** Cross section of electric field strength at the inner gas tube outlet of the plasma jet source calculated by FEM.*

For both N-BK7 and fused silica, the etch depth profiles exhibit nearly a Gaussian shape except the ones with the low O_2 flow rate where nearly no etching in the center of the profile is achieved, though

at lateral positions, a high etching is observed (**Figure 5.3(a-b))**. It is assumed that the dissociation of CF_4 generating fluorine atoms or ions preferably takes place in the region of high electric field strength. A simple finite element method (FEM) model was used to simulate the electric field distribution of the coaxial conductor system with no ignited plasma discharge. The FEM simulation of electric field strength at the inner conductor shows an annular shaped region of maximum field strength that occurs at the "edges" of the inner nozzle (**Figure 5.4)**. This result validates that the dissociation of CF_4 to form fluorine atoms mostly occurs at the edges of the inner nozzle; the region with higher electric field strength. On the other hand, in the center region where higher CF_4 concentration and lower electric field strength appear, the CF_x radical formation is more probable. If the O_2 flow rate is low (i.e., < 2 sccm for N-BK7, and < 1 sccm for fused silica), the recombination of F* and CF_x form a masking layer at the center which can stop local etching by inhibiting the fluorine radical attack, and nearly no etching is observed at the center of the profile[208], i.e.,

$$F^* + CF_3 \rightarrow CF_4 \quad (5.1)$$

$$CF_3 + CF_3 \rightarrow C_2F_6$$

The deposition rate of fluorocarbon film (i.e., CF_4 (+M)) depends on the gas composition and precursor density. When no O_2 is added into the gas mixture or the O_2 flow rate is low, the fluorocarbon film deposits fast on the surface. Then, the film continues to thicken and makes the attained local etch rates in the center nearly negligible. However, it is well-known that O_2 has the capability of reacting with neutral CF_x to form COF_2 and F_2[176],

$$CF_x + O \rightarrow COF_2(g) + F \quad (5.2)$$

$$O + COF_2 \rightarrow CO_2 + F_2$$

By increasing the O_2 content in the gas mixture, not only the deposition rate of the fluorocarbon film on the surface is impaired but also a larger concentration of F atoms is provided for etching the surface, and hence the etching rate in the center of the plasma interaction zone increases[176].

On the other hand, the addition of O_2 to the gas mixture leads to dispersing the plasma energy discharge since O_2 molecules compete with CF_4 molecules in energy uptake from the free electrons in the plasma discharge leading to excited states, dissociation, or formation of ions[176]. Furthermore, a dilution of the fluorine radical concentration becomes effective by the addition of O_2 to the gas mixture. Hence, the etching rate decreases for N-BK7 and fused silica, respectively, when the O_2 flow rate exceeds 2 sccm and 1 sccm[207]. A similar behavior of adding O_2 has been reported in case of a low-pressure CF_4-O_2 plasma etching process[218]. For the following experiments on the plasma jet machining of N-BK7 and fused silica, the optimal flow rate of O_2 was adjusted to 2 sccm and 1 sccm, respectively.

5.2.2 Effect of temperature on surface interactions with plasma

Plasma etching of optical surfaces is controlled exclusively by chemical kinetics[145]. Hence, according to the Arrhenius equation[219-220], the surface temperature T_s has a major effect on the local etching rate and consequently on VRR[221-225].

To investigate the effects of surface temperature T_s on the plasma etching performance, several grooves on the surfaces of N-BK7 and fused silica were generated at different initial temperatures T_h. For this purpose, the workpiece was preheated by a heater to initial temperatures T_h between 25 °C and 350 °C while all other process parameters were kept fixed, and the mean input power P_M was set to 16 W. The final value of surface temperature T_s is obtained by the sum of the plasma heat flow and the heat flow originating from the heater. **Figure 5.5** shows snapshots of the lateral surface temperature distribution perpendicular to the plasma jet for the initial temperatures T_h = 25 °C, 150 °C, 250 °C and 350 °C during etching. As it is illustrated in **Figure 5.5**, when the plasma affects the surface, a sudden rise of temperature is detected. Because of the extra heat of the plasma flow, the maximum surface temperature T_s occurs at the center of the plasma jet surface interaction zone and reaches to {300±10, 350±10, 415±10, 470±10} °C for the four different initial temperatures T_h, respectively. The lateral distribution of surface temperature T_s has a nearly Gaussian shape. It approaches gradually to the initial surface temperature T_h at the peripheral area of the plasma interaction zone. In case of a lower initial temperature (e.g., T_h = 25°C), the impact of plasma heat flux on the surface temperature T_s becomes greater and provides a wider lateral heat transfer to the surface. Therefore, having a higher initial temperature T_h helps to adopt a more uniform surface temperature T_s over the radial profile during the process, and to some extent inhibits the sudden rise of surface temperature T_s at the beginning of etching.

The dependence of VRR on the surface temperature T_s is shown in **Figure 5.6**. It can be observed that the performance of etching for both N-BK7 and fused silica improves in terms of the local etching rate and the VRR. At the lowest surface temperature T_s when no extra heat is applied to the surface substrate, the VRR values are minimum. By applying the initial temperature T_h, the proportion of reactant molecules with energy greater than the activation energy E_a (i.e., the minimum energy that must be provided to compounds resulting in a chemical reaction) increases. Therefore, adequate preheating of the workpiece can increase etching rate. However, it should be noted that when the surface temperature T_s is higher than the transition temperature T_g of N-BK7, the effect of temperature is not any more conducive to form a smooth surface. It rather introduces damage to the surface. Therefore, it is necessary to strictly control the surface temperature during the machining process to ensure the temperature is below T_g. The maximum surface temperature T_s used in this work is 480 °C that is still below the transition temperature T_g = 550 °C[210].

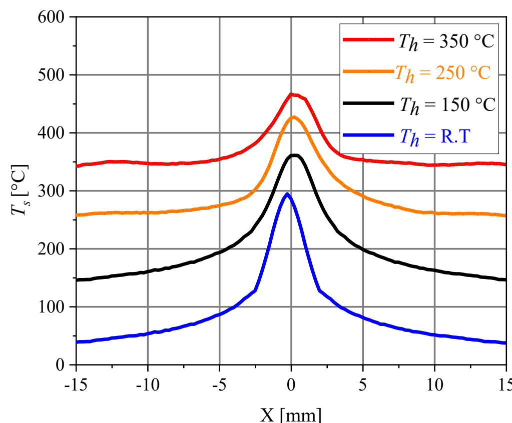

Figure 5.5 *Surface temperature profiles in the etching process obtained at four different initial temperatures T_h: 25 °C (RT), 150 °C, 250 °C and 350 °C when the mean input power P_M is fixed to 16 W*[207].

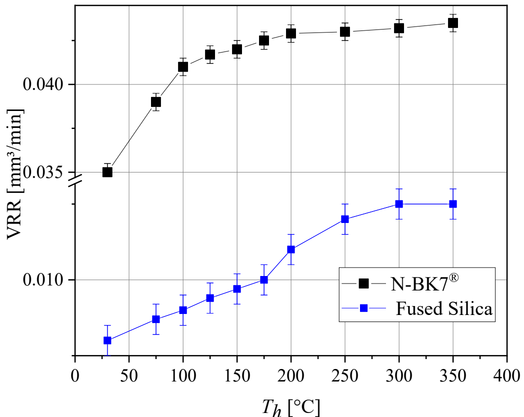

Figure 5.6 *Volumetric removal rate VRR of groove etching for N-BK7 and fused silica obtained at different initial temperatures T_h increasing from: 25 °C to 350 °C when the mean input power P_M is set to 16 W*[207].

5.2.3 Variation of etching rate with mean input power

As mentioned in **Section 4.1.1**, for igniting and sustaining plasma jet at the tip of inner nozzle, the electric field intensity is provided by a pulsed microwave field at 2.45 GHz. Then, the mean input power P_M of plasma jet can be calculated in units of W as

$$P_M = t_p\, P_p\, f_p \qquad (5.3)$$

where f_p denotes pulse repetition frequency in kHz, P_p pulse peak power in W, and t_p is the pulse width in µs. The mean input power P_M can be changed by the variation of either the pulse repetition frequency f_P or the pulse width t_p. The groove etching is performed at different values of P_M to evaluate the corresponding performance. For this purpose, P_M is varied from 6 W to 26 W by increasing t_p from 12 µs to 60 µs while P_p and f_p are set to 200 W and 2.1 kHz, respectively.

As shown in **Figure 5.7**, VRR increases by the mean input power P_M for both N-BK7 and fused silica. By increasing the mean input power P_M, the dissociation rate of CF_4 and O_2 increases, and more fluorine atoms, oxygen atoms and CF_x radicals are generated. Moreover, at higher mean input power P_M, CF_4 and O_2 diffuse more strongly into the plasma center over a larger axial area and shift into a larger distance in accordance with the extent of the active plasma zone and the thermal influence zone. These effects lead to an increasing fluorine current density on the substrate surface and better etching performance. Additionally, by raising the plasma mean input power P_M, the plasma gas temperature increases leading to higher surface temperature T_s. **Figure 5.8** shows the surface temperature profiles in the etching process with different P_M when the samples are not preheated (T_h = 25°C). The rise of surface temperature T_s enhances the kinetic energy of particles to provide the activation energy required for chemical etching reaction leading to higher VRR[207]. Nonetheless, due to the direct relation of T_s with P_M, there is a limit for acquiring high VRR by increasing P_M as T_s must be always below the transition energy T_g = 550 °C. According to the results shown in **Figure 5.8**, the optimal mean input power is found to be P_M = 16 W as the sufficiently large VRR is achieved while T_s remains well below T_g such that preheating can be applied if necessary.

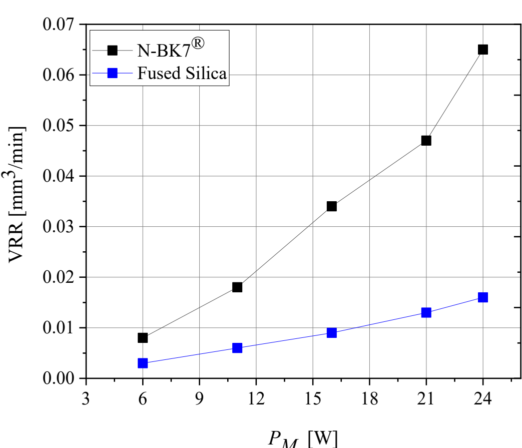

***Figure 5.7** Volumetric removal rate VRR of groove etching for N-BK7 and fused silica depending on different values of the mean input power P_M.*

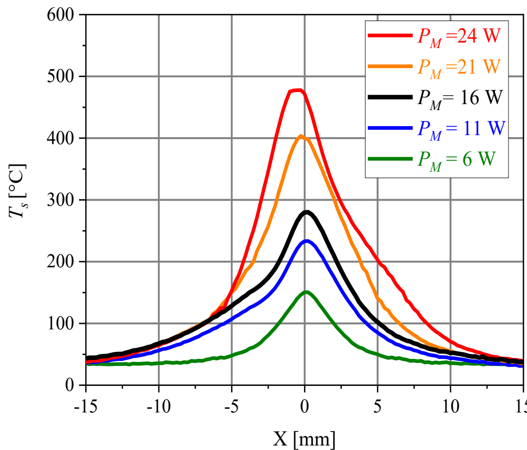

Figure 5.8 *Surface temperature profiles during groove etching at different values of mean input power P_M when the workpiece is not preheated.*

5.2.4 Influence of distance between substrate surface and plasma discharge

The efficiency of plasma etching is strongly sensitive to the distance between the plasma jet outlet and the substrate surface, known as working distance Δ*d*. The optimal efficiency of plasma etching process with respect to the working distance Δ*d* is achieved empirically by precisely adjusting the substrate surface within the active region of the plasma jet. The dependence of the etch depth profile on changing the working distance Δ*d* is shown in **Figure 5.9** for the groove etchings performed on the N-BK7 when all other process parameters were kept fixed. The corresponding VRR and FWHM for these etch depth profiles are provided as well in **Figure 5.9(a)**. It is evident that the optimal efficiency of plasma etching with respect to the etching depth and VRR is achieved at the working distance Δ*d* = 5 mm (**Figure 5.9(b)**). It is assumed, that the generation of etching particles such as fluorine radicals is promoted by O_2 entrainment from the peripheral gas flow, yielding optimal conditions for dissociation of CF_4 and oxidation to COF_2 preventing the recombination of fluorine radicals. At too short working distance (i.e., Δ*d* = 4 mm), sufficient amount of O_2 entrainment from the peripheral gas flow cannot be provided. On the other hand, for too large working distance, (i.e., Δ*d* = 6 mm) recombination effects may become stronger. In the following experiments, the optimal working distance Δ*d* = 5 mm is used[207].

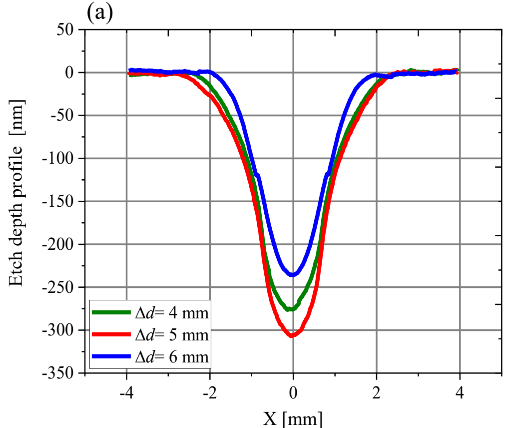

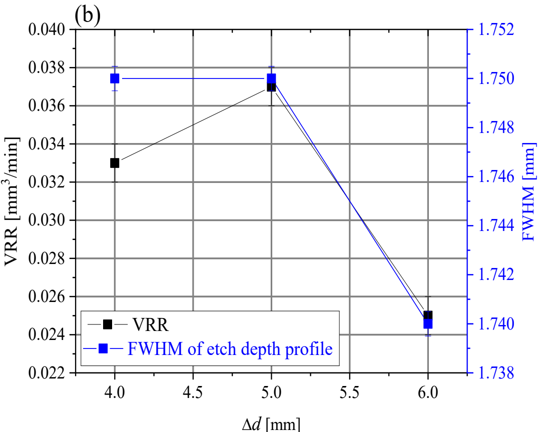

Figure 5.9 *(a) Etch depth profile, and (b) the corresponding VRR and FWHM values for groove etching at three different working distances Δd.*

5.3 Freeform figuring of optical glass by PJM

Over the past decades, optical elements made of N-BK7 are vastly used in a wide variety of optical applications even more than fused silica. Hence, the possibility to use reactive plasma technique for deterministic surface machining of N-BK7 especially with regards to freeform fabrication is of great interest. As described in **Section 4.1.1**, PJM as an etching tool with an adjustable width can be a good choice in applications towards the complex freeform surface machining by imposing no geometric limits. In this investigation, a fine focused plasma jet with a tool FWHM of 1.5 mm (**Figure 4.2**) is used as an advanced deterministic machining tool to chemically interact with the N-BK7 surface for freeform shape generation. However, the application of PJM on N-BK7, due to the presence of about 8% alkaline oxide in its chemical composition (**Table 4.1**), is not a straightforward approach.

In the etching process, etched by-products cover the surface that can affect the steady sate etching and the machining process. The aim is to evaluate the performance of PJM for N-BK7 regarding to the following main applications: (i) Local figure correction which can be a replacement approach for the ion beam figuring (IBF) or magnetorheological finishing (MRF). This step is characterized with a comparatively low material removal of few nanometers by having a small plasma dwell time aiming to correct the fine residual removal errors which remain on the surface after a complex freeform surface figuring. It is noted that the requirement here is to not alter the roughness remarkably after applying the error correction method. (ii) Freeform surface figuring on the N-BK7 surface, where PJM can be substituted for conventional methods like the mechanical grinding[189-190].

To examine the performance of PJM for freeform fabrication of N-BK7, the optimal process parameters (i.e., P_M =16 W, CF_4= 1 sccm, O_2= 2 sccm, T_h = 25 °C) found in **Section 5.2** are chosen[207]. In the

workflow of deterministic surface machining (**Figure 3.4**), firstly, a 2D-sinusoidal test structure with low depth profile (PV= 500 nm) is defined as the target removal depth ***D*** (**Figure 5.10(a)**). Afterwards, the dwell-time matrix ***t*** is calculated by the deconvolution of the plasma tool function ***R*** and the target removal depth ***D***. Due to the complex and time-varying behavior of material removal of N-BK7, it is rather hard to estimate the accurate plasma tool function on N-BK7. Hence, an approximate time independent tool function with the maximum etch rate R_{max}= 200 nm/s is used for the calculation of the dwell time matrix ***t***.

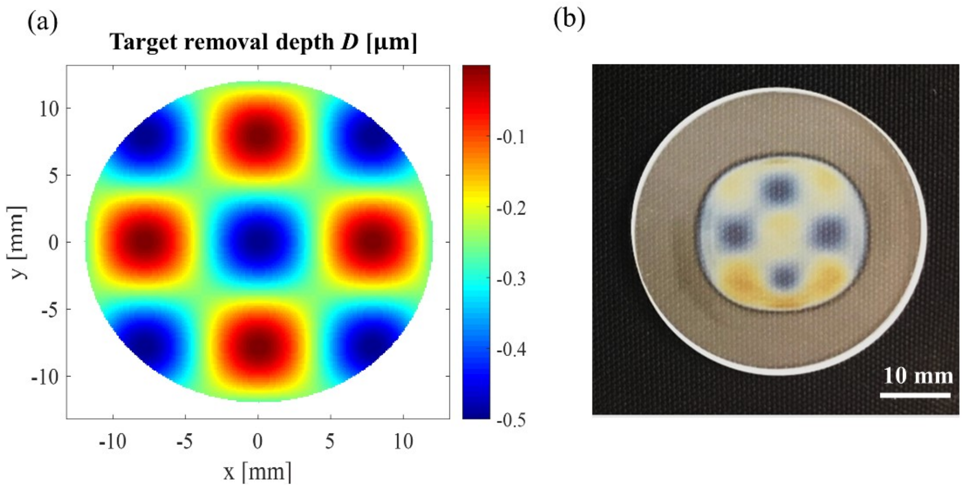

Figure 5.10 *(a) Target removal depth D with a 2D-sinusoidal test structure with low depth profile (PV= 500 nm) for deterministic surface machining, and (b) distribution of residual layer after the deterministic surface machining over the plasma treated areas.*

Afterwards, based on the calculated dwell time matrix ***t***, the feed rate commands are determined and sent to CNC controller for machining the desired removal depth on the N-BK7 optical glass. The highest velocity applied in the plasma jet system is set to 20 mm/s which yields the base removal depth about 255 nm PV. This base-removal leads to an unavoidable bias in the resulting etch depth profile which should be considered in the experimental process.

After the shape machining, an inhomogeneous layer with irregular structures is distributed over the plasma treated areas (**Figure 5.10(b)**). In this figure, colorful interference patterns are observed as the residual layer thickness varies locally**. Figure 5.11** shows the etch depth profile and the corresponding cross-sections along the horizontal and vertical axes after the residual layer removal with water/ethanol. The resulting non-volatile etch by-products influence the tool function on N-BK7 in non-linear way leading to a time-dependent tool function. However, in standard deconvolution model, an approximate time-independent tool function is used to calculate the dwell time matrix ***t***, and hence the resulting removal rate is much less than the approximate one, and it decreases continuously by increasing the plasma dwell time *t*. **Table 5.1** shows the approximate etching depth assuming the constant etch rate 200 nm/s as well as the corresponding measured one. The maximum depth, PV and the base removal

are measured on average as 180 nm, 107 nm and 50 nm, respectively, and hence their corresponding removal rates are only about 24%, 21% and 20% of the approximate one (i.e., 200 nm/s) used to calculate the dwell time.

Table 5.1 *Approximate etching depth assuming the constant etch rate 200 nm/s as well as the corresponding measured etching depth.*

Condition	Max depth	PV	Base-removal
Approximate etching depth assuming constant etch rate 200 mm/s	755	500	255
Measured etching depth	180	107	50

Therefore, unexpected asymmetric etching profile is obtained, and the cross-section profile along the x- and y-axis presents a complex and irregular shape (**Figure 5.11**). Furthermore, the increase of etch depth profile with respect to the plasma dwell time is non-linear. The residual layer, which is produced during the process, is the main factor which changes the material removal irregularly. It is obvious from the results that the degree of irregularity of material removal rate depends on the thickness of residual layer which itself depends on dwell time t. To tackle this problem, the spatiotemporal behavior of plasma tool function on N-BK7 should be estimated a priori for implementation in dwell time matrix $\boldsymbol{t}$ calculation. This topic is discussed in **Section 5.5**.

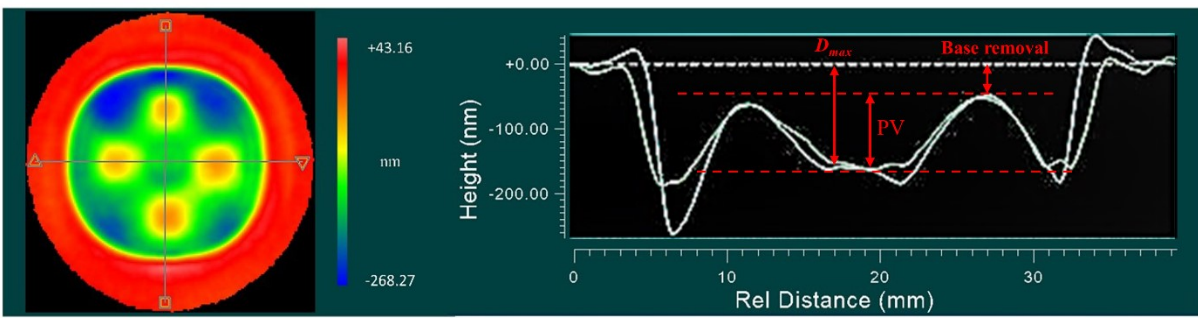

Figure 5.11 *Etch depth profile and the corresponding cross-sections along the x- and y-axis as the PJM-based deterministic surface machining is performed on the N-BK7 surface followed by the residual layer removal with water/ethanol.*

5.4 Surface characterization of plasma-treated N-BK7

As shown in **Section 5.3**, the application of PJM for freeform figuring of N-BK7 is problematic since a residual layer may form during etching, which affects the local etching rate, and consequently the plasma tool function (i.e., the characteristic lateral material removal rate function)[208]. Such behavior leads to a complex time-dependent etching process. As deterministic surface machining processes rely on a well-defined etch rate distribution that is adequately stable in time, accurate freeform figuring of

optical glasses cannot be obtained without understanding the exact chemical kinetics between plasma generated active particles and the N-BK7 surface atoms. For this purpose, here, the chemical composition, and structural properties of the residual layer, resulted from static and dynamic etchings, are extensively evaluated aiming at clarifying the mechanism of surface modification with respect to layer formation, material removal and local surface roughness. The outcomes of this investigation lead to a deeper knowledge of the mechanisms at work to develop a predictable machining process for plasma-based freeform generation.

5.4.1 Analysis of the residual layer formed on the surface

To investigate the chemical composition of non-volatile compounds formed on the N-BK7 surface after PJM, an area etching was applied. The process parameters were adjusted to the optimum parameters determined in **Section 5.2**. After the PJM, a rough residual layer forms on the plasma treated area which was analyzed by XPS without and after subsequent water/ethanol cleaning process (**Figure 5.12)**. In addition, as a reference, the chemical composition of an unprocessed N-BK7 surface was measured and shown in the same figure. The residual layer formed on the plasma treated surface consists of a variety of metal oxides and fluorides such as Na_2O, NaF, KF, BaF_2 and multi-element compounds like BaOnFm, BaF_6S, and SbOnFm(s) as well as a tetrafluoroborate anion (BF^{4-}). The XPS analysis after washing exhibits a surface with very low amount of residual etching products. The chemical and structural properties of the plasma treated area was further investigated by SEM imaging and EDX analysis. **Figure 5.13** shows the result directly after the plasma treatment without washing. A non-uniform distribution of Na/F and K/F signals assigned to the residues NaF and KF, and Si/O signals with weak homogeneously distributed Na and K signals assigned to the substrate material N-BK7 is observed. Due to the inhomogeneous coverage of the surface by the residues, the layer thickness determination could not be performed.

The XPS and EDX results indicate that the reactions of N-BK7 surface with the $He/CF_4/O_2$-based plasma can be divided into two general categories. One includes reactions between fluorine and network formers (i.e., 70% silica (SiO_2) and 8% boron trioxide (B_2O_3)). The other category entails the interaction between fluorine and the metal oxides (i.e., BaO, K_2O and Na_2O). The reactions of the first category produce volatile compounds such as SiF_4(g), CO(g), CO_2(g), BF_3(g), B_2F_4(g) and COF_2 which have very low boiling points (**Table 5.1**)[222, 223]. The desorption of these volatile compounds from the surface occurs by thermal activation which results in material removal. On the other hand, the second category of reactions forms non-volatile fluorine compounds such as NaF, KF, BaF_2 as well as the multi-elements layer like BaO_nF_m and SbO_nF_m that remain on the surface.

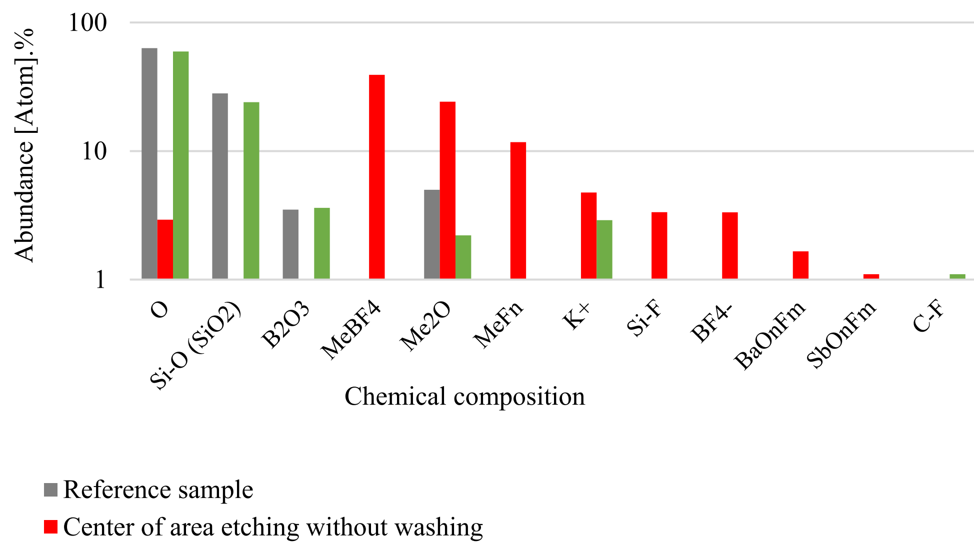

Figure 5.12 *XPS analysis for chemical composition of N-BK7 surface treated by area etching after and without washing, and the untreated surface as reference. "Me" can stand for Na, K and Ba.*

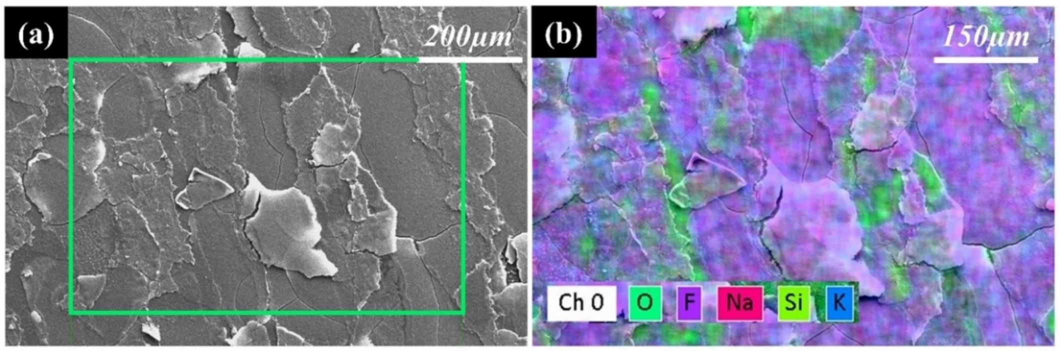

Figure 5.13 *Electron microscope images of a residual layer forming on the plasma treated surface of N-BK7 after area etching without washing: (a) Scanning electron (SEM) image of the surface morphology; and (b) color-coded elemental composition of the sample area given in (a) by the green box, analyzed by energy dispersive X-ray (EDX).*

Table 5.1 *Boiling points and vapor pressure of volatile and non-volatile components of N-BK7 surface in interaction with CF_4/O_2-based plasma discharge*[222, 223].

Reaction product	CO	BF_3	SiF_4	COF_2	CO_2	KF	NaF	aF_2
Boiling point	-191 [°C]	-100 [°C]	-86 [°C]	-84 [°C]	-78 [°C]	1505 [°C]	1700 [°C]	2260 [°C]
Vapor pressure	34 [atm] (-140 °C)	>50 [atm] (20 °C)	36.5 [atm] (20 °C)	55.4 [atm] (20 °C)	56.5 [atm] (20 °C)	0.0013 [atm] (885 °C)	0.0013 [atm] (1077 °C)	0.0013 [atm] (1436 °C)

5.4.2 Lateral distribution of residual layer

Due to the fact that the relative motion of the plasma jet leads to the convolution of the tool function *R* with the plasma dwell time *t*, area or dynamic etchings yield limited information on the local interaction of the plasma jet with the surface (i.e., **Equation 3.2**). Hence, static footprint etchings were performed to investigate the local etch depth and the lateral distributions of the residues. **Figure 5.14** and **Figure 5.15** show SEM and EDX images of a footprint obtained for a dwell time of *t=8 s*. The formation of a residual layer is clearly observed. In the central area with a radius of approximately 400 µm the layer is cracked into several patches and partly delaminated. At the peripheral area, the layer seems to be compact until the edge at *r* ~800 µm, where the layer is fully delaminated in a ring-like zone. However, at even larger radius (i.e., *r* > 800 µm), a compact layer is again visible, though partly delaminated on the edge. This finding is consistent with the EDX measurement shown in **Figure 5.14(b)**, where the main components of the substrate and residues are color-coded. Four different spots (labeled with A, B, C, D) along the radial profile *r* were further analyzed to reveal their corresponding chemical composition. The relative abundance of elements at these spots is shown in **Figure 5.16**. At the center of the footprint pattern (i.e., the location A), the largest amount of fluorine as well as Na and K is measured. This is attributed to the residual layer consisting of NaF and KF with the largest thickness that accumulates at the center of the footprint. At the position B, the signal indicating alkali-fluorides decreases, while at the position C at approximately 0.8 mm distance from center nearly no fluorine occurs, and Si and O signal exhibit a maximum. According to the SEM images in **Figure 5.14(a)** and **Figure 5.15**, the residual layer is removed at this radial position and the initial N-BK7 surface shows up. This radial distribution of the residual layer can be explained by the gas flow pattern of the plasma jet. In this configuration, an impinging jet flow is assumed that forms a stagnation point in the center. A FEM simulation of helium jet emerging from a tube with the inner diameter of 0.2 mm, that is directed to a perpendicular plate at the distance of 5 mm, was performed to obtain the radial gas velocity on the plate surface (i.e., the velocity component parallel to the surface).

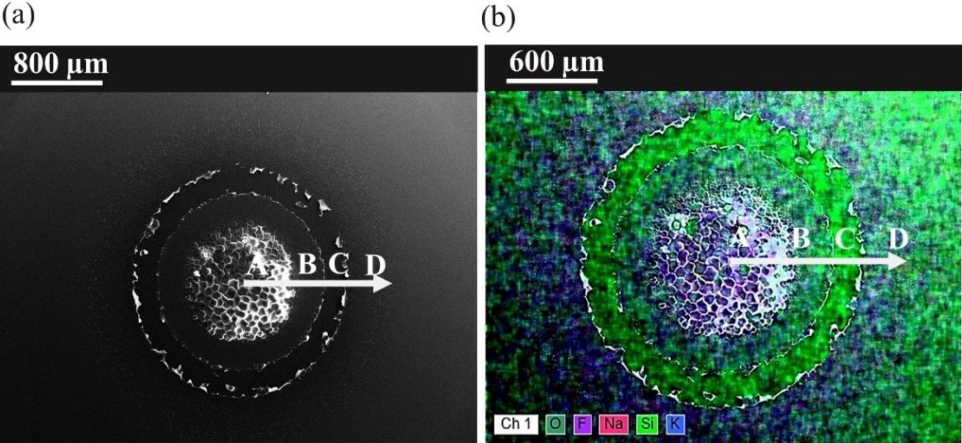

Figure 5.14 (a) SEM and (b) EDX images of a footprint obtained after static etching for the dwell time of t =8 s.

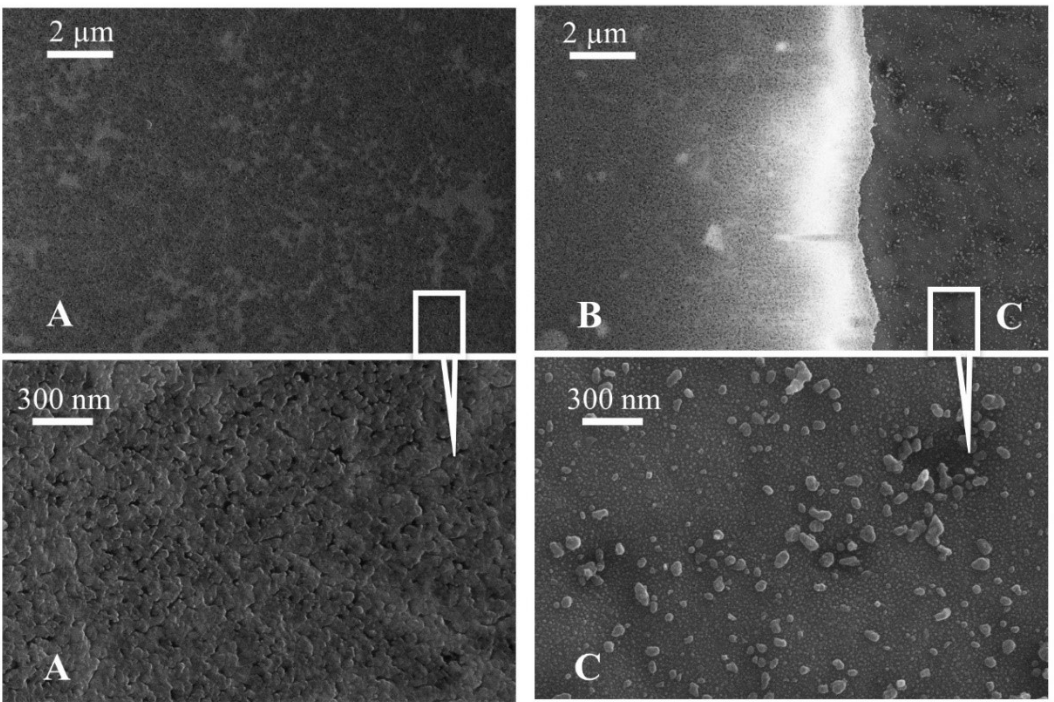

***Figure 5.15** Surface morphology SEM of the spots A, B, C corresponding to **Figure 5.14**.*

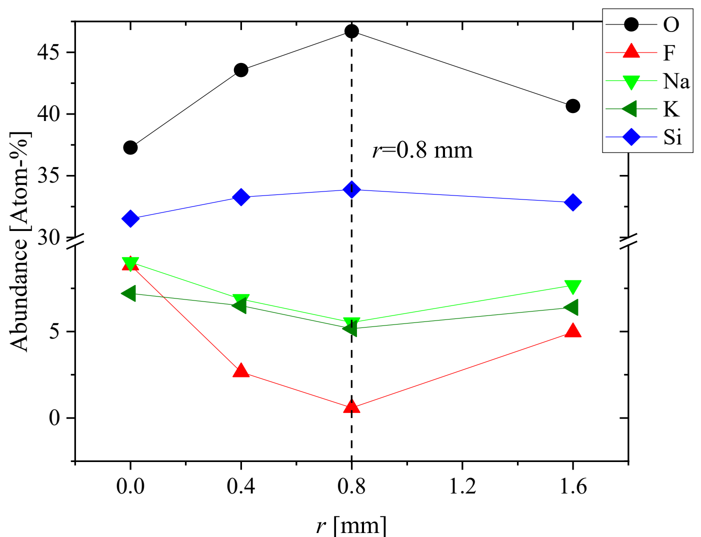

***Figure 5.16** Relative abundance of elements at the spots shown in **Figure 5.14** with the labels A, B, C, D.*

The distribution of radial gas flow velocity is shown in **Figure 5.17**. At radial position of 0.8 mm, approximately the maximum is observed. As the residual layer is probably not compact and prone to delaminate, the gas blows loose parts outwards and spreads it radially over the surface. In the SEM image (**Figure 5.14**, the location C), such particles are found around the footprint.

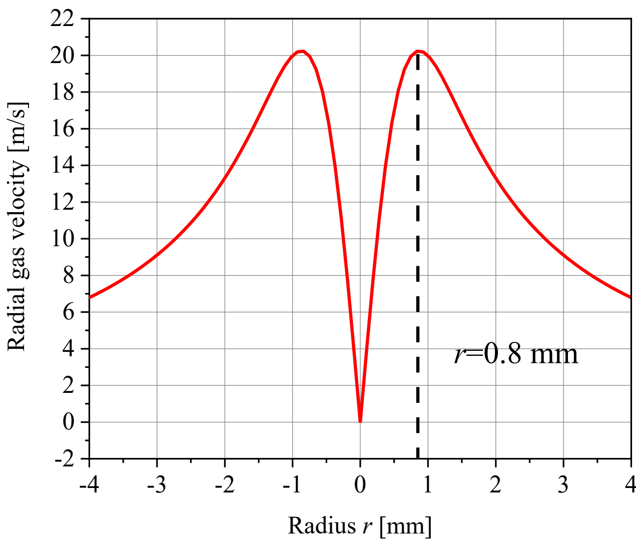

Figure 5.17 *Velocity magnitude of radial gas flow for He gas jet at z=5 mm on perpendicular plate.*

5.4.3 Etch depth profile as a function of plasma dwell-time

Static etching for different treatment times t was performed to investigate the temporal evolution of etch profiles. **Figure 5.18** depicts the etch depth profiles for the dwell times of 1 s to 12 s after removal of the residual layer with water/ethanol solution. At the beginning of the process when the dwell time t is less than 2 s, the profiles exhibit a near-Gaussian shape, that is usually found for fused silica or Si plasma jet etching.[185] Hence, the near-Gaussian profile represents the reactive particle density distribution always present on the surface. Even if a residual layer is formed, it is thin enough to be penetrated by etching species and the isotropic etching can proceed. However, as the dwell time increases, the profiles depart significantly from the Gaussian shape. Obviously, the residual layer in the center masks the surface underneath and prevents the attack of etching species. Thus, etching is inhibited leading to a flattened profile shape. Consequently, by increasing the etching time t, the material removal barely is observed at the center and the local etching rate R considerably decreases. Contrariwise, the gas velocity v_g at the radial position of 0.8 mm reaches a maximum (e.g., 20 m/s) (**Figure 5.17**) such that the brittle residual layer is cracked easily and blown away by the gas flow, and the parted residual particles stay on the surface instead of a dense residual layer. Therefore, the profile cross sections show a sharp edge at r >0.8 mm because the local material removal is not affected by the separated residual particles dispersed over the surface. The SEM image for the peripheral area of footprint at the etching time t = 8 s before washing and cleaning is shown in **Figure 5.14** (the location C).

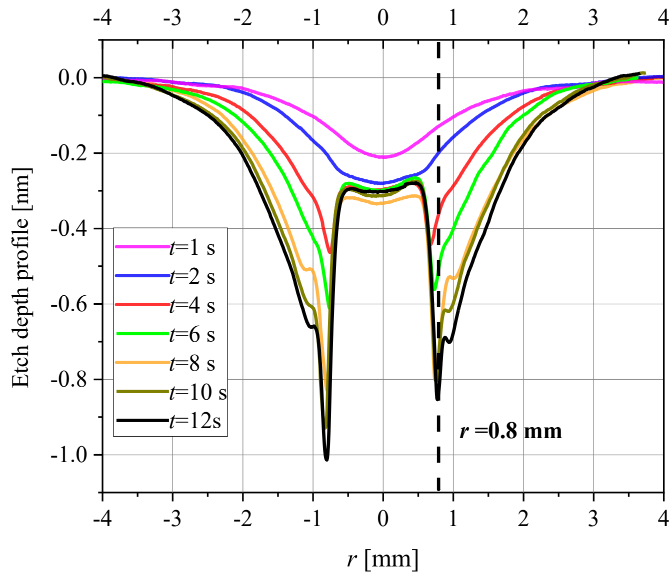

Figure 5.18 *Etch depth profiles obtained by reactive plasma jet on N-BK7 surface with static plasma processing at different dwell-times t and after the removal of the residual layer with water/ethanol solution.*

5.4.4 Roughness measurement

After washing the plasma treated sample, the roughness of footprint etching over the radial profile r was determined. **Figure 5.19** illustrates a qualitative dependence of N-BK7 surface roughness on the dwell time t ranging from 1 s to 8 s for different spots on the radial profile. At the beginning of footprint etching when the dwell time t is less than 2 s, the etching results in a relatively smooth surface, and the measured roughness of footprint (i.e., Sq = 4 nm) does not change remarkably in comparison to the polished N-BK7 surface without any plasma treatment (**Figure 5.19**, the curve at t = 1 s). However, by increasing the etching time t, the measured roughness over the radial profile r rises especially at the center, i.e., approximately r = 0.8 mm. At the center, the thick local residual layer converts into a masking layer during the process. However, as it seems to partly delaminate, the mask is not fully dense, and it leads to a rough surface. Additionally, at the peripheral area of footprint, the brittle residual layer is locally cracked and removed during the process by increasing the etching time. However, instead of a dense and packed residual layer, separated residual particles remain on the surface which cause a rough surface (**Figure 5.14**, the spot C).

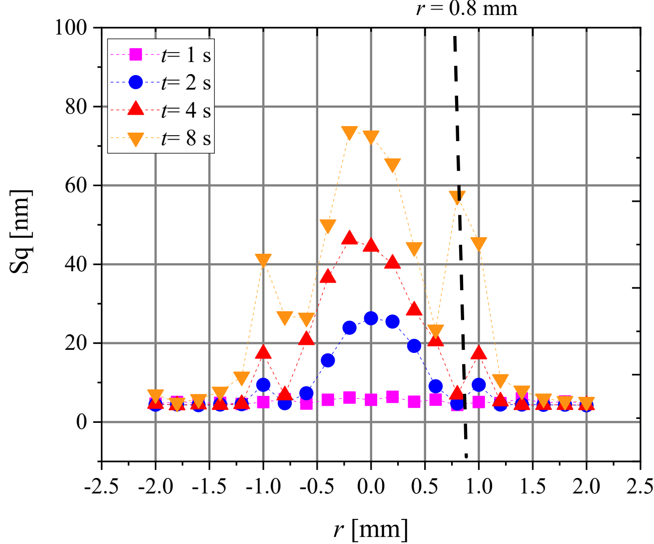

Figure 5.19 *Surface roughness of N-BK7 which forms after static etching at different dwell times t for different spots of radial profile.*

5.5 Development of a model for numerical convolution

As it was noticed in **Section 5.3**, the applicability of PJM for freeform figuring of N-BK7 becomes limited particularly for large dwell times *t*. The lateral distribution of material removal exhibits a complex behavior, and the evolution of local etch depth with dwell time *t* decreases causing the time-varying nonlinearity in the radial removal rate function. Therefore, the characteristic behavior of plasma tool function on N-BK7 surfaces must be determined specifically. Recalling the unusual static etch-profiles results in **Figure 5.18**, they were in this section to monitor the spatiotemporal behavior of etching rate. Subsequently, semi-empirical quantitative model is developed to describe the non-linear characteristics of the tool function on N-BK7 surfaces. Finally, the derived model is extended into the dynamic machining process, and the outcomes are compared with the experimental results.

5.5.1 Estimation of spatiotemporal behavior of etching rate *R(r,t)*

The experimental data presented in **Figure 5.18** is used to illustrate the local etch depth *D* of static etching for N-BK7 as a function of the radial profile *r* and dwell time *t* (**Figure 5.20**). For typical PJM-based deterministic machining in which the local etching rate *R(r)* is constant with respect to the dwell time *t*, the relation between the local etching rate *R(r)* and the depth *D(r)* can be simply expressed as

$$R(r) = D(r)/t. \tag{5.4}$$

However, as discussed in **Section 5.3**, the removal behavior of N-BK7 is not linear in terms of dwell time *t*. In order to compute the local etching rate R of N-BK7, the dwell time *t* must be considered as

an extra variable in addition to the radial position *r*. In this case, the relation between the local etching rate *R* and the etch depth *D* is expressed as follows

$$R(r\,,t)=\frac{\partial D(r\,,t)}{\partial t} \tag{5.5}$$

The local etching rate *R(r,t)* is computed by the partial derivative of local etch depth *D(r, t)* with respect to the dwell time *t*. The experimental data has been interpolated to obtain a smooth 2D function (i.e. spatiotemporal etching rate *R(r, t)*). The result of local etching rate *R(r, t)* is illustrated in **Figure 5.20(b)**.

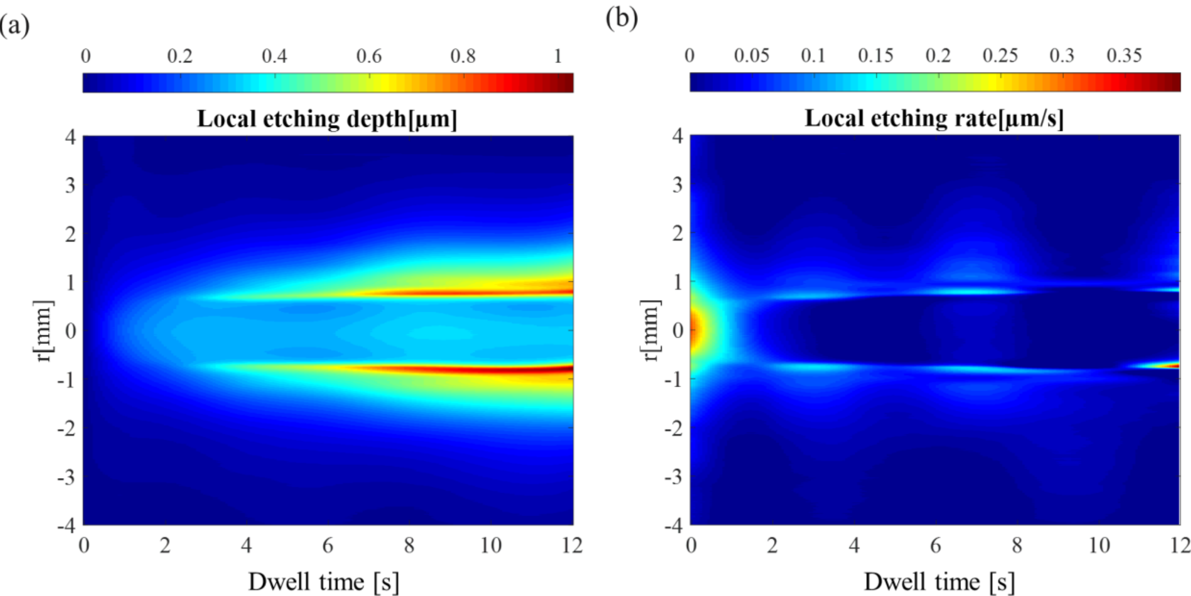

Figure 5.20 *(a) The attainable local etch depth D(r, t) of static machining for N-BK7 as a function of the radial profile r and dwell time t, (b) the corresponding local etching rate R(r, t) based on the obtained depth D(r, t) over the radial profile r and dwell time t.*

5.5.2 Non-linear characteristics of plasma tool function

Based on **Equation 5.5**, it is now possible to calculate a dependence of the rate on the already reached local etching depth *D(r, t)* for a certain radius *r*, i.e. *R(r, D(r, t))*. By using an interpolation routine, a new dataset for *R(r, D)* is generated, which is shown in **Figure 5.21**. The local etching rate *R(r, t)* is maximum at the center of radial profile *r* where the local depth is low (e.g., *D(r, t)* ≤ 0.2 µm). However, the etching rate *R(r, t)* decreases and approaches zero with some small fluctuations in its amount as the depth *D(r, t)* increases. These fluctuations of local etching rate *R(r, t)* at the center for large values of depth *D(r, t)* can be attributed to the brittle residual layer on the surface which can be removed coincidentally by the gas flow velocity v_g during the process. The peaks in depth *D(r, t)* achieved for the radial profile around *r* = - 0.8 mm and *r* = 1 mm as the gas flow velocity v_g has the highest amount (**Figure 5.17**) and results in the removal of the residual layer.

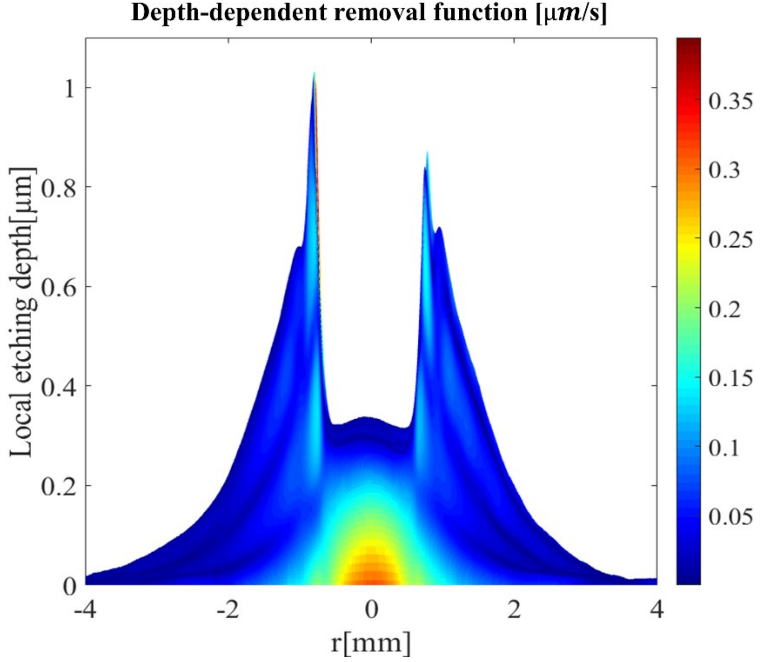

Figure 5.21 *Tool function (i.e., depth-dependent removal function R(r, D)) obtained by interpolation.*

5.5.3 Modeling of dynamic machining process

The characteristic behavior of plasma tool function (**Figure 5.21**) is intended to be used for modeling the deterministic dynamic machining process. Based on the predefined removal depth, the estimated tool function should move over the surface for the "dwell time" values calculated by the numerical deconvolution method (outlined in **Section 3.3.3**). However, the resulting tool function has a complex shape that largely deviates from the typical rotationally Gaussian form. Consequently, the standard deconvolution methods used for dwell time calculation are not anymore applicable here for modeling the dynamic machining process as they highly rely on a constant functional form. Therefore, in this section, a modeling algorithm is proposed which enables the use of the depth-dependent removal function $R(r, D(r,t))$ in a 2D coordinate space.

To demonstrate the applicability of the proposed approach for modeling the dynamic etching, the tool function $R(r, D(r,t))$ is moved either in a straight line or raster path to generate respectively etched groove or etched area. The motion is implemented by shifting the center of the tool function $R(r,D(r,t))$ with the applied velocity v and direction x/y. The radial distance r for each local dwell time t of this motion is continuously updated to get the corresponding value for the removal rate $R(r,D(r,t))$. Then, the convolution of the local removal rate R with the dwell time t results in the local etch depth $D(r,t)$. This convolution is numerically computed by the iterative summation of the multiplication of the depth-dependent removal function with dwell time t as follows

$$D_{ij}^{p+1} = D_{ij}^{p} + \left[t_{kl}\, R_{i-k,j-l}\left(D_{ij}^{p}\right)\right] \tag{5.6}$$

where *p* denotes the time-step index. According to the shape of the tool function *R(r, D(r,t))* shown in **Figure 5.21**, at certain regions (e.g., at the center of tool function), etching stops due to masking layer, and hence removal rate in these regions cannot be defined. These masking constraints are considered as stopping criterion in the simulation algorithm. **Table 5.2** summarizes the proposed algorithm. This algorithm is implemented in MATLAB®, and the simulation results are obtained for both the groove and area etching.

Figure 5.22 shows the cross-sectional shape of simulated depth profiles and experimental results for the groove etching. It can be observed that the calculated profiles agree well with the experimental results for the same setting parameters when the velocity v = 3 mm/s is used, and the number of line iterations N is set to $\{1, 2, 4, 8\}$.

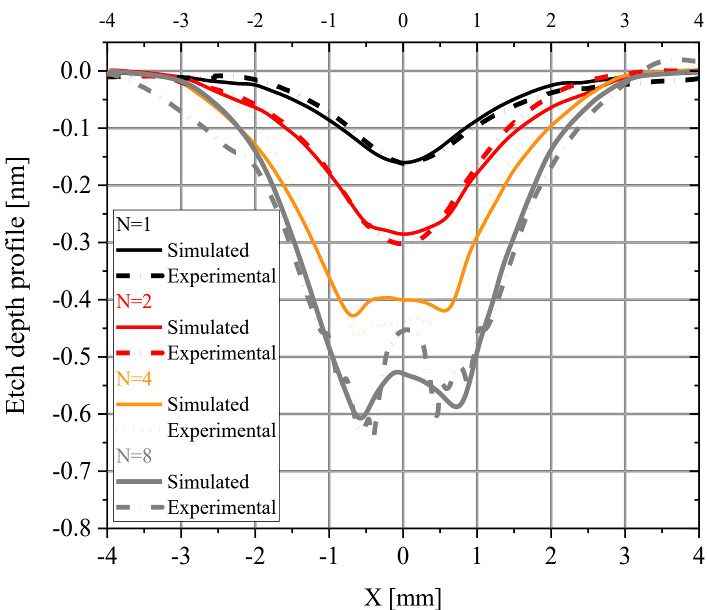

***Figure 5.22**: Etch depth profiles obtained by the experimental approach and the proposed simulation algorithm for groove etching on N-BK7 surface with the different numbers of line iterations N.*

Furthermore, **Figure 5.23(a)** and **Figure 5.23(b)** respectively show the simulated and experimental results for the case of area etching when the velocity v = 4 mm/s is used, the line feed Δy is 0.1 mm and the number of line iterations N is 70. In addition, the cross-sectional shape of etched area for both the simulated and experimental results is presented in **Figure 5.23(c,d)**. It can be observed that the simulated and experimental etch depth profiles match with each other. Both the experimental and simulated depth profiles exhibit a complex shape (**Figure 5.23**).

Obviously, the produced residual layer in the center of the etching zone reduces the removal depth. At the beginning of area etching, this dense layer reduces the diffusion of fluorine atoms into the surface

of N-BK7 repeatedly and causes the ripple-structure at a position of x = -4 mm. The same effect causes the ripple structures at beginning and end of the cross-section profile in y-direction.

***Table 5.2** Proposed algorithm for creating the dynamic surface machining from the footprint profile that is already obtained using the static process.*

Algorithm 1

Require: Simulation of dynamic surface machining

Input: Experimental static footprint etching

Output: Simulated groove and area etching

1. Initialization:

1. Define 2D space over x and y axes
2. Set the center of tool for $t = t^0$ at $x_c(t^0) = x^0$ and $y_c(t^0) = y^0$
3. Set the initial etching depth $D(x, y, t^0) = 0$
4. Set the masking constraint by setting etching rate $R^0 = 0$ for $D^0 > 0.3$ µm, $r^0 < 0.5$ mm as the local etching stops in this region according to the plasma tool function *R(r, D)* shown in **Figure 5.21**

2. While $p \leq I - 1$ where p denotes the time-step index I denotes the total number of time steps Δt for the given maximum etching time $t = t_{max}$:

a. Calculate the radial profile $r(t^p) = \sqrt{(x - x_c(t^p))^2 + (y - y_c(t^p))^2}$
   where $t^p = t^0 + p\,\Delta t$ denotes the current etching time and Δt is the time-step
b. Calculate the interpolant of local etching rate $R(r(t^p), D(r(t^p), t^p))$
c. **If:** $R(r(t^p), D(r(t^p), t^p)) = R^0 = 0$ and $D(r(t^p), t^p) > D^0$ where $r(t^p) < r^0$, then the masking becomes effective and the etching stops, i.e., $D\big((r(t^{p+1}), t^{p+1})\big) = D(r(t^p), t^p)$
d. **Else:** Perform the etching by calculating the new depth D as
   $D\big((r(t^{p+1}), t^{p+1})\big) = D(r(t^p), t^p) + \Delta t\, R(D(t^p), r(t^p))$
e. Move the center point of the tool by
   $x_c(t^{p+1}) = x_c(t^p) - (-1^n\, v\, \Delta t)$
   $y_c(t^{p+1}) = y_c(t^p)$
   where *n* denotes the line iteration index, and *v* is the velocity in mm/s

3. If: groove etching

a. Reset the center point as $x_c(t^{I-1}) \to x_c(t^0)$ and $y_c(t^0) \to y^0$
b. Go to the step 2 for the next line iteration $n \to n + 1$

4. Else If: area etching

a. Reset the center point as $x_c(t^{I-1}) \to x_c(t^0)$ and $y_c(t^0) \to y_c(t^0) + \Delta y$ where Δy denotes the groove feed in mm
b. Go to the step 2 for the next line iteration $n \to n + 1$

The obtained results in this section help to establish a plasma-based process chain for surface figuring and error correction of N-BK7 freeform optics. This introduced model is capable of simulation of different forms quite well. However, as it turned out, the surface roughness is high, the surface quality is not sufficient for optical applications, and the process chain should comprise additional polishing steps such as shape-preserving bonnet polishing. Therefore, there is still need for improvement and further research on the N-BK7 surface machining procedure with PJM. In this regard, the aspects of elevated surface temperature on surface machining are investigated in **Section 5.6**.

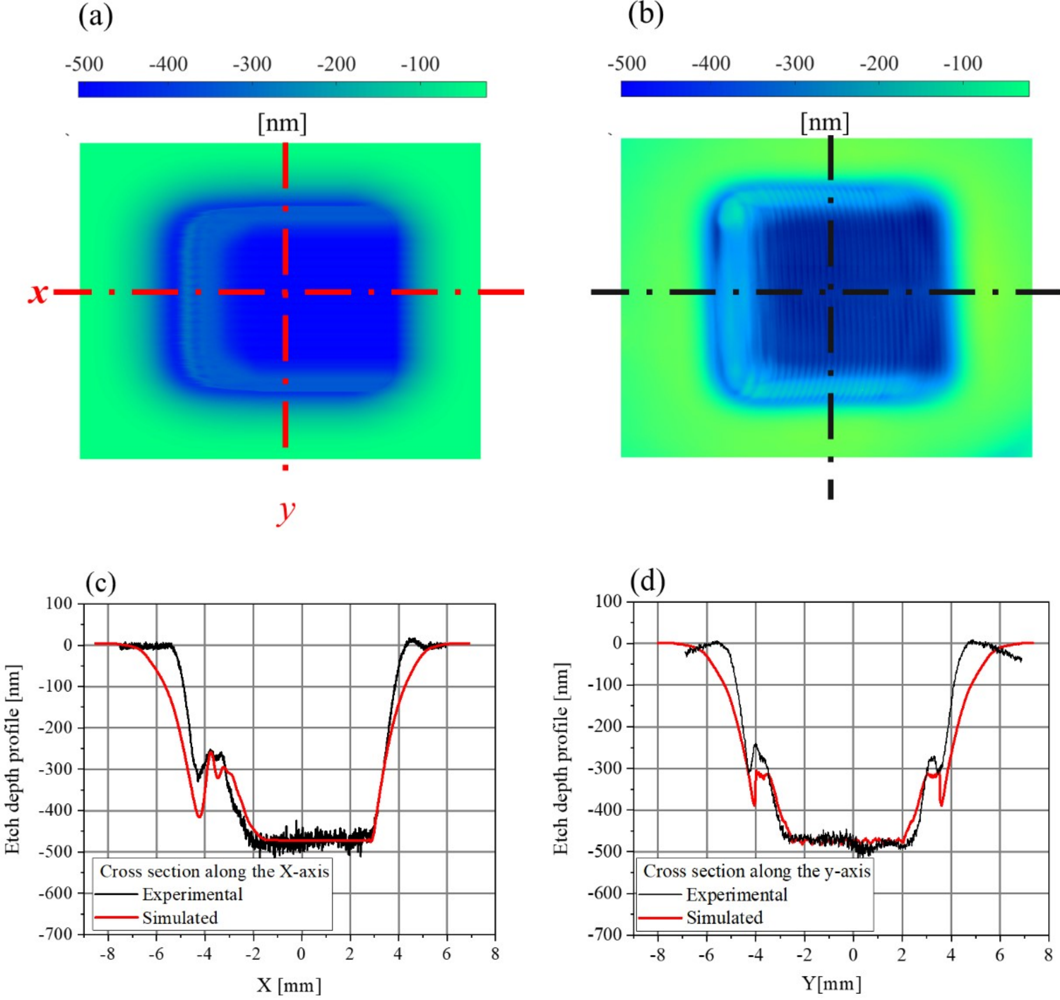

Figure 5.23 *Area etching results: (a) the outcome of proposed simulation algorithm, and (b) the experimental results when the velocity v =4 mm/s is used; Cross-sectional shape of area etching: (c) along x-axis, and (d) along the y-axis where the red line indicates the simulated etch depth profile, and the black line indicates the experimental etch depth profile.*

5.6 Improvement of the plasma jet machining process at elevated surface temperature

Looking at the results presented in **Figure 5.21**, the complex non-linear characteristics of the tool function are not suitable for stable machining process due to the formation of waviness and high level of surface roughness. The aim of the study in this section is to improve the footprint shape of the tool function, which allows to go one step forward in the production of freeform optics. In this regard, the elevated surface temperature is proposed as a decisive factor to modify the shape of tool function. As a result, it is expected that the performance of N-BK7 surface machining improves in terms of deterministic material removal, surface quality and etching rate. To evaluate the effects of surface temperature T_s, static footprint patterns as well as dynamic etching were generated on the N-BK7 surface

by PJM at different surface temperatures T_s. Subsequently, the chemical and structural characterization of the residual layer is analyzed to obtain better knowledge on the effect of temperature on the lateral distribution of residues and the local interaction of the plasma jet with the surface. Moreover, the etching performance of N-BK7 is compared with that of fused silica to verify the optimality of the obtained results. Finally, dynamic machining process is performed at elevated surface temperatures.

5.6.1 Variation of material removal by surface temperature

Figure 5.24 presents the effect of surface temperature T_s on the temporal evolution of static etch profile for N-BK7. In this regard, the etch depth profiles for different dwell times *t* (1 s, 2 s, 4 s, 6 s, 8 s, 10 s and 12 s) are shown at initial temperatures T_h = 25 °C, 150 °C, 250 °C, and 350 °C. Since surface machining of fused silica by plasma jets is well understood, the results for fused silica are also provided in **Figure 5.25** for the sake of comparison when the surface is not preheated (i.e., T_h = 25 °C), while all other conditions are kept the same. In this case, the material removal is obtained by the chemical reactions of fluorine and oxygen with the fused silica surface forming exclusively volatile etching products, i.e., SiF_4. The resulting etch-profile exhibits a near-Gaussian functional form, where the maximum etching depth (in a simple approximation disregarding temperature changes during footprint etching) is a linear function of etching time *t.* The radial depth profiles on N-BK7 surfaces generated by static footprint etchings at T_h = 25 °C exhibit a much more complex structure depending on the dwell time *t*, compared to fused silica[208]. It can be observed from **Figure 5.24(a)** that for short dwell times (i.e., $t \leq 2$ s), the shape of etch profile is near-Gaussian similarly to fused silica (see **Figure 5.25**). In this case, the N-BK7 etch profile is not significantly hindered by the residual layer as it is too thin, and hence an expected distribution of reactive particle-densities on the surface is achieved which leads to isotropic etching. The temporal behavior of the profiles shown in **Figure 5.24(a)** for $t > 2$ s is mainly attributed to the formation of an alkalifluoride layer inhibiting the etching process in the center part, while the tangential process gas transport phenomena lead to a removal of the layer at a radius of approximately 0.8 mm spreading the material in the surrounding.

For larger dwell times ($t > 2$ s) and low initial temperatures T_h <150 °C, the etch depth profiles deviate significantly from the Gaussian distribution leading to a flattened profile shape. By further increasing the etching time *t*, material removal is barely observed at the center while a sharp etching structure is achieved at the peripheral area (**Figure 5.24(a)**). Apparently, at the center, the residual compounds accumulate and mask the surface underneath by obstructing the diffusion of fluorine atoms into the surface of N-BK7. Eventually, the endpoint of etching occurs at the dwell time t = 12 s where the residual layer completely prevents the attack of etching species even at the peripheral area (**Figure 5.24(a)**). One can observe from **Figure 5.24(b,c)** that by increasing the initial temperature T_h, the flattened (non-Gaussian) shape of the etch profiles at large dwell times ($t > 2$ s) gradually change to a more Gaussian-like profile.

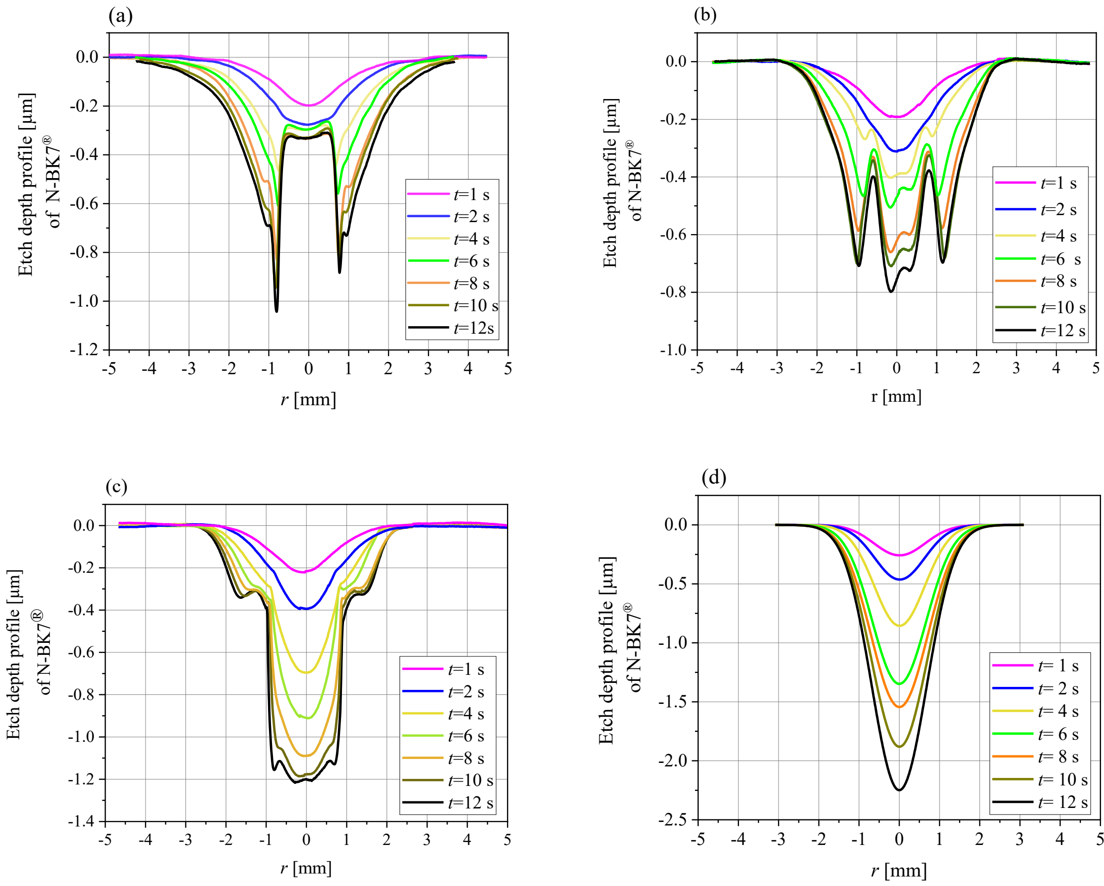

Figure 5.24 *Temporal evolution of N-BK7 etch depth profiles during static plasma etching at different initial temperatures T_h: (a) 25 °C, (b) 150 °C, (c) 250 °C and (d) 350 °C, after the removal of the residual layer with water/ethanol.*

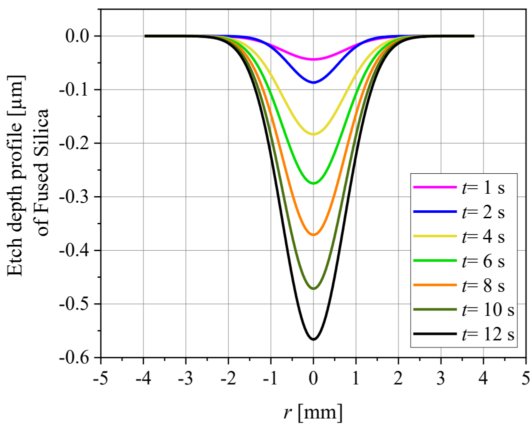

Figure 5.25 *Etch depth profile obtained by the reactive plasma jet on the un-preheated surface (T_h = 25 °C) of fused silica after static plasma processing.*

Obviously, the residual compounds do not mask the surface underneath at the center to impede the continuous and isotropic etching. Finally, when the surface is adequately preheated T_h = 350 °C, the etch profiles have a near-Gaussian shape indicating isotropic etching even for larger values of the dwell time t (**Figure 5.24(d)**). The etch depth profiles presented in **Figure 5.24** and **Figure 5.25** are used for computing the VRR at different conditions with respect to dwell time t by **Equation 4.1**, and the obtained results are shown in **Figure 5.26**. One can observe from this figure that VRR for fused silica (SiO_2) is roughly linear with respect to the dwell time t, whereas VRR for N-BK7 is a decaying non-linear function of dwell time t which exhibits a rather irregular behavior. However, by increasing the initial temperature to T_h = 350 °C, the VRR becomes more predictable exhibiting a stable behavior that could be described by an exponential decay law.

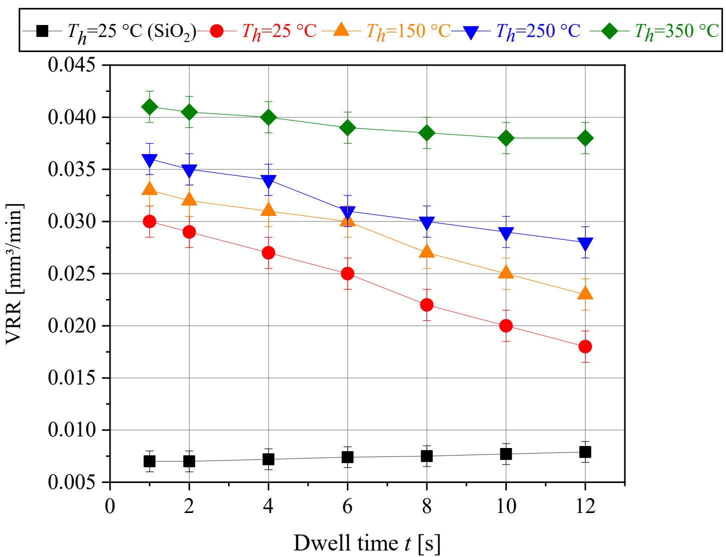

Figure 5.26 *Time-dependent volumetric removal rates VRR obtained for different surface temperatures* T_s.

5.6.2 Analysis of residual layer at different surface temperatures

As observed in **Section 5.6.1**, the elevated surface temperature treatment can improve the footprint shape of tool function leading to enhanced material removal. This improvement can be attributed to the changes imposed by temperature on the features of the formed residual layer in the etching zone such as thickness and structure. To evaluate the impact of the surface temperature T_s on the properties of the residual layer, the N-BK7 surface was preheated to initial surface temperatures $T_h \in \{25, 150, 250, 350\}$ °C and static footprint etching was performed for the dwell time t = 8 s. **Figure 5.27** illustrates EDX images of the distribution of residual compounds over the radial profile r for static footprint patterns. In this figure, the main components of the substrate (Si, O) and the residues (Na, K, F) are color-coded. It can be observed that at each specific surface temperature, the lateral distribution of the residual layer exhibits its own characteristic pattern. As it is observed in **Figure 5.24(a)** and **Figure 5.27(a)**, during

etching a masking layer is formed which strongly hinders continuous etching. However, the layer appears cracked in clods. In the periphery at $r = 800$ µm approximately, the residual layer is delaminated in a ring-shaped zone, while for larger radius a closed layer with decreasing thickness is visible. When the surface is not preheated (i.e., the initial temperature $T_h = 25$ °C), the local surface temperature T_s at the center of the footprint reaches to 300 °C. It deviates largely from that of the peripheral area because of the plasma heat flow (i.e., **Figure 5.24(a)**). Cracking and delamination are thus attributed to the relatively high temperature gradient over the radial profile leading to thermal stress in the layer. Layer removal in the ring-shaped zone may be due to the lateral gas flow that shows a maximum tangential velocity at $r = 800$ µm, as it was discussed in **Section 5.4.2**.

In the case that the sample is preheated to the initial temperature $T_h = 150$ °C (**Figure 5.24(b)**), the radial distribution of residual layer exhibits a similar structure compared to the latter case, except that the central part is delaminated. Only some of clod-like portions remain in this region. As it is conceived from the etch profiles in **Figure 5.24(b)**, the etching depth in the center is in the range of 0.8 µm (compared to 0.3 µm in the non-preheated case) suffering from a higher accumulation of residues, locally. Hence, under this circumstance, a higher thermal stress is induced to the residual layer leading to cracking and layer removal. If preheating temperature T_h is increased to 250°C, a uniformly closed residual layer is formed, and only a marginal delamination occurs in the center, which is not visible at all for $T_h = 250$ °C and $T_h = 350$ °C (see **Figure 5.24(c)** and **Figure 5.24(d)**).

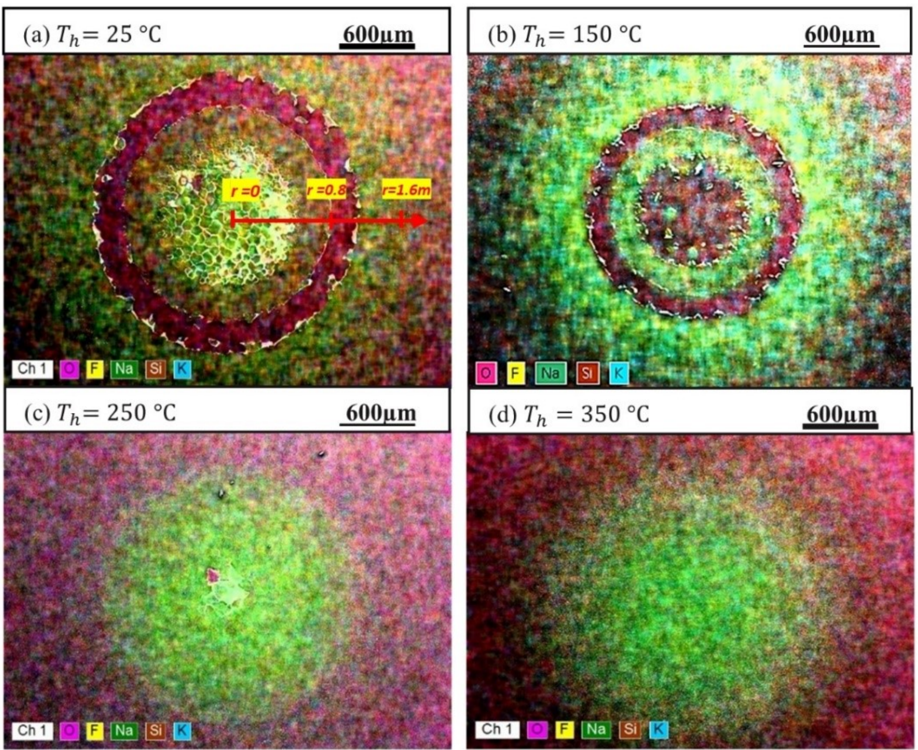

***Figure 5.27** EDX images of the footprint patterns obtained after static etching for dwell time t=8 s at different initial temperatures T_h: (a) 25 °C, (b) 150 °C, (c) 250 °C, and (d) 350 °C.*

Three different spots over the radial profile at the distances $r \sim 0$, $r \sim 0.8$ and $r \sim 1.6$ mm are selected in **Figure 5.27** for a given initial temperature T_h. The relative abundance of elements at these spots is provided in **Figure 5.28**. This figure illustrates that at the radial spots $r \sim 0$ and $r \sim 0.8$ mm the amount of fluorine, potassium and sodium increases noticeably by the rise of initial temperature T_h. This observation proves that, as the surface temperature T_s grows, more uniform and thicker residual layer consisting of NaF and KF forms at the center of footprint. On the other hand, at the low initial temperature T_h, no fluorine is detected, and the maximum oxygen is measured in the spots $r \sim 0$ and $r \sim 0.8$ mm. This is because the residual layer at these spots is removed or cracked severely (**Figure 5.27 (a,b)** and **Figure 5.28**). Moreover, the amount of fluorine and sodium measured at the radial spots $r \sim 1.6$ mm increases at lower initial temperature T_h. The reason for this observation is the outwards dispersion of fragile particles from the spots $r \sim 0$ and $r \sim 0.8$ mm radially over the surface into the spot $r \sim 1.6$ mm by the plasma gas flow at the low initial temperature T_h.

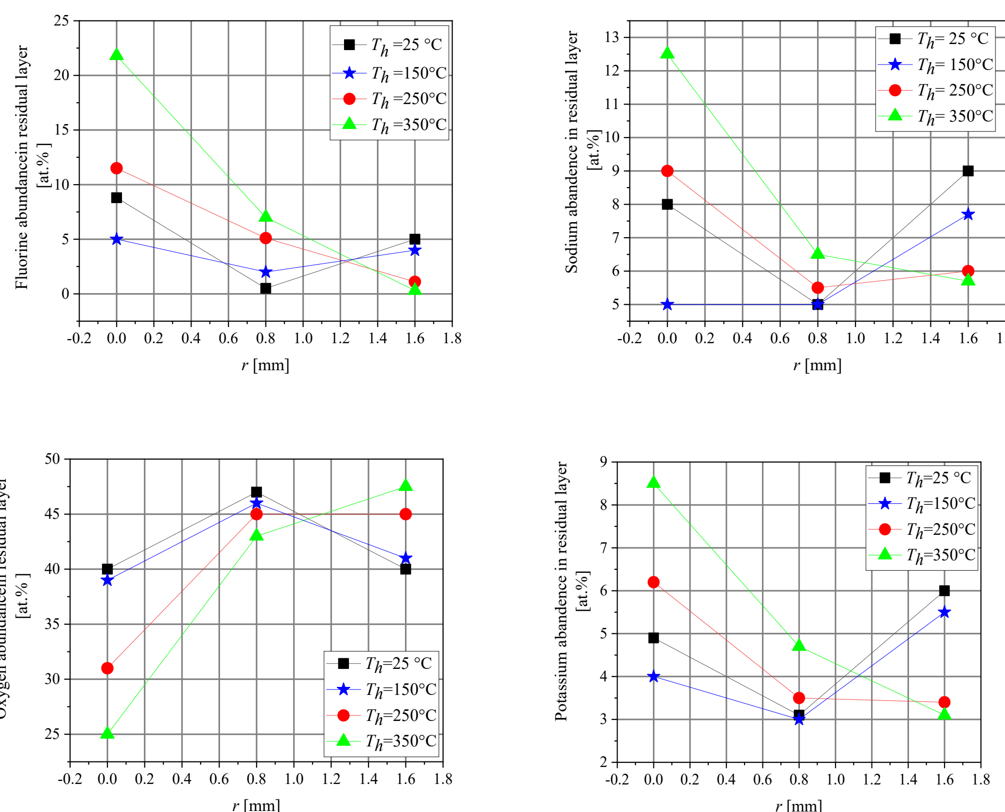

***Figure 5.28** Relative abundance of four elements including fluorine, sodium, oxygen and potassium over the radial profile at three different spots r~ 0, r~ 0.8 and r~ 1.6 mm shown in **Figure 5.27** at four initial temperatures T_h.*

The resulting surface morphology and thickness of residuals formed on the N-BK7 surface after a plasma area scanning treatment were analyzed at the constant velocity 2 mm/s, line feed Δy of 0.1 mm and different surface temperatures T_s. Focused ion beam (FIB) vertical cross-sections were prepared

and imaged by SEM. Furthermore, the SEM images in the top-view configuration were obtained. The results are illustrated in **Figure 5.29**. For T_h = 25 °C / T_s = 290 °C a layer of approx. 300 nm thickness is created exhibiting a granular but densely packed structure. Eventually, some cracks are observed (**Figure 5.29(a)**). At T_h = 150 °C / T_s = 350 °C, the layer is 1.4 µm thick and shows evenly distributed pores or voids in the cross section. The top view reveals smaller granules that are less densely packed, and the voids are visible as well (**Figure 5.29(b)**). If the surface is heated to T_h = 250 °C / T_s = 425 °C, the layer thickness increases to 1.5µm. The voids increase as well as the size of the granules, which resemble a partly crystalline structure with regular edges (**Figure 5.29(c)**). For the highest temperature applied (T_h = 350 °C / T_s = 480 °C), the layer shows a thickness of 3.7 µm, large pores are visible in the cross section, and the crystalline structure of the granules are obvious. (**Figure 5.29(d)**). The findings are discussed as follows. When the N-BK7 surface is not preheated, a sudden rise of temperature is imposed locally into the contact area of the plasma-treated zone by applying plasma heat flow. Therefore, this noticeable variation of surface temperature T_s during area etching in the plasma contact zone and surrounding causes a thermal shock to the non-volatile compounds. Hence, the residues rearrange into a less ordered form, accumulate, and create a closely compact layer. Although the formed residual layer is thin, it is dense enough to mask the surface underneath and obstruct the diffusion of fluorine atoms through the layers to the surface of N-BK7. On the other hand, by preheating the sample gradually, the surface becomes less likely subjected to an abrupt rise of temperature imposed by the plasma heat flow, and the thermal gradient seen by the surface is reduced. Therefore, the residual compounds formed during the machining process remain for a longer time at high temperature. They solidify gradually, and consequently they can rearrange into a more ordered crystalline form. As shown in **Figure 5.29(d)**, such ordered crystallites, which build up at high surface temperature T_s, have more cavities that allow the diffusion of fluorine atoms through the layers to the N-BK7 surface. Therefore, etching proceeds for much larger values of etching time t, and a much thicker layer forms on the surface.

To prove the crystallinity of the residual layer, XRD measurements were performed and the spectra are presented in **Figure 5.30**. The results show that for the lowest temperature, a broad band occurs that is identical to the spectrum obtained from an untreated N-BK7 reference sample. At increased surface temperatures, a growing number of narrow peaks appear in the XRD signals, which have maximum intensity for the highest surface temperature, indicating that the residual compounds solidify into a more crystalline form. The four different plasma-treated areas, presented in **Figure 5.29**, were further analyzed by XPS to reveal the dependence of the chemical composition of the formed residual layer on the surface temperature T_s. The chemical composition of the unprocessed surface of N-BK7 is additionally measured as reference. The results are depicted in **Figure 5.31** which shows a wide variety of chemical elements belonging to either the N-BK7 glass components (e.g., Si, O, K, Na) or plasma-generated reactants (F).

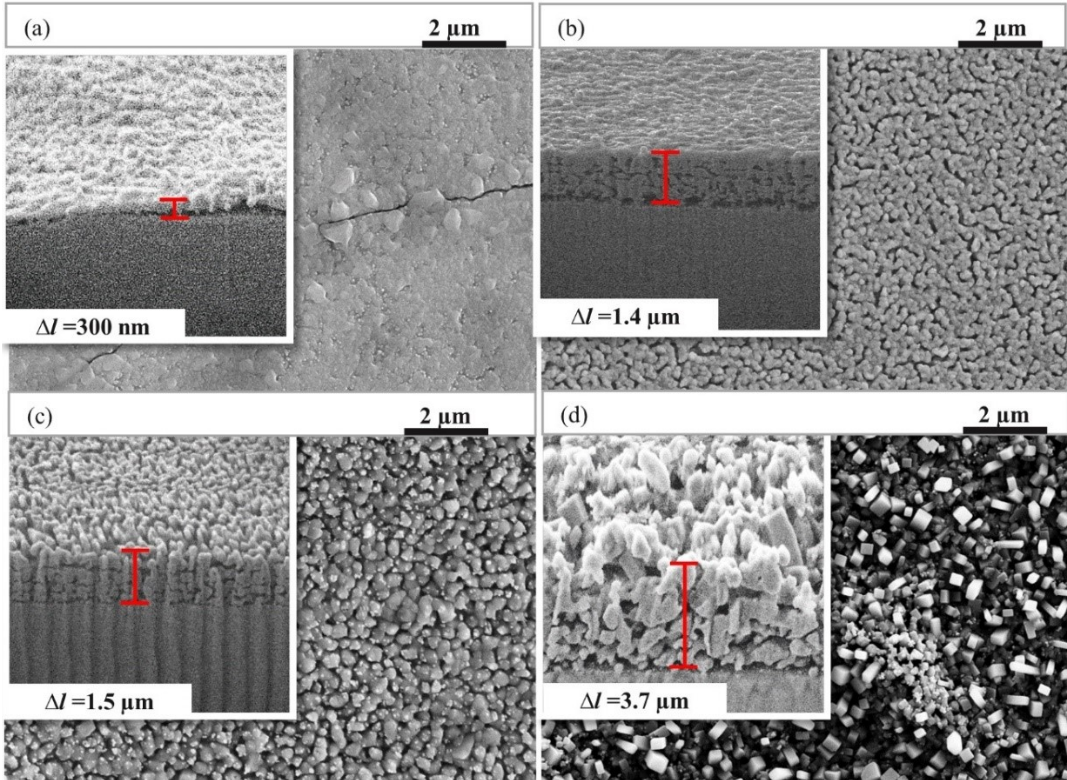

Figure 5.29 *SEM images showing surface morphology of N-BK7 after area etching at four different initial temperatures T_h: (a) 25 °C, (b) 150 °C, (c) 250 °C and (d) 350 °C. The measured layer thickness is denoted in the plots by* Δl.

By comparing the results, it can be observed that the arrangement, type, and ratio of atoms in the structure of the residual layer vary when the initial temperature T_h changes. XPS spectra were analyzed and the relative abundance in atom-% was calculated. In the case of an initial temperature T_h = 25 °C, the chemical composition of the residual layer shows a large amount of fluorine-metal compounds such as KF, NaF, BaF_2, $NaBF_4$ and Na_2SiF_6. Moreover, low amounts of oxygen and silicon are measured in the composition. However, by increasing the initial temperature from T_h = 25 °C up to T_h =250 °C, the quantities of oxygen and silicon increase whereas the quantities of fluorine, sodium, and potassium decrease. Finally, once the sample is preheated, i.e., the initial temperature T_h = 350 °C, the chemical composition of the residual layer is dominated by oxygen and silicon. Although signals indicating fluorine, sodium and potassium are detected, their intensity is still much less than that for lower initial temperatures, i.e., for T_h < 350 °C. This finding seems to be contrary to the results obtained from EDX, where the fluorine abundance is increased, and the oxygen abundance is decreased for an elevated temperature. However, information depth of EDX is in the range of some micrometer, whereas for XPS, the measurement signals arise from the topmost 10 nm, approximately. This would indicate that under high temperature conditions a significant amount of SiO_2 is present on the layer surface, while the layer itself consists mainly of alkalifluorid compounds. The presence of SiO_2 on the surface layer could be explained by a conversion of SiF_4 generated during the etching process and might be still present in the

pores and voids of the layer even after stopping the etching process. As the sample is brought to atmospheric environment after the plasma process, it comes into the contact with humidity leading to hydrolysis of SiF_4 forming a thin film of SiO_2 on top of the granules. Since the purpose of plasma jet machining technique is to process optical elements, the surface roughness evolution during the etching is of great interest. **Figure 5.32** illustrates the influence of initial temperature T_h on the variation of N-BK7 surface roughness (per Sq) over the radial profile r that was etched with different values of dwell time t. Before roughness measurement by WLI technique, the surfaces were cleaned using the procedure described in **Section 4.4**. When the dwell time t is less than 2 s, the etching for all initial temperatures T_h results into a relatively smooth surface, and the measured roughness of the footprint is Sq = 4 nm (see **Figure 5.32**, the curve at t = 1 s). However, by increasing the etching time t, the effect of initial temperature T_h on the surface roughness becomes more evident. When the surface is not preheated (i.e., **Figure 5.32(a)**) and the dwell time t is large, the measured roughness over the radial profile r rises sharply especially at the center of the etched footprint, reaching to Sq = 70 nm.

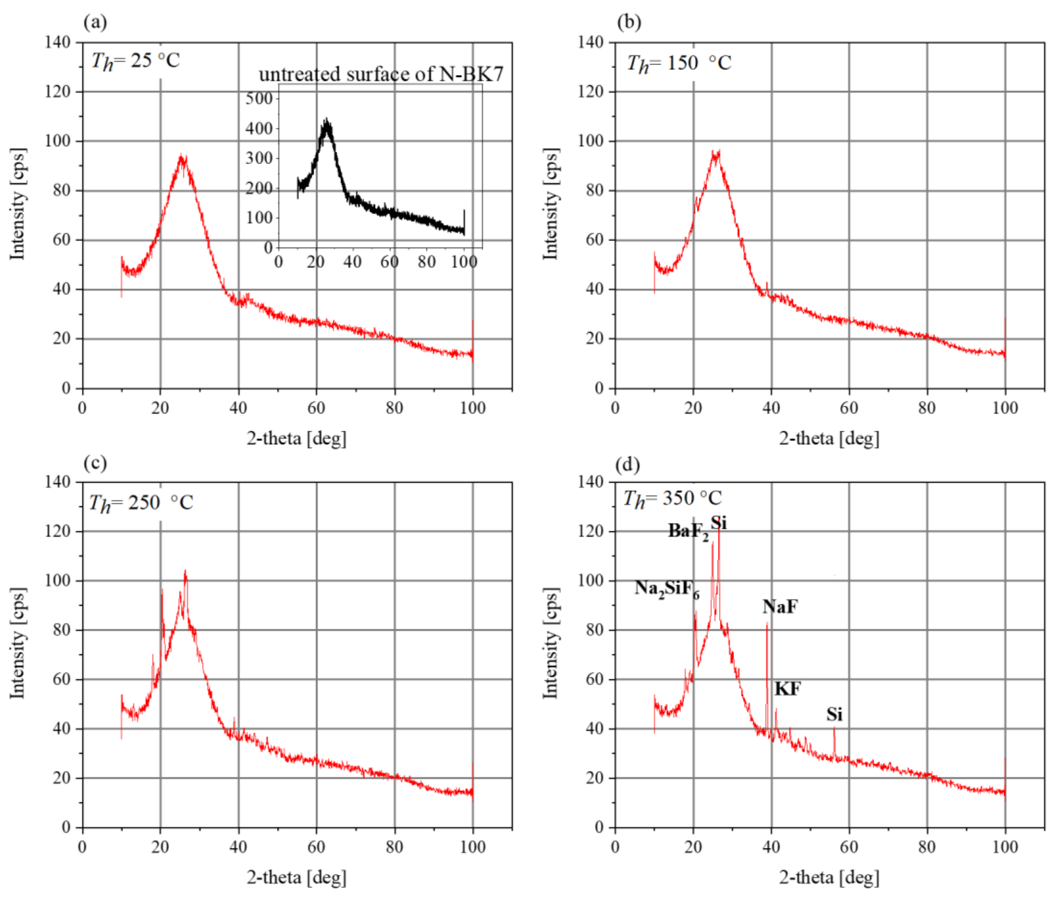

***Figure 5.30** XRD analysis of N-BK7 after area etching at four different initial temperatures T_h: (a) 25 °C, (b) 150 °C, (c) 250 °C and (d) 350 °C by preheating the sample.*

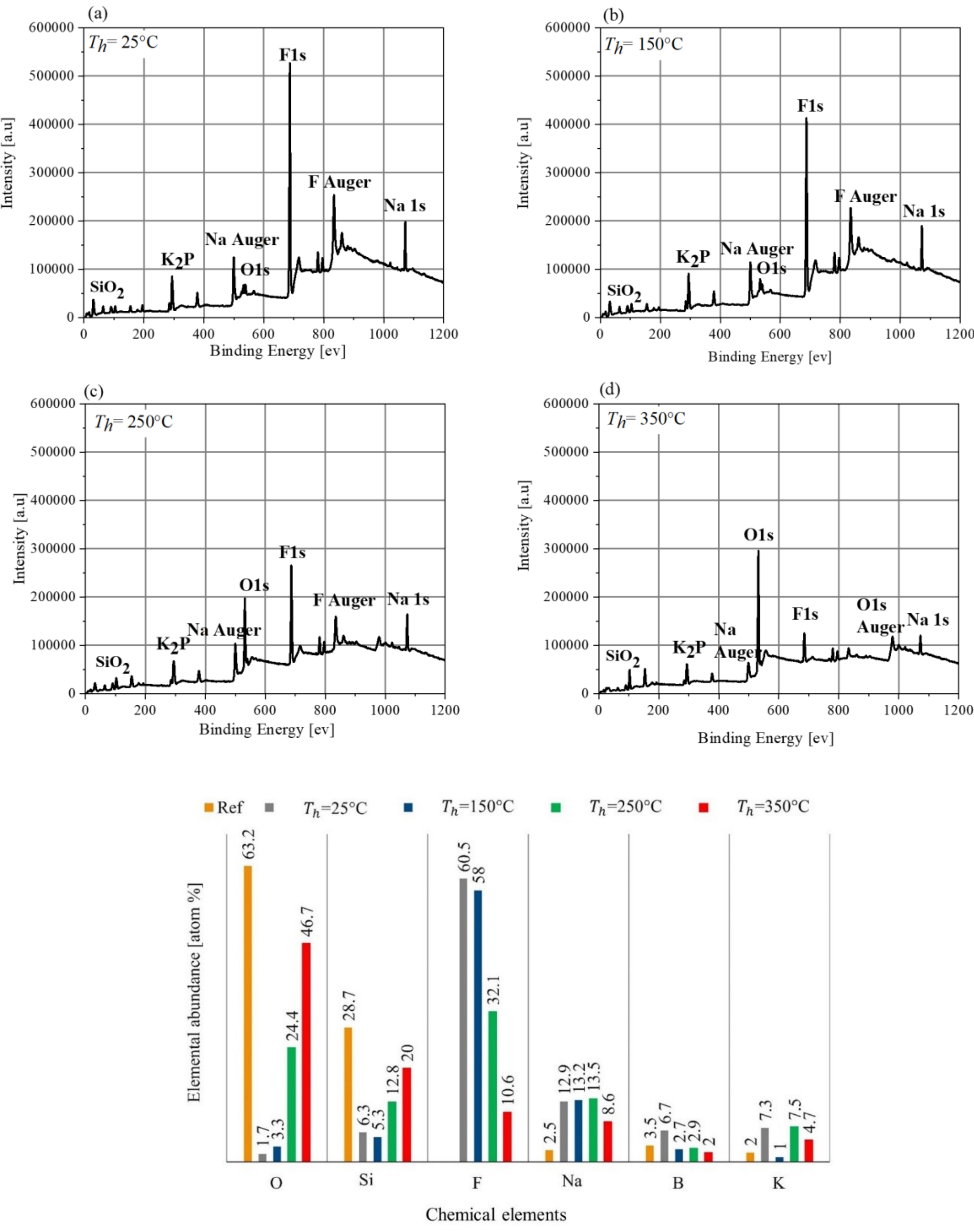

Figure 5.31 *Chemical composition of the N-BK7 surface measured by XPS after the area etching at four different initial temperatures T_h: 25 °C, 150 °C, 250 °C and 350 °C.*

This roughness distribution can be attributed to the formation of multiple cracks and clods in the relatively dense layer, which was observed in **Figure 5.27(a)**. That layer acts as a non-uniform roughness mask spatially modulating the attack of the underlying N-BK7 surface by the fluorine atoms. As the initial temperature T_h is increased to 150 °C, the radial zone of high roughness broadens, which may be attributed to an extended zone of the cracked residual layer. At T_h = 250 °C, the central part shows a significantly lower roughness of maximum Sq=30 nm, whereas in the periphery the roughness

reaches values up to Sq=80 nm. It was shown in **Figure 5.29** that for sufficiently high surface temperatures T_s, the residual layer shows a closed, non-cracked but porous structure allowing a more uniform etching attack. However, in the periphery, the layer seems to be denser but cracked indicating that at this location the surface temperature is not high enough to form a closed layer. Consequently, the roughness is higher at this location. If the initial temperature T_h is adjusted to 350 °C, the increase of surface roughness is minimum, and a homogeneous distribution is observed. Obviously, the residual layer exhibits uniform properties determined by a surface temperature high enough to form a porous layer that can be penetrated by fluorine atoms to etch the underlying N-BK7 surface.

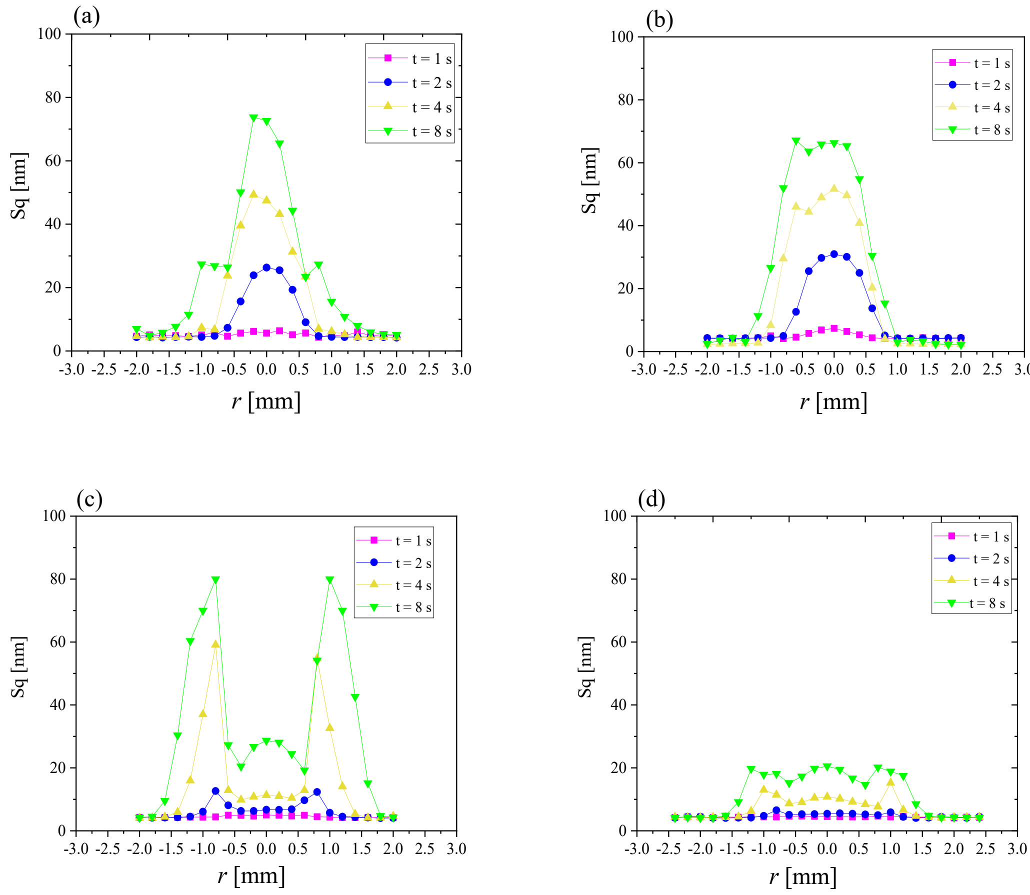

***Figure 5.32** Surface roughness of N-BK7 after static etching at different dwell times t over the radial profile r at various initial temperatures T_h: (a) 25 °C, (b) 150 °C, (c) 250 °C and (d) 350 °C; after the removal of residual layer with water/ethanol.*

5.6.3 Area etching at elevated surface temperature

It was shown in the **Section 5.6.1** that during static footprint etching, the characteristic etching profiles occur depending on the surface temperatures T_s, which show a high degree of complexity. However, it was observed that by increasing the surface temperature T_s through preheating the sample to 350°C, the influence of an inhomogeneous structured residual layer on the N-BK7 etch profile is suppressed.

Hence, a uniform material removal with comparably low surface roughness can be achieved over the radial profile. In this case, the etching rate follows a Gaussian function. Therefore, an initial temperature T_h = 350 °C was chosen to perform a dynamic etching to assess the predictability of surface machining. Predictable dynamic etching is a prerequisite for a deterministic dwell-time based machining scheme. In the experimental setup, a raster path mode was employed with a constant line feed Δy = 0.1 mm, while the velocity v was stepwise increased after every 25 lines starting from 1 mm/s up to 12 mm/s (see **Figure 5.33(a)**). Since the tool function has a symmetric Gaussian shape at elevated surface temperature (i.e., T_h =350 °C), the result of surface machining provides a uniform etching profile D which is predictable for different plasma dwell-times t (or equivalently different velocities of the plasma jet v). However, even at elevated surface temperature, the etching rate decreases at increasing plasma dwell-time t due to the continues growth of residual layer. To show the effect of the residual layer on the reduction of etching rate, the VRR for area etching presented in **Figure 5.33(d)** is computed by **Equation 4.3**. One can observe that VRR strictly increases with velocity v. Furthermore, the surface roughness Sq over the radial profile is presented in **Figure 5.33(c)** while the velocity increases from v = 1 mm/s to 12 mm/s.

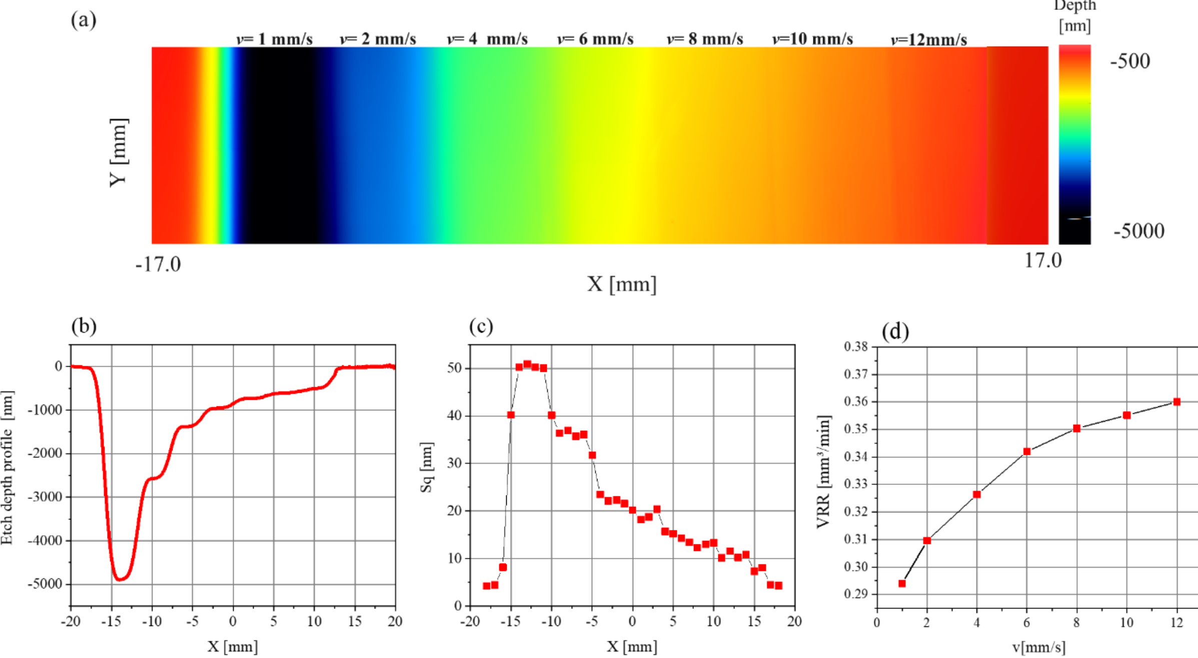

__Figure 5.33__ (a) Experimental area etching results; (b) cross-sectional shape of area; (c) surface roughness of N-BK7; (d) volumetric removal rate VRR of N-BK7 when the plasma jet moves over the surface from left to right with an increasing value of scan velocity v from 1 mm/s to 12 mm/s at an initial temperature T_h = 350 °C.

It can be observed from this figure that by increasing the velocity v, the surface roughness decreases. This finding corresponds to the previously discussed effects for high surface temperatures. By performing a deep etching, a residual layer with a thickness equivalent to the measured etching depth is formed. Although this layer can be penetrated by fluorine atoms through its pores and voids, it reduces the removal rate and causes a relatively high surface roughness. As total etching depth decreases, the volumetric removal rate rises, while surface roughness decreases. The functional form of etching depth depends on the VRR and it should be considered if a deterministic machining process is performed. This investigation is followed up in **Section 5.7**.

5.7 Modelling approaches to deterministic freeform surface machining

Following up the discussion in the previous section, etching at increased substrate surface temperatures of 300-350°C promotes the formation of a more uniformly structured residual layer leading to continuous and isotropic attack of etching species. As a consequence, the footprint tool function exhibits a near-Gaussian functional form similar to the case of fused silica. However, even then the local etching rate depends on the local thickness of the formed residual layer[221]. During a dynamic machining process (e.g., groove etching or area etching), the tool is moved over the surface and interacts with the already formed layer at a certain position leading to varying local removal rates. Therefore, the resulting tool function deviates from the simple rotationally Gaussian form (**Figure 5.33**). Consequently, standard methods used for dwell time calculation, that are based on tool functions exhibiting a constant functional form, cannot be applied here.

The aim of the study in this section is to investigate the removal rate function behavior depending on residual layer thickness. With this information, a numerical model for the calculation of material removal is developed that takes the spatiotemporal variation of the etching rate into account. The model allows to predict the material removal for a given tool path and local dwell time distribution. Hence, a recursive algorithm is introduced for the determination of local dwell times achieving a predefined removal depth map[226]. Moreover, a defined freeform was machined, and the surface topography was compared to a simulated removal depth map to validate the proposed approach.

5.7.1 Determining depth-dependent removal function $R(r, D(r,t))$ at elevated temperature

As mentioned in **Section 5.6**, by heating the substrate during the etching process a Gaussian-shaped material removal function is obtained. Additionally, the plasma jet imposes its own characteristic spatiotemporal temperature distribution during the etching process depending on the process parameters such as the mean input power, dwell time, or plasma jet scan velocity. Assuming a constant radial current density distribution $j(r)$ for etching species and a simple etching reaction (as it is the case for

fused silica), the removal function R is expected to follow the spatiotemporal behavior of the temperature distribution $T_s(r,t)$ via the Arrhenius equation

$$R(r,t) \propto j(r)\ \exp\left(-E_a/T_s(r,t)\right), \tag{5.7}$$

where r is the radial coordinate with respect to the jet center and E_a is an activation energy. Since both $j(r)$ and T_s exhibit a nearly bell-shaped form, the removal function can be approximated by

$$R(r,t) = R_{max}(t)\exp\left(-\frac{r^2}{\sigma(t)^2}\right). \tag{5.8}$$

Hence, at increasing surface temperature T_s over dwell time t, a certain increase of both the maximum R_{max} and width σ of the removal rate function is expected[145].

In the case of groove etching, the equivalent dwell time t for a certain velocity v can be computed by

$$\boldsymbol{t} = \frac{\boldsymbol{\sigma\sqrt{\pi}}}{\boldsymbol{v}}. \tag{5.9}$$

The lateral distribution of the surface temperature T_s during groove and static etching was measured at the center of plasma-surface interaction zone under preheated condition on fused silica and N-BK7. The dwell time t was set to vary from 1 s to 60 s that is equivalent to scan velocities v from 25 mm/s to 0.5 mm/s. In **Figure 5.34**, the peak values T_{max} of surface temperature distributions during static and groove etchings on N-BK7 are compared. It is observed that, for the same value of dwell time t, the surface temperatures T_s during static etching are slightly higher than that of groove etching which is due to the heat distribution over the treated line in the latter case.

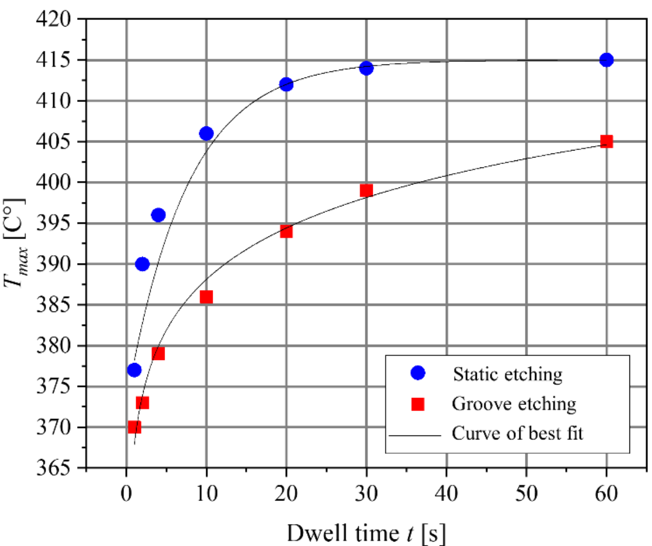

***Figure 5.34** Maximum values T_{max} of lateral surface temperature distributions during static and groove etching on N-BK7 depending on effective dwell time t. Measurements are performed at the center of plasma-surface interaction zone under the preheated condition T_h = 350 °C. Temperature distributions exhibit the same characteristics on fused silica.*

To monitor the temporal evolution of the etch profiles, static etchings were performed on preheated fused silica and N-BK7 surfaces for various discrete dwell times. **Figure 5.35** shows the cross sections of the rotationally symmetric etch profiles on N-BK7 obtained for dwell times *t* varying from 1 s to 60 s. Similar profiles were measured on fused silica.

The measured etch depths were fitted by a Gaussian function *D(r)*,

$$D\,(r) = D_{max}\, e^{-\frac{r^2}{\sigma^2}}, \quad (5.10)$$

where *r* is the lateral coordinate relative to the plasma jet axis, D_{max} denotes the maximum depth, and σ is the standard deviation. The full width at half maximum is obtained by

$$FWHM = 2\sigma\sqrt{ln\,2} \quad (5.11)$$

In **Figure 5.36(a)** and **Figure 5.36(b)**, the Gaussian parameters D_{max} and *FWHM* are plotted over dwell time *t*. In order to obtain analytical expressions for $D_{max}(t)$ and *FWHM(t)*, these data were fitted by monotonously growing functions which are shown as red curves in **Figure 5.36(a)** and **Figure 5.36(b)**, respectively, yielding an analytical expression for *D*(*r*,*t*). Additionally, corresponding results for fused silica are shown for comparison.

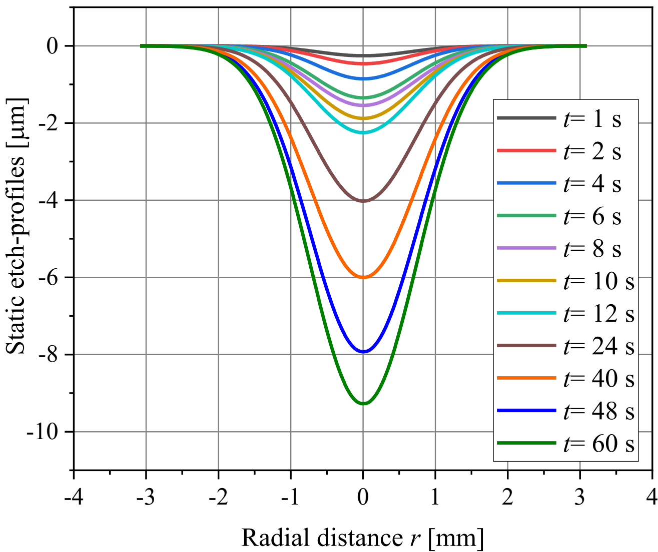

Figure 5.35 *Static etch-profiles on N-BK7 obtained for different dwell times t.*

The momentary local etch rate can then be expressed by

$$R(r,t\,) \propto \frac{\partial D(r,t\,)}{\partial t}\,. \quad (5.12)$$

By taking the derivative with respect to dwell time t, a two-dimensional representation of the time-dependent local etching rate functions for fused silica and N-BK7 are obtained, which are depicted in **Figure 5.37**. The respective maximum rates $R(0, t) = R_{max}$ at different dwell times are shown in **Figure 5.37(b)** and **Figure 5.38(b)**.

It is evident that the time-dependent etch rates exhibit a significantly different behavior. For fused silica the maximum rate exhibits an increase by approx. 30% during the first 20 s and remains nearly constant thereafter. Furthermore, the lateral width of the rate distribution broadens slightly over time, which is also seen in **Figure 5.36(b)**. Both effects are attributed to the surface temperature shown in **Figure 5.34** (for static etching) and the corresponding relationship via the Arrhenius **Equation 5.7**.

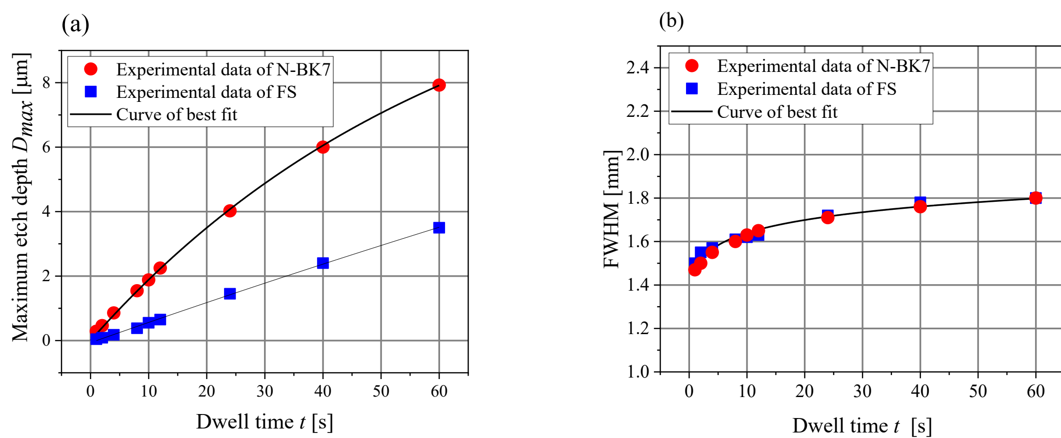

Figure 5.36 *(a) Maximum etch-depth D_{max} at discrete dwell times t for fused silica (FS) and for N-BK7 where the corresponding fitted function $D_{max}(t)$ is depicted by red line. (b) FWHM of etch-profiles over discrete dwell times t and the corresponding fitted function FWHM(t) indicated by red line.*

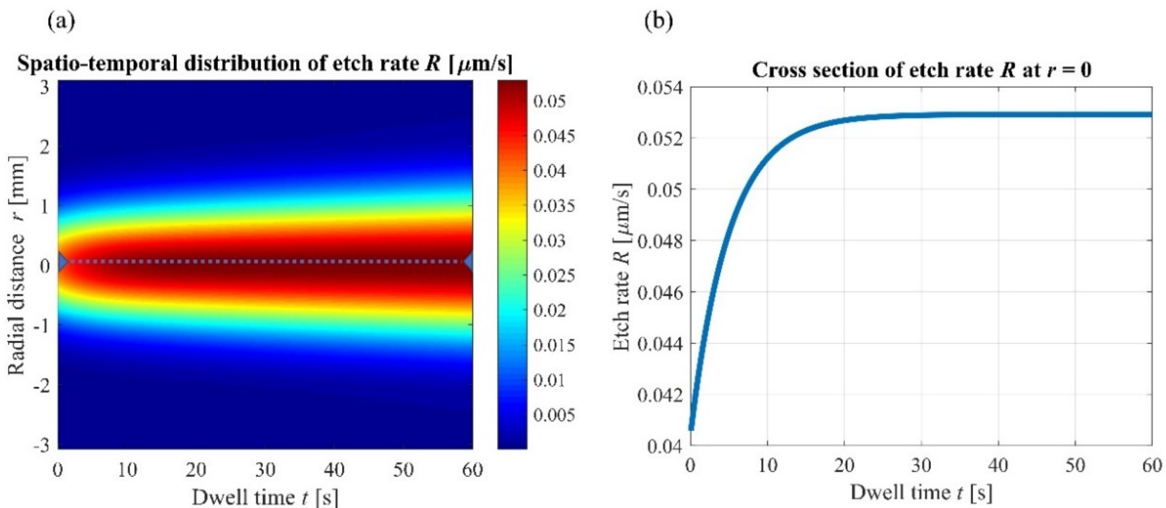

Figure 5.37 *(a) Spatiotemporal distribution of etch rate R(r,t) of fused silica; (b) corresponding cross section of etch rate at r = 0.*

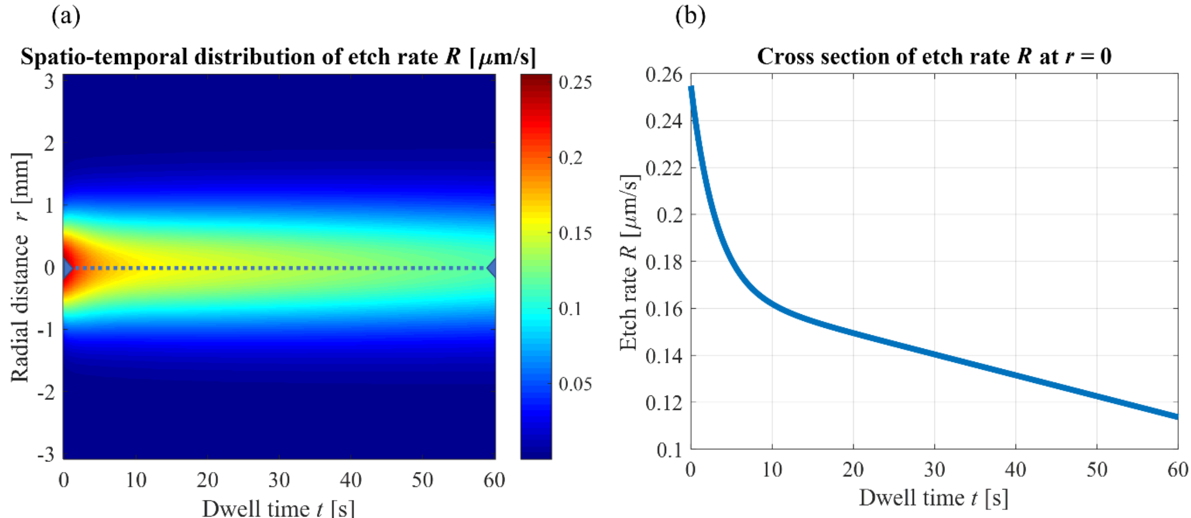

***Figure 5.38** (a) Spatiotemporal distribution of etch rate R(r,t) of N-BK7, (b) corresponding cross section of etch rate at r = 0. These results are based on experimental static etch-profiles presented in **Figure 5.35**.*

However, the rate function for N-BK7 decreases depending on dwell time. Although the surface temperature increases in the same manner as on fused silica, which leads to a corresponding broadening of the lateral rate distribution as shown in **Figure 5.36(b)**, the maximum rate decreases quickly by approximately 36% in the first 10 s followed by a nearly linear decrease to less than 50% of the initial rate at 60s. This effect is attributed to the increasing thickness of the residual layer formed on N-BK7 that inhibits the attack of the etching species and impedes a rate increase due to the rising surface temperature. When starting the process, the initial N-BK7 surface is etched with relative high rate. The successive growth of a porous residual layer inhibits the attack of the reactive species on the interface between layer and glass surface leading to a steep decrease of the rate. After approx. 10 s, the weaker decrease of the rate may be attributed to a structural change of the layer. The effect of residual layer is so pronounced that undermines the rate-driving effect of the temperature. Thus, the etch rate deviates from the Arrhenius temperature dependence showing complex temperature-dependence behavior on N-BK7.

In order to establish a relationship between the momentary rate function $R(r,t)$ and etching depth $D(r,t)$, a numerical interpolation routine was employed leading to a depth-dependent etch rate function $R(r,D)$, where the dwell time t is eliminated. This function is shown in **Figure 5.39(a)** and **5.39(b)**. It allows to predict the local etch rate for a given etching depth in the range of 0 to 8 µm. From the cross section at the center line, it can be seen that for low etching depths up to 1 µm the rate decreases strongly while for higher etch depths the rate decrease is weaker.

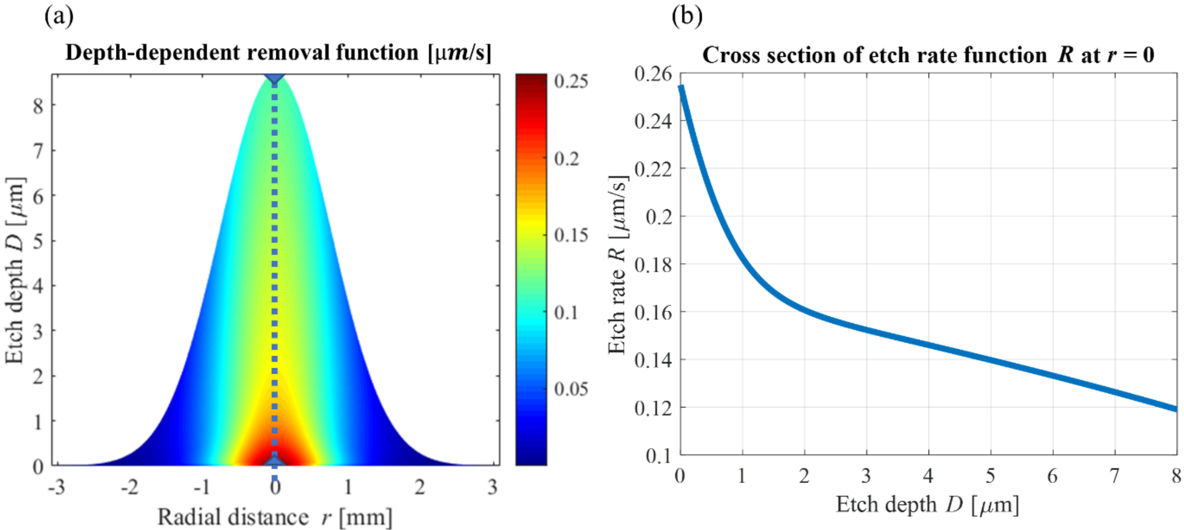

***Figure 5.39** (a) Depth-dependent removal function R(r,D) obtained by merging D(r,t) and R(r,t), (b) corresponding cross section of removal rate function at r = 0.*

5.7.2 Simulative approach to calculate material removal

As it was shown in the previous section, the local removal rate can be described as a function of local etching depth. Therefore, a standard convolution of the tool function with a given local dwell time distribution will not correctly yield the removal function. The reason for this lies in the fact that the convolution kernel is neither constant nor can be simply scaled. It rather varies its local distribution depending on the depth of already etched areas. To illustrate this, an etching process using a raster path and constant motion speed is assumed. When the plasma jet moves to create a first groove, the leading front of the tool etches the pristine glass surface while the trailing part of the tool touches areas that is covered by the residuals. Hence, the removal function is depleted there. After a feed forward motion, the next groove is etched, where the tool partly etches the pristine surface as well as different levels of residual layer thickness. To cope with this effect, the convolution operation is replaced by a numerical algorithm implemented in MATLAB®. The proposed algorithm is summarized in **Table 5.3**.

After initializing an etch depth matrix D_{ij}^0 to zero (no removal), the tool function is moved over the x-y plane along a predefined tool path with a velocity v that is determined by the local dwell time matrix. The local velocity is calculated by $v_{ij} = \Delta x/t_{ij}$, where Δx is the pixel width of the etch depth map in millimeter and t_{ij} is the corresponding dwell time. As the tool function moves over the surface, the momentary etching rate at each location can be calculated using function $R(r, D)$. The local etch depth is obtained by adding the momentary removal to the existing etching depth. After finishing the full etching process, the resulting removal map is contained in matrix D_{ij}.

By applying the described procedure using a dwell time matrix containing constant values on a linear path along the x-axis, a groove etching can be simulated.

Table 5.3 *Numerical algorithm for material removal simulation.*

Algorithm for material removal simulation

Input: Etch rate function *R(r, D)* and dwell time matrix ***t***.

Output: Simulated etch depth matrix *D*

1. Initialization:

1.1 Define 2D space over x and y axes as a matrix D_{ij}, where D_{ij} denotes the etch depth at a pixel with center coordinates (x_i, y_j)

1.2 Set the initial etch depth matrix $D_{ij}^{0} = 0$

1.3 Define a dwell time matrix t_{ij}

1.4 Define the path of the tool function over D_{ij}

1.5 Define the length of discrete time step Δt

2. While $p \leq I - 1$, where I denotes the total number of time steps Δt during etching with $I = \sum t_{ij}/\Delta t$

2.1 Set tool function center point to $(x_c(p), y_c(p))$, depending on tool path and motion velocity determined by t_{ij}

2.2 Determine local depth-dependent etch rate

$$R_{ij}^{p} = R\big(x_i - x_c(p), y_j - y_c(p), D^p(x_i - x_c(p), y_j - y_c(p))\big)$$

2.3 Calculate new etch depth matrix

$$D_{ij}^{p+1} = D_{ij}^{p} + \Delta t\, R_{ij}^{p}$$

The average VRR is calculated by **Equation 4.2**. Similarly, an areal etching can be simulated using a dwell time matrix that contains constant values. The average VRR is then calculated by **Equation 4.3**. In order to compare the simulation results of VRR to experimental values, groove and area etchings were performed according to the settings used in the simulation, i.e., the dwell times were chosen to obtain the corresponding scan velocities *v*.

The **Figure 5.40(a)** reveals that the measured VRR of grooves and areal etchings differ from each other. However, as a general trend, the removal rates increase for low velocities *v*, while at approx. $v = 2$ mm/s the removal rates start to decrease showing an exponential decay. Furthermore, when the scan velocity was fixed at v=4 mm/s and the groove etching was iterated multiple times, the VRR values decrease with iteration number *N* (see **Figure 5.40(b)**). The behavior of the removal rates reflects the combined etching and layer formation mechanism. As the residual layer grows thicker for low velocities *v*, the etching rate decreases accordingly. The higher the velocity *v* is, the thinner the residual layer is. Consequently, the removal rates tend to increase. The same argument holds for repetitive groove etching as shown in **Figure 5.40(b)**.

The residual layer increases in every scan which leads to a decrease of local removal rate, and thus to a decrease of the averaged VRR measured after completion of *N* scan iterations. The decrease of the experimental VRR starting from $v = 2$mm/s, however, is attributed to another effect, namely the surface temperature. **Figure 5.41** shows the peak temperatures T_{max} depending on the scan velocity *v* during groove etching. For increasing velocities, the temperature decreases due to shorter effective local dwell times[227,228].

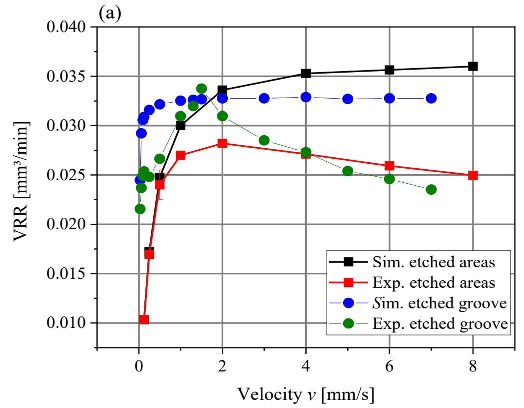

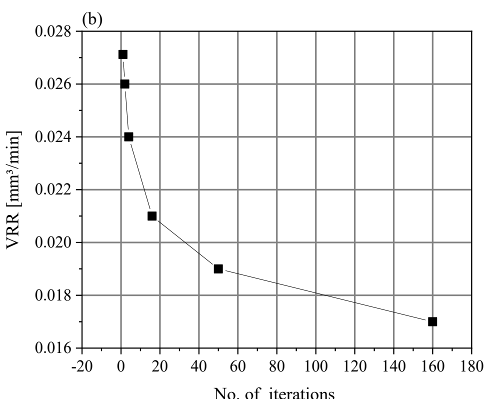

Figure 5.40 *(a) Experimental VRR of grooves and areal etchings as well as simulated values depending on scan velocity v; (b) VRR of grooves depending on number of line iterations N at the scan velocity v = 4 mm/s.*

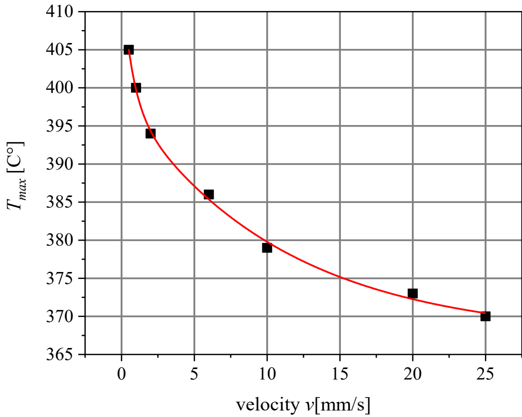

Figure 5.41 *Peak surface temperatures T_{max} depending on the scan velocity during groove etching.*

Different to the experimental values, the simulated VRR for groove and area etchings depicted in **Figure 5.42(a)** show an increase for low velocities but tend to saturate at higher velocities. The reason for the discrepancy between simulation and experiment is the temperature regime that is assumed in the simulation. As the depth-dependent etch rate function *R(r,D)* is computed based on etch profiles derived from static etching, it does not take the correct surface temperatures during scanning into account. By comparing the results in **Figure 5.34**, it is observed that at the same dwell times t, the surface temperatures T_s during dynamic etching are lower than that of the static etching.

Thus, the simulated VRR values of dynamic etching based on this depth-dependent etch rate function *R(r,D)* are overestimated especially for velocities higher than 2 mm/s. A comprehensive treatment of the plasma heat flux and corresponding surface temperature evolution problem requires physical models based on finite element analysis, which is not the scope of the current work. A pragmatic way to take

the different temperature regime in dynamic etching into account is the introduction of a compensation function *C(v)*. To estimate *C(v)* the ratios of experimental to simulated VRR values of area etchings for given velocities *v* are calculated, followed by curve fitting to obtain an analytical function which is shown in **Figure 5.42(b)**. This decaying function starts at approximately one for low velocities, which indicates a correct temperature regime in simulation and experiment. As velocity increases the surface temperature in the dynamic case becomes smaller than the one in the static case, hence the ratio is <1.

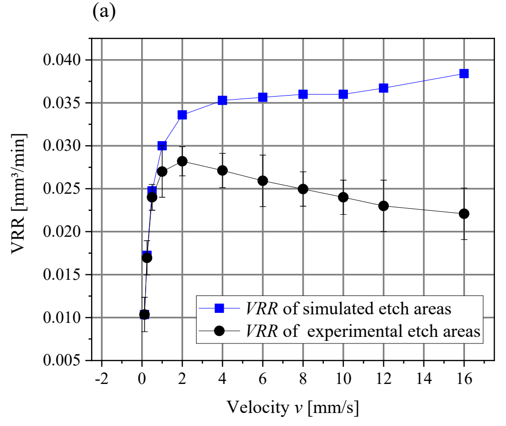

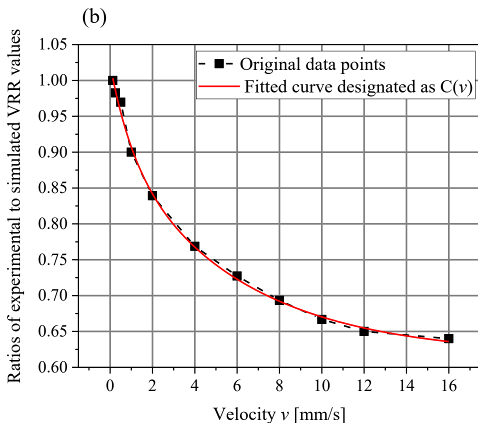

Figure 5.42 *(a) Volumetric removal rates VRR for both the simulated and experimental etch areas at individual velocities v, (b) Ratio of experimental to simulated VRR values for given velocity v and the corresponding fitted curve designated as compensation factor C(v).*

5.7.3 Recursive algorithm for calculation of dwell-time matrix

In deterministic machining, a predefined local removal is to be achieved. As it was shown in the previous sections, standard deconvolution algorithms that are based on constant tool functions, or that at least rely on a constant functional form that may be scaled, cannot simply be applied for the current problem of processing N-BK7 since shape and removal rate vary depending on the local layer thickness. In the following, a recursive algorithm is proposed which is inspired by the van Cittert deconvolution scheme to obtain a dwell time matrix suitable to achieve a desired target removal matrix[229].

In a first step, an initial dwell time matrix $\boldsymbol{t}$ is estimated for the defined target removal map $\boldsymbol{D_0}$ using a conventional deconvolution algorithm developed for ion beam figuring[187]. This algorithm performs a Gold deconvolution based on a constant time-invariant Gaussian tool function. The tool function parameters have been chosen to be near the average values for maximum rate (i.e., 0.2 µm/s) and FWHM (i.e., 1.6 mm), respectively. This preliminary dwell time matrix $\boldsymbol{t}$ is used for a simulation of the material removal depth $\boldsymbol{D_c}$ by employing the depth-dependent etch rate function *R(r,D)* scaled with the temperature compensation function *C*(*v*) in the simulation algorithm described in **Table 5.3**. Due to the incorrect assumptions regarding the tool function in the deconvolution step the resulting removal map differs from the targeted map. Hence, the difference $\Delta = \boldsymbol{D_0} - \boldsymbol{D_c}$ is added to the target removal height

yielding a new removal matrix $\boldsymbol{D_1}$. Now, a new dwell time matrix $\boldsymbol{t_1}$ is determined employing the deconvolution algorithm with the same constant Gaussian tool function settings, which is taken as basis for a next removal simulation. The iteration procedure is continued until the condition on the difference Δ (i.e. RMS(Δ) < *threshold*) is satisfied. Then, the final depth matrix $\boldsymbol{D_{final}}$ is used to generate the final dwell time matrix $\boldsymbol{t_{final}}$ for the machining process. The block diagram of the proposed algorithm is presented in **Figure 5.43**.

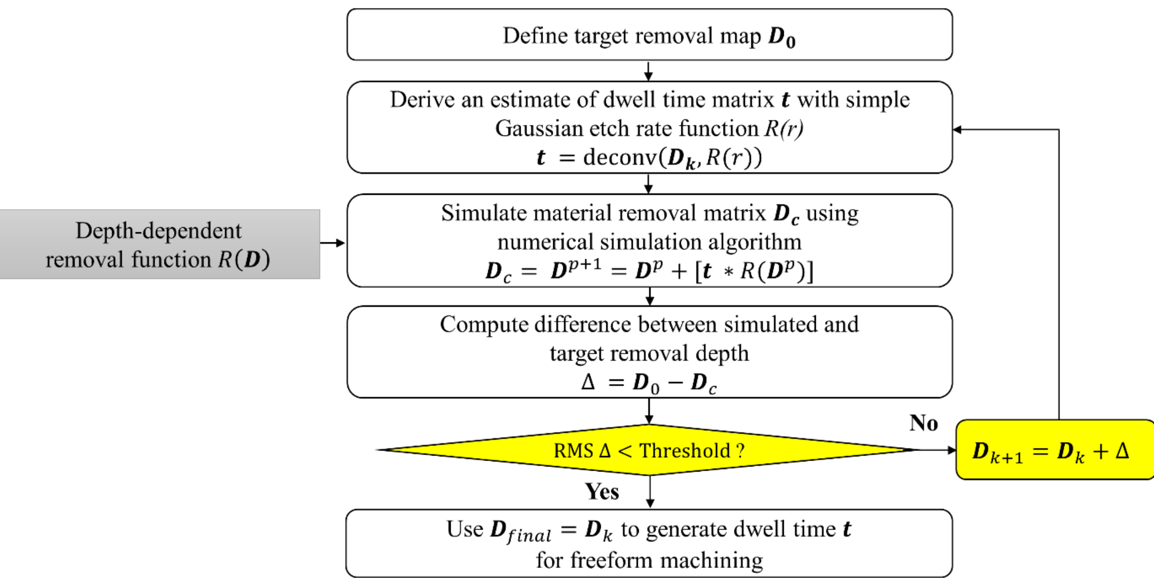

***Figure 5.43**. Block diagram of recursive algorithm proposed for freeform surface machining of N-BK7 optics inspired by van Cittert deconvolution. The index of iterations is indicated by n, and initially is set to 0.*

To evaluate the applicability of the described procedure a sinusoidal test structure with peak value PV = 1 µm is defined as the target removal map $\boldsymbol{D_0}$ (see **Figure 5.44(a)**). The preliminary dwell time matrix $\boldsymbol{t}$ as well as the histogram of velocity v for the plasma jet motion is estimated by the standard deconvolution algorithm. The maximum velocity v applied in the plasma jet system is estimated to be 20 mm/s yielding a base removal height h_{base} about 0.255 µm. The dwell time matrix $\boldsymbol{t}$ is used to simulate the material removal $\boldsymbol{D_1}$ (**Figure 5.44(b)**). Then, the difference matrix Δ_1 between the simulated map $\boldsymbol{D_1}$ and target map $\boldsymbol{D_0}$ is computed to estimate a deviation in height due to the presence of residual layer (**Figure 5.44 (c)**). A PV value of 0.15 µm is observed for this difference matrix Δ_1. The second iteration step yields the simulated map $\boldsymbol{D_2}$ shown in **Figure 5.44(d)**. Again, the difference matrix Δ_2 between the simulated map $\boldsymbol{D_2}$ and target map $\boldsymbol{D_0}$ is computed as depicted in **Figure 5.44(e)** showing a much smaller deviation in height with a PV value of 0.012 µm. As Δ_2 satisfies the convergence condition, which was chosen to be *Threshold* = 0.015 nm, a dwell time matrix is calculated, and a CNC code is derived accordingly to perform a plasma jet figuring experiment on a N-BK7 surface. (**Figure 5.44(f)**). The cross sections of $\boldsymbol{D_0}$, $\boldsymbol{D_1}$, Δ_1, $\boldsymbol{D_2}$, Δ_2 as well as the cross section of experimental removal height are

illustrated in **Figure 5.44(g)**. A close match is observed between the target and experimental removal heights respectively with PV of 1.00 µm and 1.01 µm, respectively. This result demonstrates that the proposed algorithm can accurately exploit the depth-dependent nature of N-BK7 etch-rate function *R(r,D)* to provide the new removal height matrix. Based on simulated map, the deviation in height caused by the residual layer is estimated correctly to obtain a more precise target removal height. **Figure 5.45(a) and 5.45(b)** show the PV and RMS values of the iteration result (i.e., convergence curve of the procedure) as well the achieved experimental results for a quantitative comparison. Obviously, for the current case, it is sufficient to perform two iterations only to achieve the required accuracy.

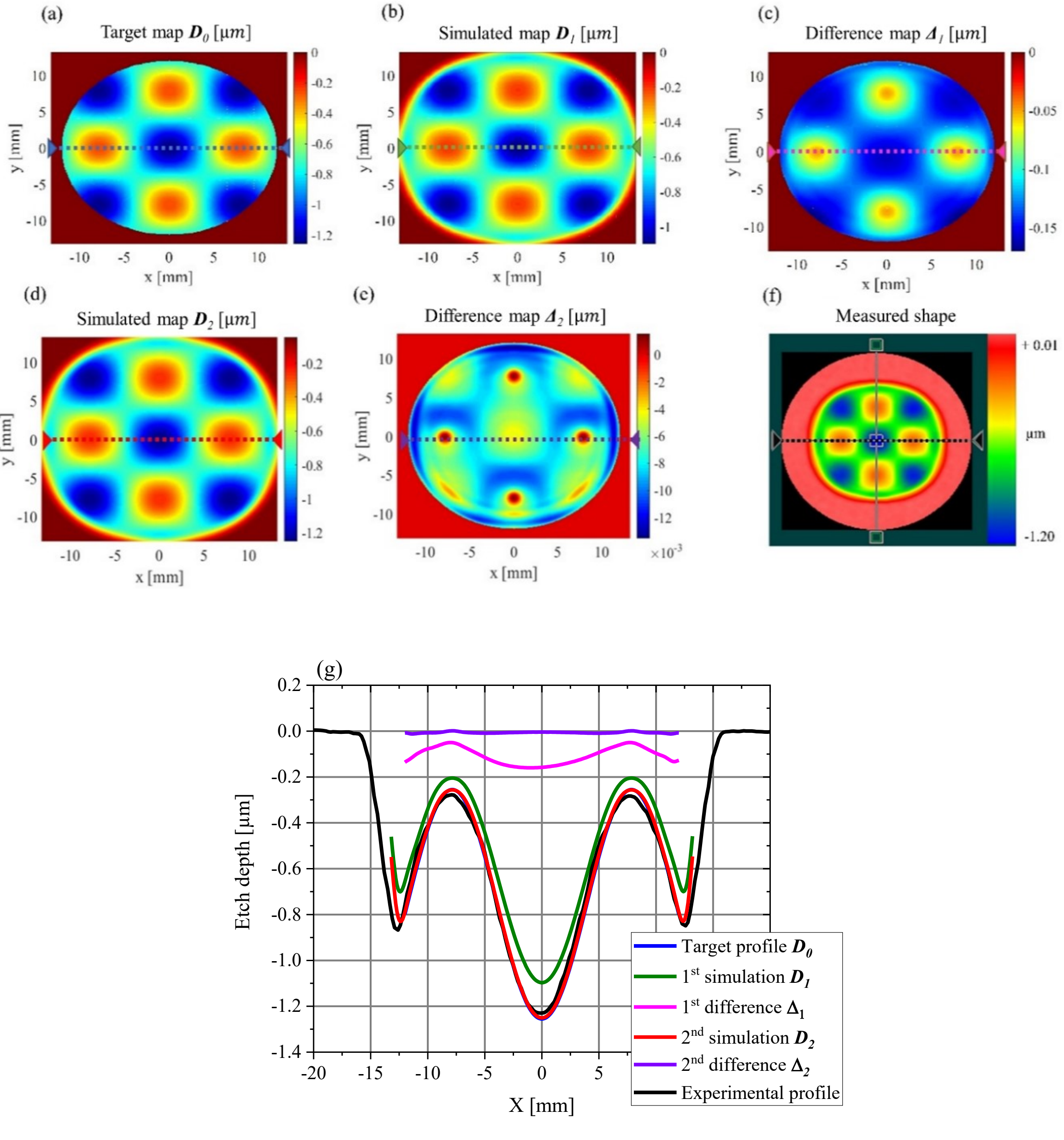

***Figure 5.44**. Surface figuring on N-BK7 for sinusoidal test structure with PV = 1 µm; a) target map $\boldsymbol{D}_0$, b) simulated map $\boldsymbol{D}_1$, c) difference map $\boldsymbol{\Delta}_1$, d) measured shape, e) simulated map $\boldsymbol{D}_2$, f) difference map $\boldsymbol{\Delta}_2$, and g) the cross sections of $\boldsymbol{D}_0$, $\boldsymbol{D}_1$, Δ_1, $\boldsymbol{D}_2$, Δ_2 and experimental removal depth.*

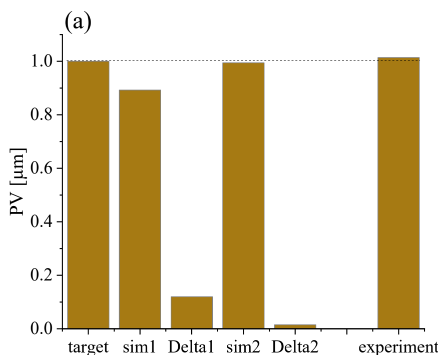

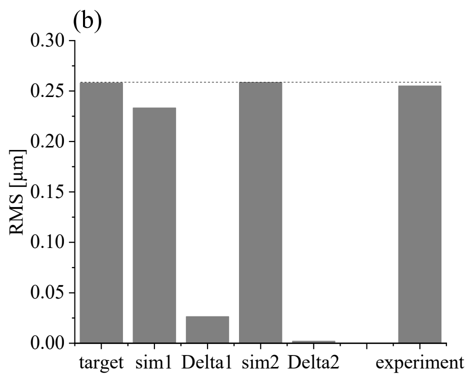

***Figure* 5.45**. *Convergence curve of surface figuring on N-BK7 (a) PV, (b) RMS values of the iteration results.*

5.8 Deal-Grove inspired model for simulating plasma etching

As shown in **Section 5.3**, the application of PJM to deterministic surface machining of metal oxide containing glass like N-BK7 exhibits some limitations. In this respect, a semi-empirical simulation model was proposed in **Section 5.7** to account for the spatiotemporal variations in the removal function allowing to perform deterministic freeform machining on N-Bk7 surface. Nevertheless, a comprehensive chemical/physical model is required that can include all aspects in the complexity of interactions at the N-BK7–plasma interface on an atomic level.

For this purpose, here, the well-known Deal-Grove (DG) model[230] is inspired to provide a useful framework to simulate the kinetics of the plasma etching process of N-BK7 for a wide range of residual layer thickness[232]. The Deal-Grove model is a well-established model for thermal oxide growth that has been introduced in the middle of the 60's, and because of its simplicity it is still frequently applied[231]. One reason for this simplicity is that the whole process is contained in two so-called DG parameters by which the growth kinetics can be described. The determination of appropriate DG model parameters is based on fitting the local etching depth data which was experimentally obtained. Additionally, local surface temperature data was used in the fitting procedure. After parametrizing, the model was extended to simulate etch profiles occurring in dynamic etching. The lateral distributions of the residual layer and etching depths are evaluated to prove that the modelled local depth distribution is equivalent to the thickness of the corresponding residual layer. The obtained simulation results are validated experimentally for the case of dynamic etching processes. By establishing such a model, it is possible to consider the effect of residual layer and surface temperature on the evolution of etching depths over dwell-time. The obtained results lead to a better understanding of the plasma-surface interactions of N-BK7 and help to develop a comprehensive chemical/physical model that can be potentially used in deterministic machining process for plasma-based freeform generation.

5.8.1 Concept of Deal-Grove model

The DG model is used commonly to interpret and predict thermal oxidation of silicon. It describes mathematically the growth of an oxide layer on the substrate surface. In particular, the model is largely used in semiconductor device fabrication[233]. The DG model explicitly considers three phenomena that the oxidizing species undergo during the process including diffusion from the surrounding gas to the surface, diffusion through the existing oxide layer to the oxide-substrate interface, and interactions with the substrate (**Figure 5.49**). The concept of the DG model is based on two fundamental assumptions: (i) Fickian diffusion with a constant diffusion coefficient, and (ii) linear dependence of the mobile oxidant concentration on its position in the oxide. Based on these assumptions, a linear-parabolic function $L = f(t)$ is obtained to illustrate the relation between oxide thickness L [nm] and oxidation time t [s]. The linear term $L{\sim}t$ applies to extremely short oxidation times leading to very thin oxide thicknesses, whereas the parabolic term $L{\sim}\sqrt{t}$ defines the growth at relatively large oxidation times. The DG model is applicable for single-crystal silicon under most conditions although empirical data indicate that very thin oxides (less than 25 nanometers) grow much more quickly in O_2 than the model predicts. This abrupt growth of oxide layer is attributed to reducing oxidation kinetics requiring a modification of the DG model. Nevertheless, the DG model provides precise results for thicker oxides if it is assumed that 25 nm of oxide exists instead of zero initial thickness (or any initial thickness less than 25 nm) before oxidation begins.

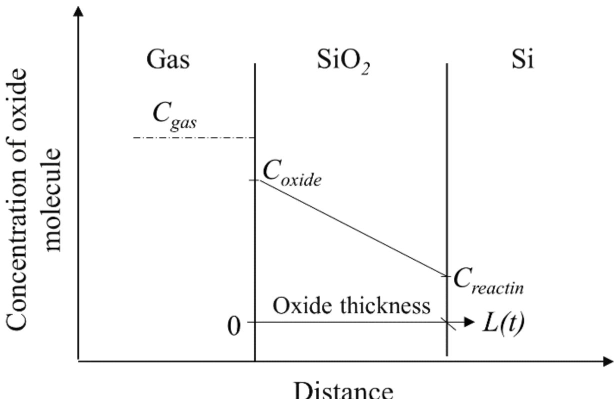

Figure 5.49: *One dimensional Deal-Grove model used for the thermal oxidation of silicon*[230].

5.8.2 Modelling plasma jet etching

To use the DG model concept for simulating the kinetics of the plasma etching process of N-BK7, first the exact interactions between plasma generated active particles (i.e., fluorine) and the N-BK7 surface atoms must be clarified. According to the DG model assumptions, the etching reactions continue at the interface between the formed residual layer and the substrate material, rather than the residual layer and the plasma discharge. During the etching process, three different phases can be recognized which the plasma generated etchant (i.e., fluorine) undergo. Depending on species concentrations, material properties and surface temperature T_s [°C] at any certain radial distance r (that is related to the symmetry

axis of the rotationally symmetric plasma jet), the flux of fluorine atoms through each of the three phases can be expressed as follows (**Figure 5.50**)

I. Transmission from the surrounding gas atmosphere to the boundary layer of the N-BK7 surface, according to Henry's law, i.e.

$$J_1 = h_1(C_1 - C_2), \tag{5.13}$$

where J_1 [mol.m^{-2}.s^{-1}] is the flux of fluorine in gas, h_1 [m.s^{-1}] the gas-phase transport coefficient, C_1 [mol.m^{-3}] the equilibrium concentration of the fluorine in the surrounding gas, and C_2 [mol.m^{-3}] denotes the concentration of the fluorine at the outer surface of the existing residual layer for absorbing inside a surface (surface reaction).

II. Diffusion through the existing residual layer to the layer-substrate interface based on Fick's law, i.e.

$$J_2 = -D_2 \frac{dC}{dx} = D_2 \frac{C_2 - C_3}{L}, \tag{5.14}$$

where J_2 [mol.m^{-2}.s^{-1}] denotes the flux of fluorine in residual layer, D_2 [m^2.s^{-1}] the effective diffusion coefficient, dC_2/dx the concentration gradient in the residual layer, C_3 [mol.m^{-3}] the concentration of residual layer near the residues-substrate interface, and L is the residual layer thickness. The flux J_2 [mol.m^{-2}.s^{-1}] is derived based on the assumed steady-state condition with $\partial J_2/\partial x$ = 0, i.e. no fluorine is reacting in the layer.

III. Reactions with the N-BK7 substrate: in the third part of the etching process, the flux of fluorine is consumed by the chemical reaction at the layer-substrate interface to further grow the residual layer and form volatile products. The reaction is considered as first-order as it controls only the concentration of one reactant (i.e., fluorine). The rate law for such a reaction is given by:

$$J_3 = kC_3, \tag{5.15}$$

where J_3 [mol.m^{-2}.s^{-1}] is the flux of fluorine in reaction with substrate material , and k denotes the surface rate constant as the number of processes occurring at the residues-substrate interface. These processes may include dissociation of the fluorine molecule ($F_2 \rightarrow 2F$), Si-O- or B-O-bond breaking, and Si-F- or B-F-bond formation. The rate at which this reaction takes place should be proportional to the fluorine concentration at the interface C_3.

It is assumed that each of the phases proceed at a rate proportional to the fluorine concentration. Due to similarities of the above-described phases of N-BK7 etching with thermal oxidation of silicon, the concept of Deal-Grove model is exploited here to model the PJM process of N-BK7 (**Figure 5.49** and **Figure 5.50**).

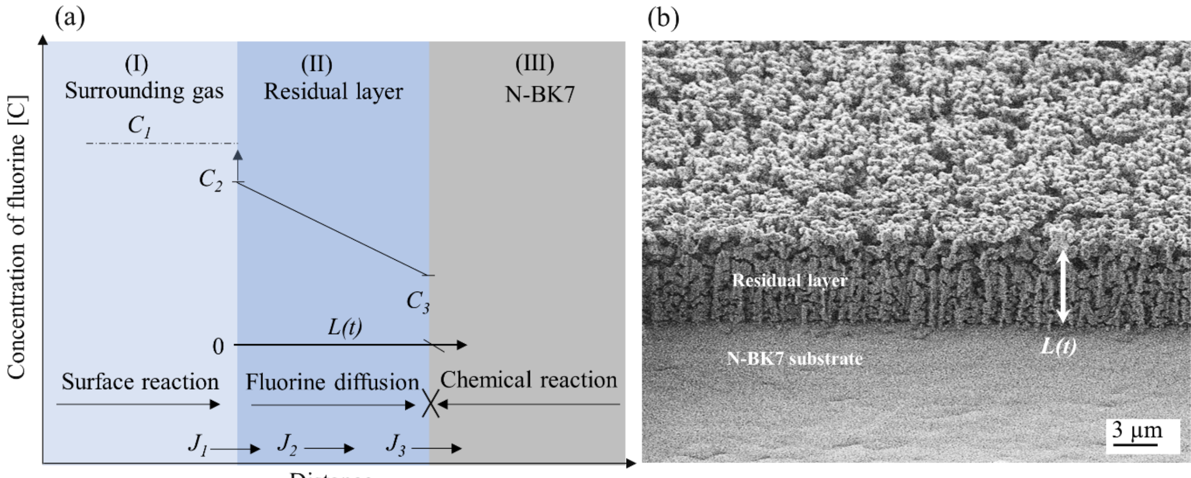

Figure 5.50 *(a) Modeling plasma jet etching with the Deal-Grove model, (b) SEM measurement illustrating the surface morphology and thickness of the residual layer after etching at an initial surface temperature T_h = 350 °C.*

With the main assumption of the DG model, the above-described fluxes of fluorine are equal within the three different phases under steady state conditions, i.e.

$$J = J_1 = J_2 = J_3. \tag{5.16}$$

Then, by substituting C_2 and C_3 with C_1, it yields

$$J = \frac{k\,C_1}{1+\frac{k}{h_1}+\frac{kL}{D_2}} \quad . \tag{5.17}$$

The growth rate $R = \mathrm{d}L/\mathrm{d}t$ [m.s^{-1}] of the residual layer can be obtained directly from the ratio of the flux J and the concentration C [mol.m^{-3}] of reactant molecules (i.e., fluorine) forming a unit volume of the residual layer, i.e.

$$R = \frac{dL}{dt} = \frac{J}{C} = \frac{1}{C}\frac{k\,C_1}{1+\frac{k}{h_1}+\frac{kL}{D_2}}. \tag{5.18}$$

By defining the following parameters A [m] and B [m^2.s^{-1}] as

$$A = 2D_2\left(\frac{1}{k}+\frac{1}{h_1}\right), \tag{5.19}$$

$$B = \frac{2D_2C_1}{C}, \tag{5.20}$$

the differential equation **Equation 5.18** can be rewritten as

$$\frac{dL}{dt} = \frac{B}{A+2L}. \tag{5.21}$$

In order to get an analytical relationship between residual layer thickness L and etching time t, the first order differential **Equation 5.21** must be solved. For this purpose, in the first step, the expression (5.21) can be rewritten as

$$(A + 2L)dL = Bdt. \tag{5.22}$$

By taking the integration of both sides of the expression **Equation 5.22**, and with the assumption of an initial layer thickness L_0 [m] at $t = 0$ s, a quadratic equation is derived for the layer thickness L:

$$\int_{x_i}^{L}(A + 2L)dL = \int_0^t Bdt, \tag{5.23}$$

$$L^2 + AL = B(t + \tau), \tag{5.24}$$

where the parameter τ [s] is given by

$$\tau = \frac{L_0^2 + AL_0}{B}. \tag{5.25}$$

The parameter τ takes into account any residual layer thickness at the start of etching process. Solving equation **Equation 5.24** for a given desired residual layer thickness L_0 results in the estimation of etching time t as

$$t = \frac{L_0^2 - x_i^2}{B} + \frac{L_0 - x_i}{B/A}. \tag{5.26}$$

In this study, the initial layer thickness L_0 is assumed to be zero as with this setting acceptable results can be obtained.

However, solving the quadratic **Equation 5.24** with respect to L leads to the following expression

$$\boldsymbol{L} = \frac{-A + \sqrt{A^2 + 4B(t+\tau)}}{2} = \begin{cases} \frac{B}{A}(t + \tau) & t + \tau \ll \frac{A^2}{4B} \\ \sqrt{B(t + \tau)} & t + \tau \gg \frac{A^2}{4B} \end{cases} \tag{5.27}$$

where the parameters B [$m^2.s^{-1}$] and B/A [$m.s^{-1}$] are called the quadratic and linear rate constants.

In the first step, static footprint etchings were performed on preheated N-BK7 surfaces with $T_h = 350$ °C to monitor the temporal evolution of the etch profiles. Afterward, the resulting layer thickness over the radial profile well as the etching profile was measured. In this experiment the plasma jet dwell time was adjusted to $t = 4$ s. The produced layer thickness cross section was measured using a thin film profiler, while the etching depth profile cross section was determined by white light interferometry after removing the layer by rinsing the surface with water/ethanol. As shown in **Figure 5.51**, the local etching depth D is equivalent to the thickness L of the residual layer, i.e.

$$D(t) = L(t). \tag{5.28}$$

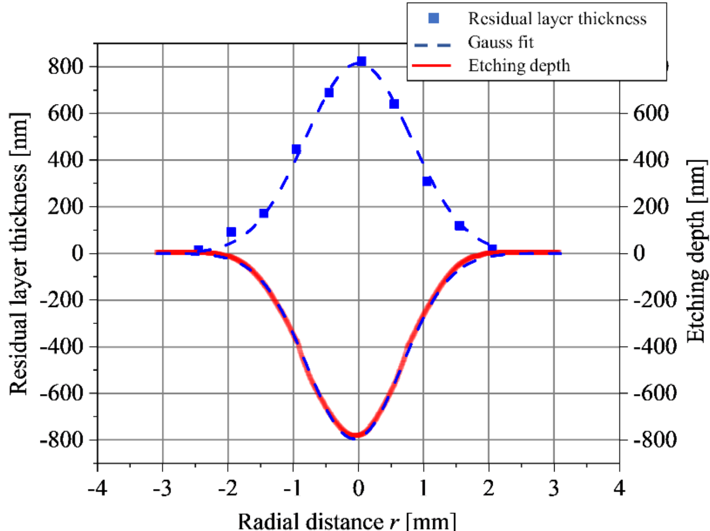

Figure 5.51 *Profiles of residual layer thickness (blue squares) and etching depth (red curve) after the removal of residual layer with water/ethanol obtained on the surface of N-BK7 using fluorine-based plasma jet at the initial temperature T_h = 350 °C for etching time t = 4 s. The dashed lines are the corresponding Gaussian fits with amplitude $D_{max} \approx$ 800 nm and $\sigma \approx 1.1$ mm.*

According to the discussion in **Section 5.7.1**, both heat and reactive species fluxes of plasma jet on substrate surface led to the characteristic bell-shaped profiles of residual layer thickness or etching depth, which can be approximated by **Equation 5.10**. Therefore, the variations of fluorine flux and temperature with the radial distance *r* must be considered in the model for simulation of local etching depths. Hence, the DG parameters B and B/A are a function of radial distance *r* and surface temperature *T(r,t)*. Provided, the local etching depth *D* can be expressed by one inclusive model equation, it follows:

$$D(t,T(r,t),r) = \frac{-A(r,T(r,t))+\sqrt{A^2(r,T(r,t))+4B(r,T(r,t))(t+\tau)}}{2}. \tag{5.29}$$

For the case of silicon oxidation, it was found experimentally that the relation of model parameters B and B/A on temperature *T* can be well described by Arrhenius expressions[230-231]. Therefore, it is assumed that the temperature dependence in the current case can be described by the Arrhenius expressions as follows

$$B(r,T(r,t)) = \alpha_1(r)\exp\left(-\frac{E_{a1}}{k_B T(r,t)}\right) \tag{5.30}$$

$$\frac{B(r,T(r,t))}{A(r,T(r,t))} = \alpha_2(r)exp\left(-\frac{E_{a2}}{k_B T(r,t)}\right), \tag{5.31}$$

where E_{a1} and E_{a2} denote the activation energy, k_B the Boltzmann constant in eV, and $\alpha_1(r)$ [$m^2.s^{-1}$] and $\alpha_2(r)$ [$m.s^{-1}$] are the pre-exponential constants which are to be determined for the given radial distance *r*. A list of model parameters for the proposed DG-model based approach are presented in **Table 5.4**.

***Table 5.4** List of model parameters for the proposed DG-model based approach.*

Model parameter [Unit]	Description	Definition
B [$m^2.s^{-1}$]	Quadratic term, a function of r and T	Equation 5.30
B/A [$m.s^{-1}$]	Linear reaction rate term, a function of r and T	Equation 5.31
α_1 [$m^2.s^{-1}$]	Pre-exponential constant of quadratic term	Estimated via fitting process at given r
α_2 [$m.s^{-1}$]	Pre-exponential constant of linear reaction rate term	Estimated via fitting process at given r
$\boldsymbol{E_{a1}}$[eV]	Activation energy in quadratic term	0.05
$\boldsymbol{E_{a2}}$[eV]	Activation energy in linear reaction rate term	0.05

In order to find the model parameters $\alpha_1(r)$ [$m^2.s^{-1}$] and $\alpha_2(r)$ [$m.s^{-1}$], an estimation procedure based on fitting experimental data is proposed. To provide such data including local depth *D(r,t)* and surface temperature *T(r,t)*, static etching was performed on a preheated surface with initial temperature T_h = 350 °C for different dwell times *t* ranging from 1 s to 60 s. The local etching depth and temperature data used for the fitting process are presented in **Figure 5.52**.

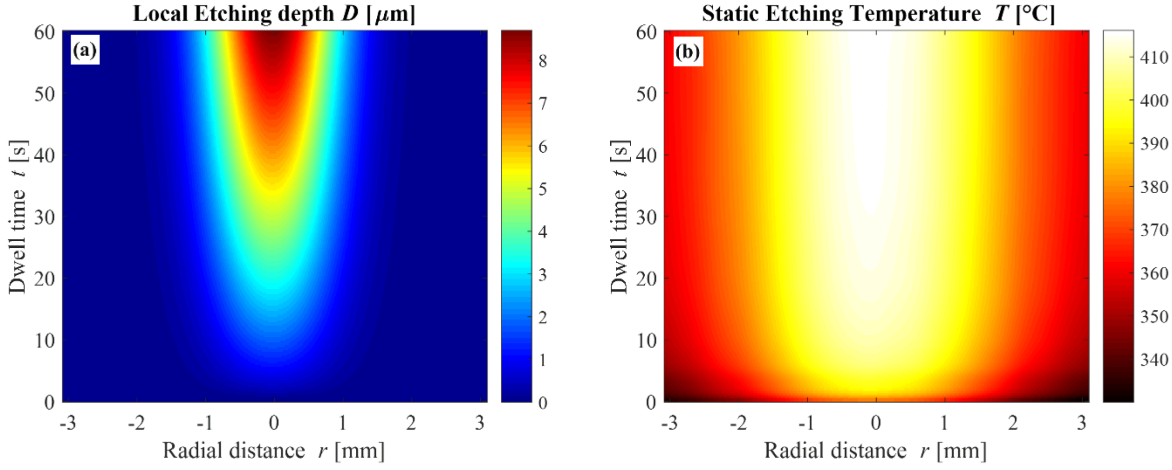

***Figure 5.52** (a) Local etching depth D(r,t) obtained by static etching at the initial temperature T_h = 350 °C after the removal of residual layer, (b) corresponding surface temperature distribution T(r,t).*

Then, by fitting the experimental data *D(r,t)* and *T(r,t)* for each individual radial distance *r* to the **Equation 5.29**, the constants $\alpha_1(r)$, $\alpha_2(r)$ and the activation energies E_{a1} and E_{a2} are determined. In this regard, it is required to solve nonlinear curve-fitting (data-fitting) problems in least-squares sense that is implemented here by the MATLAB built-in function "lsqcurvefit".

The empirically estimated activation energy for fluorine-based plasma etching of fused silica (SiO_2) has been shown to be around 0.16 eV[234]. This activation energy usually is associated with the Si-O bond breaking process during SiO_2 removal process. However, compared to SiO_2, the activation energy of

N-BK7 is expected to be less due to the presence of alkali metal ions (e.g., Na^+) in its glassy network. The results of fitting process showed that the value of E_{a1} is very close to E_{a2}, and it can be set to the constant average value 0.05 eV. Moreover, the experiments revealed that the activation energy for N-BK7 is in the range of 0.03-0.06 eV. This result suggests that the origin of activation energies E_{a1} and E_{a2} is likely associated with the diffusion of fluorine through residual layer but also with the interface chemical reaction rate k (i.e., bond breaking process related to chemical reactions).

The results of fitting the experimental etching depth D to the DG model **Equation 5.29** is shown in **Figure 5.53**. According to **Equation 5.20**, the parameters B and accordingly B/A are directly proportional to the flux of the fluorine (concentration C_1). Therefore, it is expected that the pre-exponential constants α_1 and α_2 adopt a bell-shaped functional form over the radial distance r as the distribution of fluorine flux follows a near-Gaussian shape.

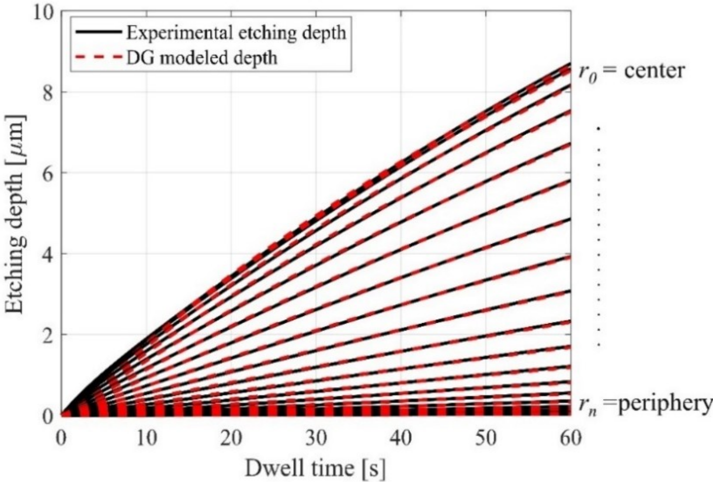

Figure 5.53 *Results of fitting the experimental etching depth D to the DG model (**Equation 5.29**) for exemplary values of radial distance r.*

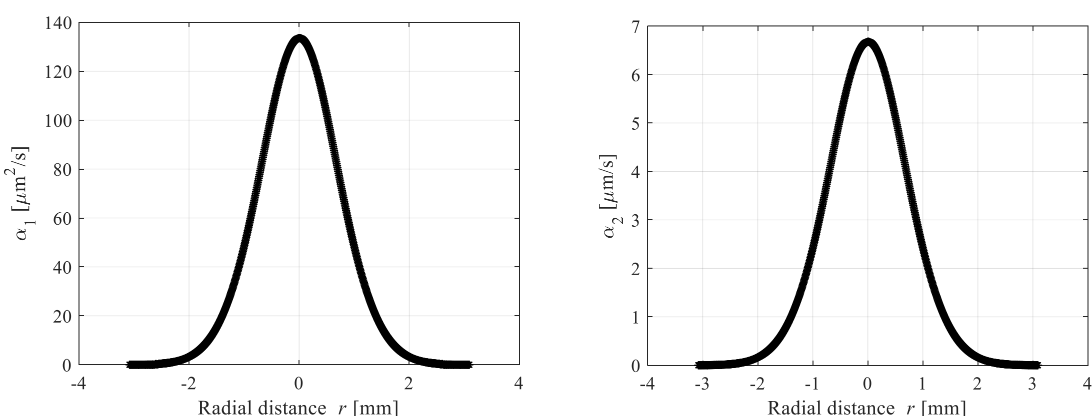

Figure 5.54 *Pre-exponential functions $\alpha_1(r)$ and $\alpha_2(r)$ obtained for a range of radial distance r values using the fitting process on static etching experimental data.*

Figure 5.54 shows the computed values of the pre-exponential functions $\alpha_1(r)$ and $\alpha_2(r)$ with respect to the radial distance *r*. With this parameter, the DG model can be employed to model layer thickness or etching depth profiles for dynamic etching.

In case of static etching, for a given temperature distribution, the relation of local etching depth *D* and the dwell time t can be expressed as follows

$$\boldsymbol{D = R_{max}\, t\, exp\left(-\frac{r^2}{\sigma^2}\right)}, \tag{5.32}$$

where $R_{\max}$ is the time-averaged maximum local etching rate.

In the case of groove etching, by computing the integral of **Equation 5.32** with respect to the time *t*, the local etching depth *D* for given scan velocity *v* can be obtained as follows

$$\boldsymbol{D = N \int R_{max}\, exp\left(-\frac{(v\,t)^2 + x^2}{\sigma^2}\right) dt \;=\; \frac{N\, R_{max}\, \sigma \sqrt{\pi}}{v}\, exp\left(-\frac{x^2}{\sigma^2}\right)}. \tag{5.33}$$

where *N* is the number of line iterations. **Equation 5.33** expresses the convolution of the Gaussian rate function **Equation 5.32** with the constant dwell time distribution along the path in y direction. The equivalent velocity *v* [mm.s^{-1}] for a certain dwell time *t* in the case of dynamic etching can be obtained when the **Equation 5.32** and **Equation 5.33** are set equal, with $x = r$, resulting in the relation:

$$\boldsymbol{v = \frac{\sigma(t)\sqrt{\pi}}{t}}, \tag{5.34}$$

where $\boldsymbol{\sigma(t)}$ is the standard deviation of the Gaussian function (i.e., a measure of the FWHM) at the given dwell time t. For modeling groove etching, the parameters $\alpha_1(r)$ and $\alpha_2(r)$ found from static etching as well as the relevant surface temperature profiles *T(r,t)*, obtained experimentally from dynamic etchings (not shown here), are inserted in **Equation 5.29** and depth profiles are calculated for depending on the dwell time t.

The corresponding scan velocity *v* can be estimated from **Equation 5.34** for each modeled groove etching profile by taking the respective $\boldsymbol{\sigma(t)}$. The standard deviation $\boldsymbol{\sigma(t)}$ is estimated by fitting the depth profile to a Gaussian function. **Figure 5.55** shows the cross-section shapes of simulated depth profile and experimental results for groove etching for different scan velocities. In general, the maximum depth of the modelled profiles agrees well with the experimental profiles. However, the modelled profiles exhibit slightly larger FWHM. This effect can be attributed to an overestimation of the etching depth especially in the periphery of the profiles since the model takes a 2-dimensional temperature profile over the cross-section x into account. In other words, the surface temperature on a position x within the etched groove is assumed to be constant. In the real experiment, the spatial temperature shows, however, a lateral distribution in the x-y plane that resembles a comet-like footprint[208]. Thus, each position x experiences an increase of temperature up to the value taken in the

model, and subsequently a decrease, when the plasma jet passes a certain position y. As the model disregards this temperature variation, the computed depth is larger than seen in the experiment.

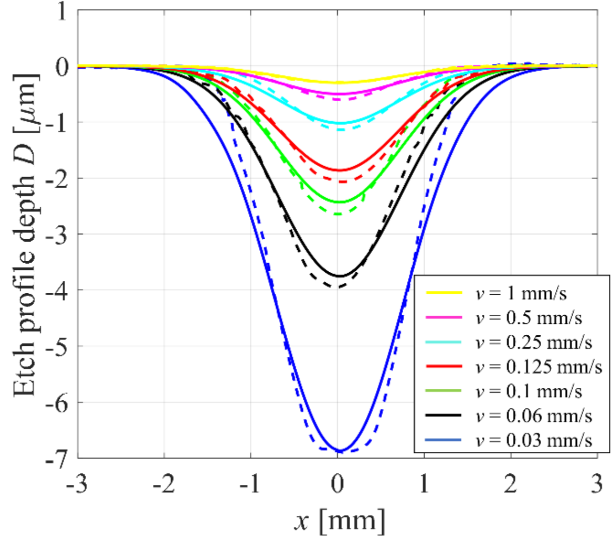

Figure 5.55 *Etch depth profiles obtained by experiments (dashed line) and the proposed Deal-Grove model (solid line) for groove etching on N-BK7 surface with different scan velocities v.*

Based on experimental and DG modeled etch profile depths of groove etching provided in **Figure 5.55**, the maximum values of residual layer thickness (or equivalently the maximum etching depth) are calculated (**Figure 5.56(a)**). The maximum value of surface temperature for each corresponding scan velocity v is shown as well. For the scan velocities v larger than 1.5 mm/s (i.e., dwell time $t < 1.1$ s), the residual layer thickness reveals the least dependence on scan velocity v; this behavior can be justified by less pronounced variation of surface temperature T_s.

For a deterministic process, the VRR as an averaged value is often used to scale the tool function. As in the current case, VRR depends on time or velocity, it can be obtained from **Equation 4.2**. To calculate VRR values, numerical integration was performed for the DG modeled and experimental etch profiles provided in **Figure 5.55**. The obtained results for different scan velocities v are presented in **Figure 5.56(b)**. With decreasing velocity, VRR increases and reaches to the maximum value 0.035 mm^3/min at $v = 1.5$ mm/s (i.e., $t = 1.1$ s). This behavior can be attributed to the effect of rising surface temperature. However, as the scan velocity becomes less than 1.5 mm/s (i.e., $t > 1.1$ s), VRR converts to a decaying nonlinear function. Apparently, the scan velocity $v = 1.5$ mm/s can be regarded as a turning point where below this velocity the growing residual layer reduces the etching rate and undermines the boosting effect of rising temperature. As shown in **Figure 5.56(b)**, this behavior is well predicted by the VRR values of the DG modeled etch profiles.

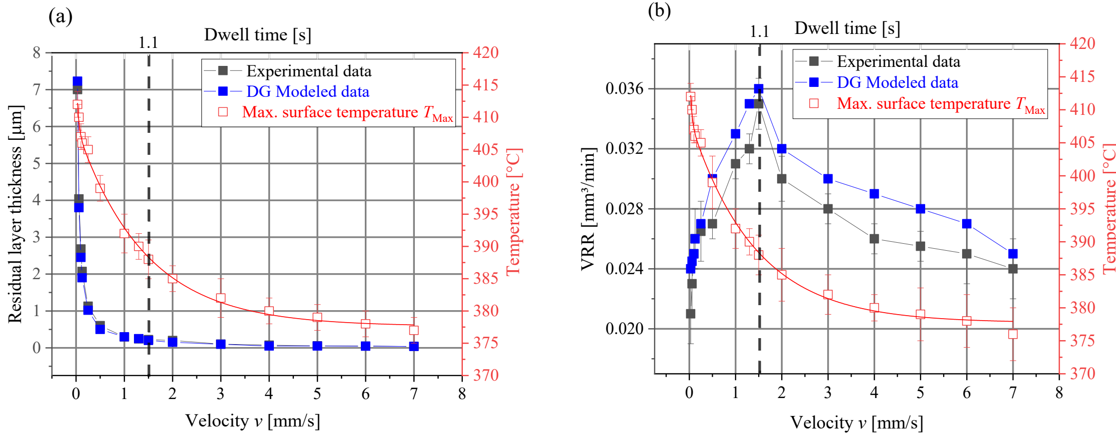

Figure 5.56 *(a) Illustration of residual layer thickness, and (b) volumetric removal rate VRR vs. scan velocity v obtained for the DG modeled and experimental groove etching. The corresponding surface temperature is shown in the graphs as well.*

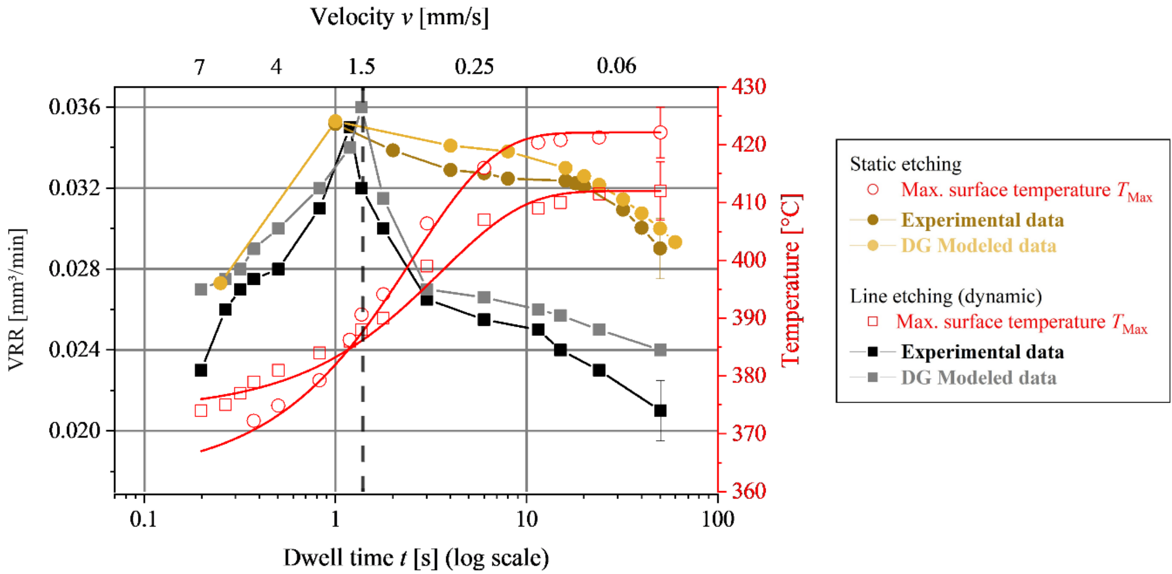

Figure 5.57 *Time-dependent volumetric removal rate VRR of experimental and DG modeled etch depth profiles obtained from both static and groove etchings. The corresponding surface temperature for static and dynamic etching is shown by red curves respectively with square and circle markers.*

The time dependent VRR values of experimental and modeled etch depth profiles obtained from both static and groove etchings (dynamic etching) are compared in **Figure 5.57**. Static etching shows higher values of VRR compared to groove etching because of its larger surface temperature distribution.

Noticeably, with increasing the dwell time t (or decreasing scan velocity), on the one hand, the temperature rises leading to higher etching rate; on the other hand, the undesirable effect of residual layer thickness becomes more destructive. Experimental as well as modeled data for both groove and static etchings shows that at low etching time $t < 1.1$ s (i.e., high scan velocity $v > 1.5$ mm/s) the effect

of surface temperature is dominant. However, at high etching time, the residual layer is thick enough to undermine the positive effect of temperature. The obtained results reveal that the proposed DG model approach can predict the effect of residual layer as well as surface temperature on the evolution of etching depths over dwell-time.

5.9 Laser-enhanced plasma jet machining (LE-PJM)

5.9.1 Cleaning techniques for surface residues on plasma etching tracks

The exclusive formation of components with chemical stoichiometry in the plasma-etched N-BK7 surface is rather unlikely due to the short plasma exposure time, the gradient of the species across the plasma beam, the diffusion of reactive species into the material, and the temperature dependence of the chemical etching reaction. Hence, because of the expected non-stoichiometry of formed reaction products, the incorporation of carbon compounds can also be assumed. Since these reaction products have different solubilities, a complete removal of them cannot be obtained by water-based solvent cleaning. To tackle this problem, it is proposed here to use a dry-cleaning with pulsed UV-laser irradiation for cleaning the PJM-treated surface from residual layer at the room temperature. This approach helps to establish a processing condition that is potentially more suitable for application in a deterministic processing scheme. To verify the optimality of the laser-enhanced (LE) cleaning approach, its performance is compared with the conventional water-based solvent cleaning.

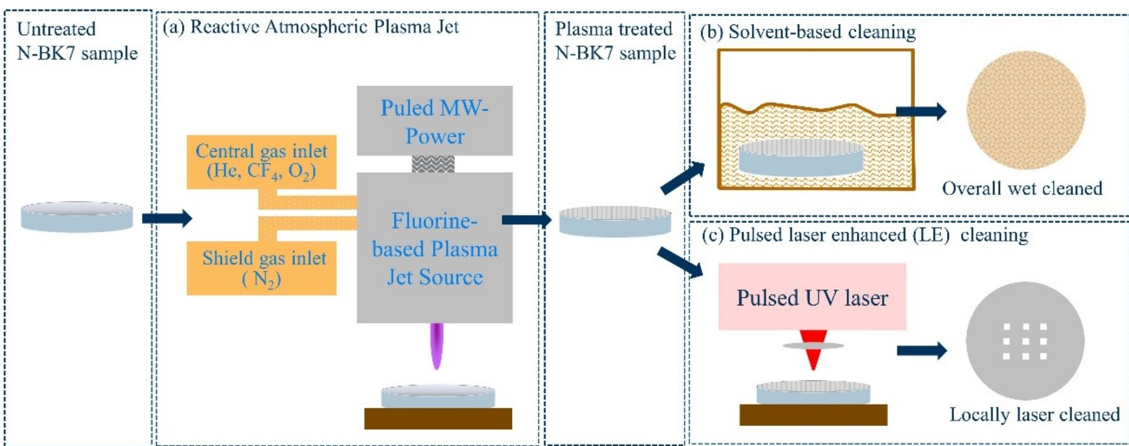

Figure 5.58 *Schema of the processing approach of PJM and subsequent cleaning by solvent-based method and laser-based processing.*

For solvent-based cleaning, as explained in **Section 4.4**, a 50% ethanol-water solution is applied followed by RCA cleaning procedure. The chemical composition of the N-BK7 surface was analyzed by XPS after etching and after a subsequent water/ethanol cleaning process, and the results are provided in **Figure 5.12**.

Laser-enhanced (LE) cleaning investigations were performed on the PJM-treated N-BK7 samples at the surface temperature T_h = 25 °C and P_M = 16 W. Within additional preliminary studies, it has turned out that a suitable laser fluence range is rather narrow so that the laser fluence was fixed to 2.8 J/cm². At lower fluences the residues could not be removed completely whereas at higher fluences laser-induced damage of the surface was observed. Finally, the pulse number was set to 200 to allow the complete removal of residues. **Figure 5.59** summarizes the obtained results. The white light interference microscopic image shown in **Figure 5.59(a)** represents the depth distribution of the plasma-etched track with the LE cleaned spot array in the center of the etched track. The cross-sectional profile of the plasma-etched track after and before LE cleaning presented in this figure were obtained after final removal of the remaining layers by water-based solvent. It can be seen from **Figure 5.59(b)** that the plasma-etched track has a lateral distribution function that exhibits a near-Gaussian form, where the maximum etching is at the center with the depth of about 400 nm. In this case, the N-BK7 etch profile formation is not significantly hindered by the residual layer as it is too thin, and hence an expected depth distribution according to the reactive particle-densities on the surface is achieved.

The optical microscopic images in **Figure 5.60** show the substrate surface after applying the PJM where LE cleaning is verified for a certain area before the residual layers have been cleaned by water-based solvent. The colors seen in the images are again assigned to an interference effect occurring at the residual layer of variable thickness formed during plasma etching. Since the plasma modified depth is more or less corresponding to the residual layer thickness, the distribution of resulting residual layer should follow nearly similar behavior to the etch profile depth. The characteristic features of the plasma etching such as the colors, the speckle appearance of the colors as well as the crack-like features are completely removed by LE cleaning.

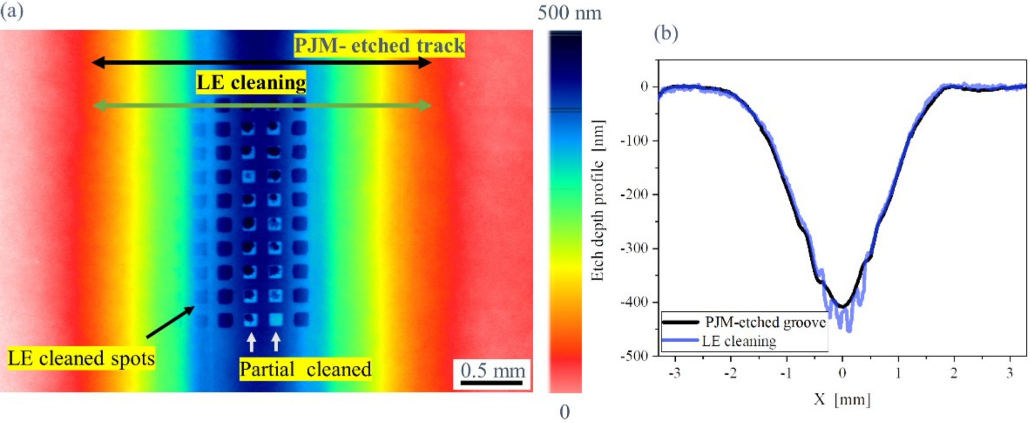

Figure 5.59 *(a) Topography of plasma-etched track with a pulsed laser-enhanced (LE) cleaning spot array in the center of the etched track measured with WLI microscope; (b) corresponding cross-sections resulting from applying PJM (black line) and after laser cleaning (orange line).*

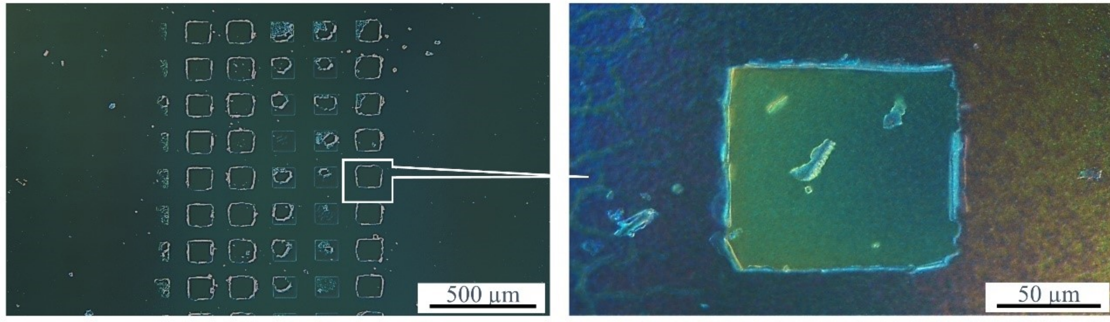

Figure 5.60 *Optical images plasma-etched surfaces of N-BK7 with laser-cleaned spots; (a) Array of laser spots, and (b) enlarged image of a laser irradiated area.*

However, typical laser ablation like features such as melting, re-deposited droplets or melt rims at the edges of the irradiated spots do not appear. The residual layer is removed but the glass surface is not ablated or damaged severely. The laser spots appear clean but feature some debris/fragments of the residual layer. In addition, at the edges of the laser-cleaned spots some flakes of the residual layer are still attached. In the optical as well as in the topographical images, some laser spots are covered with the residual layer but are no longer attached to the sample surface (**Figure 5.59** and **Figure 5.60**). These observations imply a layer detachment/spallation process rather than a laser ablation process. Laser spallation can be related to interface processes induced by a layer with a higher absorption and/or by laser-induced stress generation into the residual layer. The mechanism of the residual layer formation process suggests a continuous change of the composition of the residues at least in the vicinity of the glass surface. Therefore, as a first reason for the laser-induced residual layer spallation seems favorable. However, for laser-induced material processing, the thickness of the film has impact to the absorption as well as to the interface stress.

For the higher temperatures, which can be expected at the center of plasma-etched groove (**Figure 5.59**), a more stoichiometric and homogeneous residual layer is probably formed. The higher laser ablation resistance of these central residual films suggest that the film thickness is less important. The reason for the easy removal of the residual layers formed at lower temperatures occurring in the periphery of the plasma jet can be explained by a higher non-stoichiometry and various contaminations, e.g., carbon. Therefore, a higher absorption of UV laser photons can be expected, and the laser-induced heating of the residual layer will build up more stress in the film resulting in the observed delamination/spallation of the layer.

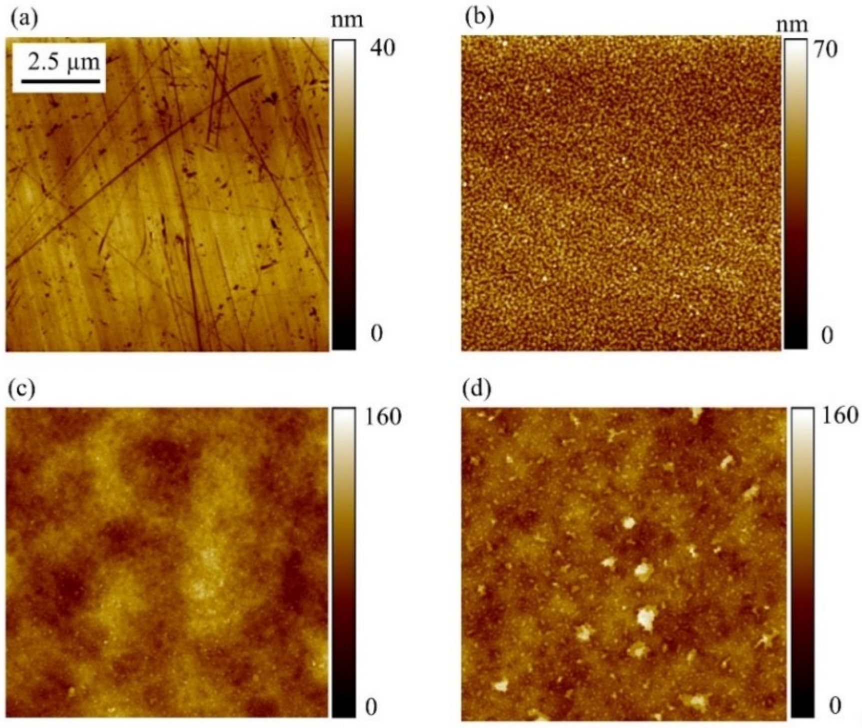

Figure 5.61 *Comparison of the surface morphology of plasma etched N-BK7 surfaces measured by AFM: (a) untreated surface, (b) etched surface with PJM without cleaning, (c) after water-based solvent cleaning and d after LE cleaning. The water and laser cleaned surfaces have similar roughness with values of 15 and 14 nm RMS, respectively.*

The morphology of plasma etched N-BK7 samples measured by atomic force microscopy (AFM) within a field of 10 x 10 µm² is shown in **Figure 5.61**. The RMS roughness values of untreated N-BK7 surface, etched surface with PJM without cleaning, after the water-based solvent and after LE cleaning are respectively 3.5 nm, 10.5 nm, 14 and 15 nm. In the case of LE cleaning the surface exhibits some debris particles while no signs of melting are observed. This supports also the conclusion that the residual film is removed by a delamination/spallation-like process. Hence, the roughness of the N-BK7 surface after LE cleaning and probably also for water cleaning is not related to the laser processing but it originates from the etching mechanism of the plasma on glass materials.

5.9.2 Proposed sequential approach for steady state etching

Reminding the discussion in **Section 5.4**, during plasma etching of N-BK7, the formed residual layer prevents the consistent transfer of active species and limits a prolonged and efficient deterministic freeform surface machining. As a solution for improving the processing condition, the plasma jet treatment at elevated surface temperature was proposed in **Section 5.6** to modify the residual layer properties obtaining an improved etching performance. However, surface machining at the room temperature is always favorable for optical applications as only little changes of material due to heating can be assumed. Therefore, instead of improving the properties of residual layer by elevated temperature

treatment for a steady state etching, it is proposed to use a sequential application of LE cleaning and PJM so called the LE-PJM method. In this method, at each processing cycle, first etching of N-BK7 glass is performed by PJM for short time, and subsequently the residues are selectively removed from the surface by pulsed UV laser irradiation (**Figure 5.62**). Both PJM and LE cleaning techniques are performed at atmospheric pressure and room temperature, and therefore can be combined in a hybrid system. Such a hybrid system can increase the efficiency including processing time and simultaneous surface machining. Nevertheless, it may also increase the complexity of manufacturing and setup. The aim of this work is to provide a proof of concept for realizing a hybrid system by using two available separate setups including PJM and LE cleaning.

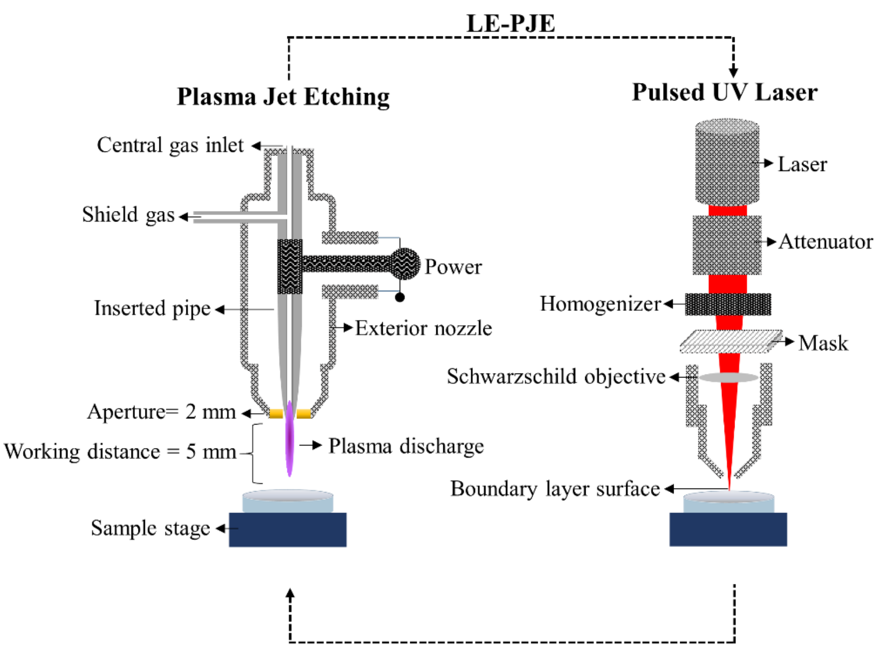

Figure 5.62 *Schematic of sequential laser enhanced plasma jet machining (LE-PJM).*

To evaluate the performance of the proposed approach, pulsed UV laser irradiation was applied sequentially to certain spots within an etched groove of the surface by PJM. In the following, the results are shown after applying the 3rd cycle of a LE-PJM process (**Figure 5.63**). The WLI image in **Figure 5.63(a)** gives an overview on the studied area; a section of the PJM etched groove with an array of laser spots are seen. The cross-sections along the marked lines are given in **Figure 5.63(c)** showing the depth distribution across the etched groove with and without additional intermediate laser cleaning. It is clearly seen that the etching depth within the laser clean spots (black line) is much larger than the etching depth without laser cleaning (blue line). The marked box in **Figure 5.63(a)** is enlarged in **Figure 5.63(b)** and provides a closer view to the array of laser-cleaned spots machined with the same parameter set. **Figure 5.63(d)** and **Figure 5.63(e)** present the x/y cross-sections of the laser processed array in a PJM-etched groove shown in **Figure 5.63(b)**.

The cross-section along the scan direction of the PJM (**Figure 5.63(d)**) shows (i) almost the same depth difference of the laser irradiated spots, and (ii) also demonstrates the less rough surface at the bottom of the laser exposed areas. This can be easily understood as for all laser spots the same parameters have been applied. Contrary to that, the depth across the PJM scan direction is reduced with increasing distance from the center of the PJM groove. Here, a depth difference (PJM vs LE-PJM) reduction appears despite the laser processing parameters are kept constant. One main result is that plasma jet etching depth of N-BK7 can be substantially increased with an intermediate laser cleaning step, and the roughness of the etched surface can be reduced. It should be noted that no characteristic melting features are observed so that ablation of the N-BK7 glass cannot be expected.

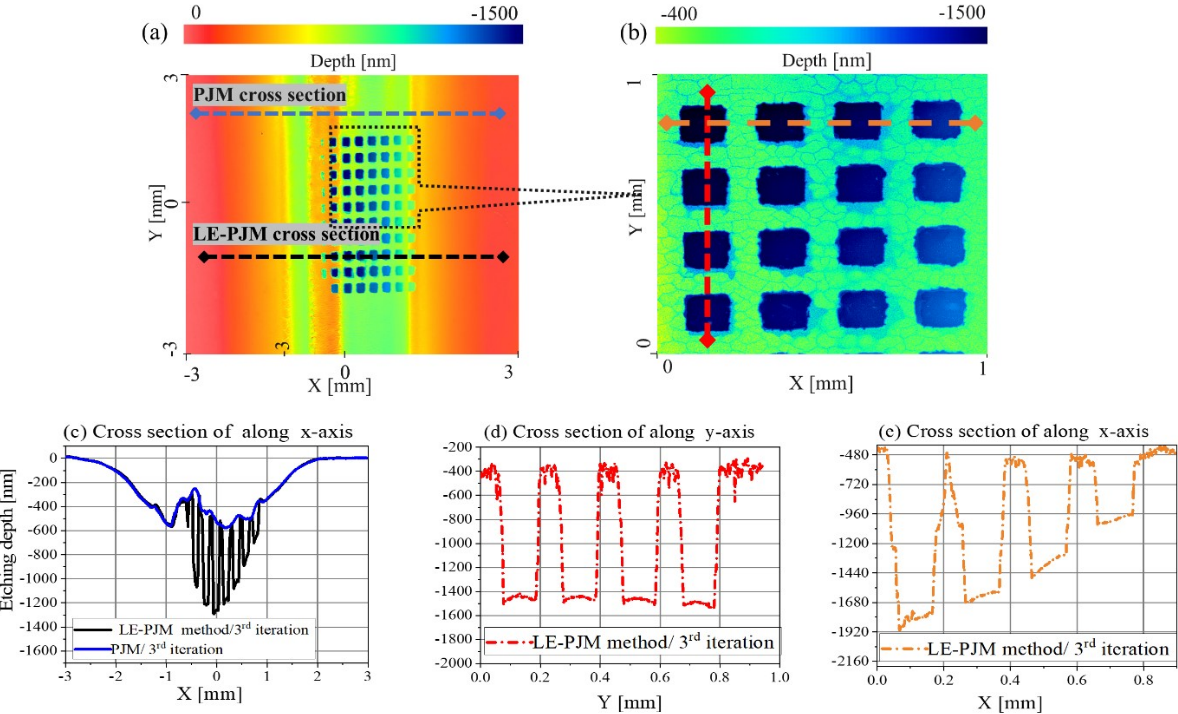

Figure 5.63 *Color coded depth images and etching depth profile of N-BK7 surface after processing 3 times with the LE-PJM approach. (a) Overview on plasma jet etched groove with an array of laser spots. (b) Enlarged image of the section bordered by the dashed box. (c) Depth profiles across etched groove by PJM with and without intermediate laser cleaning. (d/e) cross sections of the laser processed array along and across the etching groove by PJM. The data were taken with WLI after washing the residual layer.*

A closer view to the surfaces treated by PJM and LE-PJE technique after the 3rd cycle of etching is observed in **Figure 5.64** showing SEM images. The overview in **Figure 5.64(a)** reveals four local laser cleaning spots from residues.

The detailed images (**Figure 5.64(b)** to **Figure 5.64(c)**) show that the cracks are forming chip-like areas. The cracks seem to be built up in the residues layer and provide also new access to the fresh N-

BK7 surface. This might be also a reason for the uneven surface with an increased roughness. In comparison to the purely plasma etched surface (**Figure 5.64(a)**) the surface at the laser cleaned areas are much smoother (**Figure 5.64(c)**). The difference in height measured by WLIM (**Figure 5.63**) can be directly observed in **Figure 5.64(b)** as a step edge. The edge is rather steep in comparison to the expected optical resolution of the objective of approximately 1 µm. Hence, the mechanism of the transfer of the optical edge to the topographical edge should feature a rather high contrast.

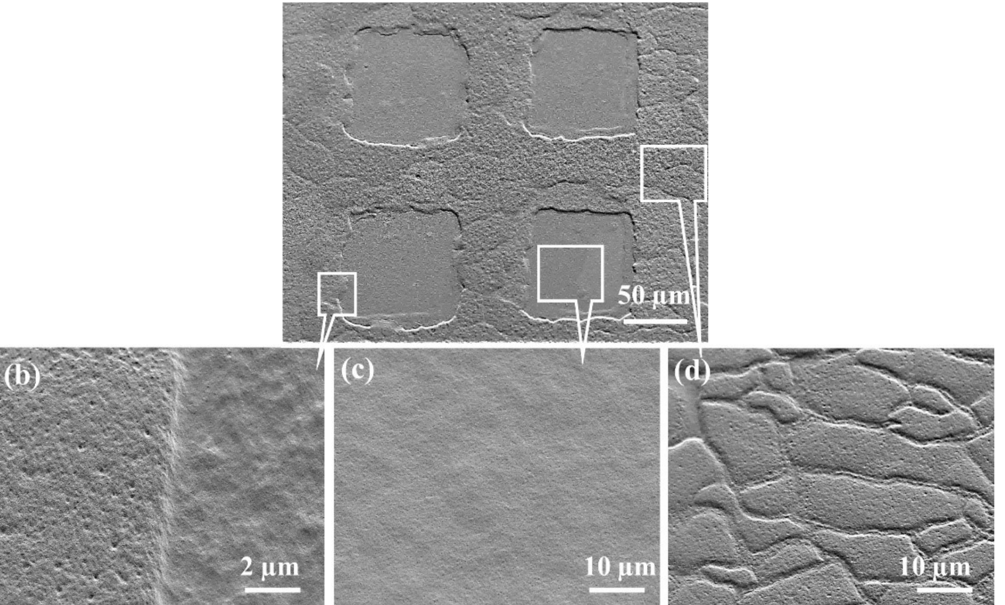

Figure 5.64 *SEM images of an N-BK7 surface after plasma jet etching and local laser cleaning from PJM-residues after 3 LE-PJM cycles: (a) Overview with marked areas of the other images; (b) edge of a laser cleaned area; (c) laser-cleaned area; and (d) reference surface that is only etched by PJM. The images were taken after washing the residual layer.*

The etching depth as well as the surface roughness is measured by using white light interference microscope for each cycle of a PJM and LE-PJM sequence up to five cycles. **Figure 5.65(a)** shows the computed etching rate based on the measured etch depth profile for PJM and LE-PJM methods in comparison. For PJM, the etching rate decreases significantly by additional sequential etching cycles due to the saturation of the etching depth after the first cycle. Particularly, the etching rate of the 1st PJM cycle is estimated to 275 nm/s but it decreases to 112 nm/s at the 5th cycle. However, by adding the laser cleaning step between subsequent PJM, the etching depth evolves significantly within each additional cycle of LE-PJM. In this case, the etching can be continued with almost constant rate. As it is shown in **Figure 5.65(a)**, the etching rate of LE-PJM method decreases only from 290 nm/s at 1st LE-PJM etching cycle to 270 nm/s at the 5th cycle.

The current studies suggest, however, that gentle saturation may also happen; the reason might be still remaining residues that cannot be cleaned up completely by the laser.

The qualitative dependence of N-BK7 surface roughness on the iteration number of process is illustrated in **Figure 5.65(b)**. At the beginning, the PJM process results into a relatively smooth surface with a roughness of Sq = 4.7 nm. With increasing the number of etching cycles, the measured surface roughness rises finally to Sq = 150 nm which is significantly larger than the original roughness of (i.e., Sq = 4 nm). This increase of the roughness can be related to the formation of a thick local residual layer that provides a masking layer for the PJM process. This masking layer is partly delaminated, porous, and not fully dense such that it causes at one hand a rough surface and on the other hand a locally different diffusion barrier for the etching fluorine, so that the etching of fresh N-BK7 is locally different.

However, by using the LE-PJM method, the measured surface roughness rises moderately to Sq= 17 nm, which is significantly lower than the high roughness achieved by PJM (i.e., Sq = 150 nm).

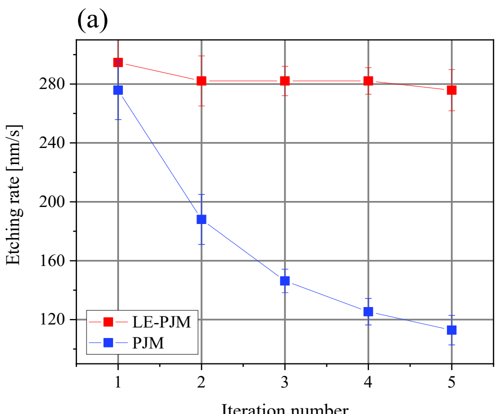

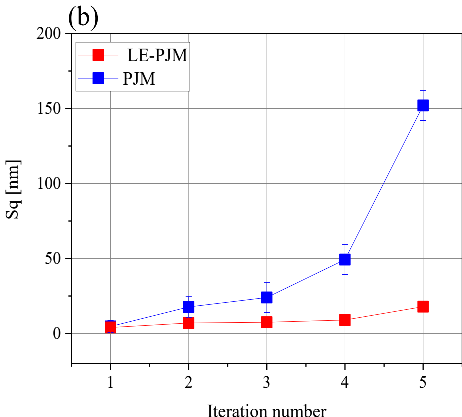

Figure 5.65 *Impact of the cycle number on variations of (a) etching rate, and (b) surface roughness after applying PJM and LE-PJM approaches. Results are extracted from WLIM measurements after washing the residual layer.*

Additionally, XPS analysis was carried out on the LE-PJM processed samples to investigate the efficiency of pulsed UV laser irradiation for removal of residual layer aiming to produce a clean optical surface. The amount of the chemical elements was determined from the measured XPS spectra and is shown in **Figure 5.66**. For comparison, the chemical compositions of the untreated and PJM-etched samples are provided in this figure.

The surface machined by LE-PJM method compared to PJM-processed surface contains a lower amount of metal compounds and fluorine but higher contents of silicon and oxygen. Nevertheless, the contents of silicon and oxygen for the surface processed by LE-PJM method are less than that of untreated surface. Obviously, fluorides are formed and accumulated at the N-BK7 surface because PJM removes SiO_2 preferentially while the original glass composition is not recovered.

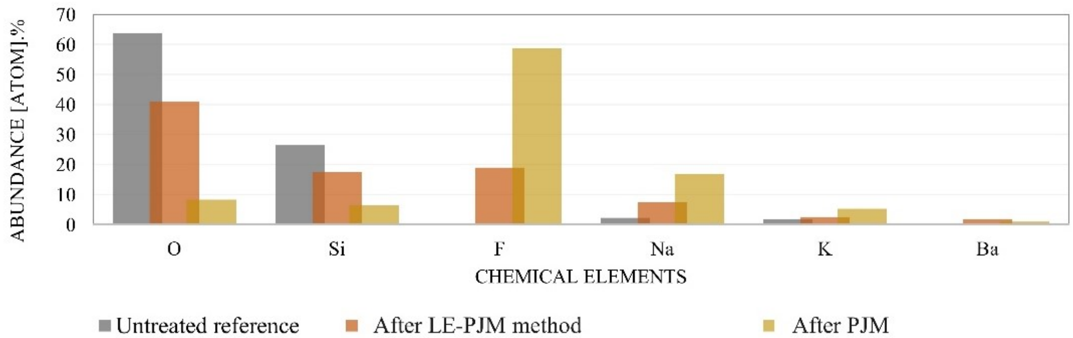

***Figure 5.66**: Chemical composition of the untreated, the PJM and the LE-PJM processed N-BK7 surfaces: (a) XPS spectra, and (b) elemental composition from XPS data.*

Due to the sequential execution of the reactive plasma jet etching and the pulsed laser processing, the mechanism of both processing steps can be discussed separately. However, it must be considered that the subsequent processing step is performed with a material that is modified by the previous process. Currently, it is not clear if within a sequence of LE-PJM cycles the properties of the material are changing due to side effects such as long-term plasma or laser modifications. After plasma etching, the glass surface features several modifications. The chemical composition of the uppermost layer is changed by the formation of additional compounds, e.g., fluorides, a depletion with silicon and boron occurs, and the surface morphology changes. All these modifications can influence the absorption of the pulsed UV laser beam and in general the interaction of the laser pulses with the near surface material. From **Figure 5.63** and **Figure 5.64**, it can be concluded that the removal process of the modified glass is rather a spallation process than a laser ablation. Such spallation or delamination process can be the result of a localized energy deposition at the interface of a film to a substrate or due to stress in the residues layer. This delamination/spallation process can be understood in relation to the differences with the thermal expansion processes of the glass and the week attachment of the residual layer to the N-BK7 material. Hence, any absorption near the etched surface by PJM (N-BK7, residues layer and nonstoichiometric interface in between) results in a fast heating and stress formation that can be relaxed by spallation of the residual layer. Considering the cracks in the residues layer one can understand that the cracks are a natural limit for a local spallation process as the stress relaxes also across the crack. It can be expected that the stress relaxes within a transition layer from the residues to the substrate as the found composition at LE-PJM is in between the substrate and the residual layer.

At the bottom of the laser cleaned spot still some roughness can be seen that resembles features of chemical etching. In consideration of the fluoride containing residues layer, the crack formation in this layer, the rather porous structure of the residues layer and the reduced density of the residual layer many processes with locally different activities are influenced, e.g., diffusion of reactive species and reaction products. For instance, porous layers can result in different densities of reactive species at the N-BK7

surface resulting in a locally different etching rate and therefore in the formation of an interface roughness.

Hence, already during the plasma etching the formation of a rough interface between the pristine glass and the modified N-BK7 layer can be expected. Furthermore, the inhomogeneous modification of the near surface range (composition, porosity, cracks, interface) will result in a different interaction of the pulsed laser with the modified surface. These differences also can cause roughness contributions as the remaining fluorides provide masking sides during the beginning of the next etching cycle.

6 Conclusions

In this thesis, extensive studies were conducted as key to overcoming several challenging limitations in applying fluorine-based plasma jet machining (PJM) for deterministic surface processing of optics made of complex glass composition like borosilicate crown glass known as N-BK7®. In this regard, the experimental results were analyzed, modeled by simulation algorithms, and compared with a pure silica optical glass (i.e., fused silica) as a benchmark case providing a comprehensive study and a valuable contribution to the state-of-the-art in manufacturing precision optical elements. The chosen materials in this work were restricted to fused silica and N-BK7 mainly due to their wide applications in various optical systems and their dissimilar chemical compositions causing different interactions with plasma. However, the developed concept and the proposed model can be extended to other optical glasses. The outcomes of this thesis thematically can be outlined as follows.

Investigation of fluorine-based plasma jet interactions with optical glass

The surface machining of N-BK7 with the fluorine-based microwave-driven PJM was investigated, and the etching performance was compared to fused silica to identify processing conditions that are potentially suitable for application in a deterministic processing scheme. The machining process relies on a purely chemical mechanism that converts the solid substrate surface to gaseous compounds without any contribution of energetic ions. The relationship between the plasma jet parameters and the etching performance of N-BK7 and fused silica was investigated concerning the effect of the surface temperature T_s, mean input power P_M, and the O_2 addition into the CF_4/He gas mixture. It was demonstrated that the increase of the surface temperature T_s and the mean input power P_M improves the etching performance. Moreover, it was shown that the addition of O_2 into the gas mixture is essential to suppress the polymerization of the CF_x radical on the surface and to achieve a continuous etching.

Freeform figuring of optical glass

The outcomes of this work revealed that, residual byproducts formed during freeform surface machining of N-BK7 cause a nonlinearly decreasing temporal behavior of the material removal rate. The features of the residues in the plasma-treated areas depend on their local thickness. Hence, under the un-preheating condition, PJM can be used only for the fine local figure correction with low-depth profiles (<100 nm). However, as the treatment time increases, the residues convert to a layer masking the surface underneath. Under this circumstance, the resulted removal rate decreases significantly compared to the approximate one in standard deconvolution model and causes an asymmetric etching profile.

Surface characterization of plasma-treated N-BK7

The exact chemical kinetics between plasma generated active particles and N-BK7 surface atoms are analyzed to understand the general principles of the process leading to a modified surface with respect to layer formation and material removal. Based on the findings in this thesis, the surface machining

process of N-BK7 relies on the generation of volatile compounds such as SiF_4(g), CO(g), CO_2(g), BF_3(g), B_2F_4(g) and COF_2 which is caused by the interaction between the surface and the fluoride atoms formed in the plasma jet. The desorption of these volatile compounds from the N-BK7 surface occurs spontaneously by thermal activation which results into the etched surface. However, non-volatile compounds form a residual layer on the surface which changes the typical Gaussian-like etch profile. Based on XPS and EDX/SEM analysis of the plasma-treated surface of N-BK7, it was shown that the residual layer consists of a variety of metal oxides and fluorides such as Na_2O, NaF, KF, BaF_2 and multi-element compounds like BaO_nF_m, BaF_6S, and SbO_nF_m as well as a fluoridic B compound (BF_4^-). However, XPS analysis also proved that most of these residual etching products are washable by a water/ethanol solution and can be thus removed. Furthermore, the chemical mechanism between plasma generated active particles and the N-BK7 surface atoms were described by evaluating lateral distributions of the residual layer during static footprint etching. The static footprint etching for different treatment times was performed to monitor the temporal evolution of etch profile depth. At the beginning of the process, although the residual layer is formed, it is thin enough to be penetrated by etching particles, and isotropic etching occurs. However, as the treatment time increases, the residual layer masks the surface underneath and prevents the attack of etching species. Thus, etching is inhibited leading to a flattened profile shape in the footprint center leading to a complex shaped profile.

Development of a model for numerical convolution

Static footprint etching for different treatment times were used to quantitatively determine the spatiotemporal behavior of the plasma tool function. Subsequently, a model was established that is capable to account for the spatiotemporal variations in the tool function for simulating a dynamic etching process. The comparison of simulated and measured groove and area profiles showed a high degree of agreement. The results prove the applicability of the model for the convolution operation of the tool function with a dwell time distribution predicting correct surface profiles. However, it turned out that the developing surface roughness is insufficient for freeform optical application due to the complex shape and waviness of plasma tool function. Hence, the process chain must comprise additional mechanical polishing steps to obtain sufficient optical quality in mid- and high-spatial roughness. Alternatively, improving the shape of plasma tool function through identifying the effective processing conditions (e.g., elevated surface temperature) was investigated for application in a deterministic processing scheme.

Improvement of the plasma jet machining process at elevated surface temperature

The investigations in this thesis revealed that plasma jet machining process at elevated surface temperatures can modify the footprint shape of the tool function, which allows to go one step forward in the production of freeform optics. In fact, the surface temperature T_s is a significant factor that affects not only the etching rate of N-BK7 but also the characteristic features of the formed residual layer in the etching zone such as thickness and structure. To evaluate the effects of substrate temperature on the

etching mechanism, the substrate was heated by a hot plate to an initial temperature T_h making the final value of the local surface temperature T_s equal to the sum of the plasma heat flow and the initial temperature T_h. It was shown that whenever the surface is adequately preheated to an initial temperature T_h = 350°C, a predictable static etching is achieved with a near-Gaussian shape profile depth, even at large values of dwell time. The main reason for this observation is the porous structure of the residual layer formed at this temperature level.
As dynamic etching is a prerequisite for a deterministic dwell-time based machining scheme, the initial temperature T_h= 350°C was chosen to perform a dynamic process on N-BK7 to assess the predictability of the etching profile for different plasma dwell times (or equivalently different velocities v of the plasma jet). It is concluded that at the initial temperature T_h= 350°C, a uniformly etched area with a predictable depth is achieved, even though a deep surface machining is performed. However, it was also shown that by reducing the scan velocity v or increasing dwell time t, the volumetric removal rate decreases, and the surface roughness increases. This roughness increase is much more moderate compared to the case of plasma etching with no preheated surface.

Modelling approaches to deterministic freeform surface machining

Based on etching profiles obtained from static etching tests under preheated condition, the spatiotemporal distribution of the removal rate function was determined in relation to the local etching depth. By use of the determined removal rate function, the numerical algorithm developed to calculate the local material removal in a dynamic etching process, i.e., groove etching or areal etching with a given local dwell time distribution was employed to simulate etching profiles. By comparison of simulated and experimental values for volumetric removal rates, the influence of the surface temperature was identified and compensated by a scaling function in order to improve the material removal prediction. Subsequently, a numerical algorithm inspired by the van Cittert deconvolution method was proposed to determine appropriate dwell-time distributions. A desired prescribed shape with a mathematical freeform prescription (PV of 1.00 µm) was modeled by using the proposed algorithm to show its applicability in a deterministic machining process. To validate the developed approach, the calculated dwell-time matrix was employed in a machining process. The experimental result revealed that the etched surface yields a PV of 1.01 µm and agrees well with the targeted surface form. Thus, the developed dwell-time calculation method was proven to be feasible for deterministic plasma jet-based surface machining of N-BK7.

Deal-Grove inspired model for simulating plasma etching

Due to various chemical interactions at the N-BK7–plasma interface on an atomic level, deriving a comprehensive physical/chemical model that includes all aspects in their complexity is challenging. In this thesis, the Deal-Grove (DG) model was exploited to interpret the interactions between plasma-generated active fluorine and the N-BK7 surface atoms. The DG model has been used conventionally to mathematically describe the growth of an oxide layer on the surface of silicon. Some behavioral

similarities that exist between the N-BK7 plasma etching and thermal oxidation of silicon are the reason for the choice of this model. It was shown that the plasma etching of N-BK7 is accomplished through three different phases that the plasma-generated fluorine atoms undergo, including diffusion from the surrounding gas to the surface, diffusion through the existing layer to the residue–substrate interface, and interactions with the substrate. Based on this inspiration, a mathematical model, that results in a simple formula, was developed for the prediction of the plasma etching of N-BK7. This model can describe the relationship between the residual layer thickness and plasma dwell-time with very good agreement. By estimation of the lateral distributions of the residual layer and etching depth, it was proven that the local etching depth is equivalent to the thickness of the residual layer. Finally, the derived model was extended to dynamic etching, such as groove and area etching of N-BK7, and the outcomes were compared with experimental results. By introducing such a model, it is possible to account for the effect of the residual layer and surface temperature to predict the growth of etching depths over dwell time. The results led to a better understanding of the plasma-surface interactions of N-BK7 and help to develop a predictable machining process for plasma-based freeform generation.

Laser-enhanced plasma jet machining (LE-PJM)

Ultra-precise surface machining for optical application requires a high topographical precision of the machining as well as a low surface roughness. Although PJM enables precise etching, it results in the development of a residual layer in the case of glass etching that causes the formation of roughness and influences the etching rate. The residual layer can be removed by using a water-based solvent exposing a rough glass surface. As an alternative, laser ablation cleaning, here by pulsed UV laser irradiation, was introduced to enable a dry removal of the residual layer. The topography and roughness analysis showed that the morphology and roughness of the surfaces after water and laser cleaning are similar. The mechanism of laser cleaning is not laser ablation as no indication for melting was found. Therefore, a stress-related spallation/delamination process can be considered as the dominating mechanism of laser cleaning of plasma etched N-BK7 glass. The dry removal of the residues layer can result in debris probably resulting from the redeposition of flakes from the residues film during the laser process.

It was proven, however, that the sequentially combined laser-enhanced plasma jet machining (LE-PJM) approach can overcome the deficiency of the pure PJM. Especially, the combination of plasma and laser tools can be beneficial for surface processing at room temperature without preheating the surface. A hybrid plasma-laser technique seems promising for the application in ultra-high precision machining and structuring of optical glass due to the low roughness, constant etching rate, and the possibilities for additional shaping of the tool function.

7 Outlook

This thesis focused on advanced strategies for extending the application of plasma jet machining to N-BK7 as an optical glass with complex chemical composition. Within the experimental results as well as the simulations, different aspects of this process were investigated and encountering challenges were discussed.

One of the solutions, proposed in this thesis, was to use semi-empirical quantitative as well as analytic models for describing non-linear characteristics of the tool function on N-BK7. As a future work, this solution and the developed framework can be extended to other optical glasses (e.g., lanthanum borate glass) which similarly to N-BK7 produce non-volatile compounds during plasma etching. In fact, for a new given optical element, relevant experimental data must be first collected under different conditions to find a process condition that is potentially suitable for deterministic processing scheme. Then, the model can be adapted correspondingly to derive the spatiotemporal variations in the tool function. After that, the estimated tool function can be used in the numerical algorithms, developed in this thesis, and an appropriate dwell-time distribution can be determined to obtain a pre-defined target removal.

Moreover, in this thesis, the Deal-Grove (DG) concept was exploited to derive a mathematical model that includes all aspects in the complexity of chemical interactions at the N-BK7–plasma interface on an atomic level. This model allows to predict the effect of the residual layer and surface temperature on the evolution of etch depth profiles over dwell time independently. The whole process is contained in two so-called Deal–Grove parameters, which are extracted from experimental data including local etching depth and surface temperature distribution that can be affected by surrounding environment. Thus, in a future work, the dependencies of Deal–Grove parameters on the environmental conditions like pressure and initial amount of fluorine gas can be investigated. Furthermore, the inspired DG model can be generalized for other optical glasses to realize the general principles of plasma jet-surface interactions that lead to a modified surface with respect to layer formation and material removal. For this purpose, the specific model parameters must be found through the fitting process.

As an alternative solution, in this thesis, the plasma and laser tools were used sequentially for surface machining of N-BK7 at room temperature without preheating the surface. However, due to the separate use of these tools, the sample needs to be moved between them which can result in an increasing processing time. Hence, as a future work, both plasma and laser systems can therefore be combined in a hybrid system since these tools are performed at atmospheric pressure. Such a hybrid system can be promising by increasing the efficiency with respect to processing time and simultaneous surface machining. Nevertheless, it may also increase the complexity of manufacturing and setup. Furthermore, by optimization of the PJM duration or laser cleaning step, the sequential use of the tools in the hybrid system can be more efficient.

8 References

1. Darrigol, O. *A history of optics from Greek antiquity to the nineteenth century*. Oxford University Press (2012).

2. Hoad, T.F. *The Concise Oxford Dictionary of English Etymology* (1993).

3. Zimmerman, A. Looking beyond history: the optics of German anthropology and the critique of humanism. *Studies in History and Philosophy of Science Part C: Studies in History and Philosophy of Biological and Biomedical Sciences*. **32**, 385-411 (2001).

4. Smith, A. M. What is the history of medieval optics really about?. *Proceedings of the American Philosophical Society*.**148**, 180-194 (2004).

5. El-Bizri, N. A philosophical perspective on alhazen's optics. *Arabic Sci. and Philos*. **15** , 189–218 (2005).

6. El-Bizri, N. In defence of the sovereignty of philosophy: al-baghdadi's critique of ibn al-haytham's geometrisation of place. *Arabic Sci. and Philos*. **17**, 57–80 (2007).

7. Simon, G. The Gaze in Ibn al-Haytham. *The Medieval History J*. **9**, 89–98 (2006).

8. Jackson, MW. *Spectrum of belief: Joseph von Fraunhofer and the craft of precision optics*. Mit Press (2000).

9. Henderson, K. Spectrum of Belief: Joseph von Fraunhofer and the Craft fo Precision Optics. *Contemporary Sociology.* **31**, 280 (2002).

10. Al-Amri, M. D., El-Gomati, M., Suhail Zubairy, M. *Optics in Our Time*. Springer Nature (2016).

11. Henry C. King . *The History of the Telescope*. Courier Dover Publications (2003).

12. Abbe, E., Lawson, H. (ed.). Translated by Fripp, H. E. A contribution to the theory of the microscope and the nature of microscopic vision. *Proceedings of the Bristol Naturalists' Society.* London, UK: Williams & Northgate. **1**, 200–261 (1876).

13. Feynman, R. QED: *The strange theory of light and matter*. Princeton University Press. Chap. **1**, p. 6. (1985).

14. Lipson, A., Lipson, S., Lipson, H. *Optical Physics*. Cambridge University Press (2010).

15. Taylor, N. *Laser: The inventor, the nobel laureate, and the thirty-year patent war.* Simon & Schuster (2000).

16. Shen, Y.R. *The principles of nonlinear optics*. New York, Wiley-Interscience (1984).

17. Fischer, R., Tadic-Galeb, B.,Yoder, P. *Optical system design* (2nd ed.). New York: McGraw-Hill. **8**, 179–198 (2008).

18. Ulrich, W., Rostalski, H. J., Hudyma, R. Development of dioptric projection lenses for deep ultraviolet litrogtaphy at Carl Zeiss. *J. microlittrography, microfabrication and microsystems*. **3**, 87-96 (2004).

19. Margaritondo, G., Rebernik, R. P. A simplified description of X-ray free-electron lasers. *J. of Synchrotron Radiation*. **18**, 101–108 (2011).

20. Weichmann, U. Light sources for small-elendue applications: a comparison of xenon and UHP lamps, *Proc. SPIE Int. Soc. Opt. Eng*. **5740**, 13 (2005).

21. Braunecker, B., Biber, M. Patent: Method for correcting optical wavefront errors and optical systems, such as a telescop, produced accordingly. US 6, 426, 834 (1999).

22. Baister. G. C. The ISLFE terminal development project results from the engineering breadboard model. 20th *AIAA international communication Satellite Systems Conference*, (2002).

23. Descartes, R., Dioptrique, *L. Paris*, (1638).

24. Gerchman, MC. *Production methods for fabricating aspheric optical elements*. PhD diss. University of Rochester (1978).

25. Faehnle, O. W., Van Brug, H. Novel approaches to generate aspherical optical surfaces. *SPIE*. **3782**, 170-180 (1999).

26. Braat, J. J., Smid, A., Winjakker, M. M. B. Design and production technology of replicated aspheire objectiv lenses for optical disk systems. *Applied Optics*. **24**. 1853(1985).

27. Randall, H.W., Brost, R.C., Strip, D.R., Sudol, R.J., Youngworth, R.N., McLaughlin, P.O. Considerations for tolerancing aspheric optical components. *Applied Optics*. **43**, 57-66 (2004).

28. Born, M., Wolf, E. *Principles of optices*, Cambridge University Press., Cambridge, (1999).

29. Rayleigh, L. Investigations in optics, with special reference to the spectroscope. *Philosophical Magazine*. **5**, 261–274 (1879).

30. Eppig, T., Scholz, K., Löffler, A., Messner, A., Langenbucher, A. Effect of decentration and tilt on the image quality of aspheric intraocular lens designs in a model eye. *Journal of Cataract and Refractive Surgery*. **35**, 1091–1100, (2009).

31. Pohl, D. W., Denk, W., Lanz, M. Optical stethoscopy: Image recording with resolution λ/20. *Applied Physics Letters*. **44**, 651 (1984).

32. Yagci, R., Uzun, F., Acer, S., Hepsen, I. F. Comparison of visual quality between aspheric and spherical IOLs. *European J. of Ophthalmology*. **24**, 688–692 (2014).

33. Santhiago, M. R., Netto, M. V., Barreto Jr. J. Wavefront analysis, contrast sensitivity, and depth of focus after cataract surgery with aspherical intraocular lens implantation. *American J. of Ophthalmology*. **149**, 383–389 (2010).

34. Litin, G. *Technische optik in der praxis*. Edited by Gerd Litfin. Springer, (2005).

35. Guenther, R. *Modern optics*. Cambridge: John Wiley & Sons Inc. 130 (1990).

36. Rajabi, M. T., Korouji, S., Farjadnia, M. Higher order aberration comparison between two aspherical intraocular lenses: MC6125AS and Akreos advanced optics. *International J. of Ophthalmology*. **8**, 565–568 (2015).

37. Bliedtne, J. *Optiktechnologie. Grundlagen-Verfahren- Anwendungen*. Carl Hanser Verlag GmbH Co KG (2008).

38. Dereniak, E. L., Teresa, D. D. *Geometrical and Trigonometric Optics*. Cambridge: Cambridge University Press., (2008).

39. Gullstrand, A. Allgemeine theorie der monochromat. aberrationen, etc. *Annalen der Physik. Upsala*. **18**, 941 (1905).

40. Smith, T. T. Spherical aberration in thin lenses. *Scientific Papers of the Bureau of Standards*. **18**, 559–584 (1922).

41. Thibos, L. N., Bradley, A., Still, D. L., Zhang, X., Howarth, P. A. Theory and measurement of ocular chromatic aberration. *Vision Research*. **30**, 33–49 (1990).

42. Amako, J., Nagasaka, K., Kazuhiro, N. Chromatic-distortion compensation in splitting and focusing of femtosecond pulses by use of a pair of diffractive optical elements. *Optics Letters.* **27**, 969–71 (2002).

43. Marimont, D. H., Wandell, B. A. Matching color images: The effects of axial chromatic aberration. *J. of the Opt. Soc. of America A*. **11**, 3113 (1994).

44. Pedrotti, F., Pedrotti, L., Bausch, W., Schmidt, H. *Optik für Ingenieure*. Springer Berlin Heidelberg (2005).

45. Bryner, J. Key to all optical illusions discovered. *Live Science* (2008).

46. Ives, H.E. An Introduction to the Theory of Optics. 341-343 (1925).

47. Braunecker, B., Hentschel, R., Tiziani, H. J. *Advanced optics using aspherical elements*. **173**, Spie Press (2008).

48. Tikhonravov, A., Trubetskov, M. Computational manufacturing as a bridge between design and production. *Appl. Opt*. **44**, 6877- 6884 (2005).

49. Forbes, G. Shape specification for axially symmetric optical surfaces. *Opt. Express*. **15**, 5218–5226 (2007).

50. Spur, G., Stöferle, T. Handbuch der Fertigungstechnik, Band 3, Spanen. *Carl Hanser Verlag München* (1980).

51. George, R. W., Michaud, L. L. Optical fabrication by precision electroform, in Current Developments in Optical Engineering II. *Proc. SPIE* 818 (1987).

52. Ahmad, A. *Optical Fundamentals*, in Handbook of Optomechanical Engineering. CRC Press, Boca Raton (1997).

53. Cooke, F. *Optics cooke book*, Washington (1991).

54. Williamson, R., Wook Kim, W., Rascher, R. Optical manufacturing and testing XII. *Proceedings of SPIE*. **10742** (2018).

55. Wilson, A., Hua, H. Design and demonstration of a vari-focal optical see-through head-mounted display using freeform Alvarez lenses. *Opt. Express* **27**, 15627–15637 (2019).

56. Arnold, J. B., Sladky, R. E., Steger, P. J., Woodall, N. D., Saito, T. Machining nonconventional-shaped optics. *Optical Engineering*. **16**, 347-354 (1977).

57. Bajuk, D. J. Computer controlled generation of rotationally symmetric aspheric surfaces. *Optical Engineering*. **15**, 401-406 (1976).

58. Hoshi, H., Taniguchi, N., Morishima, H., Akiyama, T., Yamazaki, S., Okuyama, A. Off-axial HMD optical system consisting of aspherical surfaces without rotational symmetry. *Proc. SPIE*. **2653**, 234–242 (1996).

59. Braunecker, B., Hentschel, R., Tiziani, H. J. Advanced optics using aspherical elements. Spie Press, 173(2008).

60. Taylor, J. S., Piscotty, M., Lindquist, A. Trends in optics and photonics, fabrication and testing of aspheres. *J. of the Opt. Soc. of America A*., Washington, DC (1999).

61. Geyl, R., Ruch, E., Bourgois, R., Mercier-Ythier, R., Leplan, H., Riguet, F. Freeform optics design, fabrication and testing technologies for Space applications. *International Conference on Space Optics -ICSO* 11180 (2019).

62. Birchall, H. J. Lens of variable focal power having surfaces of involute form, *U.S. Patent* 2, 475, 275 (1949).

63. Wilson, A., Hua, H. Design and demonstration of a vari-focal optical see-through head-mounted display using freeform Alvarez lenses. *Opt. Express* **27**, 15627–15637 (2019).

64. Nakano, T., Tamagawa,Y. Configuration of an off-axis three-mirror system focused on compactness and brightness. *Appl. Opt*. **44**, 776–783 (2005).

65. Fuerschbach, K., Davis, G. E., Thompson, K. P., Rolland, J. P. Assembly of a freeform off-axis optical system employing three phi-polynomial Zernike mirrors. *Opt. Lett*. **39**, 2896–2899 (2014).

66. Cheng, D., Wang, Y., Xu, C., Song, W., Jin, G. Design of an ultra-thin near-eye display with geometrical waveguide and freeform optics. *Opt. Express,* **22**, 20705–20719 (2014).

67. Benítez, p., Miñano, J. C., Grabovickic, D., Zamora, P., Buljan, M., Narasimhan, B., Nikolic, M. Freeform optics for virtual reality applications, in optical design and fabrication. *OSA Technical Digest*, *J. of the Opt. Soc. of America A*. (2017).

68. Ries, H., Muschaweck, J. Tailored freeform optical surfaces. *J. Opt. Soc. Am. A* **19**, 590–595 (2002).

69. Greivenkamp, J.E. Field Guide to Geometrical Optics. *SPIE* (2003).

70. Riedl, M. Diamond turned diffractive optical elements for the infrared. *Proc. SPIE*. **2540**, 257 (1995).

71. O'Shea, D., Suleski, T., Kathman, A., Prather, D. Diffractive optics: design, fabrication, and test. *SPIE* (2003).

72. Behrmann, G., Bowen, J. The influence of temperature on diffractive lens performance. *Appl. Opt.*, **32**, 2483–2489 (1993).

73. Arieli, Y., Noach, S., Ozeri, S., Eisenberg, N. Design of diffractive optical elements for multiple wavelengths. *Applied optics*. **37**, 6174-6177(1998).

74. Fu, Y. Kok, N, Bryan, A. Hybrid micro-diffractive-refractive optical element with continuous relief fabricated by focused ion beam for single-mode coupling. *Appl. Opt*. **40**, 5872–5876, (2001).

75. Wang, C., Chan, Y.C., Zhao, L.P., Li, N. Design of diffractive optical elements array with wide field of view for integration with photodetectors. *Opt. Commun*. **195**, 63–70 (2001).

76. Baumer, S. *Handbook of plastic optics*. 2nd Edition, Wiley-VCH (2010).

77. Sparrold. S. Placement of aspheres in an optical system to increase optical performance. *NASA Tech Briefs*, **34**,48–52 (2010).

78. Daly, D., Stevens, R.F., Hutley, M.C., Davies. N. The manufacture of micro lenses by melting photoresist. *Proceedings of seminar Microlens Arrays, IOP Short Meeting* **30**, 23–34 (1991).

79. Borrelli, N. F. *Microoptics technology: fabrication and applications of lens arrays and devices*. CRC Press (2017).

80. Veldkamp,W. B., McHugh, T. J. Binary optics. *Scientific American*. **266**, 50–55, (1992).

81. Popovic, CD., Sprague, RA. Techniques for monolithic fabrication of microlens arrays. *Appl. Opt*. **27**, 1281–1284 (1988).

82. Gratzke, A. Projektarbeit im Masterstudiengang Laser und Optotechnologien der Fachhochschule Jena (2005).

83. Smith, W. J., Fischer, R, E., Price, W, H., Smith, W. J. Fundamentals of establishing an optical tolerance budget. Geometrical Optics, *Proc. SPIE* **531** (1985).

84. Parks, R. E., Fischer. R. E. Optical component specifications. *International Lens Design Conference, Proc. SPIE* **237** (1980).

85. Parks, R. E., Smith, W. J., Fischer, R. E. Optical specifications and tolerances for large optics. *Optical Specifications: Components and Systems, Proc. SPIE* **406** (1983).

86. Schuster, K.H. Projection objective for microlithography. US Patent 6, 801,364 B2.

87. Rostalski, H.J., Hudyma, R., Ulrich. Refractive projection objective. Patent WO / 075049 A2 (2003).

88. Schuster,K.H., et al. Microlithographic reduction objective, projection exposure equipment and process. US Patent 6,349,005 B1.

89. Wilson, R. N. *Reflecting telescope optics II: manufacture, testing, alignment, Modern Techniques*. Springer Science & Business Media (2013).

90. Bauer, H. Kraftfahrzeugtechnik- Lichttechnik und Scheibenreinigung am Kraftfahrzeug (2002).

91. Keuper, M.H. et al. RGB LED Illuminator for Pocket-Sized Projectors, *SID Symposium Digest*. **35**, 1078 (2002).

92. Weichrnan, L. S., Dickey, F, M., Shagam, R, N. Beam Shaping Element for Compact Fiber Injection Systems. *Proc. SPIE*. **3929** (2000).

93. Rhodes, P, W., Shealy, D. L. Refractive optical systems for irradiance redistribution of collimated radiation: their design and analysis. *Appl. Opt*. **19**, 3545-3553 (1980).

94. Huang, Z., Kim, K. J. Review of x-ray free-electron laser theory. *Physical Review Special Topics: Accelerators and Beams*. **10**, 034801 (2007).

95. Stowers, I.F., et al. Review of precision surface generation processes and their potential application to the fabrication of large optical components. *Advances in Fabrication and Metrology for Optics and Large Optics. Proc. SPIE* **966** (1988).

96. Blalock, T., Medicus, K., Nelson, J. Fabrication of freeform optics. *Optical Manufacturing and Testing XI*, *Proc. SPIE.* **9575** (2015).

97. Parks, R. E. Overview of optical manufacturing methods. *Contemporary Methods of Optical Fabrication, Proc. SPIE* ***306*** (1981).

98. Sanger, G. M. The Precision Machining of Optics. *Applied Optics and Optical Engineering*, *Academic Press, Inc*, **10** (1987).

99. Fang, F. Z., Zhang, X. D., Weckenmann, A., Zhang, G. X., Evans, C. Manufacturing and measurement of freeform optics. *CIRP Annals.* **62**, 823–846 (2013).

100. Weber, MJ. *Handbook of optical materials*. CRC press. **19** (2002).

101. Jones, R. A. Grinding and polishing with small tools under computer control. *Optical Engineering*, **18**, 390-393 (1979).

102. Korhonen, T., Lappalainen, T. Computer-controlled figuring and testing. *Advanced Technology Optical Telescopes. Proc. SPIE* **1236** (1990).

103. Ohmori, H. Ultra precision Grinding of Optical Materials and Components Applying ELID (Electrolytic In-Process Dressing). *International Conference on Optical Fabrication and Testing, Proc. SPIE* **2576**, (1995).

104. Zschommler, W. Precision Optical Glass working, *Proc. SPIE* **472** (1984).

105. Hoff, A. M., Ning, X., Hebert, R. T. Basic considerations for injection molding of plastic optics. *Design, Fabrication, and Applications of Precision Plastic Optics, Proc. SPIE* **2600** (1995).

106. Bäumer, S. *Handbook of Plastic Optics*, Wiley- VCH (2010).

107. Rosato, D. V., Rosato, M. G. *Injection molding handbook*. Springer Science & Business Media (2012).

108. Klocke, F., Pongs, G. Precision glass molding of optical components. *WGP Annals*. **11**, 21-24(2004).

109. Aquilina, T., Riedl, M. J. Characterization of Molded Glass and Plastic Aspheric Lenses. *Replication and Molding of Optical Components, Proc. SPIE* **896** (1988).

110. Cheung, F., Ho, L., Liu, M.Y., Lee, B.W. A novel multi-jet polishing process and tool for high-efficiency polishing, *Int. J. Mach. Tool Manufact*.**115**, 60–73 (2017).

111. Heynacher, E. Aspheric optics- How they are made and why they are needed. *Physics in Technolog*, **10**, 124-131(1979).

112. Fähnle, O. W., and Van Brug, H. Nobel Approaches to Generate Aspherical Optical Surfaces. *Optical Manufacturing and Tesing III. SPIE*, **3782,** 170-180 (1999).

113. Bifano, T. G., Dow,T. A., Scattergood, R.O. Ductile-regime grinding of brittle materials: Experimental results and the development of a model. *Advances in Fabrication and Metrology for Optics and Large Optics, Proc. SPIE*, **966**, (1988).

114. Gerchman, M. Specifications and manufacturing considerations of diamond machined optical components. *Optical Component Specifications for Laser-Based Systems and Other Modern Optical Systems*, *Proc. SPIE* **607** (1986).

115. Golini, D., Jacobs, S. D. Transition between brittle and ductile mode in loose abrasive grinding. *Advanced Optical Manufacturing and Testing*, *Proc. SPIE* **1333** (1990).

116. Golini, D., Jacobs, S. D. The Physics of Loose Abrasive Micro grinding. *Applied Optics*. **30**. 2761 – 2777 (1991).

117. Martin, H. M, Anderson, D. S., Angel, J. R., Nagel, R. H., West, S. C., Young, R. S. Progress in the stressed-lap polishing of a 1.8-m f/1 mirror. *Advanced Technology Optical Telescopes IV, Proc. SPIE* **1236** (1990).

118. Koch, N.E. *Technologie zum Schleifen asphärischer optischer Linsen*. Thesis RWTH Aachen (1991).

119. Klinger, C. Vibe: A New Process For High Speed Polishing Of Optical Elements. *International Society for Optics and Photonics*, **10316** (2007).

120. Karow, H. H. *Fabrication Methods for Precision Optics*. Wiley, New York, (1993).

121. Köhler, C., Schindler, E. Mastering the Art of Freeform Optics Manufacturing. *OptoNet Workshop: Ultra Precision Manufacturing of Aspheres and Freeforms*, Jena (2016).

122. Giggel, V. in Process chain for ultra precise freeform optic components. *OptoNet Workshop: Ultra Precision Manufacturing of Aspheres and Freeforms* (2010).

123. Preston, F. W. The theory and design of plate glass polishing machines. *J. Soc. Glass Technol*. **11** (1927).

124. Pollicove, H. M. Innovations in deterministic optical manufacturing processes. *Proc. SPIE* **4921**, 16-19 (2002).

125. Pan, R., Zhong, B., Chen, D., Wang, Z., Fan, J., Zhang,C., Wei, S. Modification of tool influence function of bonnet polishing based on interfacial friction coefficient, *Int. J. March. Tool Manufact*. **124**, 43–52 (2018).

126. Wang, C. j., Cheung, C.F., Ho, L.T., Liu, M.Y., Lee, W. B. A novel multi-jet polishing process and tool for high-efficiency polishing, *Int. J. Mach. Tool Manufact*. **115**, 60–73 (2017).

127. Kansal, H., Singh, A.K., Grover,V. Magnetorheological nano-finishing of diamagnetic material using permanent magnets tool. *Precis. Eng*. **51** (2018).

128. Marimuthu, A., Triantaphyllou, M., Antar, D., Wimpenny, H., Morton, M. Laser polishing of selective laser melted components, Int. J. Mach. Tool Manufact. **95**, 97–104 (2015).

129. Arnold, T., Pietag, F. Ion beam figuring machine for ultra-precision silicon spheres correction, *Precis. Eng.* **41**, 119–125 (2015).

130. Porsching, T. A., Hall, C. A. Approximation methods and the computer numerically controlled fabrication of optical surfaces. *Advanced Optical Manufacturing and Testing II; Proc*. SPIE, **1531**, 205-215 (2001).

131. Song, C., Dai, Y., Peng, X. Model and algorithm based on accurate realization of dwell time in magnetorheological finishing. *Appl. Optic*. **49**, 3676–3683 (2010).

132. Wang, C., Yang, W., Wang, Z., Yang, X., Hu, C., Zhong, B., Guo, Y., Xu, Q. Dwell-time algorithm for polishing large optics. *Appl. Optic.* **53**, 4752–4760 (2014).

133. Wilson, S.R., McNeil, J.R. Neutral ion beam figuring of large optical surfaces. *Curr. Dev. Opt. Eng* (1987).

134. Jones,R.A. Optimization of computer controlled polishing. *Appl. Optic.* 16, 218–224, (1977).

135. Dong, Z., Cheng,H. Toward the complete practicability for the linear-equation dwell time model in subaperture polishing. *Appl. Optic.* **54**, 8884–8890 (2015).

136. Yang, M. Dwell time algorithm for computer-controlled polishing of small axis-symmetrical aspherical lens mold. *Opt. Eng.* **40** (2001).

137. Carnal, C. L., Egert, C. M., Hylton, K. W. Advanced matrix-based algorithm for ion-beam milling of optical components. *Curr. Dev. Opt. Des. Opt. Eng. II*, (1992).

138. Arnold, T., Boehm, G., Eichentopf, I., Janietz, M., Meister, J., Schindler, A. Plasma Jet Machining:A novel technology for precision machining of optical elements. *Vakuum in Forschung und Praxis,* **22**, 10-16 (2010).

139. Dong, Z., Cheng, H., Tam, H.Y. Robust linear equation dwell time model compatible with large scale discrete surface error matrix. *Appl. Optic.* **54**, 2747–2756 (2015).

140. Zhu,W., Beaucamp, A. Zernike mapping of optimum dwell time in deterministic fabrication of freeform optics, *Optic Express*, **27**, 28692–28706 (2019).

141. Hu, H., Dai, Y., Peng, X. Restraint of tool path ripple based on surface error distribution and process parameters in deterministic finishing, *Optic Express.* **18**, 22973–22981 (2010).

142. Han, Y., Zhang, L., Fan, C., Zhu, W., Beaucamp, A. Theoretical study of path adaptability based on surface form error distribution in fluid jet polishing, *Appl. Sci.* **8**, 1814 (2018).

143. Cheung, C. F., Wang, C., Ho, L.T., Chen, J. Curvature-adaptive multi-jet polishing of freeform surfaces, *CIRP Ann* **67**, 357–360 (2018).

144. Yang, Y., Li, H., Liao, Z., Axinte, D., Zhu, W., Beaucamp, A. Controlling of compliant grinding for low-rigidity components. *Int. J. Mach. Tool Manufact.* **152**, 103543 (2020).

145. Meister, J., Arnold. T. New process simulation procedure for high-rate plasma jet machining. *Plasma Chem. Plasma Process*. **31**, 91-107(2010).

146. Leech, W. Reactive ion etching of quartz and silica-based glasses in CF 4/CHF3 plasmas. *Vacuum*. **55**, 191, 1999,

147. Hana, Y., Zhu, W., Zhang, L., Beaucamp, A. Region adaptive scheduling for time-dependent processes with optimal use of machine dynamics. *International Journal of Machine Tools and Manufacture*. **156**, 103589 (2020).

148. Ihlemann, J., Muller, S., Pischmann, S., Schafer, D., Wei, M., Li, J., Herman, P.R. Fabrication of submicron gratings in fused silica by F-2-laser ablation*. Appl. Phys. A.* **76**, 751-753 (2003).

149. Heidrich, S., Willenborg, E., Weingarten, C., Temmler, A. Laser polishing and laser form correction of fused silica optics. *Materialwiss. Werkstofftech*. **46**, 668–674 (2015).

150. Kautek, W., Kruger, J., Lenzner, M., Sartania, S., Spielmann, C., Krausz, F. Laser ablation of dielectrics with pulse durations between 20 fs and 3 ps. *Appl. Phys. Lett.* **69**, 3146-3148 (1996).

151. Perry, M.D., Stuart, B.C., Banks, P.S., Feit, M.D., Yanovsky, V., Rubenchik, A.M. Ultrashort-pulse laser machining of dielectric materials. *J. Appl. Phys.* **85**, 6803-6810 (1999).

152. Wang, J., Niino, H., Yabe, A. Micromachining of quartz crystal with excimer lasers by laser-induced backside wet etching. *Appl. Phys. A,* **69**, S271-S273 (1999).

153. Böhme, R., Zimmer, K. Low roughness laser etching of fused silica using an adsorbed layer. *Appl. Surf. Sci*. **239**, 109-116 (2004).

154. Hopp, B., Vass, C., Smausz, T. Laser induced backside dry etching of transparent materials. *Appl. Surf. Sci.* **253**, 7922-7925 (2007).

155. Böhme, R., Zimmer, K. Effects of halogenated organic solvents at laser-induced backside wet etching. *Appl. Phys. A*. **83**, 9-12 (2006).

156. Bäuerle, D. *Laser Processing and Chemistry*. Springer Science & Business Media, 2013.

157. Gerhard, C., Roux, S., Bruckner, S., Wieneke, S., Viol, W. Low-temperature atmospheric pressure argon plasma treatment and hybrid laser-plasma ablation of barite crown and heavy flint glass. *Appl. Opt*. **51**, 3847-3852 (2012).

158. Tasche, D., Gerhard, C., Ihlemann, J., Wieneke, S., Viol, W. The impact of O/Si ratio and hydrogen content on ArF excimer laser ablation of fused silica. *J Eur Opt Soc-Rapid*. **9** (2014).

159. Gerhard, C., Dammann, M., Wieneke, S., Viol, W. Sequential Atmospheric Pressure Plasma-Assisted Laser Ablation of Photovoltaic Cover Glass for Improved Contour Accuracy. *Micromachines-Basel*. **5**, 408-419 (2014).

160. Blattmann, V., Trusheim, D. Hybrid laser-etching-process for wafer texturing, Enrgy Proced. **77**, 766-773 (2015).

161. Matthews, M. J., Yang, S. T., Shen, N., Elhadj, S., Raman, R. N., Guss, G., Bass, I. L., Nostrand, M. C., Wegner, P. J. Micro-shaping, polishing, and damage repair of fused silica surfaces using focused infrared laser beams. *Adv. Eng. Mater.* **17**, 247–252 (2015).

162. Choi, H. K., Ahsan, M.S., Yoo, D., Sohn, I.B., Noh, Y.C., Kim, J.T., Jung, D., Kim, J. H., Kang, H. M. Formation of cylindrical micro-lens array on fused silica glass surface using CO_2 laser assisted reshaping technique. *Opt. Laser Technol.* **75**, 63–70 (2015).

163. Taylor, L.L., Qiao, J., Qiao, J. Optimization of femtosecond laser processing of silicon via numerical modeling. *Opt. Mater. Express* **6**, 2745–2758 (2016).

164. Shershnev, E. B., Yu,V., Nikitjuk, S., Sokolov, I. Shershnev, A. E. Study of laser beam polishing of quartz glass. *Prob. Fiz. Mate. Tekh*. **4**, 45–49 (2015).

165. Heptonstall, A. Enhanced characteristics of fused silica fibers using laser polishing. *Class. Quantum Grav*. **31**, 105006 (2014).

166. Wlodarczyk, K.L. Laser smoothing of binary gratings and multilevel etched structures in fused silica. *Appl. Opt*. **49**, 1997–2005 (2010).

167. Liao, W., Zhang, C., Sun, X., Zhang, L., Yuan, X. Full aperture CO_2 laser process to improve laser damage resistance of fused silica optical surface. *Adv. Condens. Matter Phys.* **12**, 1–5 (2014).

168. Weingarten, C., Buchbinder, D., Pirch, N., Meiners, W., Wissenbach, K., Poprawe, R. Formation and reduction of hydrogen porosity during selective laser melting of AlSi10Mg. *J. Mater. Process. Technol.* **221**,112–120 (2015).

169. Staupendahl, G. A novel Q-switched CO_2 laser and its application. Efficient generation of short pulses with peak power up to 100 kW and high average power. *Laser Tech. J.,* **11**, 22–25 (2014).

170. Weingarten, D., Buchbinder, D., Pirch, N., Meiners, W., Wissenbach, K., Poprawe, R. Formation and reduction of hydrogen porosity during selective laser melting of AlSi10Mg. *J. Mater. Process. Technol.* **221**,112–120 (2015).

171. Feit, M. D., Matthews, M. J., Soules, T. F., Stolken, J. S., Vignes, R. M., Yang, S. T., Cooke, J. D. Densification and residual stress induced by CO2 laser-based mitigation of SiO2 surfaces. *Laser Damage Symposium XLII: Annual Symposium on Optical Materials for High Power Lasers* (2010).

172. Weingarten, C., et al. Glass processing with pulsed CO_2 laser radiation. *Appl. Opt*. **56**, 4, 777–783 (2017).

173. Frost. F., Fechner. R., Ziberi. B., Völlner. J., Flamm. D., Schindler. A. Large area smoothing of surfaces by ion bombardment: fundamentals and applications. *J. Phys.: Condens. Matter.* **21**, 224026 (2009).

174. Zeuner. M., Kiontke, S. Ion beam figuring technology in optics manufacturing. *Opt. Photonik.* **7**, 56–58 (2012).

175. Liao, W., Dai, Y., Xie, X. Influence of material removal programming on ion beam figuring of high-precision optical surfaces. *Opt. Eng.* **53**, 095101 (2014).

176. Fridman, A. *Plasma Chemistry*. Cambridge University Press, Cambridge, United Kingdom (2008).

177. Fricke.K., Reuter. S., Schroder. D., Von Der Gathen, S., Weltmann, K., Von Woedtke, T. Investigation of surface etching of poly (ether ether ketone) by atmospheric-pressure plasmas IEEE Trans. *Plasma Sci*. **40**, 2900–11, (2012).

178. Arnold, T., Boehm,G., Eichentopf, I. M., Janietz, M., Meister, J., Schindler, A. Plasma Jet Machining: A novel technology for precision machining of optical elements. *Vak. Forsch. Prax.* **22**, 10–16 (2010).

179. Takino, H., Shibata, N., Itoh, H., Kobayashi, T., Tanaka, H., Ebi, M., Yamamura, K., Sano, Y., Mori, Y. Plasma chemical vaporization machining (CVM) for fabrication of optics. *J. Appl. Phys.* **37**, 894– 896 (1998).

180. Verma, Y., Chang, A. K., Berrett, J. W., Futtere,K., Gardopee, G. J., Kelley, J., Kyler, T., Lee, J., Lyford, N., Proscia, D., Sommer, P. R. Rapid damage-free shaping of silicon carbide using reactive atom plasma (RAP) processing. *Proc. SPIE.* **6273**, 62730B (2006).

181. Na, L., Qiang, X., Peng, Z., Bo, W. Atmospheric pressure plasma processing of fused silica in different discharge modes. *Plasma Sci. Technol.* **17**, 567–573 (2015).

182. Shi, B., Dai, Y., Xie, X., Li, S., Zhou, L. Arc-enhanced plasma machining technology for high efficiency machining of silicon carbide. *Plasma Chem. Plasma Process*. **36**, 891–900 (2016).

183. Arnold, T., Boehm, G., Schindler, A. Ultrahigh-Rate Plasma Jet Chemical Etching of Silicon. *J. Vac. Sci.Technol. A.* **19**, 2586 (2001).

184. Paetzelt, h., Bueohm, G., Arnold, T. Etching of silicon surfaces using atmospheric plasma jets. *Plasma Sources Sci. Technol.* **24**, 025002 (2015).

185. Arnold, T., Boehm, G., Paetzelt, H. New freeform manufacturing chain based on atmospheric plasma jet machining. *J. of the Opt. Soc. of America A* (2015).

186. Eichentopf, IM., Boehm, G., Arnold, T. Etching mechanisms during plasma jet machining of silicon carbide. *Surf. Coat. Technol.* **205**, S430-S434 (2011).

187. Arnold, T., Boehm, G., Fechner. R., Meister. J., Nickel. A., Frost. F., Haensel. T., Schindler, A. Ultra-precision surface finishing by ion beam and plasma jet techniques-status and outlook. *Nuclear Instruments & Methods in Physics Research Section a-Accelerators Spectrometers Detectors and Associated Equipment*. **616**, 147-156 (2010).

188. Arnold, T., Boehm, G., Paetzelt, H. New freeform manufacturing chains based on atmospheric plasma jet machining. *Journal of the European Optical Society* **11** (2016).

189. Arnold, T., Boehm, G., Paetzelt, H. Precision asphere and freeform optics manufacturing using plasma jet machining technology. *Conference: Optifab* (2017).

190. Arnold, T., Boehm, G., Paetzelt, H. Nonconventional ultra-precision manufacturing of ULE mirror surfaces using atmospheric reactive plasma jets. *Conference: SPIE Astronomical Telescopes + Instrumentation* (2016).

191. Greivenkannp, J. E., Bruning, J. H. Phase shifting interferometry. *Optical Shop Testing*, 2nd edition, Malacara. 577(1992).

192. Jensen, A. E. Absolute calibration method for laser Twyman-Green wavefront testing interferometers. *J. of the Opt. Soc. of America A*. **63**, 1313 (1973).

193. Wyant, J. C., Bennett, V.P. Using computer generated hologram to test aspheric wavefronts. *Appl. Optics*. **11**, 2833-2839 (1972).

194. Platt, B., Shack, R. V. Lenticular Hartmann screen. *Optical Science Center Newsletter*. **5**, 15 (1971).

195. Pfund, J., Lindlein, N., Schwider, J. Non null testing of rotationally symmetric aspheres: A systematic error assessment. *Appl. Opt*. **40**,439-446 (2001).

196. Lindlein, N., Pfund, J., Schwider, J. Expansion of the dynamic range of a Shack Hartmann sensor by using astigmatic microlenses. *Opt. Eng*. **39**, 2220-2225 (2000).

197. Greivencamp, J. E., Smith, D. G., Goodwin, E. Calibration issues with Shack Hartmann sensor for metrology applications. *SPIE proceedings*, St. Etienne (2004).

198. Duparre, A., Ferre- Borull, J., Gliech, S., Notini, G., Bennett, J. Surface characterization techniques for determining the root-mean-square roughness and power spectral densities of optical components. *Applied Optics*. **41**, 154-171, (2002).

199. Stover, J., Optical Scattering: Measurement and Analysis, *2nd ed. SPIE Optical Engineering Press*, Bellingham, WA, (1995).

200. Lüth, H. Scattering from Surfaces and Thin Films. Solid Surfaces, Interfaces and Thin Films. Springer, Cham, 2015. 129-216.

201. Murphy, P., Flieg, J., Forbes, G., Miladinovic, D., Vries, G.D., Donohue, S.O. Sub aperture stitching interferometry for testing mild aspheres. *Proc. SPIE*, **6293**,1-10 (2006).

202. Robinson, D. W., Reid, G. T. Interferometer Analysis-Digital Fringe Pattern Measurement Techniques. *IOP publishing Ltd,* Bristol (1993).

203. Dörband, B., Tiziani, H. J. Testing aspheric surfaces with compute generated holograms: Analysis of adjustment and shape errors. *Appl. Optics*. **24**, 2604-2611 (1985).

204. Reichelt, S., Tiziani, H. J., Zappe, H. Self-calibration of wavefront testing interferometers by use of diffractive elements. *SPIE Proc*., San Diego (2006).

205. Liesener, L., Tiziani, H. J. Interferometer with dynamic reference, *Proc. SPIE*. **5252**, 264-271 (2004).

206. Pruss, C., Tiziani, H. J. Dynamic null lens for aspheric testing using a membrane mirror. *Optics Communications*. **233**, 15-19 (2004).

207. Kazemi, F., Boehm, G., Arnold, T. Ultra-precise surface machining of N-BK7 using microwave-driven reactive plasma jet machining. *Optics and Measurement 2019 International Conference*. **11385**, 1138509 (2019).

208. Kazemi. F., Boehm. G., Arnold. T. Development of a model for ultra-precise surface machining of N-BK7® using microwave-driven reactive plasma jet machining. *Plasma Processes Polym*. **16**, 12 (2019).

209. Kazemi, F., Arnold, T., Lorenz, P., Ehrhardt, M., Zimmer, K. Residual Layer Removal of Technical Glass Resulting from Reactive Atmospheric Plasma Jet Etching by Pulsed Laser Irradiation. *Plasma Chem Plasma Process*. **40**,1241–1251(2020).

210. Wang, G., Wang, H., Shen, L., Hou,J., Xu, Q., Wang, J., Chen, X., Liu, Z. Effect of temperature on surface error and laser damage threshold for self-healing BK7 glass. *Appl. Opt*. **57**, 2032 (2018).

211. Reinhardt, K., Kern, W. *Handbook of Silicon Wafer Cleaning Technology*. Elsevier Science (2008).

212. Walecki, W.J., Szondy, F., Hilali, M.M. Fast in-line surface topography metrology enabling stress calculation for solar cell manufacturing for throughput in excess of 2000 wafers per hour. *Meas. Sci. Technol.* 19, 025302 (2008).

213. Stout, K. J., Blunt, L. Three-Dimensional Surface Topography (2nd ed.). *Penton Press.* **22** (2000).

214. Binnig, G., Calvin, F., Gerber, C. Atomic force microscope. *Physical review letters.* **56**, 930–933 (1986).

215. Kazemi, F., Arnold, T., Lorenz, P., Ehrhardt, M., Zimmer, K. Combined Reactive Plasma Jet-laser Etching Method for Technical Optical Glass Containing Metal Oxides, *Applied Surface Science*, (2021).

216. Kreilkamp, H. *Analyse der Einflüsse auf die Gestaltabwei-chung gepresster Glasoptiken beim nicht-isothermen Blank-pressen*. Apprimus Verlag, Aachen, Deutschland, (2018).

217. Kazemi, F., Boehm, G., Arnold, T. Optical freeform generation of N-BK7 by fluorine-based plasma jet machining. *Seventh European Seminar on Precision Optics Manufacturing*. 1147805 (2020).

218. Mogab, C. J., Adams, A. C., Flamm, D. L. Plasma etching of Si and SiO_2 The effect of oxygen additions to CF_4 plasmas. *J. Appl. Phys.***49**,3796 (1978).

219. Arrhenius, S. A. Über die Dissociationswärme und den Einfluß der Temperatur auf den Dissociationsgrad der Elektrolyte. Z. *Phys. Chem.* **4**, 96–116 (1889).

220. Arrhenius, S. A. Über die Reaktionsgeschwindigkeit bei der Inversion von Rohrzucker durch Säuren. Z. *Phys. Chem*. **4**, 226–48 (1889).

221. Kazemi. F., Boehm.G., Arnold, T. An Investigation on Effectiveness of Temperature Treatment for Fluorine-based Reactive Plasma Jet Machining of N-BK7®. *Plasma Process Polym*. **17**, (2020).

222. Schmitt, J., Meier, A., allrabe, U. W., Voelklein, F. RIE (CF_4/Ar) and IBE etching of various glasses for diffractive optical element fabrication. *Int.J. Glass. Sci*. 9, 499 (2018).

223. National Institute of Standards and Technology. *NIST Standard Reference Database*, https://webbook.n ist.gov/chemistry/ (2018).

224. Magee, C. W., Honig, R.E. Secondary ion quadruple mass spectrometer for depth profiling design and performance evaluation. Review of Scientific Instruments. **49**, 477–485 (1978).

225. Piechulla, P., Bauer, J., Boehm, G., Paetzelt, H., Arnold, T. Etch Mechanism and Temperature Regimes of an Atmospheric Pressure Chlorine-Based Plasma Jet Process. *Plasma Processes and Polymers* **13**, 2016.

226. Kazemi, F., Boehm, G., Arnold, T., Recursive algorithm for modeling non-linear etching rates in reactive plasma jet based optical surface machining of borosilicate crown glass. Precision Engineering.

227. Wang, C., Yang, W., Wang, Z., Yang, X., Hu, C., Zhong, B., Guo, Y., Xu, Q. Dwell-time algorithm for polishing large optics. *Appl. Optic.* **53**, 4752–4760 (2014).

228. Su. X, Zhang. P., Liu, K., Xia, L., Li, P., Zhao, R., Wang, B. Fabrication of continuous phase plate using atmospheric pressure plasma processing. *The International Journal of Advanced Manufacturing Technology*. **105**, 4559–4570 (2019).

229. Van Cittert, P. H. Zum Einfluß der Spaltbreite auf die Intensitätsverteilung. *in Spektrallinien. II. In: Zeitschrift für Physik.* **69**, 298–308, 1931.

230. Deal, B. E., Grove, A.S. General Relationship for the Thermal Oxidation of Silicon. *J. Appl. Phys.* **36**, 3770 (1965).

231. Gerlach, G., Maser, K. A Self-Consistent Model for Thermal Oxidation of Silicon at Low Oxide Thickness. *Adv. Condens. Matter Phys*. **13**,7545632 (2016).

232. Kazemi. F., Boehm.G., Arnold, T. A novel Deal–Grove□inspired model for fluorine based plasma jet etching of borosilicate crown optical glass. *Plasma Process Polym*. **18** (2021).

233. Hopper, M. A., Clarke, R. A., Young, J.Thermal Oxidation of Silicon: In Situ Measurement of the Growth Rate Using Ellipsometry. *Electrochem. Soc.* **122**, 1216 (1975).

234. Mahorowala, A., Sawin, H. etching of polysilicon in inductively coupled Cl2 and HBr discharges. I. Experimental characterization of polysilicon profiles. *Journal of Vacuum Science & Technology B: Microelectronics and Nanometer Structures Processing, Measurement, and Phenomena*. **20**, 1055 (2002).

235. Kushner, M. J. A model for the discharge kinetics and plasma chemistry during plasma enhanced chemical vapor deposition of amorphous silicon. *Journal of applied physics* **63**, 2532-2551 (1988).

236. Nicholson, D. R. *Introduction to plasma theory*. New York: Wiley (1983).

237. Smirnov, B. M. *Theory of gas discharge plasma*. Cham: Springer International Publishing, (2015).

238. Conrads, H., and Schmidt, M. Plasma generation and plasma sources. *Plasma Sources Science and Technology* **9**, 441(2000).

239. Hutchinson, I. H. Principles of plasma diagnostics. *Plasma Physics and Controlled Fusion*. **44**, 2603 (2002).